

Impact of tissue microstructure on a model of cardiac electromechanics based on MRI data



Valentina Carapella
St Catherine's College
University of Oxford

A thesis submitted for the degree of
Doctor of Philosophy
Michaelmas 2013

Abstract

Cardiac motion is a highly complex and integrated process of vital importance as it sustains the primary function of the heart, that is pumping blood. Cardiac tissue microstructure, in particular the alignment of myocytes (also referred to as fibre direction) and their lateral organisation into laminae (or sheets), has been shown by both experimental and computational research to play an important role in the determination of cardiac motion patterns. However, current models of cardiac electromechanics, although already embedding structural information in the models equations, are not yet able to fully reproduce the connection between structural dynamics and cardiac deformation. The aim of this thesis was to develop an electromechanical modelling framework to investigate the impact of tissue structure on cardiac motion, focussing on left ventricular contraction in rat. The computational studies carried out were complemented with a preliminary validation study based on experimental data of tissue structure rearrangement during contraction from diffusion tensor MRI.

Acknowledgements

I am very grateful to Dr Vicente Grau, my principal supervisor, for all his help and patience over the course of my DPhil. I would also like to thank my other supervisors: Dr Rafel Bordas and Dr Pras Pathmanathan, for their help on any problem arising on the modelling side, and Professor Kevin Burrage, for his fruitful advice. I am grateful to Dr Maelene Lohezic for her assistance on the analysis of imaging data. Finally, I would like to express my warmest gratitude to my husband, Ernesto, for his unfailing support and loving encouragement.

Glossary of symbols

Latin letters

Symbol	Description
$a_{endo}, b_{endo}, c_{endo}$	semi-axes defining the endocardial surface of the ellipsoidal mesh
$a_{epi}, b_{epi}, c_{epi}$	semi-axes defining the epicardial surface of the ellipsoidal mesh
ADC	apparent diffusion coefficient
AP	action potential
b_{ij} for $i, j = f, s, n$	stiffness parameters of the strain-energy function W
\mathbf{c}	circumferential unit vector in the global cylindrical coordinate system
\mathbf{C}	Green deformation tensor
C_b	level of compressibility of the strain-energy function W
C_m	membrane specific capacitance
cl -plane	circumferential-longitudinal plane (in either the global or local reference frames)
cr -plane	circumferential-radial plane (in either the global or local reference frames)
cv_f, cv_{cf}	conduction velocity in the fibre and cross-fibre directions
d	normalised transmural depth
D	diffusion tensor
E	Lagrangian strain tensor
$\langle edge \rangle$	average edge length (of the elements of a mesh)
EF	ejection fraction
\mathbf{f}	unit vector for the fibre direction at a point in the undeformed body
$\tilde{\mathbf{f}}$	unit vector for the fibre direction at a point in the deformed body
F	deformation gradient tensor
FA	fractional anisotropy
I_{stim}	external stimulus
J	Jacobian (determinant) of F
K2003	contraction model by Kerkchoffs et al. [75]
Karadag	label for the locally optimised fibre model [71]
\mathbf{l}	longitudinal unit vector in the global cylindrical coordinate system

Symbol	Description
$lr\text{-plane}$	longitudinal-radial plane (in either the global or local reference frames)
$mesh_e$	electrophysiological mesh for simulations without pressure
$mesh_m$	mechanical mesh for simulations without pressure
\mathbf{n}	unit vector for the sheet-normal direction at a point in the undeformed body
$\tilde{\mathbf{n}}$	unit vector for the sheet-normal direction at a point in the deformed body
$ortho^U$	orthotropic material law by Usyk et al. [166]
$post\text{-}P\ mesh_e$	electrophysiological mesh for the simulations with pressure
$pre\text{-}P\ mesh_m$	mechanical mesh for the simulations with pressure
P_{es}, P_{ed}	prescribed end-systolic and end-diastolic pressure values
$\langle q \rangle$	average skewness (quality measure for tetrahedral meshes)
\mathbf{r}	radial unit vector in the global cylindrical coordinate system
R	maximum rotation angle for a given model of fibre direction
Rat_C, Rat_S	contracted and slack (relaxed) states for the rat imaging dataset
\mathbf{s}	unit vector for the sheet direction at a point in the undeformed body
$\tilde{\mathbf{s}}$	unit vector for the sheet direction at a point in the deformed body
S	1st Piola-Kirchhoff stress tensor
S_0	baseline signal acquired in DT-MRI without diffusion-sensitizing gradients
SL	shortening in the base-to-apex direction
$SnxRy$	label for global rule-based fibre models
t	time
T	2nd Piola-Kirchhoff stress tensor
t_{iso}	transversely isotropic material law obtained from averaging the parameters of $ortho^U$
t_{iso}^U	original transversely material law by Usyk et al. [166]
t_{iso}^*	corrected transversely material law from t_{iso}^U
\mathbf{u}	radial unit vector in the local cylindrical coordinate system
\mathbf{v}	circumferential unit vector in the local cylindrical coordinate system
V	transmembrane voltage
VR	volume reduction
\tilde{w}	wall thickness at the base of the ellipsoidal mesh measured in the local reference frame
$\langle w \rangle$	average wall thickness over the entire ellipsoidal mesh measured in the global reference frame
\mathbf{w}	longitudinal unit vector in the local cylindrical coordinate system
W	strain-energy function
Wang2008	AP model by Wang and Sobie [176]
WT	wall-thickening
$\mathbf{X} = (X_1, X_2, X_3)$	Cartesian coordinates of a point in the undeformed body Ω_0
$\mathbf{x} = (x_1, x_2, x_3)$	Cartesian coordinates of a point in the deformed body Ω_t

Greek letters

Symbol	Description
α, β, γ	the helix, sheet and transverse angles
$\tilde{\alpha}, \tilde{\beta}, \tilde{\gamma}$	intrinsic helix, sheet and transverse angles
$\partial\Omega_0$	boundary of the spatial domain at time $t = 0\text{ ms}$
$\partial\Omega_0^D$	part of the boundary of Ω_0 for Dirichlet boundary conditions
$\partial\Omega_0^N$	part of the boundary of Ω_0 for (traction) Neumann boundary conditions
ϵ	effective conductivity tensor
$\lambda_1, \lambda_2, \lambda_3$	eigenvalues of the diffusion tensor D
λ_f	stretch in the fibre direction
ν_1, ν_2, ν_3	eigenvectors of the diffusion tensor D
σ	Cauchy stress tensor
σ_a	Cauchy stress generated by the contraction model
χ	surface area-to-volume ratio
Ω_0	reference (undeformed) spatial domain at time $t = 0\text{ ms}$
Ω_t	deformed spatial domain at a generic time t

Contents

Introduction	1
1 Anatomy and physiology of the heart	6
1.1 Cardiac anatomy and function	6
1.1.1 The cardiac cycle	7
1.1.2 Cardiac tissue microstructure	9
1.2 Cardiac myocyte	11
1.2.1 The action potential	12
1.2.2 The contractile activity of the myocyte	14
1.3 Indices of cardiac function	16
1.3.1 Indices of global cardiac function	16
1.3.2 Indices of local cardiac function	17
1.4 The chosen animal model: the laboratory rat	18
2 Imaging and quantifying cardiac tissue microstructure	21
2.1 Cardiac imaging modalities	21
2.2 Imaging tissue structure with diffusion tensor MRI	23
2.2.1 Physical basics of MRI	24
2.2.2 Fick's model of diffusion	25
2.2.3 Measuring diffusion with MRI	25
2.2.4 Diffusion anisotropy indices	27
2.2.5 From diffusion tensor to tissue structure	28
2.2.6 Other imaging modalities used to study cardiac tissue structure . . .	30
2.3 Quantifying tissue structure: angular metrics	31
2.3.1 Coordinate systems for tissue structure characterisation	31
2.3.2 Formal definition of the angular metrics	33
2.4 Description of the images datasets	35

3	Computational models of cardiac electromechanics	38
3.1	State-of-the-art on cardiac modelling	38
3.1.1	Ventricular geometry	38
3.1.2	Modelling cardiac electrophysiology	40
3.1.3	Modelling cardiac mechanics	41
3.1.4	Models of cardiac electromechanics	44
3.1.5	Modelling and imaging, two converging fields	46
3.1.6	The role of tissue structure in cardiac modelling	47
3.2	Mathematical background	49
3.2.1	Electrophysiology	49
3.2.1.1	Tissue electrical propagation	49
3.2.1.2	Myocyte electrical activity	50
3.2.2	Mechanics	51
3.2.2.1	Tissue constitutive properties	52
3.2.2.2	Tissue stress generation	53
3.2.2.3	Myocyte contractile activity	54
3.2.2.4	Blood Pressure as additional boundary condition	55
3.2.3	Numerical scheme for the electromechanical model	55
3.2.3.1	Temporal discretisation	55
3.2.3.2	Spatial discretisation: the finite element method	55
3.3	Electromechanical simulations	56
4	Development of a model of rat left ventricular electromechanics	59
4.1	General components of the EM model	59
4.2	Geometrical model of rat left ventricle	60
4.3	Electrophysiological component	63
4.3.1	AP model	63
4.3.2	Electrophysiological parameters	64
4.3.3	Numerical parameters for the electrophysiological problem	67
4.4	Modelling rat mechanics	68
4.4.1	The contraction model	69
4.4.2	Passive deformation	71
4.4.3	Numerical parameters for the mechanical problem	72
4.5	Mathematical definition of tissue structure	74
4.5.1	Tissue structure definition on the ellipsoidal mesh	75
4.5.2	Global models of fibre direction	76

4.5.3	Locally optimised model of fibre direction	77
4.5.4	Models of sheet orientation	78
4.5.5	Relation between extrinsic and intrinsic angles	78
5	Effect of fibre orientation optimisation in an electromechanical model of left ventricular contraction in rat	81
5.1	Introduction	81
5.2	Global metrics for the evaluation of cardiac function	82
5.2.1	Global metrics measurements on cine-MRI	83
5.3	Further model development	84
5.3.1	Boundary conditions	84
5.3.2	Passive deformation	85
5.3.2.1	Effect of average stiffness versus material symmetry . . .	85
5.3.2.2	Finding C_b value for near incompressibility	86
5.3.3	Cross-fibre active tension	88
5.4	Effect of fibre optimisation on contraction	90
5.4.1	Results	90
5.4.2	Discussion	92
6	A quantitative study of the effect of tissue structure on contraction in a computational model of rat left ventricle	94
6.1	Introduction	94
6.2	Local metrics for the evaluation of cardiac function	96
6.3	Adding pressure to the electromechanical model	97
6.3.1	Passive expansion under constant pressure	98
6.3.2	Time-varying pressure trace	100
6.4	Effect of tissue structure on left ventricular contraction	102
6.4.1	Results for global metrics	103
6.4.2	Results for local metrics	105
6.5	Discussion and concluding remarks	109
7	Measuring tissue structure distribution on two-state DT-MRI	112
7.1	Introduction	112
7.2	Part A: measuring angular metrics on DT-MRI	117
7.2.1	Methods	117
7.2.1.1	Segmentation of the left ventricle on DT-MRI	118

7.2.1.2	Assignment of local and global reference frames to the segmented left ventricle	119
7.2.2	Results	123
7.2.2.1	Measuring the helix angle	123
7.2.2.2	Measuring the transverse angle	129
7.2.2.3	Measuring the sheet angle	133
7.3	Angular measures on simulations	136
7.4	Discussion and concluding remarks	139
8	Conclusions and future directions	142
8.1	Summary	142
8.2	Future work	143
	Appendices	145
A	Protocol for Angular Metrics	146
B	Phantom imaging for validation and hypothesis testing	151
B.1	Definition of the binary ellipsoidal phantom	152
B.2	Assignment of global and local cylindrical system of coordinates to phantom	153
B.2.1	Algorithm for the global coordinate system	153
B.2.2	Algorithm for the local coordinate system	155
B.3	Measuring angular metrics on phantom	157
B.3.1	Alternative method for computing local angular metrics based on projection	162
B.4	Conclusions	164
	Bibliography	165

Introduction

Cardiac motion is a highly complex and integrated process of vital importance as it sustains the primary function of the heart, that is pumping blood. For this reason cardiac motion abnormalities are often associated with severe pathologies. Clinical techniques can assess this fundamental connection between motion anomalous behaviour and pathology only to a certain extent. Computational models of cardiac function that address both its electrophysiological and mechanical components and their interplay, can thus be of great help in linking the underlying physiology to local and global motion. This in turn provides insight into the emergence of pathological conditions.

However, while the electrophysiological properties of the heart, from single cell to the whole organ level, can rely on a well established tradition of computational studies, the mechanical behaviour of the heart is not as well characterised from a modelling point of view. This is particularly true for the contraction phase of the cardiac cycle, in which the combination of contractile force and passive material response makes the mechanical problem difficult to be modelled and computationally expensive. Even some of the more recent models of cardiac (electro)mechanics struggle to correctly predict some important indices of cardiac function, such as deformation patterns, stress distributions, wall-thickening or local tissue structure rearrangement.

Cardiac tissue microstructure, in particular the alignment of myocytes (also referred to as fibre direction) and their lateral organisation into laminae (or sheets), plays an important role in cardiac function, as suggested by experimental and computational research. Current models of cardiac electromechanics, although already embedding structural information in the models equations, are not yet able to fully reproduce the connection between structural dynamics and cardiac deformation. Furthermore, while the distribution, dynamics and role of fibres have been extensively investigated, those of sheets are still a developing field, both in terms of experimental techniques and modelling approach.

Fibre direction provides the local preferential direction for electrical wave propagation and subsequent contraction. The information about fibre direction is often embedded into the

model by using prescribed, that is mathematically defined, orientations, although in recent years the use of orientations extracted from diffusion-tensor magnetic resonance imaging (DT-MRI), also called realistic fibre orientations, has become more frequent, with the caveat that DT-MRI scans can so far be acquired with good resolution only ex-vivo. The laminar structure of cardiac tissue has been long experimentally proven and it is considered to greatly contribute to the even distribution of stress and strain through the tissue. Nonetheless, from the modelling point of view, it is not as well characterised. Sheet rearrangement in particular seems to play a fundamental role in wall-thickening during contraction. Sheet orientation data has been obtained from histological studies as well as from DT-MRI. However, sheet planes distribution and rearrangement during the cardiac cycle are more difficult to quantify and model with respect to the local myocyte orientations.

The hypothesis driving this thesis is that current models of cardiac (electro)mechanics fail to reproduce some important features of cardiac function - such as wall-thickening or local shear strains - because of the above mentioned limitations in the integration of the role of tissue structure in their modelling framework. A more thorough understanding of the mutual interplay of tissue structure and cardiac deformation, in particular concerning sheet dynamics, and the development of new modelling approaches to address this interplay are of the utmost importance. Therefore, the aim of this thesis was to explore the mutual relationship between tissue structure and deformation by focussing on the contraction of the left ventricle, with the rat as the chosen animal model. On the one hand, computational modelling of cardiac electromechanics was employed to understand how different models of tissue structure would change the predicted mechanics. On the other hand, the effect of deformation on tissue structure distribution was measured on two-state ex-vivo DT-MRI data in order to (a) quantify tissue structure rearrangement between relaxed and contracted mechanical states, and (b) validate at the microstructural level the simulations carried out by comparing the measured tissue structure distributions to the predicted ones.

The contributions of this thesis are:

- The development and implementation of an electromechanical model of left ventricular contraction in rat. The computational model is available to the scientific community as part of the open-source software package `Chaste`, which was employed to run all the simulations presented in this thesis.
- A computational study of the effect of different tissue microstructure models on left ventricular contraction. In particular, the use of a more subject-specific approach to tissue structure definition is questioned and showed to be as informative as simple

global approaches, within the developed modelling framework. Additionally, the need for further investigation of the role of sheet dynamics is supported by the results of the study.

- The development of methods to measure tissue structure distribution on DT-MRI data. In particular, a method to quantify tissue structure based on a local coordinate system is proposed and developed. Furthermore, this method is compared with a more standard approach based on a global reference frame, showing that the variability in tissue structure distribution is better quantified by the proposed method based on the local reference frame.
- The presentation of a preliminary validation framework for cardiac electromechanical simulations based on the comparison of predicted and measured redistribution of tissue microstructure during contraction.

The project relies on the integration of cardiac imaging data and mathematical modelling in the belief that realistic models of cardiac function need to reach the best compromise between the level of modelling detail and the amount and quality of information that can be obtained from data in order to instruct or validate such models.

Plan of the dissertation

The thesis is subdivided into the following chapters:

Chapter 1: Anatomy and physiology of the heart. General notions of cardiac anatomy and physiology are summarised. The cellular dynamics underlying the action potential and the contractile ability of the myocyte are addressed. Tissue structure is also described from the anatomical and functional point of view. Then, some common indices of cardiac function at the global and local level are introduced. Finally, the laboratory rat - the chosen animal model for this thesis - is described. The advantages of this choice from the imaging and modelling point of view are discussed.

Chapter 2: Imaging and quantifying cardiac tissue microstructure. DT-MRI is a powerful modality, widely used for imaging and quantifying tissue microstructure in the heart. This chapter explains how diffusion is measured by means of MRI and related to tissue structure. Helix, sheet and transverse angles - the angular metrics usually employed to characterise tissue structure distribution - are defined. Two cylindrical coordinate systems are introduced, a global and a local one, that will be then employed in the measurement of angular metrics in Chapter 7. Finally, the imaging datasets involved in this study are

described. Of particular importance is the dataset of the two-state DT-MRI of perfused hearts, which allows tissue structure to be imaged at relaxed (slack) and contracted states.

Chapter 3: Computational models of cardiac electromechanics. Computational modelling of cardiac electromechanics is discussed, and the state-of-art of the field is described, with a particular focus on the role of tissue microstructure in cardiac modelling as well as on the increasingly important role of imaging in cardiac modelling. The mathematical background of the various components of the electromechanical model is summarised. The numerical scheme (based on the finite element method) for the approximation to the solution of the model is also briefly described.

Chapter 4: Development of a model of rat left ventricular electromechanics. This chapter encompasses the preliminary work performed to obtain a rat-specific electromechanical model of the left ventricle. The generation of the left ventricular mesh, the choice of the appropriate cellular electrophysiological model, the studies performed on a cubic wedge to obtain tissue electrophysiological and mechanical parameters, as well as the choice of cellular contraction model and constitutive law, are described. Finally, the mathematical models of fibre and sheet distribution are described and the way in which such information is integrated in the model is explained.

Chapter 5: Effect of fibre orientation optimisation in an electromechanical model of left ventricular contraction in rat. The results are presented of the first computational study performed on the effect of fibre orientation on contraction in rat left ventricle by means of the electromechanical model (with zero pressure boundary condition) described in the previous chapter. A preliminary study of the effect of sheet plane orientation is performed by comparing a transversely isotropic and an orthotropic constitutive law.

Chapter 6: A quantitative study of the effect of tissue structure on contraction in a computational model of rat left ventricle. The results are presented of the second computational study of the effect of tissue structure on contraction of the left ventricle in rat. This study is a substantial extension to the one described in the previous chapter. A time-varying pressure boundary condition is added to the electromechanical model described in Chapter 4. The study of the effect of different models of fibre direction on mechanics is performed under the more physiological pressure condition. Additionally, the analysis of the effects of cardiac laminar structure is extended with respect to the previous chapter by comparing, in the case of orthotropic material behaviour, two models of sheet angle transmural variation, a linear and a bimodal one.

Chapter 7: Measuring tissue structure distribution on two-state DT-MRI. The changes in tissue structure distribution during contraction are measured on one rat subject from the two-state DT-MRI dataset. Two methods for measuring angular metrics are compared,

the first based on a global cylindrical coordinate system, the second on a local reference frame. The proposed method based on the local approach shows to be more sensitive to the regional and temporal variability of tissue structure than the standard global method. Then, the comparison of measured and predicted variation in angular metrics for a subset of the simulations with pressure is shown. This is a preliminary validation of the simulations output based on microstructural changes.

Chapter 8: Conclusions and future directions. Concluding remarks on the computational studies presented as well as on the complementary study of the effect of deformation on tissue structure distribution on DT-MRI data are given. Future directions unfolded by the research presented in this thesis are also discussed.

Appendix A: Protocol for angular metrics. More details are given on the way angular metrics are measured either on images or in simulations.

Appendix B: Phantom imaging for validation and hypothesis testing. Supplementary material to Chapter 7, describing the development of the algorithms for the measurements of angular metrics and initial hypothesis testing on a phantom image, is provided here.

Chapter 1

Anatomy and physiology of the heart

This chapter provides a brief introduction to the anatomy and physiology of the heart. The organ-level function is related to the specific characteristics of the cardiac myocyte, with its excitable nature and contractile activity, which are also described. Then, some of the indices that are commonly used to assess cardiac function are introduced. Finally, the laboratory rat - the animal model of reference for this thesis - is described and the advantages of this choice from the imaging and modelling point of view are discussed.

1.1 Cardiac anatomy and function

This section is concerned with the broad anatomy of the heart and its function. The concepts hereby presented are generally valid for the mammalian hearts. For a more detailed description of cardiac anatomy and physiology please refer to [81], [14].

The heart is a four-chambered organ, whose function is to pump blood to the whole body. Figure 1.1(a) shows a drawing of the main components of the heart. The two upper chambers are called the right and left atria, and the two lower chambers are the right and left ventricles. The top of the ventricles is called the base, while the lowest part is the apex. The muscle tissue of the heart is the *myocardium*, which is contained between an internal layer, the *endocardium*, and an external layer, the *epicardium*. The whole heart is contained and constrained by the *pericardial membrane*. Blood flows from the right atrium into the corresponding ventricle through the tricuspid valve. Similarly, blood flows from the left atrium into the left ventricle through the mitral valve. The two valves are tied to the ventricular cavity by means of the *papillary muscles* and *chordae tendineae*. The two atria can be thought of as reservoirs for the corresponding ventricles, which are the actual pumping machinery of the heart. The right ventricle pumps blood through the pulmonary valve into the pulmonary artery which delivers blood to the pulmonary circulation system. The left

ventricle pumps blood through the aortic valve into the aorta, the largest artery of the human body, which delivers blood to the systemic circulation, that is the rest of the body. On the way back to the heart, the blood coming from the systemic circulation is gathered into the right atrium, while the blood from the pulmonary circulation goes to the left atrium. Figure 1.1(b) shows a schematic of the blood flow from the heart to the circulatory system and vice versa. When blood is pumped from the left ventricle to the systemic circulation it has been newly oxygenated by the pulmonary system, therefore it is capable of carrying oxygen and nutrients to rest of the body. Conversely, the de-oxygenated blood returns to the right atrium and is then pumped by the right ventricle into the pulmonary circulation to be oxygenated again.

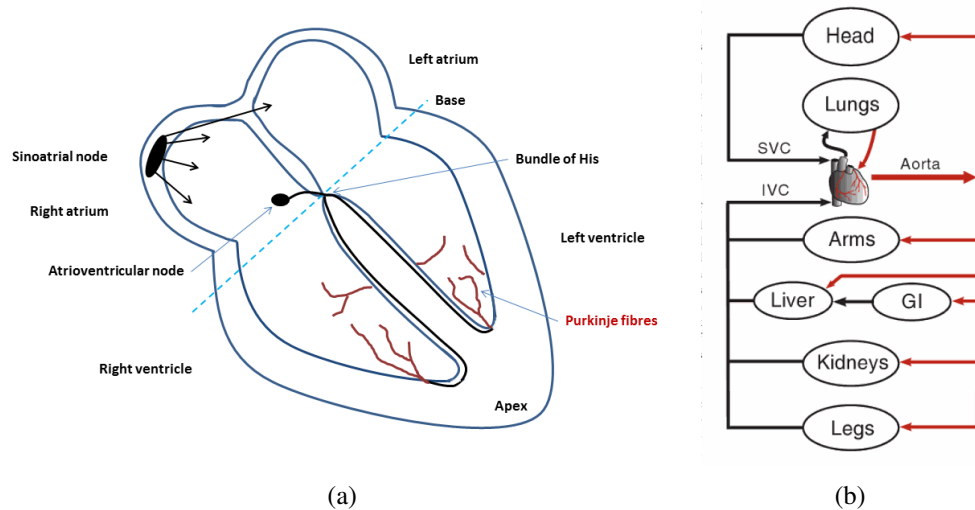


Figure 1.1: (a) Main components of the heart. (b) Schema of blood flow from the heart to the circulatory system and back. Red arrows show the flow from the heart to the body, black arrows show the reverse [81], reproduced with permission from Lippincott Williams & Wilkins.

1.1.1 The cardiac cycle

The basic unit of this continuous loop is the heartbeat, which results from the combination of electrical and mechanical activity at the subcellular, cellular, tissue and whole organ level. At the whole organ level, the cardiac cycle begins with the generation of an electrical pulse at the *sinoatrial node*, a region in the upper part of the right atrium, consisting of specialised cardiac cells, the *pacemaker cells*, which are able to self-initiate an electrical stimulus. This stimulus spreads quickly from one cell to its neighbours through the gap-junctions, specialised channels connecting adjacent cells. At the organ level, the stimulus travels through the right and left atria eliciting their contraction and therefore the flow of

blood from the atria to the ventricles. The atria are electrically isolated from the ventricles, the only connection being the *atrioventricular (AV) node*. This causes a certain delay between the atrial and ventricular spread of the electrical wave, which is fundamental for the efficiency of the pumping function of the heart. From the AV node, the electrical pulse travels through the *Bundle of His*, which is subdivided into the left and right bundle branches, each of which is responsible for the signal propagation in the corresponding ventricle. The electrical propagation into the ventricles follows a reversed direction with respect to the atria. The signal is carried through the bundle branch right to the apex and then propagates upwards throughout the tissue. The efficiency of contraction of the ventricles requires the tissue to contract almost simultaneously. This is achieved through a dense network of *Purkinje fibres*, which consists of specialised cells optimised for fast electrical conduction. Purkinje fibres excite the myocardium, whose contraction is initiated by the propagation of the electrical wave.

The ordered sequence of contraction and relaxation of atria and ventricles represents the cardiac cycle. This is broadly divided into *systole*, corresponding to ventricular contraction, and *diastole*, corresponding to ventricular relaxation. Each of these phases is usually further subdivided into major components as detailed below. Each phase is associated with a specific behaviour of blood pressure and ventricular volume, two fundamental parameters of cardiac function that are mutually dependent and whose variation during the cardiac cycle is summarised in the plots of Figure 1.2.

In the following, the phases of the cardiac cycle are summarised (see Figure 1.2(a)). Phase 1 is at the beginning of ventricular systole when atrial contraction occurs. At the end of phase 1 the tricuspid and mitral valves close, blocking the flow of blood from the atria into the ventricles. This is when *isovolumetric contraction* begins (phase 2). This is a short phase in which all valves are closed, therefore no change of ventricular volume is possible although the ventricles are already contracting. As a consequence, blood pressure increases rapidly until it equals the arterial pressure, after which the aortic and pulmonary valves open, and the *rapid ejection* phase begins (phase 3). This is followed by a *reduced ejection* phase (phase 4) in which pressure decreases as blood keeps flowing out of the ventricles, therefore blood flow tends to get slower. Once the pressure in the ventricles drops below the arterial one, the aortic and pulmonary valves close and diastole begins. There is a first phase of *isovolumetric relaxation* (phase 5) in which all valves are closed while the ventricles relax, therefore the pressure drops even further. When it becomes lower than the blood pressure in the atria, the tricuspid and mitral valves open and let the blood flow from the atria into the ventricles. Due to the pressure gradient, there is a first *rapid filling* phase

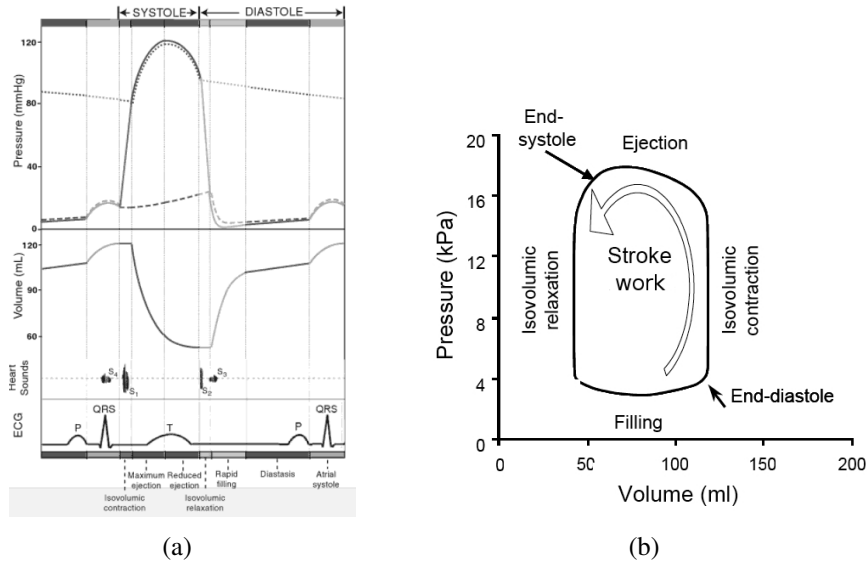


Figure 1.2: (a) Wigger's diagram, a composite plot of blood pressure (upper plot) and volume (middle plot) variation in time in the average human left ventricle [72]. Cardiac phase names are shown at bottom. Reproduced with permission from Lippincott Williams & Wilkins. **Legend:** AP (dotted line) represents the aortic pressure, LVP (solid line) the left ventricular pressure, LAP (dashed line) is the left atrial pressure, LVEDV and LVESV are left ventricular end-diastole and end-systole volumes, respectively. Reproduced with permission from Lippincott Williams & Wilkins. (b) Ventricular blood pressure versus ventricular volume during the cardiac cycle for the left ventricle, adapted from [167], reproduced with permission from Springer.

(phase 6), followed by a *reduced filling* phase (phase 7) in which the ventricular pressure is increasing slowly. At rest, by the end of this phase 90% of the ventricular filling has taken place. The final 10% filling is due to atrial contraction. During this final step, contraction triggers again the closure of the tricuspid and mitral valves and the following ventricular systole begins.

1.1.2 Cardiac tissue microstructure

As explained in the previous section, the pumping function of the heart is a complex and perfectly timed sequence of events. In particular, the electrical wave propagation and subsequent contraction follow a complex pattern across the tissue that is sustained by the high heterogeneity of tissue structure. The extracellular matrix (ECM) is responsible for the organisation of myocytes into structure and hence its passive mechanical properties. The main component of ECM is collagen, the most abundant protein in mammals. Collagen in the heart can be divided into three classes: epimysium, endomysium and perimysium. Epimysial collagen surrounds the entire cardiac muscle, endomysial collagen embeds single myocytes and capillaries. Perimysial collagen groups myocytes into layers 4-6 cells thick, separated by cleavage planes to form a branching architecture, usually referred to as

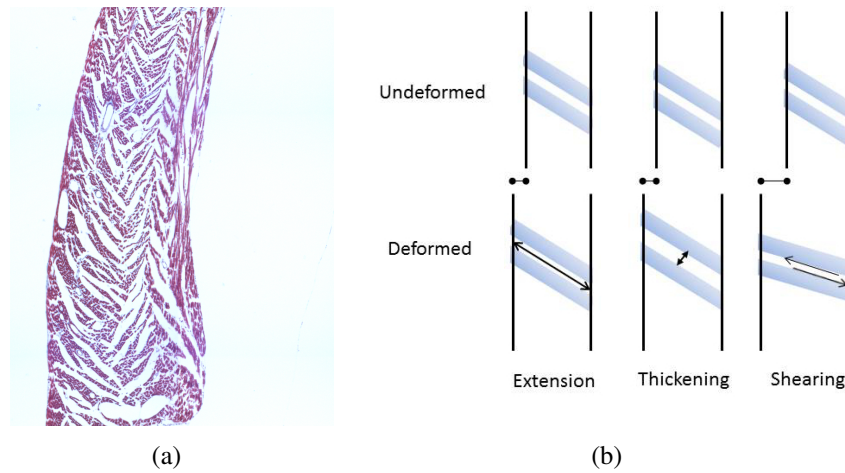


Figure 1.3: (a) Cleavage planes and sheets are highlighted in this transverse histology cut (Courtesy of Dr Rebecca Rowland). (b) Hypothesised sheet dynamics during contraction, redrawn from [32].

laminar structure, while a single layer is called a lamina or a sheet, see Figure 1.3(a).

Although there is general agreement about the local alignment of cells and their organisation into sheets, disagreement remains on their exact characteristics in beating hearts, their alteration due to pathology and in general their degree of contribution to cardiac function [51]. Sheet dynamics has been suggested as the main driving force of the thickening of the left ventricular wall during contraction [27], a phenomenon that cannot be explained solely by the change in shape of the individual myocytes upon contraction [35]. In particular, three mechanisms have been identified that could explain the rearrangement of sheets due to deformation and the resulting wall thickening: extension of the sheet in the transmural depth of the ventricle, thickening of the sheet, and relative sliding (or shearing) of one sheet with respect to the other [32]. Figure 1.3(b) shows a diagram of these three mechanisms.

Because of their elongated shape, myocytes possess a principal direction given by the long axis of the cell. At the tissue level, this local myocyte orientation provides a net axial direction, usually called the *fibre direction*, see Figure 1.4(a). It is along the fibre direction that electrical excitation propagates fastest and that the principal component of contraction takes place.

From the experimental point of view, the study of the distribution of tissue structure in the heart has a long tradition. In the late 1960s, Streeter [158] carried out a fundamental histological study of canine tissue structure and developed one of the first models of fibre distribution in the transmural depth of the ventricular wall. Mathematical models of fibre

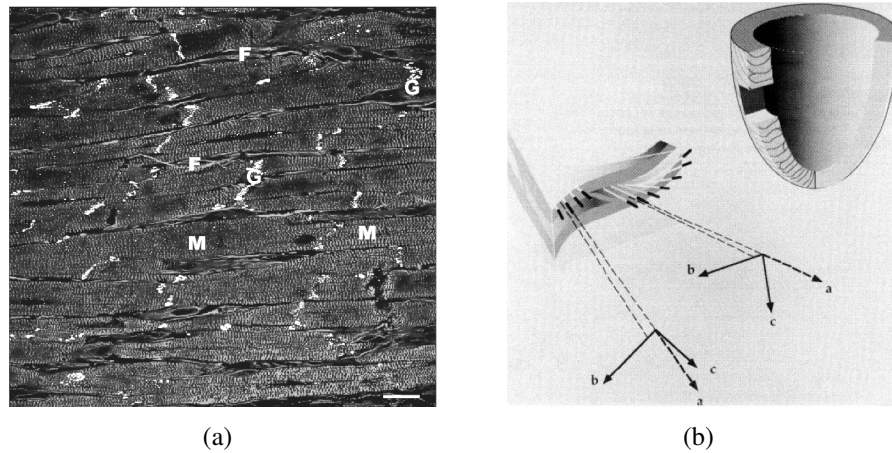


Figure 1.4: (a) Elongated shape of myocytes in cardiac tissue, and local preferential orientation, adapted from [127], reproduced with permission from Wiley. **Legend:** M represents the myocyte, G is the gap-junction connecting adjacent myocytes while F stands for fibroblast, the cell producing collagen. (b) A model of fibre and sheet distribution in the left ventricle [94].

distribution based on Streeter findings were employed in the simulation studies of Chapters 5 and 6, and are described in Section 4.5.2. In the early 1990s, the histological study by LeGrice et al. [94] was a significant contribution to the understanding and modelling of sheet distribution. Figure 1.4(b) shows the model of transmural variation of fibre and sheet orientation they developed. Histology was the first experimental technique to be employed in the study of tissue structure, but more recently other imaging modalities have been successfully applied, as discussed in Sections 2.2.5 and 2.2.6. Finally, the role of tissue structure in cardiac modelling is addressed in Section 3.1.6.

1.2 Cardiac myocyte

The electrical and mechanical properties of the heart have their foundation in the cardiac muscle cell, the cardiac myocyte, with its excitable nature and its ability to contract. In this section the properties of the myocyte are described that underlie its electrical behaviour and contractile ability.

Every cell has a cell membrane, which is a lipid bilayer acting as a selective barrier to diffusion of molecules and ions [73]. Distributed along the membrane there are a number of pores, essentially agglomerates of proteins which create a tunnel across the membrane and, depending on various factors (for example, gradient of ionic concentration or mechanical stretch) allow or prevent the passage of selected chemical entities. Such pores can be divided into *ion channels*, which once open allow the passive flow of ions along their concentration gradient, and *ion pumps*, which instead use energy (often in the form of ATP)

in an active process that forces the ion to flow against its concentration gradient. While ion channels tend to restore the electrochemical equilibrium between the intracellular and extracellular spaces, for its own survival the cell needs to maintain a gradient of concentration of the various ions, which results in an electrical potential difference across the membrane - referred to as the transmembrane voltage - hence the need of both ion channels and pumps. The peculiarity of excitable cells, among which are neurons, muscle cells and cardiac myocytes, is the fact that upon electrical stimulation the permeability of their membrane changes, through different ion channels opening or closing depending on the value of the transmembrane voltage. The three main ions in cardiac electrophysiology are: sodium (Na^+), calcium (Ca^{2+}) and potassium (K^+) ions. There are several different types of ion channels and pumps that regulate the inward and outward flow of such ions, whose detailed description goes beyond the aim of this chapter. The interested reader can refer to [140]. For example, Figure 1.5(a) shows a schematic of the ion channels included in the electrophysiological model for the guinea pig myocyte developed by Luo et al. [101].

1.2.1 The action potential

The electrical propagation in cardiac tissue is the result of the perfectly timed sequential excitation of the myocytes, whose electrical coupling takes place via the gap junctions. The excitation event the cell undergoes, called the *action potential* (AP), is a sudden and large increase in the transmembrane potential from its resting value, approximately -85 mV , to the excited state of about 45 mV [133]. The AP arises from the equilibrium of inward and outward ionic currents across the cell membrane. In a typical cardiac cell, the inward currents of Na^+ and Ca^{2+} depolarise the cell, that is, they increase the transmembrane potential. Conversely, the outward current due to K^+ repolarises it. The AP is an all-or-none response and consists of different phases, as shown in Figure 1.5(b). Phase 0, the upstroke, occurs when an electrical stimulus raises the membrane voltage above a threshold value (approximately -65 mV), which causes sodium channels to open, leading to a rapid influx of Na^+ into the cell. This depolarises quickly the membrane up to the maximum voltage. In phase 1 there is a partial early rapid repolarisation of the membrane due to the outflow of K^+ . During phase 2, or plateau phase, the membrane voltage remains constant for a relatively long period, due to the balance of inward calcium and outward potassium currents. During phase 3, the calcium current stops and the potassium current fully repolarises the cell membrane. In phase 4, the cell membrane voltage returns to its resting value. From phase 0 to phase 2 the myocyte is unable to initiate a new AP upon receiving a new stimulus, which is called the *effective refractory period*. During phase 3, in the *relative refractory period*, a new AP can be elicited by a strong stimulus resulting in an early AP, which will

have a slower and reduced upstroke and an overall shorter duration due to the fact that the ion channels involved in the AP generation have not recovered yet. This phenomenon can have dramatic consequences for example in the development of arrhythmias [162].

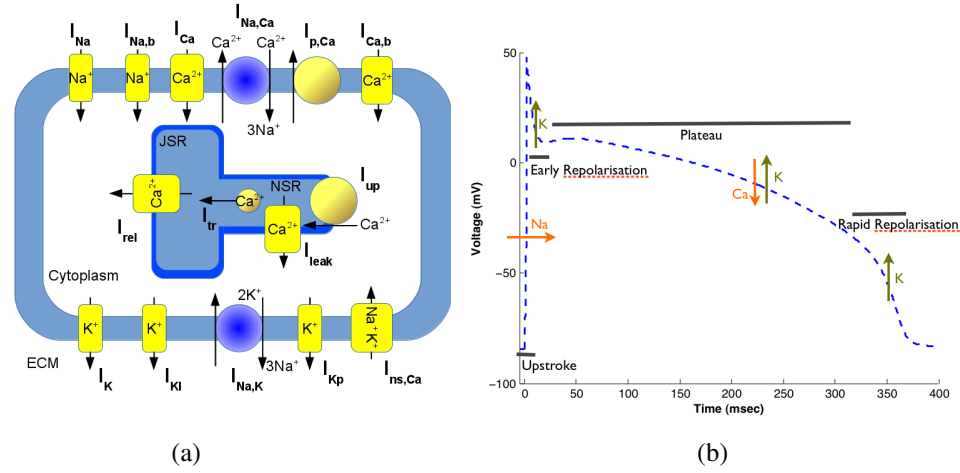


Figure 1.5: (a) Diagram of some of the ionic channels and pumps involved in the generation of AP. (b) General subdivision of AP into its phases. The underlying AP for both images is from the Luo et al. [101] model for the guinea pig myocyte.

Although the dynamics underlying the AP are similar in all cardiomyocytes, the shape and duration of the AP is subject to great variability, not only between species and same-species subjects, but even within the same heart. For example, the average AP duration in guinea pig myocytes is approximately 380 ms [100], similar to that in human 340 ms [160], while the AP duration in rat is significantly shorter (100 ms [122]). The rat AP has a very short plateau phase, as can be seen in Figure 4.2(a). Within the same heart, there is a significant difference between the AP of the pacemaker cells or those forming the Purkinje fibres and the average myocyte, which is to be expected, given the different role that each of these cells has. Significant spatial variability of AP exists also among myocytes, with the AP of epicardial cells being significantly shorter than that of middle and endocardial cells. Such variability led to the formulation of the controversial M-cells hypothesis [150], that is the existence of a specific myocyte type in the myocardium different, for example, from those closer to endocardial and epicardial surfaces. However, experimentally-observed differences in AP due to transmural location (see for example variability in human [52] and in rat [174]) is greater when isolated myocytes are compared; in tissue such differences are smoothed due to a phenomenon known as the electrotonic effect, that is the local passive dispersion of charge due to voltage gradients in the tissue.

1.2.2 The contractile activity of the myocyte

The cardiac myocyte, as with the skeletal muscle cell, is an elongated cell with multiple nuclei. The myocyte is mostly composed of myofibrils, tubular bundles of alternating thick and thin filament proteins running parallel to the long axis of the cell, that are packed together by the sarcoplasmic reticulum. The myocyte volume is mostly explained by myofibrils and mitochondria, that represent about 85% of its volume [72]. The alignment of the myofibrils in cardiac and skeletal muscle cells gives them their characteristic striated appearance. Such alignment is fundamental to the simultaneous contraction of neighbouring myocytes. The myofibril is composed by the repetitive sequence of its contractile unit, the sarcomere, that controls the energy/force generated by the myocyte [95]. The alternating filaments that compose the sarcomere (and hence the myofibril) are made of myosin (for the thick filament) and actin, tropomyosin and troponin C (for the thin filament). Figure 1.6(a) shows a schematic of the sarcomere unit as composed of alternating thin and thick filaments.

Early experimental studies carried out to quantify the relationship between length, time and tension production in the muscle were based on a simple model of the interaction between sarcomere and the surrounding structure [72]. The muscle was modelled as one contractile element connected to a spring-like elastic element, as depicted in Figure 1.6(b). This simple model was able to explain, for example, the latency between the beginning of contraction and generation of tension, and is at the base of some mathematical models of cellular contraction, such as the one employed in this thesis [75] (Section 4.4.1).

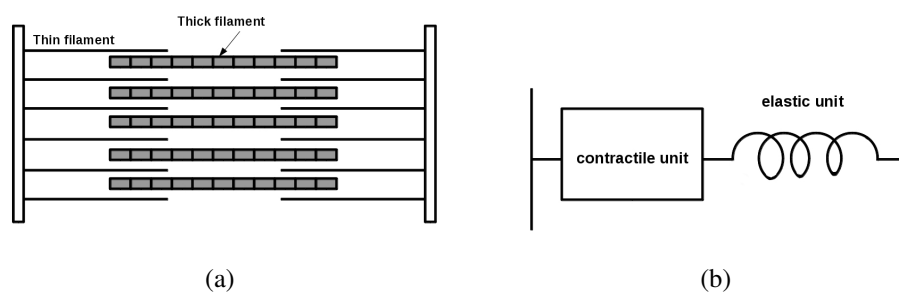


Figure 1.6: (a) Schematic of a sarcomere unit showing the alternate distribution of thick and thin filaments. (b) Model of muscle composed by a contractile and an elastic unit.

Although the mechanisms involved at the subcellular level in sarcomere contraction are not yet fully understood, the sliding filaments theory summarised below is a well established explanation [73]. When an AP is fired in the myocyte, it produces an inward current of

Ca^{2+} that then triggers the release of more calcium from the sarcoplasmic reticulum. Cell contraction takes place because the increased calcium concentration activates contraction at the level of the sarcomere by binding to troponin C. This causes a conformational change of troponin C which allows the exposure of actin to myosin. The crossbridge, that is the actin-myosin bond, makes thin filaments slide along the thick ones, producing a contraction of the sarcomere. The sliding occurs because the crossbridge is not a favourable conformation, therefore it tends to move to a new more energetically favourable position. Figure 1.7(a) represents the mechanism of sliding. Once the new configuration is reached, the bond dissociates and the entire process is repeated as long as there is enough Ca^{2+} available. On the other hand, relaxation depends both on the re-uptake of calcium by the sarcoplasmic reticulum and expulsion from the cell. Figure 1.7(b) shows the temporal overlap of AP and contraction. There is typically a delay (about 10 ms in human [127]) between the onset of the upstroke and the beginning of contraction, while peak contraction occurs when the AP has reached half of the plateau phase.

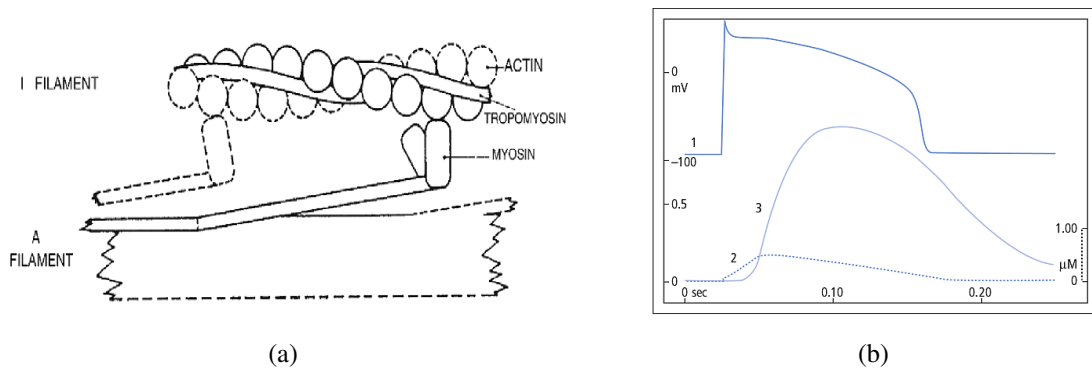


Figure 1.7: (a) Interaction of actin and myosin inducing the sliding of thin filaments (labelled I) over thick ones (labelled A) [73], reproduced with permission from Springer. (b) Delay between AP and contraction [127]. The solid line no. 1 is the AP (mV scale), while the solid line no. 3 represents contraction (relative scale, 0.5 represents half of contraction). The dotted line no. 2 is the trace of intracellular Ca^{2+} concentration (the μM scale). Reproduced with permission from Wiley.

Cardiac *excitation-contraction coupling* is the name given to the process by which electrical excitation causes changes in intracellular calcium concentration that then regulates contraction and relaxation [127]. On the other hand, contraction does influence electrical excitation, in a process called *mechano-electric feedback* (MEF), which is mainly due to mechano-sensitive ionic channels distributed along the cell membrane. Upon stretch, these channels cause an inward current that slightly depolarises the cell, in some cases enough to trigger an AP [83]. Therefore cardiac function is a regulatory loop constituted by a feed-forward pathway, the ECC, and a feed-back pathway, the MEF. External regulation is also

important, both neuro-hormonal and environmental input can in fact influence the system. Finally, it is important to notice that the differences in ionic current found in myocytes at different locations in the heart not only affect the AP but also contraction through the calcium currents variability [79] which in turn induces contraction variability [33].

1.3 Indices of cardiac function

The assessment of the efficiency of cardiac function can be carried out by measuring a number of indices, typically by means of imaging modalities such as ultrasound (US) and magnetic resonance imaging (MRI). This section describes some of the most common ones, dividing them into indices of global and local cardiac function.

1.3.1 Indices of global cardiac function

Indices that are related to the global ventricular efficiency of ejection focus on the variation of blood volume between diastole and systole, especially in the ventricles. For a given ventricle, the *end-diastolic volume* (EDV) is the maximum volume reached by the ventricle during filling, and the *end-systolic volume* (ESV) is the minimum ventricular volume during ejection. The following important quantities can then be derived: the *stroke volume*, $SV = EDV - ESV$, and the *ejection fraction*, $EF = (EDV - ESV)/EDV$. These two measurements respectively give the total amount of blood and the fraction of blood pumped out of a given ventricle [14].

These indices do not take into account the cardiac cycle duration and its variability. On the other hand, *cardiac output* $CO = HR \cdot SV$, is the product of heart rate (HR) (that is the number of heartbeats per unit of time) and stroke volume [81]. Heart rate is modulated mostly by the nervous system, which induces changes in the pacemaker rate of the sinoatrial node. Stroke volume depends on three factors that are deeply interconnected: preload, myocardial contractility and afterload. Preload is the maximum stretch reached by the sarcomere during ventricular filling. Since it is not possible to measure preload on the intact heart, this is usually approximated in clinical assessment by the end-diastolic volume or pressure. The relationship between preload and stroke volume is described by the Frank-Starling mechanism: an increase (or decrease) in preload produces an increase (or decrease) in stroke volume. This is due to the fact that changes in preload affect the stretch of the sarcomere inducing changes in the force of contraction, that is contractility. Pathological mechanisms or drugs affecting the intracellular concentration of Ca^{2+} can also affect contractility thereby affecting stroke volume. The term afterload refers to the

stress in the cardiac wall that opposes contraction. Factors that determine wall stress include the radius of the ventricle, its wall thickness and the arterial pressure. In particular, the variation in wall thickness during contraction is a simple index of how well the cardiac wall is contracting.

Stroke work, SW , is an index that allows to evaluate global cardiac function in terms of the energy produced. It is the area of the pressure-volume loop (see Figure 1.2(b)) and it can be computed as $SW = P \cdot SV$, where P is usually the peak or mean aortic pressure [72]. Stroke work can also be computed as an index of local function, as explained in the following section.

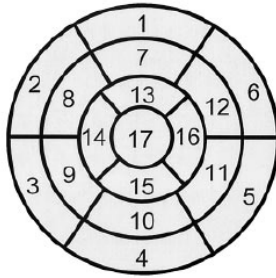
Later on in the thesis I will make use of global indices such as ejection fraction and wall thickness to evaluate the output of my computational studies (Chapters 5 and 6), see for example Section 5.2.

1.3.2 Indices of local cardiac function

The indices described so far are routinely measured in the clinical setting to assess the global function of the heart, but provide little insight into the regional changes occurring during the cardiac cycle. Although there is no standard index to evaluate the local functionality of the heart, measurements of local tissue deformation (strain) and of deformation rate of change (strain rate) have been proven useful in several research studies [151]. Such studies are typically based on the use of imaging modalities such as US and MRI. I will review the most common imaging modalities employed for the assessment of cardiac function in Section 2.1. A formal definition of strain will be given in Section 3.2.2. Strain will be considered as an index of local cardiac function of the heart in the computational studies of Chapters 5 and 6.

Derived indices of local cardiac function based on strain have been developed and suggested for the clinical assessment of cardiac resynchronisation therapy (CRT) [78]. For example, CURE (Circumferential Uniformity Ratio Estimate), is an index that measures the level of uniformity of strain distribution in the circumferential direction. Stroke work can also be computed at the regional level and employed in derived indices such as COVW (Coefficient of Variation of regional Work). In this case stroke work is computed from local stress-strain loops rather than the pressure-volume loop, as in the case of the global SW introduced in the previous section. Details on how to compute CURE and COVW can be found, for example, in [78] (in the supplementary material).

In order to assess local cardiac function, it is useful to subdivide the heart into regions according to a standard approach, such as the one developed by the American Heart Association (AHA) [25]. Figure 1.8 shows a bulls-eye representation of the AHA subdivision of the left ventricle into 17 regions. The left ventricle is first divided into three blocks with respect to its long axis: the basal, midventricular (or equatorial) and apical blocks. Then each block is divided into regions. The basal and midventricular blocks are divided into 6 regions each, while the apical region is divided into 5 regions. The bulls-eye representation projects into a plane this subdivision such that the outer ring is the basal block, the two innermost rings are the apical portion and the remaining middle ring is the midventricular block. Table 1.1 provides the labels for the 17 regions of the left ventricular subdivision of Figure 1.8.



1. basal anterior	7. mid anterior	13. apical anterior
2. basal anteroseptal	8. mid anteroseptal	14. apical septal
3. basal inferoseptal	9. mid inferoseptal	15. apical inferior
4. basal inferior	10. mid inferior	16. apical lateral
5. basal inferolateral	11. mid inferolateral	17. apex
6. basal anterolateral	12. mid anterolateral	

Table 1.1: Legend of Figure 1.8.

Figure 1.8: Bulls-eye diagram for 17-region subdivision of left ventricle [25].

An adaptation of the AHA subdivision of the left ventricle was employed by Karadag et al. [71] to generate a locally optimised model of fibre distribution that will be described in Section 4.5.3.

1.4 The chosen animal model: the laboratory rat

The animal model chosen for this study is the laboratory rat, a type of *Rattus Norvegicus*, specifically bred for research purposes. In particular the imaging data used are from subjects of the Sprague-Dawley type. The rat is a well acknowledged animal model for the study of many human diseases, from cardiovascular to neurological and metabolic ones [121]. Its genome has also been thoroughly mapped and investigated [69]. In general, the use of small animals in preclinical research is largely pursued for its relative low cost, the short lifetime of the animals and the ease of handling [121]. It is a powerful way to develop new imaging and diagnostic methods as well as further the understanding of the underlying mechanisms of many diseases by means of experiments and computational models that

might not be applied directly on human for safety or ethical reasons. While, on the one hand, the ultimate goal of the studies carried out on small animals is to understand and possibly diagnose and cure human pathologies, on the other hand, it is important to bear in mind that there are substantial inter-species differences. For example, Table 1.2 compares some general cardiac parameters for the typical laboratory rat and an average healthy human.

Table 1.2: Typical cardiac parameters for the laboratory rat and the healthy human. The values of stroke work have been computed from the mean aortic pressure (obtained by averaging the arterial blood pressure in systole and diastole) and stroke volume, according to the formula provided in Section 1.3.1 and it is expressed in milliJoule (mJ).

Physiological parameters	Rat	Human
Heart weight	0.95 g - 1.19 g [85]	330 g [38]
Heart volume	1.2 mL [85]	310 mL [38]
Heart rate	296 bpm - 388 bpm [85]	70 bpm [127]
Stroke volume (whole heart)	0.22 mL [31]	70 mL [127]
Stroke volume (left ventricle)	0.18 ± 0.12 mL [88]	59 ± 20 mL [153]
Arterial blood pressure in systole	15 kPa - 19 kPa [85]	17.03 ± 2.86 kPa [26]
Arterial blood pressure in diastole	10 kPa - 13 kPa [85]	10.25 ± 1.12 kPa [26]
Left ventricular blood pressure in diastole	1.19 ± 0.21 kPa [31]	1.9 ± 0.4 kPa [154]
Left ventricular blood pressure in systole	16.7 ± 0.93 kPa [31]	17.5 ± 2.4 kPa [154]
Stroke work (whole heart)	3 mJ	960 mJ

The use of the rat as animal model in my study has important advantages. First of all, imaging modalities such as diffusion tensor (DT) MRI, which are still mostly ex vivo, can only be performed on animal models. DT-MRI, as explained in Section 2.2, is a valuable imaging tool for the study of cardiac tissue microstructure. A detailed description of the imaging data used in this thesis is given in Section 2.4. From the computational point of view, the reduced size of the rat heart allows simulations to run relatively fast and on a single computer. In this way, a wide range of numerical tests and simulations can be performed in a reasonable amount of time. At the moment, the simulation package employed in this study (Chaste, see Section 3.3) does not allow for electromechanical simulations to be run in parallel on multiple CPUs, therefore a computational study such as that presented in this thesis but performed on a larger heart would be greatly hindered by this limitation, as further discussed in the Conclusions to the thesis.

In this chapter an overview of the general anatomy and physiology of the heart has been provided with a particular focus on tissue structure. Then, the most common indices of cardiac function at the global and local level have been described. Some of these indices were employed in the analysis of the results of the computational studies described later on. Finally, the laboratory rat has been introduced as the chosen animal model. The next chapter is focused on DT-MRI, a powerful imaging modality for the measurement of tissue structure distribution in the heart. The physical basis of DT-MRI is described, and the methods to determine tissue structure distribution from imaging data are explained.

Chapter 2

Imaging and quantifying cardiac tissue microstructure

In this chapter the most commonly used cardiac imaging modalities are reviewed to then focus on Diffusion Tensor MRI, which is employed to image cardiac tissue structure. The physical basis of MRI is explained as well as how diffusion can be measured by means of this modality and related to tissue structure. The angular metrics commonly employed in the quantitative description of tissue structure are then introduced. Finally, the cine-MRI and DT-MRI datasets employed in the research studies presented in Chapters 5-7 are described.

2.1 Cardiac imaging modalities

There are several imaging modalities used for routine clinical assessment or for research purposes to image the heart, such as echocardiography, X-ray computed tomography (CT), nuclear imaging (PET, SPECT) or magnetic resonance imaging (MRI). Each modality comes with its strengths and limitations in aspects such as spatio-temporal resolution, signal to noise ratio, the use of ionising radiation and the ability to detect changes in tissue. It is widely accepted that none of these imaging modalities alone is capable of providing all the structural and functional information needed for the complete evaluation of heart function in both normal and diseased conditions. For a complete analysis of the topic refer to [103], [151].

Echocardiography is an ultrasound technique, with many advantages such as low cost and real-time response. It is routinely used for the analysis of myocardial and valve function but it suffers from important limitations such as operator dependence (the scanning probe

is manually operated) and a restricted point of view (the reduced size of the probe constrains it). Tissue Doppler imaging is a special type of ultrasound technique, based on the Doppler shift in the ultrasound frequency, that allows velocities and strain rates to be mapped [1]. Speckle-tracking [88], by tracking the interference patterns in the ultrasound image, provides a displacement map that can then be used to compute strain.

CT is still the best imaging technique to get 3D detailed anatomic information *in vivo*, but it is unable to provide information on functional parameters, such as blood flow and velocity. Furthermore, it relies on the use of ionising radiation and contrast agents. Positron emission tomography (PET) and single-photon emission computed tomography (SPECT) are two nuclear imaging techniques and involve radiation. They are powerful in detecting myocardial perfusion and viability, but lack anatomical information and are very poor in resolution, and so are most commonly used in combination with CT (as shown in Figure 2.1(a)).

Cardiac MRI in recent years has been the subject of vast improvements, establishing it as one of the most versatile methodologies in clinical assessment, combining high spatial and temporal resolution, high contrast, wide field-of-view and the fact that it does not rely on radiation nor, in most cases, the use of contrast agents. Limitations such as long scanning times and the fact that it is not applicable to patients with pacemakers or defibrillators are now being greatly reduced [18]. Two types of imaging modalities are commonly used in cardiac MRI, black-blood and white-blood imaging. The first type provides very detailed anatomical information but requires longer scanning times. On the other hand, white-blood imaging relies on fast scanning protocols, as in the case of Cine-MRI imaging. With this technique a series of images is obtained at progressive points of the cardiac cycle which can then be used to form a cine loop. Although only a few slices can be sequenced and the resolution is relatively low, this technique is successful in the detection of local myocardial dysfunction and abnormal flow patterns, but in the latter case the use of a contrast agent is necessary [170].

Diffusion Tensor (DT) MRI, Tagged-MRI and Phase-contrast MRI (PC-MRI) are additional MRI techniques that have been so far applied mostly for research purposes. Cardiac DT-MRI is usually performed *ex vivo* and measures the magnitude as well as direction of water diffusion across the tissue. The preferred diffusion direction of water is in fact aligned with the principal structure which, in the case of cardiac muscle, is the main orientation of the myocytes, namely the fibre direction. Sheet orientation can also be obtained

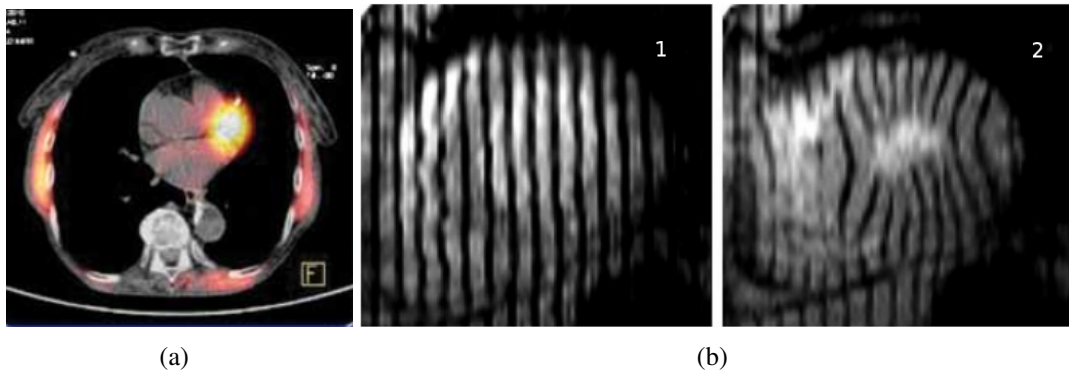


Figure 2.1: (a) Short-axis view of a combined CT/PET scan of the human heart [82]. CT (in grey) provides the anatomical information, while PET (in colour) represents myocardial viability. Reproduced with permission from Via Medica. (b) Short-axis view of a Tagged-MRI [9] scan at (1) end-diastole and (2) end-systole. Reproduced with permission from Elsevier.

from these data as it has been shown that the primary and tertiary eigenvectors of the diffusion tensor, for a given voxel of the image, are associated with the fibre direction and to the normal to the sheet plane, respectively. Tagged-MRI is a fairly recent in vivo technique to non-invasively track cardiac motion in which a grid is generated by saturation of magnetisation and is acquired together with the tissue image. This grid overlaps the tissue and deforms with it. Later processing of the images allows the reconstruction of local motion patterns from the grid deformation. The limitation of this technique is that it is most often applied in 2D [9], making the 3D reconstruction a difficult task. However, 3D grids have also been employed [183]. Figure 2.1(b) shows short-axis views of a Tagged-MRI scan at two phases of the cardiac cycle. PC-MRI is used to map velocity and strain rate, while the measurement of strain is prone to large errors. It is mostly employed in the study of blood flow, in which case it is generally referred to as Magnetic Resonance Angiography (MRA), but studies of cardiac tissue velocities have also been carried out [37]. PC-MRI can also be encoded to measure displacement (DENSE MRI). Recently, DENSE cine-MRI, has been employed to track temporal changes in cardiac tissue displacement in order to measure strain and torsion [185] throughout the cardiac cycle.

2.2 Imaging tissue structure with diffusion tensor MRI

In this section the phenomenon of nuclear magnetic resonance (NMR) is described. Then the process of molecular diffusion, how it is measured and correlated to tissue structure in DT-MRI, are explained.

2.2.1 Physical basics of MRI

DT-MRI is an imaging modality based on the phenomenon of nuclear magnetic resonance (NMR), that is the ability of some atoms (whose nuclei have a nonzero magnetic moment, called spin) to align with the direction of an applied external magnetic field (Figure 2.2(a)) and precess around this direction at a specific frequency (Figure 2.2(b)). The aligned spins can be oriented parallel or antiparallel to the magnetic field, as shown in Figure 2.2(a). The parallel configuration is slightly more favourable from the energetic point of view, hence the population of parallel spins is slightly more numerous than that of antiparallel spins. When an electromagnetic pulse with the same frequency as that of the precessing spins is applied to the system, it causes the nuclei spins to change in bulk their position with respect to the external magnetic field by a certain angle, which varies with the strength and duration of the pulse applied. Once the pulse is over, spins slowly recover their position by emitting energy. The magnetic resonance (MR) signal comes from the very small difference in energy between parallel and antiparallel spin populations as they recover their position. With time the MR signal decays due to the release of energy and the loss of phase among the spins, a phenomenon called relaxation [130]. When applied to biological tissues, NMR techniques measure the interaction between protons in the water contained by the tissue and the applied external magnetic field. Different tissues will have different relaxation times depending on the tissue structure and water content. There are many techniques based on the NMR phenomenon and not all of them produce an image as their output. Magnetic Resonance imaging (MRI) combines the external magnetic field and timed sequences of different electromagnetic pulses with magnetic field gradients, the latter being the ones modulating the spatial information, thus allowing the MR signal to be transformed into a contrast image encoding tissue relaxation [39].

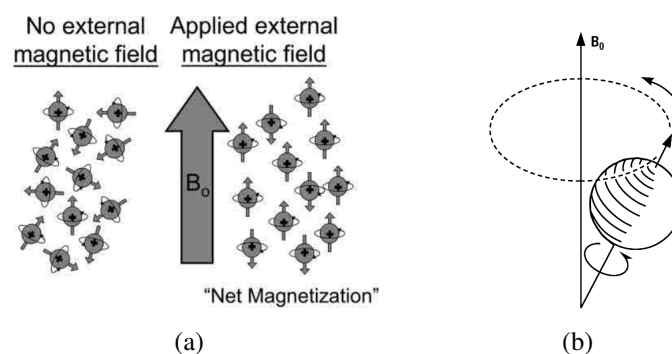


Figure 2.2: (a) Spins aligned with the applied external magnetic field B_0 , taken from [130]. Reproduced with permission from RSNA. (b) Precession of the aligned spin around B_0 , from [39], reproduced with permission from Elsevier.

2.2.2 Fick's model of diffusion

The transport phenomenon of diffusion is based at the microscopic level on the random motion of particles free to move in a fluid. This microscopic random mechanism is known as Brownian motion. At a coarser scale, a higher concentration results in a net movement of molecules in a given direction within the solvent. Fick's law [73] is a mathematical model that describes the relationship between the flux of molecules $\mathbf{j} = (j_x, j_y, j_z)$ (i.e. the number of molecules flowing through the unit area per unit time) and the molecules gradient of concentration across the solvent ∇c

$$\mathbf{j} = -D\nabla c . \quad (2.1)$$

In a three-dimensional environment D is the *diffusion tensor*, a 3×3 second order tensor, which has units $[length^2 time^{-1}]$. The minus sign in eqn (2.1) means that the flux occurs from regions of high concentration to those of low concentration. The diffusion tensor D depends on the specific molecule considered (especially its size), the temperature and structure of the medium across which the molecules are diffusing. In general D may be a function of space and time. If this is not the case, and also the material is constantly isotropic, D becomes a constant scalar, the *diffusion constant*. Biological tissue is, on the other hand, highly anisotropic, with a number of large proteins, organelles and compartments, all of which interfere with the diffusion process [91].

2.2.3 Measuring diffusion with MRI

The first attempt to measure diffusion by means of NMR dates back to the mid-sixties and was developed by Stejskal and Tanner by introducing diffusion-sensitizing gradients in the standard NMR pulse sequences [155]. They hypothesised that the spins of the protons in moving water behave differently from those in still water. In particular, between two subsequent rephasing electromagnetic pulses, protons travel, causing the second rephasing step of the spins to be less coherent. In other words, diffusion produces a signal attenuation, and the degree of attenuation is related to that of water motion. The effect of water motion on signal attenuation depends on a number of factors, such as the amplitude and duration of the gradients and the time elapsed between them. This dependence is encapsulated in the diffusion-weighting factor, or *b-value*, b . The diffusion coefficient D is related to the NMR signal by the following equation

$$S = S_0 e^{-bD} , \quad (2.2)$$

where S and S_0 are the signal intensity with and without diffusion-sensitizing gradients, respectively. From eqn. (2.2) it is possible to infer that the signal S is more attenuated the faster the diffusion and the higher the b-value. This monoexponential model was derived in the case of an homogeneous isotropic system but is usually a good approximation for biological tissues, although this depends on the image resolution and the magnitude of the b-value [80]. When more than one type of tissue, for example ischemic and normal tissue, are imaged in the same pixel/voxel, the measured diffusion will be an average between the diffusion of the various tissues, an effect called the *partial volume effect* [4].

In the mid-eighties the diffusion-encoded NMR sequence was combined with the spatial magnetic field gradients of MRI to image diffusion in biological tissues thanks to LeBihan et al. [91]. The paper also highlighted that, due to the high compartmentalisation of biological tissues and microcirculation, they were not measuring the real diffusion coefficient (as in the free diffusion model by Fick, see eqn. (2.1)) but rather an *apparent diffusion coefficient (ADC)*. Since then, a number of different biological tissues have been studied including kidney, muscle, brain and tendon [60]. However, the first applications of MRI to the quantification of diffusion were limited to the measurement of diffusion in one direction only, an approximation that is correct only in the case of isotropic tissue. Diffusion-weighted imaging (DWI) is the name applied to the MRI modalities that only consider one diffusion direction, producing for each pixel (or voxel, if it is a 3D image) a single value of the diffusion coefficient. On the contrary, in DT-MRI diffusion is measured along at least six non-collinear directions in order to provide a 3×3 diffusion tensor for each pixel/voxel, allowing to quantify the level of anisotropy in the tissue and differentiate structures in biological tissue depending on that [10]. Eqn. (2.2) needs now to be applied to each of the six directions. In a Cartesian coordinate system (x, y, z) , the diffusion tensor D can be written as

$$D = \begin{pmatrix} D_{xx} & D_{xy} & D_{xz} \\ D_{xy} & D_{yy} & D_{yz} \\ D_{xz} & D_{yz} & D_{zz} \end{pmatrix} ,$$

where each component of D is the diffusion coefficient D_{ij} for the direction ij ($i, j = x, y, z$) and is related to the signal in that direction S_{ij} by the formula

$$S_{ij} = S_0 e^{-b_{ij} D_{ij}} , \quad (2.3)$$

where b_{ij} is the ij th component of the 3×3 \mathbf{b} matrix, replacing the mono-directional b-value of eqn. (2.2).

The brain is the most thoroughly investigated organ with respect to DWI and DT-MRI, where these techniques can be applied in vivo with good resolution and signal-to-noise ratio, since the brain is a stationary organ (as opposed to the beating heart). Diffusion-based MRI techniques have proven to be an indispensable non-invasive tool for brain injury detection [149] and neuro-oncologic assessment [19], to cite a few examples.

The application of DWI and DT-MRI to the heart in vivo is made difficult by the fact that it is a moving organ and the order of magnitude of displacement in diffusion is three times smaller than that involved in cardiac motion [152]. Furthermore, the heart rate is highly variable, and the breath frequency also needs to be taken into account since the expansion of the lungs affects the motion of the heart inside the chest. Nonetheless, promising attempts to develop robust and reliable in vivo DT-MRI sequences for assessment of cardiac pathologies have been made, as some recent clinical research studies show [116].

2.2.4 Diffusion anisotropy indices

DT-MRI data provides a significant amount of information about tissue structure, perfusion and anisotropy, all encoded in a tensor, actually one tensor for each pixel/voxel of the acquired image. But a tensor by itself is not an easy parameter to look at or to infer tissue characteristics. Hence, a number of indices and post-processing approaches have been developed to make the information captured by the diffusion tensor more accessible. A first elegant representation of diffusion relies on the diagonalisation of the tensor D to obtain the eigenvalues $\lambda_1, \lambda_2, \lambda_3$ and their corresponding eigenvectors ν_1, ν_2, ν_3 [55]. D is a real-valued symmetric matrix, hence, according to the Spectral Theorem, it can

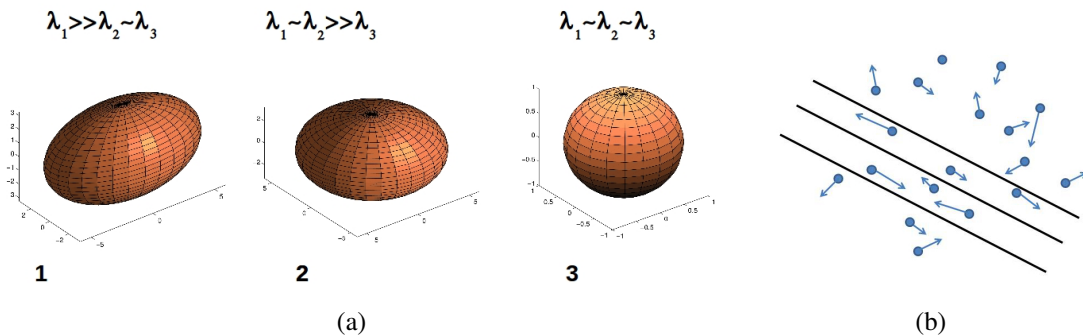


Figure 2.3: (a) Ellipsoidal representation of the eigenvalues of the diffusion tensor. The case of one preferential direction for diffusion is shown in (1), the case of two equally preferred directions is given in (2), while fully isotropic diffusion is shown in (3). (b) Diffusion of water molecules along the fibre is favoured with respect to diffusion across the fibre barrier.

always be diagonalised and this results in a set of orthogonal eigenvectors, and real-valued eigenvalues. The diffusion ellipsoid is the ellipsoid with the three semi-axes pointing in the direction of the three eigenvectors and length of each semi-axis equal to the corresponding eigenvalue. The level of anisotropy of diffusion at a given location in the image can be evaluated from the shape of the corresponding diffusion ellipsoid. For example, in Figure 2.3(a), case (1) shows one clear preferential direction of diffusion along ν_1 , since λ_1 is significantly larger than the other two eigenvalues, case (2) shows a planar preferential diffusion, finally in case (3) diffusion is isotropic.

Often a single value representing diffusion at a given location is preferable. For example, the apparent diffusion coefficient ADC can be calculated using the eigenvalues, being equal to their mean [80],

$$ADC = \frac{1}{3}(\sum_i \lambda_i) . \quad (2.4)$$

This is a measure of the average local diffusion at each pixel/voxel. The most common index of anisotropy is the *fractional anisotropy* (FA), ranging from 0 for isotropic diffusion to 1 for fully anisotropic diffusion. the FA can be computed as

$$FA = \left\{ \frac{3 \sum_i (\lambda_i - ADC)^2}{2 \sum_i \lambda_i^2} \right\}^{\frac{1}{2}} \quad (2.5)$$

for each location, but alternative definitions can be found [80].

2.2.5 From diffusion tensor to tissue structure

Water diffusion in tissue changes depending on the level of tissue compartmentalisation, as explained in Section 2.2.2. For example, fibrous structures in living tissue allow more diffusion to occur along the fibre direction rather than perpendicular to it (see Figure 2.3(b)). This phenomenon is at the basis of tractography, a data analysis technique that was initially developed to trace neural tracts in the brain using in vivo DT-MRI [11]. In vivo cardiac DT-MRI is still a developing field, but it has been already applied to trace the fibres in cardiac tissue, as highlighted in Section 2.2.3. For example, Reese et al. [137] performed a study of human heart fibre architecture at end-systole, by combining diffusion information from DT-MRI with myocardial strain-rate information from PC-MRI, finding that the fibre distribution was in good agreement with that extracted from histology by Streeter [158]. The main limitation of the method was the essentially 2D nature of the acquisition - only a few short-axis slices (in the order of 10-15) were acquired with good resolution and reasonable scanning time. More recently, Toussaint et al. [161] have developed an algorithm that

maps the 2D diffusion tensor distribution for the acquired short-axis slices onto a prolate spheroidal model of the heart to then apply a shape-based interpolation method [135] to reconstruct a 3D profile of the fibre orientation.

From the mathematical point of view, the fibre direction is obtained as the preferential direction of diffusion at each voxel. Referring to the notation of Section 2.2.4, it can be assumed that the three eigenvalues of the diffusion tensor D are sorted as $\lambda_1 \geq \lambda_2 \geq \lambda_3$. Hence, ν_1 is the primary eigenvector, while ν_2 and ν_3 are the secondary and tertiary eigenvectors, respectively. The primary eigenvector ν_1 has been shown to provide the preferential direction for water diffusion. The correlation in cardiac tissue between fibre direction and primary eigenvector was validated by comparing fibre orientation maps obtained with ex vivo DT-MRI with histology [145].

The orientation of sheets across the tissue is more difficult to measure by means of DT-MRI. It has been found that the normal to the sheet plane in tissue correlates with the tertiary eigenvector (ν_3) [59], but it has to be considered that in cardiac tissue there is commonly little difference between the magnitude of λ_2 and λ_3 , making the identification of the normal to the sheet ambiguous. Furthermore, validation with histology is rather difficult given the discontinuous and highly variable distribution of sheets in the heart [164].

Statistical atlases of tissue structure have been obtained from ex vivo DT-MRI in dogs [128] and humans [98]. Such atlases provide important information about average tissue structure distribution and inter-subject variability, showing that on average there is more variability in sheet distribution than in fibre orientation [51].

DT-MRI is a powerful technique but, especially for the study of cardiac tissue structure, it suffers still from significant limitations. In vivo studies tend to show low resolution and are necessarily restricted to a few short-axis slices. Ex vivo studies allow for higher resolution, especially when the excised heart is fixed, for example by embedding it in agarose [129]. In all such cases, though, the heart is captured only at one specific moment of the cardiac cycle, typically end-systole for in vivo studies, and a relaxed state close to end-diastole for the ex vivo ones. A novel experimental set-up has been recently developed by Hales et al. [57] that allows DT-MRI scans of Langendorff-perfused hearts to be performed at two different cardiac mechanical states, namely at a relaxed and a contracted state, respectively. The Langendorff-perfused heart can be considered as an intermediate step between ex vivo and in vivo imaging of the heart by means of DT-MRI. Hales et al. developed a Langendorff-perfusing set-up fully compatible with the MR scanner, that is made of plastic

materials, with an outer solution reservoir and a tubing system capable of providing nutrients to the excised heart while inside a water-tight compartment fitted in the scanner. The perfused heart was first imaged at approximately end-diastole, that was induced by injecting a cardioplegic solution. The heart was then made to contract by perfusing it with a lithium-rich solution and images were acquired again. Thanks to its ability to capture different mechanical states of the whole-heart, this technique has provided useful insight into the dynamics of fibre and sheet reorientation between end-diastole and end-systole. For example, it showed that during contraction the sheet intersection angles increase inducing the sheets to lie more parallel to the short-axis plane. This angular change is compatible with the hypothesis that sheet dynamics is the major driving force of wall-thickening in the heart [57].

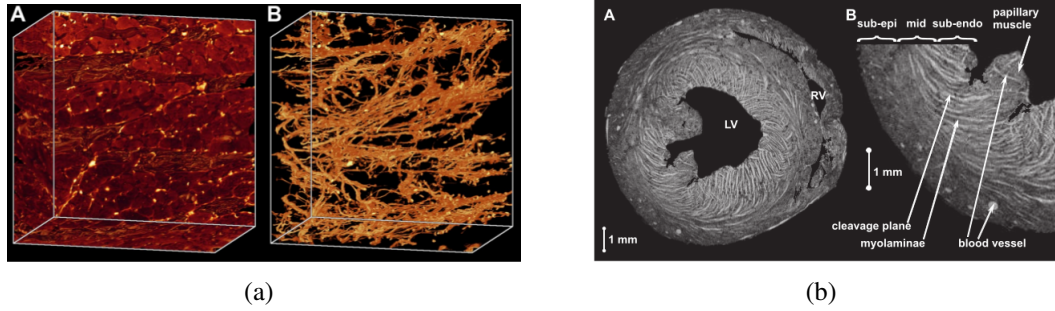


Figure 2.4: (a) Midwall image of size $320 \times 320 \times 240 \mu m$ of myocardial tissue (left) and extracted collagen network (right) obtained with confocal microscopy, from [131]. (b) Equatorial short-axis slice with resolution $25 \times 25 \mu m$ (left) and magnification of one of its sides (right) obtained with T_2^* -enhanced MRI, from [50].

2.2.6 Other imaging modalities used to study cardiac tissue structure

This section provides a summary of some of the other imaging modalities that have been used through the years to characterise tissue structure in the heart. The first studies of fibre and sheet orientation were performed on histological samples [158], [94]. Histology allows for a great level of detail but is restricted to small portions of the cardiac wall. Furthermore, being essentially a 2D technique, it is not straightforward to infer the 3D structure of the tissue. Regarding the visualisation of the sheets, it has been found that histology tends to overestimate the cleavage planes intercalating the sheets because of the process of dehydration [51]. Confocal microscopy has allowed the first high-resolution 3D reconstructions of sheet distribution in small cardiac tissue samples [143], [131] (see for example Figure 2.4(a)). The high-resolution MRI technique called T_2^* -enhanced MRI has been employed on excised hearts to study tissue structure distribution of the whole heart [50], an example of which is shown in Figure 2.4(b). Although there is a good level

of detail, it seems difficult to distinguish small vessels from cleavage planes as they have intensities in the same range. DT-MRI and T_2^* -enhanced MRI has been compared in rat, showing good agreement in the measured tissue structure distribution [84]. Finally, in vivo contrast-enhanced MRI has also been employed to study tissue structure in mice [58], showing promising results but still with the problem of low resolution.

2.3 Quantifying tissue structure: angular metrics

Whole heart tissue microstructure can be extracted from DT-MRI, and to some extent with other imaging techniques as well, as described in the previous section. However, it is often necessary to introduce parameters in order to quantify fibre and sheet distribution, so as to compare more easily between subjects and to identify physiological variability or pathological conditions. A common way to do so is to define a set of angles that describe the angular variation of fibres and sheet orientation within the tissue. The most common angles employed are the *helix angle* α , the *transverse angle* (or imbrication angle) γ and the *sheet angle* β . I refer to these angles as angular metrics, since they are used to quantify tissue structure distribution. The helix angle α and the transverse angle γ define the orientation of the fibres in myocardial tissue and are measured on the unit vector locally associated to the fibre direction \mathbf{f} , that in DT-MRI is the primary eigenvector $\boldsymbol{\nu}_1$. The sheet angle β is a measure of the inclination of the sheet plane, which is uniquely identified by its normal \mathbf{n} , that is associated with the tertiary eigenvector $\boldsymbol{\nu}_3$ estimated from DT-MRI, as explained in Section 2.2.5. Slightly different definitions of these angles have been employed, depending on the system of coordinates and the planes with respect to which the angles have to be measured - for a survey refer to [51].

In this section the two most common systems of coordinates employed for the definition of these angular metrics are defined. A formal definition of the angular metrics is then provided. These metrics were employed in the study of tissue structure distribution on DT-MRI data described in Chapter 7.

2.3.1 Coordinate systems for tissue structure characterisation

The Cartesian coordinate system (x, y, z) is not the best option to describe tissue structure in the ventricles. A useful system of coordinates for measuring quantities related to tissue structure distribution in the heart is the cylindrical coordinate system (r, c, l) [47]. This reference frame is defined at each point \mathbf{x} of a given ventricle as follows:

1. Assignment of the longitudinal direction l .

As shown in Figure 2.5(a), this system is based on the estimation of the principal axis of rotation of the ventricle l , also called the long axis, that is directed from apex to base. At each point x in the ventricular tissue, the longitudinal direction is a unit vector that coincides with the long axis, hence it is also referred to as l .

2. Assignment of the radial direction r .

While the long-axis l is constant, the radial direction r is position-dependent. For each point with position x in the ventricle, r is defined as the unit vector along the line perpendicular to the long-axis and passing through the point. The radial direction r is set to point outwards with respect to the ventricular cavity.

3. Assignment of the circumferential direction c .

The circumferential direction c is position-dependent, as it is defined as the cross-product $c = l \times r$. In Figure 2.5(a), c is represented by a crossed circle, meaning that it is perpendicular to the visualisation plane and pointing away from the observer.

The coordinate system (r, c, l) is thus a right-handed set of three orthonormal basis vectors defined at each position x in the ventricular domain. I will refer to this system of coordinates as the *global (cylindrical) coordinate system*, although the only vector that is actually defined globally is the long-axis.

Another system of coordinates used for tissue structure characterisation is the one shown in Figure 2.5(b). This is the material coordinate system (u, v, w) , which is a fully local system as the three vectors are position-dependent. This reference frame is defined at each point x of a given ventricle as follows:

1. Assignment of the radial direction u .

For each point x in the ventricle, u is the unit vector along the normal to the epicardial surface that passes through the point. This is the local analogue of r , therefore it is referred to as the local radial direction.

2. Assignment of the circumferential direction v .

The vector v is instead the local circumferential direction. It is obtained as the cross-product between the global long axis l and the local radial direction u , $v = l \times u$.

3. Assignment of the longitudinal direction w .

The local longitudinal direction w is the cross-product $w = u \times v$.

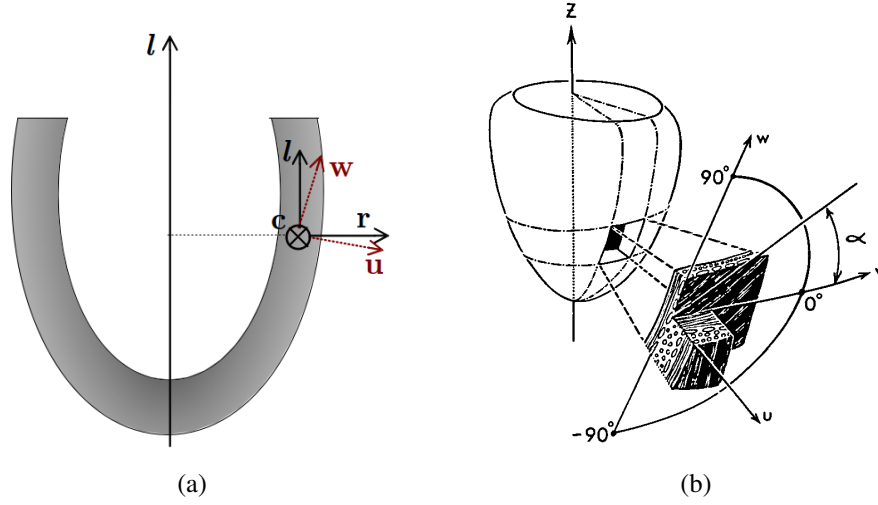


Figure 2.5: (a) Comparison of global (r , c , l) and local (u , v , w) cylindrical systems of coordinates. (b) Local system of coordinates, from Streeter et al. [158]. Reproduced with permission from Wolters Kluwer Health.

For each point in the domain, the set (u, v, w) is right-handed and orthonormal. I will refer to this system of coordinates as the *local (cylindrical) coordinate system*. Comparison between the global and local reference frames is given in Figure 2.5(a).

For the global coordinate system, it is useful to define the following three-planes: the cr -plane, the cl -plane and the lr -plane. They are the circumferential-radial, circumferential-longitudinal and longitudinal-radial planes, respectively. With an abuse of terminology I will also refer to local versions of these planes. For example, the cr -plane in the local case will be the plane identified by the local circumferential vector v and the local radial u vector, whereas in the global case, it will be defined by the c and r vectors.

2.3.2 Formal definition of the angular metrics

For the purposes of my thesis, I decided to follow the definition of the angular metrics described in Hales et al. [57] and reported below. The angles are defined with respect to a cylindrical system of coordinates, either global or local. This means that depending on the system of coordinates, the same definition produces different values for the angles. I will analyse in detail this aspect in Chapter 7 as it is at the basis of the image analysis presented there. All angles are defined on the range $[-\pi/2 \quad \pi/2]$.

In particular, paraphrasing Hales et al. [57], the following definitions can be made:

Helix Angle α is the angle between the projection of the fibre direction onto the cl -plane f_{cl} , and the cr -plane. The angle α is positive if it is consistent with the right-handed helical

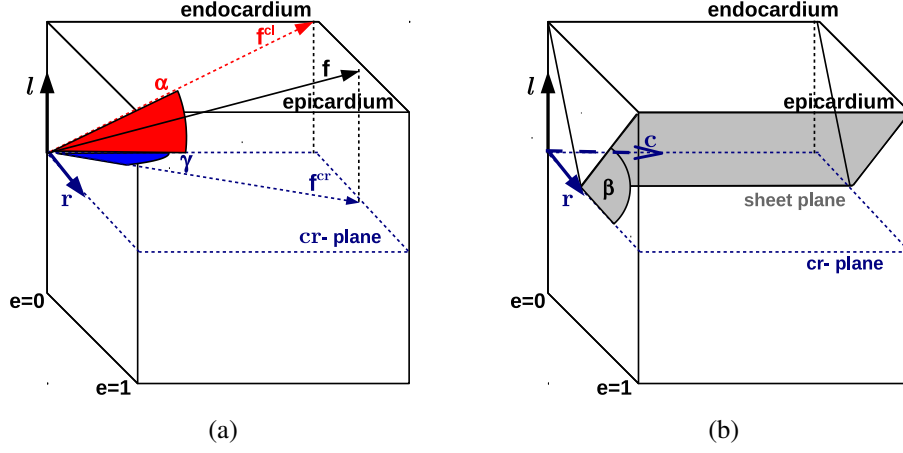


Figure 2.6: (a) Helix (α) and transverse (γ) angles in a transmural cut. (b) Sheet angle β in a transmural cut. The diagrams are valid for both the global and local system of coordinates. Depending on the coordinate system definition, (r, c, l) will be substituted by (u, v, w) , but not the definition of the angles with respect to a given set of vectors.

screwing motion of the fibres that is found in left ventricular sub-endocardium. It is negative if it is consistent with a left-handed helical screwing motion, as found in sub-epicardial layers.

Transverse Angle γ is the angle between the projection of the fibre direction onto the cr -plane f_{cr} , and the circumferential direction. The sign of γ is positive if f_{cr} is directed toward the ventricular cavity, otherwise it is negative.

Sheet Angle β is the angle between the sheet plane and the cr -plane. The sign of β is positive if the sheet plane is oriented from apex to base when moving from endocardium to epicardium in the lr -plane, and negative if it is oriented from base to apex.

Figures 2.6(a) and 2.6(b) help in the understanding of these three angles definitions. The detailed description of how these angles can be measured according to their definition is given in Appendix A.

In Section 4.5 I will define an analogous set of angles, $\tilde{\alpha}$, $\tilde{\beta}$, $\tilde{\gamma}$ which are used to generate different mathematical models of tissue structure. I will refer to them as intrinsic helix, sheet and transverse angles. Section 4.5.5 explains how the two sets of angles, the one for measuring tissue structure distribution (α, β, γ) and the one for prescribing it $(\tilde{\alpha}, \tilde{\beta}, \tilde{\gamma})$, are related.

2.4 Description of the images datasets

In my study I have used images coming from two different datasets, both provided by the group of Dr Jurgen E. Schneider, Department of Cardiovascular Medicine, University of Oxford. Each dataset consists of a number of rats scanned in vivo with a cine-MRI sequence and then ex vivo with a DT-MRI protocol. While the cine-MRI sequence does not change between the two datasets, after the heart is excised the applied DT-MRI protocol is rather different, the heart being either embedded in agarose (*dataset*₁) or Langendorff-perfused (*dataset*₂), the latter being imaged at two different mechanical states. Details about how the two-state DT-MRI of the Langendorff-perfused heart dataset was acquired have been given in Section 2.2.5.

1. *dataset*₁: In vivo cine-MRI and subsequent ex vivo DT-MRI of rat hearts were acquired on a 9.4T (400 MHz) MR system (Agilent, Santa Clara, CA, USA). The cine-MRI dataset used a 2D multi-frame gradient echo sequence, and consisted of a stack of eight contiguous short-axis slices covering the heart from apex to the atrioventricular separation. Each short-axis slice comprised of 32-36 frames acquired throughout the cardiac cycle with an in-plane resolution of $100 \times 100 \mu m$ and a slice thickness of $1.5 mm$. A short-axis view in end-diastole is shown in Figure 2.7(a). The DT-MRI images were subsequently acquired on excised rat hearts in six non-collinear directions, fixed either in the resting state or in contraction and embedded in agarose, at an isotropic resolution of $100 \mu m$, as described in [129]. Figure 2.7(b) shows three views of the *ADC* 3D image computed from the DT-MRI scan of one subject belonging to the dataset.

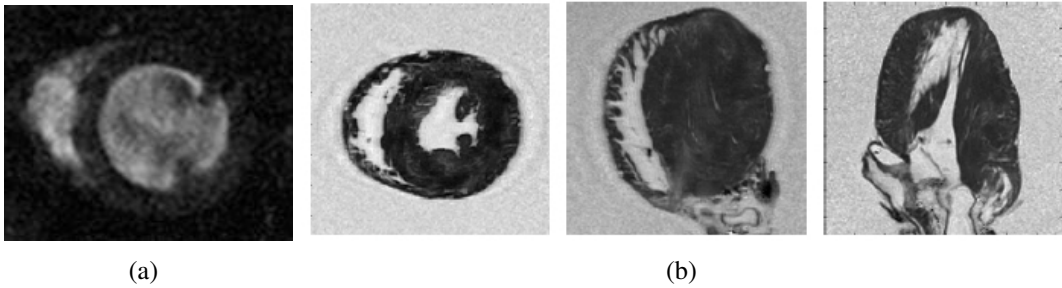


Figure 2.7: (a) Midventricular short-axis cine-MRI image at approximately end-diastole from *dataset*₁. (b) *ADC* image of one agarose-embedded heart DT-MRI dataset (*dataset*₁).

The cine-MRI scan of one rat from this dataset was used to (a) estimate the dimensions of the left ventricular mesh for the simulations of Chapters 5 and 6 (as described in Section 4.2); (b) measure indices such as ejection fraction, in order to compare between measured and predicted values from simulation (see Section 5.2.1). The DT-MRI data were employed

by Karadag et al. [71] to obtain the locally optimised fibre model used in the simulation study of Chapters 5 and 6.

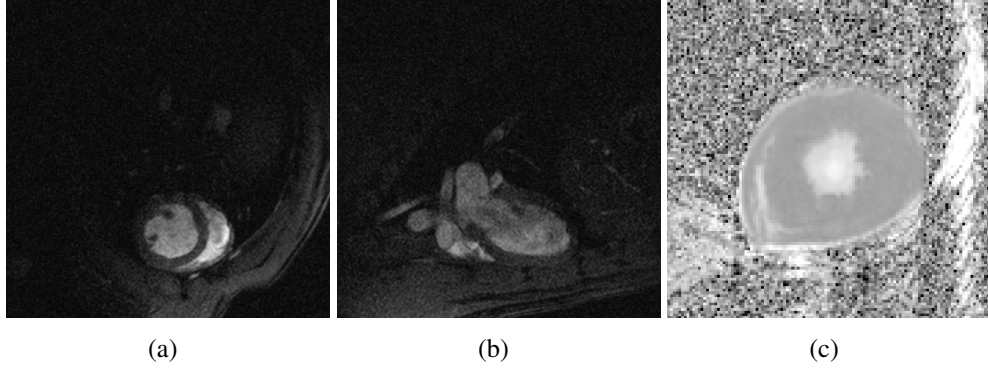


Figure 2.8: (a) Short-axis cine-MRI image at end-diastole from *dataset₂*. (b) 2-chamber long-axis cine-MRI image at end-diastole from *dataset₂*. (c) Midventricular short-axis slice of the *ADC* image from *dataset₂*.

2. **dataset₂** : The MR system details and the in vivo cine-MRI sequence are the same as *dataset₁*. The cine-MRI scans contained two long-axis images, a 2-chamber and a 4-chamber image, for each time frame, in addition to the short-axis views. For example, Figure 2.8(a) shows a midventricular short-axis slice at approximately end-diastole, while Figure 2.8(b) is the corresponding 2-chamber long-axis view. The DT-MRI images were performed on Langendorff-perfused hearts, that were imaged in both a slack (relaxed) and contracted state. Acquisition was performed in 10 non-collinear diffusion directions. The in-plane resolution is $150 \times 150 \mu m$ and the slice thickness is $1 mm$ for a total of approximately 13 slices from apex to the atrioventricular separation. A more detailed explanation of the experimental set up can be found in [57]. For each rat, and for each state (either slack or contracted), the dataset consists of the following images:

1. **Directly acquired images:**

- S_0 – the 3D baseline signal.
- Diffusion tensor D – a $6 \times 3D$ set of images, one 3D image for each independent component of the symmetric 3×3 tensor.

2. **Calculated from the directly acquired images:**

- FA – a 3D image.
- $L1$, $L2$, $L3$, the eigenvalues λ_1, λ_2 and λ_3 for each voxel – each a separate 3D image.

- V_1, V_2, V_3 , the eigenvectors ν_1, ν_2 and ν_3 for each voxel – each a separate 3×3 D image, one image for each component of the vector.

The image analysis study presented in Chapter 7 was performed on one rat from this DT-MRI dataset.

This chapter has described the most common cardiac imaging modalities focussing on DT-MRI and how tissue structure can be obtained from it. Methods to quantify tissue structure distribution in terms of angular metrics have also been introduced. Finally, the imaging datasets employed in the research studies of Chapters 5-7 have been described. In the following chapter the state-of-the-art in cardiac modelling will be reviewed and the mathematical background of the electromechanical model developed will be provided.

Chapter 3

Computational models of cardiac electromechanics

This chapter focuses on computational models of the heart and is divided into two parts. The first part discusses the state-of-the-art in cardiac modelling, from single cell electrophysiological models to ventricular electromechanical ones. The importance of imaging in more recent modelling approaches is highlighted and the role of tissue structure in cardiac models is also emphasised. In the second part of the chapter the mathematical background necessary to understand the electromechanical model developed and employed in this thesis is provided. Finally, the numerical scheme for the approximation of the solution of the model and the software used to run the simulations are described.

3.1 State-of-the-art on cardiac modelling

Cardiac electromechanical models are complex modular systems that build upon submodels coming from a number of fields while encompassing spatial and temporal scales of various orders of magnitude. It is therefore difficult to give an historical perspective on such models without first discussing separately each of their major components, commenting on how the most important modelling aspects of each component have been addressed. A thorough review of all these components is outside the scope of this section. However, the review focuses on those key features that will help the reader understand and put into context the electromechanical model developed in this thesis.

3.1.1 Ventricular geometry

The first step in the development of a cardiac model is the definition of the spatial domain and its discretisation. Typically, no spatial domain is taken into account for single cell models. At the tissue level, the focus might be on the behaviour of a 2D or 3D slab of

tissue rather than simulating cardiac function of one ventricle or even of the whole heart. While the spatial domain for tissue slab models is typically mathematically prescribed, models involving the ventricles can either rely on a mathematical approximation of the ventricular geometry, or on the extraction of realistic representations from imaging data. For example, it is common to use a thick-wall truncated ellipsoid to approximate the shape of the left ventricle [157], [93]. Recently, the use of realistic geometries extracted from imaging data such as MRI [141] has become more frequent. The increasing interaction between modelling and imaging will be discussed in Section 3.1.5, along with the related topic of patient-specific modelling.

Even when the shape of the ventricle is obtained from imaging data, the level of detail captured by the geometrical model depends on a number of factors. In Section 3.2.3.2 the Finite Element Method (FEM), the most commonly employed numerical scheme for approximating the solution of cardiac models on complex geometries, will be described. The FEM requires the geometry to be subdivided into elements. Therefore, depending on the resolution of such subdivision and on the shape of the reference element used, the resulting approximation of the ventricular shape will vary greatly.

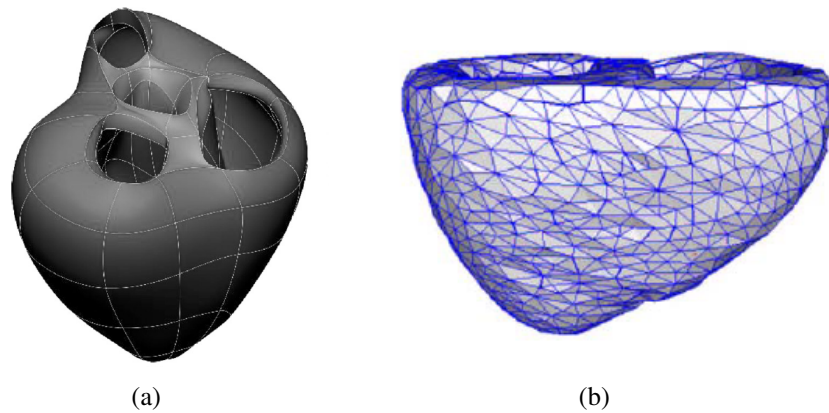


Figure 3.1: (a) Model of the two ventricles in the pig heart reconstructed from histological measurements, from [156]. (b) Model of the two ventricles in the human heart extracted from MRI, from [141]. Both figures are reproduced with permission from Elsevier.

As an example, in Figure 3.1 two types of geometrical approximations of the left and right ventricles of the heart are shown. On the left (Figure 3.1(a)), the model [156] is smooth and made of a few cubic Hermite hexahedral elements. The shape was fitted on histological measurements of the endocardial and epicardial surfaces, as described in [93]. On the right (Figure 3.1(b)), a tetrahedral model [141] is shown of the two ventricles of the human heart reconstructed from clinical MRI [148]. Meshes with higher resolution than those shown in Figure 3.1 have been employed in high-resolution studies of electrical propagation [17].

The best choice for a geometrical model depends on the type of computational study to be performed, the computer power available and the temporal and spatial scales.

3.1.2 Modelling cardiac electrophysiology

The first models of cardiac electrical activity focused on the mathematical description of the action potential (AP). Two approaches can be identified in AP models, a biophysically detailed and a phenomenological one. The first aims at describing the AP by using parameters and variables in the model that are linked to the physiology underlying the AP, while the second aims at reproducing AP characteristics such as the voltage trace by a simple model whose parameters have no direct physiological meaning. Biophysical models of myocyte AP all derive from the seminal work of Hodgkin and Huxley, who first modelled the electrical activity of the single nerve cell back in 1952 [65]. In their model, the transmembrane voltage of the cell is related to the ionic currents across the membrane, which are modelled according to Ohm's Law. The first model of cardiac AP was developed by Noble in 1962 [118], who modified the Hodgkin and Huxley model to reproduce the currents and voltage traces of a Purkinje fibre. These models describe ionic currents as being dependent on time, voltage and channel open-probability, while the dependence on ionic concentration was included later, starting with Beeler and Reuter [12]. Subcellular components such as the sarcoplasmic reticulum started to be included in AP models in order to better characterise the intracellular calcium dynamics [101]. Since then more subcellular structures have been included [102]. AP models for a number of species (for example, rat [122], mouse [176], guinea-pig [101], rabbit [102] and human [160]) have been developed, and the variability of the AP within the same heart has been modelled as well (epicardial versus endocardial AP in rat [122], transmural AP variability in human [160], to cite a few). Another important advancement was the introduction of Markov models to explicitly describe the various states a single ion channel goes through, such as open, closed, activated and inactivated. In this way it is possible to model how the specific dynamics of a given ion channel at the molecular level is able to directly affect AP shape and duration [140].

On the one hand, the continuous refinement of AP models in order to capture as many physiological and biochemical details as possible has led to a wider understanding of the ionic basis of AP. On the other hand, the increasing complexity of such models has higher computational costs and the higher number of parameters makes the model more difficult to analyse. A totally different approach is based on phenomenological models. Their main aim is to keep the number of variables and parameters involved in the model at minimum while still being able to reproduce the characteristics of interest, such as AP shape and

duration or the upstroke velocity. Such models are inspired by the work of Fitzhugh [43] and Nagumo [108] who developed a simplified model of the Hodgkin and Huxley model. Recent phenomenological models of human AP have been able to reproduce main characteristics of AP with good agreement with some of the most complex biophysical models by employing a minimal set of only four pseudo-ionic currents [22].

Models of electrical propagation at the tissue level are most commonly based on the use of a type of reaction-diffusion equations known as bidomain equations [61]. The bidomain model assumes that cardiac tissue is made of two coexisting and overlapping spaces, the intracellular and extracellular space, so that at each point it is possible to define an intracellular and extracellular potential. The resulting transmembrane potential is the difference between the two potentials. The bidomain equation can be simplified into the monodomain equation, that, by assuming a proportionality between intracellular and extracellular conductivities, has only the transmembrane voltage as the unknown. The monodomain model has the advantage of being less computationally expensive than the bidomain one. Furthermore, it has been shown that there is good agreement between the two approaches when modelling electrical propagation under physiological and pathological conditions, while for models of defibrillation, in which high current stimuli are applied, the bidomain model is to be preferred [132].

Computational studies of electrical propagation based on the bidomain/monodomain model have been carried out to explore the effect of heart size on the electrotonic coupling [142] or variability in propagation patterns due to geometrical heterogeneities [17]. Most studies focus though on pathological conditions [162]. For example, there are studies of how defibrillation procedures induce anomalous propagation patterns in the ventricles [139], the effect of ischemia on propagation [70] or the mechanisms underlying the initiation and sustenance of arrhythmias [5], [169]. The effect of mechanoelectric feedback (MEF) has also been investigated in electrophysiological computational studies, by modelling the activation of stretch-induced ion channels upon physical impact in order to understand how this can lead to arrhythmogenesis [46].

3.1.3 Modelling cardiac mechanics

The development of cardiac mechanical models has been historically slower, more controversial and complex than its electrophysiological counterpart. This is due to its higher level of mathematical complexity, issues of numerical instability and significantly higher computational demand [77]. Cardiac mechanics is based on the combination of passive material response to deformation and active contraction of myocardial tissue.

Modelling the passive response of myocardial tissue is strictly related to the determination of a *constitutive law*, that is a functional relation between stress and strain in the tissue. The most common approach to constitutive modelling is to fit the parameters of some function to experimental tests of stress-strain response in small samples of tissue. Uni-axial [106], bi-axial [96] or multi-axial [40] tension tests have been employed to experimentally study the stress-strain relationship. Uni-axial tests are very limited in the characterisation of cardiac tissue material properties, while bi-axial and especially multi-axial tests have proven more informative. However, tension testing has significant limitations, in fact it is performed on excised samples of tissue, whose mechanical behaviour is different from that of the intact heart, due to, for example, the presence of residual stress [54]. More recently, non invasive approaches to constitutive modelling have been developed that involve the use of imaging modalities such as cine-MRI and Tagged-MRI, together with nonlinear optimisation [177] or data assimilation methods [182]. The main advantages of these methods are their non invasive nature and the fact that they provide personalised parameter fitting. However the solution obtained is not unique. Constitutive laws based on a function fitted to experimental results are usually considered phenomenological, since no specific physical meaning can be assigned to the fitted parameters. A more biophysical strategy includes the effect of tissue structure in functional relationship between stress and strain. Such models can be partially structure-based, as for example the pole-zero law [109], or fully structure-based [66], [175], depending on the importance of tissue structure in the function. Structurally-based constitutive laws have a more general theoretical basis than phenomenological laws [66] but they are more complex.

All constitutive models of cardiac tissue, whether phenomenological or structure-based, assume a certain level of symmetry in the material passive behaviour. The most common type of symmetry considered are transverse isotropy and orthotropy. In the first case, the material is regarded as having significantly different passive response in the fibre direction compared to the cross-fibre plane. Constitutive laws assuming transverse isotropy are usually based on experimental results obtained from bi-axial tension tests. Orthotropy identifies three distinct directions of passive material response, that is the fibre, sheet and sheet-normal directions. The latter constitutive strategy is supported by multi-axial tests. As a first approximation, transverse isotropy is widely employed in computational studies of cardiac mechanics (or electromechanics) [114] [78], although it has been shown that orthotropic models are able to better predict strain variation during cardiac cycle [166], [21].

There is a vast literature of cardiac mechanical models that only take into account passive mechanics. Such models have been employed in constitutive modelling [54], especially in the estimation of constitutive parameters from Tagged-MRI [8], [177], or in the study of the diastolic phase, with a particular interest on how the mechanoelectric feedback interacts with ventricular filling [172]. Interestingly, Watanabe et al. [178] investigate the effect of preload and afterload on diastolic filling, in an integrated model of circulatory flow and passive mechanics.

Active contraction of myocardial tissue has its physiological basis at the cellular level. The contractile force generated by the myocyte is dependent on a cascade of events involving Ca^{2+} , as explained in Section 1.2.2. It also depends on strain and strain rate, that is, on length variation of the sarcomere unit and on the velocity at which this variation occurs. Nonetheless, the mechanisms underlying the generation of contractile force are still not fully understood and thus difficult to model [90]. Contraction models used in ventricular or whole-organ simulation studies tend to be simple, aiming only at reproducing the temporal variation of the contractile force by relying on a reduced set of parameters. Sermesant et al. [147] and Nash and Panfilov [110] developed phenomenological models of force generation dependent on transmembrane voltage. Kerckhoffs et al. [75] model the force dependence on contractile activation time, which in turn depends on transmembrane voltage, and strain. More detailed models include calcium dynamics and strain rate [115]. Markov-model approaches to the modelling of the actin-myosin crossbridge have also been considered [90], [107]. When cellular contraction models are embedded into tissue mechanical models, the force generated at the cellular level has to be transformed into a tissue active tension (as it is commonly referred to, but it is actually a stress) [124]. Usually the force at the tissue level is modelled as being generated only along the fibre direction, although force generation has been experimentally shown to be anisotropic across the tissue [96]. For these reasons, some models introduce two types of active tension, one in the fibre direction and one in the cross-fibre plane [166]. Even though the mechanisms of cross-fibre tension generation are not clear yet, the inclusion of such a component in the models may improve the match between experiments and simulations [21]. Similarly, the fitting of constitutive law parameters has shown to benefit from the introduction of this cross-fibre tension generation [173].

Models of cardiac mechanics combining passive deformation with active force generation have been employed to understand how stresses and strains distribute during cardiac cycle in the ventricles and how tissue structure affects such distributions [166]. Since stresses cannot be reliably measured [167], the common assumption adopted is that, if a model is

able to predict realistic strain patterns, which can be quantified experimentally, then the resulting predicted stress distribution will also be realistic [109]. Cardiac mechanics models have also been employed to understand how infarction changes the contractile ability of the tissue in the vicinity of the infarct zone [104], [179], to suggest a model-based procedure of treatment of the infarct region [44] or in the presence of ischemia [64].

3.1.4 Models of cardiac electromechanics

Modelling the electrophysiological and mechanical properties of the heart separately has brought important insights. However, it is by combining these two parts that it would be possible to capture the integrated nature of cardiac function. The most common approach to electromechanical modelling is that of coupling previous models of electrophysiology with existing models for mechanics [77]. Coupling can involve one or more variables and can be performed at various degrees. In terms of the degree of coupling, models are commonly divided into weakly and strongly coupled. In weak coupling the electrophysiological model is solved first, and the output (voltage alone or in combination with calcium related variables) is passed to the mechanical component to solve for deformation and active contraction [92]. Although weak coupling allows the model to be more modular and computationally tractable, it excludes mechanoelectric feedback. Such models often prefer a simplified model of electrical wave propagation, for example, the *Eikonal model* to the reaction-diffusion approach. The Eikonal model only provides the spatial distribution of electrical activation times in tissue [134]. In this way models can focus, for example, on the spatial distribution of the electromechanical delay (the delay between electrical activation on beginning of contraction) in pathological conditions [168], [56]. In strongly coupled models the electrical and mechanical parts are solved simultaneously. Rice et al. [138] developed a strongly coupled cellular model to investigate the effect of interbeat intervals on force generation by including the feedback of force generation variability onto intracellular calcium concentration. At the tissue level, strongly coupled models have been employed to investigate the effect of deformation on electrophysiology, for example in the study of the effect of deformation on arrhythmogenesis [110], [74]. The computational complexity of strongly coupled electromechanical models has often to be balanced by making simplifying assumptions in some other components of the model. For example, Nash and Panfilov [110] used phenomenological AP and contraction models in a finite element framework, whereas Keldermann and Nash [74], while using biophysical models for AP and contraction models, introduced a finite difference scheme to simplify the electrical part at the tissue level, combined with a finite element formulation for the mechanics. Numerical stability

can also be an issue for strongly coupled models because of their complexity and lack of flexibility [92].

Blood pressure is another fundamental aspect of the mechanical balance in the heart that needs to be included in a cardiac mechanical model in order to correctly reproduce the phases of the cardiac cycle, such as the turnover of isovolumetric and non-isovolumetric phases during systole and diastole. The simplest way to introduce pressure in a model is by adding a pressure trace as an additional boundary condition to the endocardial surface [41]. This is the approach chosen in this thesis, as further explained in Section 6.3 as it allows reasonably realistic traces to be obtained for the ventricular cavity volume and the pressure-volume relationships with little additional complexity of the electrochemical model. However, it is not possible to enforce isovolumetric phases in the simulations, which require the explicit use of volume constraints [114]. More advanced models rely on the coupling between the electromechanical model and a model of blood circulation. One example of this type of coupling is with a *Windkessel model* [77]. This model can contain from two to four parameters that take into account, for example, the arterial response to stretch and the resistance encountered by blood flow as it passes from arteries to veins and capillaries. The main limitation of Windkessel models is that diastolic and aortic pressures are prescribed, whereas with more complex models such as the *lumped models*, which represent a closed-loop circulatory system, these two properties emerge from the model itself [163]. The main advantage of coupling with circulation models is the fact that boundary conditions such as those on pressure and volume constraints are not required any more. However, the complexity and computational cost of the overall model is dramatically increased. The high complexity of such circulatory models can be reduced if part of the parameter estimation is embedded in the model itself by considering subsystems adaptation to changes in pressure load [7].

Electromechanical models in recent years have been employed to improve the understanding of the mechanisms underlying cardiac function, or to help predict the emergence and impact of pathological conditions. Niederer et al. [114], for example, have investigated how dynamics produced at the cellular level is transformed into pumping function at the organ level. Many studies have focused on the effect of tissue microstructure on cardiac mechanics and electrical propagation, as described in Section 3.1.6. Chronic pathologies can induce tissue remodelling that in turn is responsible for cardiac dysfunction. Choi et al. [28] have studied the effect of left ventricular shape changes onto cardiac function, finding that increased sphericity of the left ventricle is correlated with reduced contraction

efficiency and increased regional stress. Adaptive modelling is a particularly suitable approach for the study of cardiac tissue remodelling as it is able to reproduce the long-term effects of pathology on physiological parameters and tissue structure and resulting effects such as reduced pumping function or dissynchrony [87]. The emergence of dissynchrony or asynchrony in response to pathology and cardiac resynchronisation therapy (CRT) have been the principal application of electromechanical models in recent years. Early studies have focused on dissynchrony/asynchrony between electrical propagation and subsequent contraction [168] and how this can be induced in the case of external pacing [76]. Electromechanical models have been employed to study the synergy of different pathological conditions and to develop more efficient indices for the quantification of their effect [78]. The ability of the CRT to restore cardiac pumping function has also been studied by modelling how regional work is affected by it [113]. Optimal location of pacing sites for CRT in combination with minimal energy consumption has also been investigated [184].

In the following two sections, two aspects of electromechanical modelling that are particularly related to the research studies presented in this thesis are further discussed. First, the increasing combined use of (electro)mechanical models and imaging modalities and how this has favoured the development in the modelling community of a subject-specific (or patient-specific) approach will be addressed. Second, the role of tissue microstructure in cardiac models will be reviewed.

3.1.5 Modelling and imaging, two converging fields

The connection between cardiac modelling and imaging has in recent years become increasingly tight. On the one hand, cardiac imaging modalities have become a powerful non-invasive way to monitor cardiac function, as discussed in Section 2.1. Image datasets from a number of modalities are available not only for the study of animal models but also for the investigation of human healthy and diseased subjects. On the other hand, the significant improvement in the computational power available has made it possible to run complex multi-scale cardiac models that employ imaging data at various steps. Most commonly, there are two steps in which the imaging data are employed in the development of a cardiac model: the generation of the geometry (as seen in Section 3.1.1) and model validation. For example, strain patterns measured on tagged-MRI have been used to validate electromechanical models [165] [21]. More complex frameworks include the estimation of constitutive parameters and tissue structure distribution from imaging modalities [146].

The reverse is also true, mechanical models of the ventricles have been employed to aid in the processes of image segmentation from MRI [147] or to extract wall motion patterns

from ultrasound scans in order to detect ischemic regions [63]. Billet et al. [15] employ data assimilation techniques for the recovery of cardiac motion from cine-MRI. Another interesting application can be found in Veress et al. [171] who use finite element modelling of the heart and the surrounding torso to simulate a torso phantom for medical imaging research.

Cardiac imaging and modelling appear to be two fields of research where the areas of overlap and integration are continuously evolving. Such synergy is at the base of the so-called patient-specific approach in modelling, which aims to develop models of cardiac function to target not the average behaviour of the heart but that of a specific individual. The patient-specific approach is believed to have the potential of becoming a valuable tool in support of clinical decision making [111]. However, this patient-specific approach adds complexity to the models, making the modelling frameworks more complex while the improvement in the predictive power of the model is not always significant [48], [24]. I will come back to this point in Chapters 5 and 6 as this is one of the conclusions of my research on the effect of tissue microstructure on left ventricular contraction.

3.1.6 The role of tissue structure in cardiac modelling

Tissue structure has been described from an anatomical point of view in Section 1.1.2, highlighting its importance for tissue electrical propagation and mechanical contraction. In this section the focus is on the way tissue structure is commonly embedded in cardiac electrophysiological or (electro)mechanical models, addressing fibres and sheets separately.

Fibres are often mathematically prescribed [71] when included in cardiac tissue models. Recent advances in technology have made it possible to measure local microstructure using diffusion tensor MRI (DT-MRI). As described in Section 2.2.5, the primary eigenvector of the diffusion tensor has been shown to correlate with the fibre direction, while the tertiary eigenvector usually identifies the normal to the sheet plane. Electromechanical models based on DT-MRI data suggest that fibres are a dynamical system in cardiac structure, undergoing adaptation that minimises shear strains, behaviour that can have important consequences in tissue remodelling in pathology [86]. The role of tissue structure on contraction has also been investigated by means of sensitivity analysis of different tissue structure distributions [42], [24]. Eriksson et al. [42] find that global parameters of cardiac function are not significantly affected by different tissue structure distribution, whereas regional parameters such as strain are affected. On the contrary, in my study I have identified global indices of cardiac function that appear to be influenced by tissue structure variability, as detailed in Chapters 5 and 6.

The importance of local myocyte orientation in cardiac function, both in healthy and diseased states, has promoted considerable effort in recent years towards subject-specific modelling of cardiac electromechanics [23]. Pathological conditions such as dissynchrony [2] have been investigated, with realistic ventricular to whole-organ geometries, combined with fibre orientations obtained from imaging [169]. The results are promising, but, as discussed in the previous Section, it is still an open question whether current electromechanical models are close enough to becoming a real support tool in clinical decision-making.

The laminar structure of myocardial tissue is also important for cardiac electromechanics. It has been established that sheets undergo shortening in the fibre direction, extension in the in-sheet/cross-fibre plane, thickening and shear, whose regional variability and transmural distribution are important for the distribution of strain and stress throughout the ventricle during cardiac motion [32]. In particular, the sheet plane has been shown to be the plane of maximum shear during systole, corroborating the hypothesis that sheet dynamics is a fundamental component of ventricular contraction [6]. More recently, changes in sheet intersection angles have been identified to occur during the cycle of contraction and relaxation [57]. This sheet dynamics forms one of the underlying mechanisms to explain wall-thickening during contraction [27]. Sheets have been modelled as continuously varying transmurally [94], although more recent experimental findings suggest that the transmural distribution of sheets is more complex and discontinuous [57], see for example Figure 1.3(a). Sheet orientations directly obtained from histological data, usually obtained from a small number of ventricular locations only, have been employed in computational studies of the effect of tissue microstructure on electrophysiology [68]. However, other studies question the importance of sheet distribution in electrical propagation [30]. As discussed in Section 3.1.3, the role of tissue structure in determining the passive behaviour of myocardial tissue has been investigated and has led to the development of structure-based constitutive laws. Usyk et al. [166] have explored the benefits of changing from a transversely isotropic material law, that is considering only the fibres as a preferential direction in the material, to an orthotropic material law, that allows the sheet plane also to be taken into account. This greatly improves the prediction of strains. A similar conclusion was reached by Bovendeerd et al. [21], especially in the case of shear strains. Both models include the cross-fibre active tension generation, that is another way of taking the laminar structure of the heart into account.

Despite these modelling efforts, the importance of sheets in the cardiac modelling community has not been fully acknowledged in spite of the experimental evidence. I will come

back to this point in Chapters 5 and 6, as this is a fundamental aspect of the scientific hypotheses and results presented there.

3.2 Mathematical background

This section provides the mathematical background for the electromechanical model I have developed and used in the simulation studies of Chapters 5 and 6. The main building blocks of the model are addressed separately, and the defining equations for each of them are provided. The same strategy is used later in Chapter 4, where it is explained how these equations were applied and the related parameters adjusted in order to simulate contraction of the left ventricle in rat. Figure 3.2, shows a diagram of the components of a general electromechanical model. The modelling framework I have used is a subset of that. The arrows in blue in the diagram correspond to those parts of the modelling framework that are taken into account in my model.

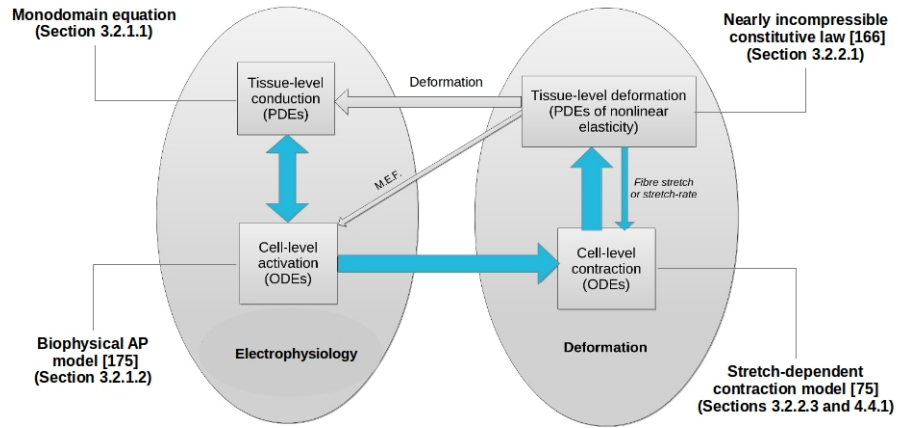


Figure 3.2: Typical components of an electromechanical model. Blue arrows represent the input/output relationships that are taken into account in the model employed in this study. Additional information about the model developed in this thesis is provided alongside the diagram and refers to the relevant sections.

3.2.1 Electrophysiology

3.2.1.1 Tissue electrical propagation

For the electrical propagation in tissue the monodomain approach was used. As described in Section 3.1.2, the tissue is modelled as a virtual syncytium resulting from the homogenisation of the cellular domain by combining a reaction-diffusion equation (eqn. (3.1)) coupled with the system of ordinary differential equations (ODEs) representing the cellular model (eqn. 3.2):

$$\chi(C_m \frac{\partial V}{\partial t} + I_{ion}(\mathbf{g}, V)) - \nabla \cdot (\epsilon \nabla V) + I_{stim} = 0 \quad (3.1)$$

$$\frac{\partial \mathbf{g}}{\partial t} = \phi(\mathbf{g}, V) . \quad (3.2)$$

Here V is the transmembrane voltage (mV), t is time (ms), C_m is the membrane specific capacitance ($\mu F/cm^2$), χ is the surface area-to-volume ratio (cm^{-1}), ϵ is the effective conductivity tensor (mS/cm), a matrix of conductivities taking into account the fibre, sheet and sheet-normal directions. The vector \mathbf{g} represents the set of state variables forming the cell electrophysiological model, whose temporal variation is regulated by the ODE system in eqn. (3.2) (ϕ is a generic symbol representing a functional dependence). The variable $I_{ion}(\mathbf{g}, V)$ is the ionic current provided by the cell model ($\mu A/cm^2$) and I_{stim} is the external stimulus per unit volume ($\mu A/cm^3$). Boundary conditions for the monodomain problem usually require no flow of current across the boundary (eqn. 3.3)

$$(\epsilon \nabla V) \cdot \mathbf{v} = 0 \quad \text{on } \Omega_0 , \quad (3.3)$$

where \mathbf{v} is the vector normal to the surface of the domain $\partial\Omega_0$. A transmembrane stimulus I_{stim}^* can also be added as the right-hand side of eqn. (3.3).

3.2.1.2 Myocyte electrical activity

Two equations are at the core of the biophysical approach to modelling the AP: the Nernst equation and the current-voltage equation [133]. The first describes the equilibrium voltage for an electrochemical system with respect to each of its chemical entities. Considering an ion type Q (in the case of the cardiac myocyte this could be Na^+ , K^+ etc.), then the electrochemical potential across the cell membrane at the equilibrium is given by

$$E_Q = \frac{RT}{zF} \ln \frac{[Q]_{out}}{[Q]_{in}} , \quad (3.4)$$

where R is the gas constant ($8.31 J/(K \cdot mol)$), F is the Faraday constant ($9.65 \cdot 10^4 C/mol$), T represents the temperature (in Kelvin), z is the number of charges the ion carries and $[Q]_{out}$ and $[Q]_{in}$ are the extracellular and intracellular equilibrium concentrations of the ion Q , respectively. From the Nernst equation, the current I_Q due to the flow of a given ion across the membrane can be obtained as

$$I_Q = f(g_Q, (V - E_Q)) , \quad (3.5)$$

which is a function of the conductance g_Q of the ion channel, the ion potential at equilibrium E_Q and the transmembrane potential V . The conductance g_Q is usually a non-linear function of potential, time and, in some cases, concentration [133]. This is equivalent to considering the cell as the electrical circuit shown in Figure 3.3(a). The sum of all ionic currents in the cell is then passed to the monodomain equation 3.1 through the variable $I_{ion}(\mathbf{g}, V)$. As discussed in Section 3.1.2, the number and formulation of ionic currents involved greatly varies from one cell model to the other.

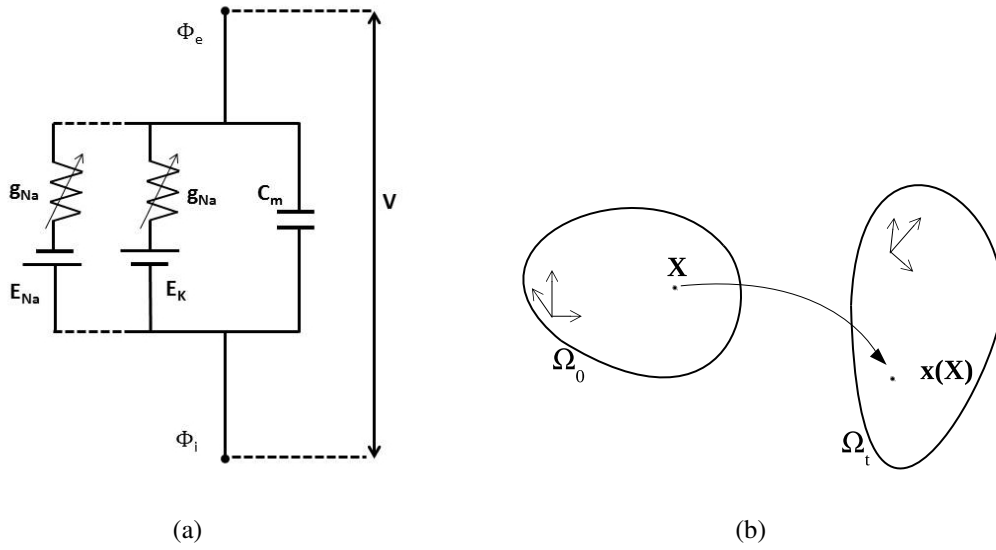


Figure 3.3: (a) Model of the cell membrane as an electrical circuit, redrawn from [133]. (b) The point with coordinate \mathbf{X} in the undeformed (or reference) state Ω_0 is associated with the coordinate $\mathbf{x}(\mathbf{X})$ in the deformed state Ω_t at time t .

3.2.2 Mechanics

Cardiac tissue is non-homogeneous, nearly incompressible, viscoelastic (although usually modelled as hyperelastic) and it undergoes large deformations during the cardiac cycle [66]. Therefore, its mechanical behaviour is modelled according to finite elasticity theory. In the following, the summation convention is used, where repeated indices imply a summation over that index. Let us consider two systems of Cartesian coordinates: a reference system defined on the undeformed body, $\mathbf{X} = (X_1, X_2, X_3)$, and a second system representing the deformed state, $\mathbf{x} = (x_1, x_2, x_3)$ (see diagram of Figure 3.3(b)). The components of the *deformation gradient tensor* F , which describes the transformation from the undeformed state to deformed one, can be written as $F_{iM} = \frac{\partial x_i}{\partial X_M}$. The *Green deformation tensor* $C = F^T F$, with components $C_{MN} = F_{iM} F_{iN}$, describes the deformation in the undeformed

coordinate system. Finally, the *Lagrangian strain tensor* is given by $E = \frac{1}{2}(C - I)$, where I is the identity matrix.

Three types of stresses can be defined, depending on the system of coordinates considered. The *Cauchy* stress tensor σ measures the force per unit of deformed area on the deformed body. The *1st Piola-Kirchhoff* stress tensor S measures the force per unit of the undeformed area on the deformed body. Finally, the *2nd Piola-Kirchhoff* stress tensor T measures the force per unit of the undeformed area on the undeformed body. The following relationships hold between the stress tensors:

$$T = JF^{-1}\sigma F^{-T}; \quad S = JF^{-1}\sigma; \quad T = SF^{-T}, \quad (3.6)$$

where $J = \det(F)$. It is common practice in electromechanical modelling to represent the stresses at the tissue level by means of the 2nd Piola-Kirchhoff tensor T . F can be used to relate the undeformed fibre \mathbf{f} , sheet \mathbf{s} and normal directions \mathbf{n} and the deformed variants $(\tilde{\mathbf{f}}, \tilde{\mathbf{s}}, \tilde{\mathbf{n}})$. For example $\tilde{\mathbf{f}}$ is obtained from the \mathbf{f} by

$$\tilde{\mathbf{f}} = \frac{F\mathbf{f}}{\|F\mathbf{f}\|}. \quad (3.7)$$

Similarly, $\tilde{\mathbf{s}}$ and $\tilde{\mathbf{n}}$ can be obtained from \mathbf{s} and \mathbf{n} , respectively.

3.2.2.1 Tissue constitutive properties

In order to describe the material response to deformation a constitutive law is required, as explained in Section 3.1.3. When modelling cardiac tissue, the constitutive law is typically dependent on strain only, that is the tissue is treated as hyperelastic. However, tissue is intrinsically viscoelastic in nature, that is the material response is dependent on strain rate. The hyperelastic approximation is justified by the fact that the timescale of the viscoelastic response is significantly larger than that of the cardiac cycle [66]. In the hyperelastic case, the constitutive law is characterised by a strain-energy function W , defined per unit of volume. The constitutive modelling approach followed in my thesis is based on the Fung-type strain energy law [67]. This family of strain-energy laws have been derived from the original formulation by Fung [45] that approximated the viscoelastic soft tissue material properties by means of a general hyperelastic model (eqn.(3.8))

$$W = \frac{1}{2}[q + C(e^Q - 1)] \quad \text{with} \quad q = a_{ijkl}E_{ij}E_{kl} \quad \text{and} \quad Q = b_{ijkl}E_{ij}E_{kl}, \quad (3.8)$$

where a_{ijkl} , b_{ijkl} and c are constants. In particular, the constitutive model developed by Costa et al. [34] for incompressible tissue, and extended by Usyk et al. to make the tissue

nearly incompressible [166], was employed in the model. The constitutive law of Usyk et al. [166] is rewritten in eqn. (3.9) as

$$\begin{aligned} W(E) &= \frac{C_a}{2}(e^Q - 1) + C_b(J \ln(J) - J + 1) \quad \text{where} \\ Q &= \sum_i \sum_j b_{ij} E_{ij}^2 \quad i, j \in \{f, s, n\} \quad \text{and} \quad b_{ij} = b_{ji}, \end{aligned} \quad (3.9)$$

where C_a is a stiffness constant, b_{ij} for $i, j \in \{f, s, n\}$ are the stiffness parameters and E_{ij} is the component in the ij direction of the Lagrangian strain tensor. The parameter C_b regulates the level of compressibility allowed by the material law: the higher the value the closer is the material to being incompressible. Usyk et al. [166] added the compressible component $C_b(J \ln(J) - J + 1)$ to the incompressible formulation $W(E) = \frac{C_a}{2}(e^Q - 1)$ of Costa et al. [34].

3.2.2.2 Tissue stress generation

The 2nd Piola-Kirchhoff stress tensor T for the overall stress produced by the tissue is the sum $T = T^{passive} + T^{active}$ of the stress due to the tissue passive response, $T^{passive}$, and active contraction, T^{active} . As with the formulation of the strain-energy function $W = W(E)$, the manner in which $T^{passive}$ is expressed in terms of W determines whether the tissue is treated as incompressible or compressible. The constitutive relation between passive stress $T^{passive}$ and strain is given by eqn. (3.10) in the incompressible case

$$T_{MN}^{passive} = \frac{1}{2} \left(\frac{\partial W}{\partial E_{MN}} + \frac{\partial W}{\partial E_{NM}} \right) - \mu C_{MN}^{-1} \quad M, N = 1, 2, 3, \quad (3.10)$$

where the final element of the eqn. (3.10) arises from the constraint of incompressibility at each point, with μ being a Lagrange multiplier. In the case of compressible tissue, this component is omitted.

From the Cauchy stress computed by the contraction model σ_a , the associated Cauchy stress tensor σ^{active} is calculated with respect to the deformed fibre direction $\tilde{\mathbf{f}}$ by $\sigma^{active} = \sigma_a \tilde{\mathbf{f}} \tilde{\mathbf{f}}^T$. The 2nd Piola-Kirchhoff stress tensor $T^{passive}$ is then obtained by applying eqn. (3.6).

Contraction models assume that the force is generated along the fibre direction, nonetheless, as discussed in Section 3.1.3, some force is also generated in the cross-fibre plane. For example, Usyk et al. [166] take the active stress generated along the fibre direction, scale it by a stretch-related parameter and apply it along the sheet and sheet-normal directions.

This can be translated into a new formulation for the Cauchy stress tensor σ^{active} , as shown in eqn. (3.11):

$$\sigma^{active} = \sigma_a \tilde{\mathbf{f}}\tilde{\mathbf{f}}^T + k_s \sigma_a \tilde{\mathbf{s}}\tilde{\mathbf{s}}^T + k_n \sigma_a \tilde{\mathbf{n}}\tilde{\mathbf{n}}^T . \quad (3.11)$$

Here k_s and k_n are in the range $[0 \ 1]$ and represent the fraction of the scalar stress σ_a that is applied in the sheet and sheet-normal direction, respectively.

Finally the equations for the conservation of linear momentum shown in eqn. (3.12) are solved. The time-dependent inertial term of the equilibrium is usually neglected [180][110], as well as the effect of gravity.

$$\frac{\partial}{\partial X_M}(T_{MN}F_{iN}) = 0 , \quad i = 1, 2, 3 . \quad (3.12)$$

If the tissue is treated as being incompressible the condition $J = 1$ is added. Suitable boundary conditions for eqn. (3.12) consist of two divisions of the boundary: $\partial\Omega_0^D$ for (displacement) Dirichlet boundary conditions, and $\partial\Omega_0^N$ for (traction) Neumann boundary conditions as follows

$$\mathbf{x}(\mathbf{X}) = \mathbf{x}^*(\mathbf{X}) \quad \forall \mathbf{X} \in \partial\Omega_0^D \quad (3.13)$$

$$(TF^T)^T \mathbf{v} = \mathbf{m}(\mathbf{X}) \quad \forall \mathbf{X} \in \partial\Omega_0^N . \quad (3.14)$$

Here \mathbf{x}^* , is a prescribed position in the deformed body surface $\partial\Omega_0$, \mathbf{v} is the vector normal to the surface of the undeformed body $\partial\Omega_0$, pointing outwards, and \mathbf{m} is a prescribed force per undeformed surface area acting on the undeformed body Ω_0 .

3.2.2.3 Myocyte contractile activity

In Section 3.1.3 an overview of contraction models was given. The most general mathematical formulation for these models is:

$$\frac{d\mathbf{w}}{dt} = \psi(\mathbf{w}, [Ca^{2+}]_i, \lambda_f, \frac{d\lambda_f}{dt}) \quad (3.15)$$

$$\sigma_a = \sigma_a(\mathbf{w}, [Ca^{2+}]_i, \lambda_f, \frac{d\lambda_f}{dt}) . \quad (3.16)$$

Here \mathbf{w} is the set of internal state variables of the model. The temporal variation of \mathbf{w} is a function ψ of the same \mathbf{w} , intracellular calcium concentration $[Ca^{2+}]_i$, stretch in the fibre direction $\lambda_f = \sqrt{\mathbf{f}^T C \mathbf{f}}$ and stretch-rate $\frac{d\lambda_f}{dt}$. Depending on the type of model, one or more of the functional dependencies are considered, as discussed in Section 3.1.3. Finally,

the output of these models is a Cauchy stress σ_a generated along \mathbf{f} . This is then used to compute the tissue stress tensor according to eqn. (3.11), as explained in Section 3.2.2.2. The equations for the contraction model of Kerckhoffs et al. [75] will be provided in Section 4.4.1.

3.2.2.4 Blood Pressure as additional boundary condition

Blood pressure is included in an electromechanical model by means of a Neumann boundary condition, as in eqn. (3.14). Simulations that do not consider blood pressure, such as those of Chapter 5, are in fact imposing a constant zero pressure as a boundary condition. This is not a physiological pressure for the heart. A time-varying trace for pressure is a more realistic description and it was employed in the simulations of Chapter 6. In particular, in Section 6.3 the process of choosing the appropriate pressure temporal variation and the additional steps required in the model development will be described.

3.2.3 Numerical scheme for the electromechanical model

No analytical solution can be obtained for the electromechanical model described, given its complexity, therefore a numerical approach is necessary. As described in the previous sections of this chapter, the electromechanical problem is a complex system of PDEs, ODEs and algebraic equations and it is time and space dependent. The numerical approach used in this study is to first apply the discretisation in time followed then by the spatial discretisation.

3.2.3.1 Temporal discretisation

The discretisation of a time derivative of a given function is essentially the substitution of that derivative by a difference quotient obtained from Taylor expansion of the function. Explicit discretisation schemes are usually conditionally stable but offer the advantage of being easier to implement and computationally less expensive than implicit schemes, which on the other hand often guarantee unconditional stability. A semi-implicit approach to time discretisation can also be considered in which linear terms follow an implicit approach whereas the nonlinear terms are treated explicitly. This is the temporal discretisation employed in this study.

3.2.3.2 Spatial discretisation: the finite element method

The finite element method (FEM) is a powerful numerical method for spatial discretisation widely used in computational modelling for the approximation of the solution of differen-

tial equations [136]. It consists of three key components. First, the domain over which the problem is defined is approximated by means of a *finite element mesh*. In other words, the mathematical and often complex domain is subdivided into smaller and regular elements connected by points, or *nodes*. For example, a curve in space is a 1D domain that can be approximated by a sequence of linear segments. A 3D domain, such as the left ventricle, is subdivided into 3D elements, typically tetrahedra (as in this study) or hexahedra.

Secondly, the differential problem is converted into an equivalent integral-weighted formulation, or *weak formulation*. The weak formulation is then reduced to a *discretised problem*, in which the weak formulation equations are taken to hold only for a finite number of (independent) weighting functions. These weighting functions are chosen to be the finite element *basis functions*, which are most often polynomial and whose order depends on the specific problem considered [159]. Each basis function is continuous over the entire computational domain and is defined to be not-zero only at one node of the mesh. In this study only linear and quadratic polynomial basis function belonging to the family of the *Lagrange* basis functions were used. When this type of basis function is employed the continuity of the approximation function is ensured. If the continuity of its first derivative is also required, then other types of basis functions, such as the *Hermite* basis functions, have to be used. In this case, the increased accuracy achieved is counteracted by the significant increase in the number of degrees of freedom, and therefore unknowns, to be computed.

The final stage is *assembly*, in which discretised weak formulation is used to construct a set of linear or nonlinear equations to be solved using standard numerical solvers. This involves computing integrals over each of the individual elements in the mesh and imposing boundary conditions. Please refer to [159] for a concise but detailed description of the theory onto which the FEM method is based, and to [136] for a wide list of applications and examples.

3.3 Electromechanical simulations

All simulations were run using `Chaste` [105], the open source package for computational and systems biology simulations developed in the Computational Biology group in the Department of Computer Science. In particular, two of my supervisors (Rafel Bordas and Pras Pathmanathan) belong to the main `Chaste` development team. This has given me the unique opportunity of being part of the model implementation process, receiving precious help in model development and testing. `Chaste` is known in the cardiac modelling community as a cutting-edge open source tool for electrophysiological simulations [123] but, when I started

my thesis, the electromechanical component was still at an initial stage. The core of the electromechanical code of Chaste had been developed and thoroughly tested for numerical convergence [125] on 2D and 3D slab geometries. However, mine was the first attempt to develop a rat-specific electromechanical model within Chaste and to use the model to perform simulations on a left ventricular geometry. Hence, I had to rely on a pure trial-and-error approach in some cases, leaving for the future more rigorous strategies. In the next chapter the work done in relation to model development and testing will be presented.

I have actively contributed to the extension of Chaste functionality for electromechanical simulations in two projects

- Adding cross-fibre tension generation, as in eqn. (3.11). Previously, active tension was only generated along the fibre direction. With this new functionality, which was coded starting from the model of Usyk et al. [166], the user can choose to employ uniform tension in the cross-fibre plane, or two different types of tension in the sheet and sheet-normal direction, in addition to the tension generated in the fibre direction. Since the mechanisms of cross-fibre tension generation are not known, the tension generated in the sheet and sheet-normal direction are a fraction of that generated in the fibre direction. The user can choose different fractions for the sheet and sheet-normal directions.
- Creating a "cell factory" for contraction models. This is the major contribution to code development I have worked on. There are three physiological contraction models available in Chaste, Nash and Panfilov [110], Niederer et al. [112] and Kerckhoffs et al. [75]. Such models were hard-coded, meaning that it was not possible to change their parameters values from the simulation file, but one had to directly modify the original code for the model. Furthermore, it was only possible to assign a single contraction model to the entire spatial domain. The contraction cell factory is an environment that allows the user to (a) assign different contraction models to different regions of the domain, which he/she has to define mathematically, and (b) change one of more parameters values within the simulation file. With this new functionality it is now possible to run, for example, sensitivity analysis on the parameters of the contraction model, or simulate pathological conditions such as ischemia by identifying regions of the domain where a different level of active tension is generated.

All the specific code for running the simulations described in Chapters 5 and 6, the meshes and tissue structure models I have developed, are fully available to the community of Chaste users, some directly from the software webpage, some upon request.

In this chapter the state-of-the-art on cardiac modelling has been reviewed, focussing in particular on electromechanical models and the role of tissue structure in them. The mathematical background to the electromechanical model developed for this thesis has also been provided. Chaste, the software tool employed to run the simulations presented in this thesis, has been introduced. My contribution to the software development has also been summarised. The next chapter will focus on the development of the electromechanical model, discussing, for example, the preliminary numerical tests, the mesh generation step or the choice of constitutive law and contraction model.

Chapter 4

Development of a model of rat left ventricular electromechanics

In the previous chapter an overview of the electromechanical model from a mathematical point of view was provided. In this chapter the focus is on the implementation and preliminary numerical tests performed in order to assemble the electromechanical model employed in the simulations studies of the following chapters. First, a list of the components of the model that need to be considered is given, then each component is addressed separately. Most of the components are described in this chapter, while the others will be discussed as part of the methods in the preliminary computational study presented in the following chapter.

4.1 General components of the EM model

In order to implement the weakly coupled electromechanical model for the study of left ventricular contraction in rat, the following components need to be considered:

1. The **geometry**. In other words, the choice of geometrical model for the left ventricle and generation of the finite element mesh (to be discussed in Section 4.2).
2. The **electrophysiological problem**:
 - 2a. The AP model (to be discussed in Section 4.3.1).
 - 2b. Electrophysiological parameters for tissue electrical propagation: conductivity tensor, surface-area-to-volume ratio, intensity and duration of the electrical stimulus (Section 4.3.2).
 - 2c. Numerical parameters for the electrophysiological problem (Section 4.3.3).
 - 2d. The electrical stimulation protocol. This modelling choice is discussed in the following chapter (Section 5.3.1).

3 The **mechanical problem**:

- 3a. The cellular contraction model. The choice and adaptation of the contraction model in order to be consistent with rat heart physiology is discussed (Section 4.4.1).
 - 3b. Active tension generation in tissue. The choice of uni-axial active tension generation, as opposed to introducing additional cross-fibre active tension, is justified in the following chapter (Section 5.3.3).
 - 3c. Passive behaviour of the tissue. The choice of constitutive law and its parameters (Section 4.4.2) is briefly discussed, while the preliminary study of different parameters sets and levels of tissue compressibility is presented in the next chapter (Section 5.3.2).
 - 3d. Numerical parameters for the mechanical problem (Section 4.4.3).
 - 3e. Mechanical boundary conditions are also discussed in the following chapter (Section 5.3.1).
 - 3f. Pressure boundary conditions. They were not included in the first computational study (Chapter 5). The reason for introducing pressure in the model and the implementation of the pressure boundary condition are discussed before presenting the results of the second computational study (Chapter 6).
4. **Tissue structure distribution.** The mathematical framework to assign a set of fibre, sheet and sheet-normal directions to each element of the mesh is described. In particular, the different fibre and sheet models applied within the general framework are explained (Section 4.5).

4.2 Geometrical model of rat left ventricle

The shape of the left ventricle was approximated by a thick-walled truncated ellipsoid. This is a common approach, as described in Section 3.1.1, and presents some advantages with respect to a realistic mesh obtained from imaging data. For example, the ellipsoidal mesh is smooth, which makes the mechanical component of the simulation more numerically stable. It is easy to prescribe tissue structure based on the analytical properties of the ellipsoid and the resulting distribution is also smooth. However, the contribution of geometrical heterogeneity to cardiac electromechanics is lost in the case of the ellipsoid with respect to more realistic geometries. On the other hand, this can be considered an advantage as it allows the study to focus on the effect of tissue structure on contraction, reducing the number of other sources of variability.

In order to construct the ellipsoidal mesh, first a Cartesian coordinate system (x, y, z) is defined. The truncated ellipsoid has the base, that is the opening of the cavity, on the xy -plane and develops in the negative half-space defined by $-z$ as shown in Figure 4.1(a). Three semi-axes define the epicardial surface of the ellipsoid, a_{epi} , b_{epi} , c_{epi} . In the same way, three semi-axes define the endocardial surface of the ellipsoid, a_{endo} , b_{endo} , c_{endo} . The semi-axes a_{epi} and a_{endo} are along the x axis, b_{epi} and b_{endo} are along the y axis and c_{epi} and c_{endo} are along the z axis. The length of the semi-axes in the xy -plane were estimated from one midventricular short-axis frame taken at end-diastole frame of cine-MRI (shown in Figure 2.7(a)) of *dataset*₁ (Section 2.4). The value of c_{epi} and c_{endo} were estimated as the number of short-axis slices representing the ventricles times the image resolution in the long-axis direction. This is not an optimal way to measure the long axis of the left ventricle, but at the time of the mesh generation step, *dataset*₂ had not yet been provided, hence I could not use the long-axis view of the cine-MRI scans it contains.

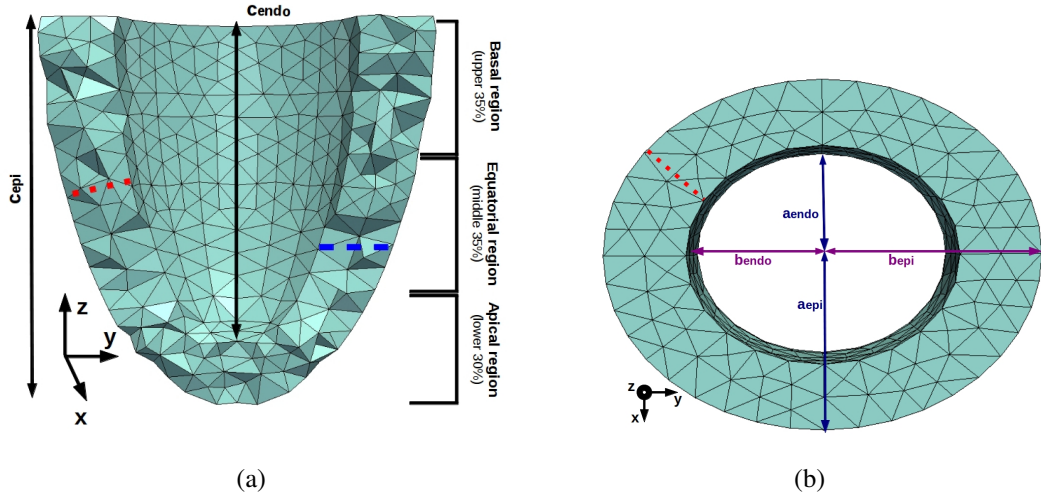


Figure 4.1: (a) The ellipsoidal mesh seen in a transmural-longitudinal cut highlighting the subdivision of the ventricle into three regions: the basal region (upper 35% of c_{epi}), the equatorial region (middle 35% of c_{epi}) and the apical region (lower 30% of c_{epi}). The red dotted line is the plane along which the wall thickness is measured with respect to a local coordinate system (\tilde{w}), whereas the blue dashed line is the plane along which the wall thickness is measured with respect to a global reference frame (the average is then $\langle w \rangle$, see text for details). (b) Top view of the base of the ventricular mesh showing the relative length of the semi-axes in the short-axis plane. The red dotted line is the wall thickness \tilde{w} measured with respect to a local coordinate system.

The epicardial surface has semi-axes $c_{epi} = 1 \text{ cm}$, $a_{epi} = 0.4 \text{ cm}$ and $b_{epi} = 0.5 \text{ cm}$. The wall thickness with respect to a local cylindrical coordinate system is constant and equal to $\tilde{w} = 0.15 \text{ cm}$ (that is the difference between corresponding epicardial and endocardial semi-axes, the red dotted line in Figures 4.1(a) and 4.1(b) has length equal to \tilde{w}). If the

wall thickness is measured with respect to a global coordinate system (hence in a short-axis plane perpendicular to the z axis, such as the one represented by the blue dashed line in Figure 4.1(a)), its magnitude varies from base to apex, with average wall thickness throughout the mesh $\langle w \rangle = 0.16 \text{ cm}$. Please refer to Section 2.3.1 for a description of the global and local cylindrical coordinate systems. It is important to distinguish between these two ways of measuring the wall thickness of the heart, since the local measure \tilde{w} is the one employed to define the surfaces of the ellipsoidal geometry, but the global measure of wall thickness $\langle w \rangle$ is used to compute the wall-thickening (definition in Section 5.2), one of the global metrics used for the evaluation of the simulation output in Chapters 5 and 6.

The resulting ellipsoidal geometry is different from the more common prolate spheroidal geometry employed in many cardiac computational studies [165], [166], [114]. The prolate spheroidal geometry was identified as an appropriate model for the sphericity of the canine left ventricle [117]. It also allows a prolate coordinate system to be used in order to simplify the modelling process [167]. However, the cine-MRI data employed in this study show that there is a difference between the two semi-axes in the short-axis plane, at least in the specific rat heart imaged, hence the ellipsoidal geometry.

Two tetrahedral finite element meshes were generated, a fine mesh for the electrical activity (referred to as $mesh_e$), with approximately $1.06 \cdot 10^5$ tetrahedra and average edge length of $3 \cdot 10^{-2} \text{ cm}$, and a coarse mesh for the mechanical part (referred to as $mesh_m$), with about $8 \cdot 10^3$ elements with average edge length equal to $7 \cdot 10^{-2} \text{ cm}$. Mesh resolutions were chosen to ensure sufficient numerical accuracy, as determined using the numerical tests described in Sections 4.3.3 (for the electrical mesh) and 4.4.3 (for the mechanical mesh). All meshes were generated with the open-source 3D finite element grid generator Gmsh [49].

The quality of the meshes was assessed by computing the average skewness $\langle q \rangle$, that measures how close on average the elements of the mesh are to a regular tetrahedron (a tetrahedron with equal length edges). If q_i denotes the skewness of the element i of a given mesh, then q_i is given by:

$$q_i = k \frac{vol_i^2}{(A_i + B_i + C_i + D_i)^3} \quad (4.1)$$

where $k = 216\sqrt{3}$ is a normalisation factor, vol_i is the volume of element i and A_i, B_i, C_i, D_i are the areas of the four faces of the element. The average skewness of the mesh is then $\langle q \rangle = \frac{1}{N} \sum_i q_i$, with N total number of elements. The closer $\langle q \rangle$ is to 1 the more equilateral are the elements in the mesh. Both meshes showed a low level of skewness: 0.74 ± 0.2 ,

0.72 ± 0.2 for the electrical and mechanical meshes, respectively. All the information on the meshes is summarised in Table 4.1.

Table 4.1: Summary of the ellipsoidal dimensions and meshes properties

Ellipsoid dimensions (<i>cm</i>)			
a_{epi}	0.4	a_{endo}	0.35
b_{epi}	0.5	b_{endo}	0.45
c_{epi}	1.0	c_{endo}	0.85
\tilde{w}	0.15	$\langle w \rangle$	0.16
Electrics mesh $mesh_e$			
No. of nodes	$2.0 \cdot 10^4$	No. of elements	$1.06 \cdot 10^5$
$\langle edge \rangle$	$3.06 \cdot 10^{-2} \text{ cm}$	$\langle q \rangle$	0.74 ± 0.2
Mechanics mesh $mesh_m$			
No. of nodes	$1.84 \cdot 10^3$	No. of elements	$8.22 \cdot 10^3$
$\langle edge \rangle$	$7.18 \cdot 10^{-2} \text{ cm}$	$\langle q \rangle$	0.72 ± 0.2

4.3 Electrophysiological component

As explained at the beginning of this chapter, for the electrophysiological part of the electromechanical model to be implemented it was necessary to choose the most suitable AP model and electrophysiological parameters for tissue electrical propagation as well as the best time scales and spatial resolution for the type of simulations I wanted to perform.

4.3.1 AP model

The features I needed to reproduce of the rat AP were mostly its shape and duration. Sub-cellular parameters, such as calcium concentration, were not required as an input to the chosen the contraction model (see Section 4.4.1). It is true that a simple phenomenological model for the rat AP could have been employed, but I decided that starting already with a good biophysical model would be useful for future model development. A wide range of AP models from the CellML repository [97] are available within Chaste. I first tried to use Pandit model [122], that was specifically developed to represent adult rat myocytes and successfully employed in ventricular electromechanical studies [114]. However, the CellML version of this model, as implemented in Chaste, proved to be numerically unstable. It was not possible to find an appropriate value of the tissue electrical stimulus, either the electrical wave propagation was not elicited or the electrophysiological simulation would diverge. Given the complexity of the model it would have required too much

time to address this problem, therefore I decided to use the model of neonatal mouse AP developed by Wang and Sobie [176]. As shown in Figure 4.2(a), the duration and shape of the AP are very similar, while the maximum voltage of Pandit model is higher than Wang model. Even so, Wang and Sobie AP is an acceptable approximation for the purposes of my electromechanical model. In the remainder of the thesis I will refer to the chosen AP model as Wang2008 for simplicity.

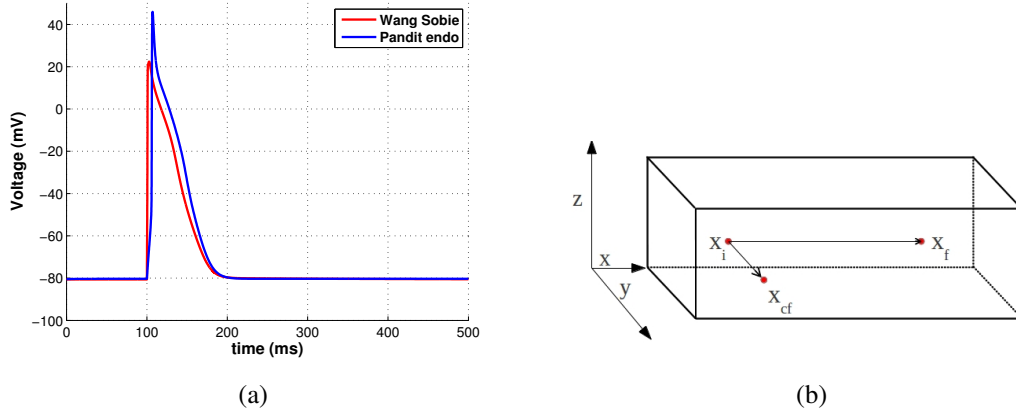


Figure 4.2: (a) Comparison between the AP trace generated with Pandit (blue) and Wang (red) models respectively. (b) Schematic of the 3D slab used for numerical tests described in Section 4.3.2. The points x_i and x_f are taken along the fibre direction and used to compute conduction velocity in the fibre direction cv_f . The points x_i and x_{cf} are used to compute conduction velocity in the cross fibre direction cv_{cf} .

4.3.2 Electrophysiological parameters

The values of the following parameters of the monodomain equation (3.1) need to be defined:

- Specific capacitance C_m .
- Surface area-to-volume ratio χ .
- Amplitude of the external stimulus current I_{stim}^{tissue} .
- The conductivity tensor ϵ .

Specific capacitance C_m . The membrane specific capacitance is experimentally found to be approximately constant for the average myocyte, regardless of the animal species [144]: $C_m = 1.0 \mu F/cm^2$.

Surface area-to-volume ration χ . I relied on the measurements reported by Satoh et al. [144], who used confocal microscopy and patch-clamp experiments on isolated rat myocytes to provide an average value of $\chi = 8400 cm^{-1}$.

Amplitude of I_{stim}^{tissue} . Each AP model has specific values for the amplitude and duration of the external stimulus current I_{stim}^{cell} from which the corresponding amplitude and duration of the tissue external stimulus current I_{stim}^{tissue} can be estimated. The following relationship holds

$$I_{stim}^{tissue} \approx I_{stim}^{cell} C_m \chi = \left(\frac{-80 \mu A}{\mu F} \right) \left(\frac{1 \mu F}{cm^2} \right) \left(\frac{8.4 \cdot 10^3}{cm} \right) = 6.64 \cdot 10^5 \mu A/cm^3. \quad (4.2)$$

The final value for $I_{stim}^{tissue} = 6.0 \cdot 10^5 \mu A/cm^3$ was chosen because it proved to be sufficient to trigger the electrical wave at the tissue level. I chose a stimulation duration $t_{stim} = 1 ms$ rather than the $0.5 ms$ duration of I_{stim}^{cell} which proved to be insufficient for I_{stim}^{tissue} . The region electrically stimulated was the apex, as further discussed in Section 5.3.1.

Estimation of ϵ . A series of electrophysiological simulations was designed on a 3D slab with dimensions $l_x = 1.2 cm$, $l_y = 1.2 cm$ and $l_z = 0.2 cm$ in the x, y, z directions, respectively. The mesh was generated with a discretisation step size of $0.03 cm$ (suggested resolution for electrophysiological simulations [162]), resulting in a total of 8405 nodes, 38400 tetrahedral elements and an average edge length $\langle edge \rangle = 0.0378 cm$. The cell model was Wang2008. All other electrophysiological parameters were as in Table 4.2. The electrical stimulus was applied along the z axis (defined by $x = 0, y = 0$) so that the electrical wave would travel from the leftmost corner to the rest of the slab (see for example Figure 4.3(a) for a snapshot of one of the simulations). Fibres were defined to run parallel to the x axis. The simulation duration was $100 ms$, allowing full depolarisation to occur in the slab.

The aim of this set of simulations was to vary the values of the conductivity tensor and measure the conduction velocity in the fibre and cross-fibre direction, denoted by cv_f and cv_{cf} respectively. The conductivities were adjusted in order to ensure that the resulting cv_f and cv_{cf} had reasonable values and gave a ratio cv_f/cv_{cf} similar to that experimentally found in rat tissue cultures [20]. Figure 4.2(b) shows the schematic of the slab and the approximate positions of the three points (or watch nodes) used to measure conduction velocities. These watch nodes were chosen sufficiently far from the stimulation site and the border of the slab, in order to avoid the bias of edge effects on the measure. Conduction velocity in the fibre direction cv_f was measured between $\mathbf{x}_i = (0.03, 0.06, 0.06)$ and $\mathbf{x}_f = (1.17, 0.06, 0.06)$ as $cv_f = |\mathbf{x}_f - \mathbf{x}_i| / (t_f - t_i)$. Here, t_f and t_i are the times (in ms) at which the transmembrane potential at nodes \mathbf{x}_f and \mathbf{x}_i first becomes positive. Similarly cv_{cf} was measured between watch nodes \mathbf{x}_i and $\mathbf{x}_{cf} = (0.03, 1.17, 0.06)$.

I decided to model the tissue as transversely isotropic and found that conductivity values of $\epsilon_f = 3.0 \text{ mS/cm}$ in the fibre direction and $\epsilon_s = \epsilon_n = 1.0 \text{ mS/cm}$ in the sheet and sheet-normal directions produced, with the given mesh resolution and electrophysiological parameters, values of conduction velocity $cv_f = 3.1 \cdot 10^{-2} \text{ cm/ms}$ and $cv_{cf} = 1.3 \cdot 10^{-2} \text{ cm/ms}$ with resulting ratio $cv_f/cv_{cf} = 2.3$. The results compare well with the experimental findings of Bourgeois et al. [20]. These are, for a 350 ms paced culture: experimental conduction velocities of $2.5 \cdot 10^{-2} \pm 0.7 \cdot 10^{-2} \text{ cm/ms}$ and $1.1 \cdot 10^{-2} \pm 0.3 \cdot 10^{-2} \text{ cm/ms}$ in the fibre and cross-fibre directions, respectively, with resulting ratio $cv_f/cv_{cf} = 2.3 \pm 0.3$.

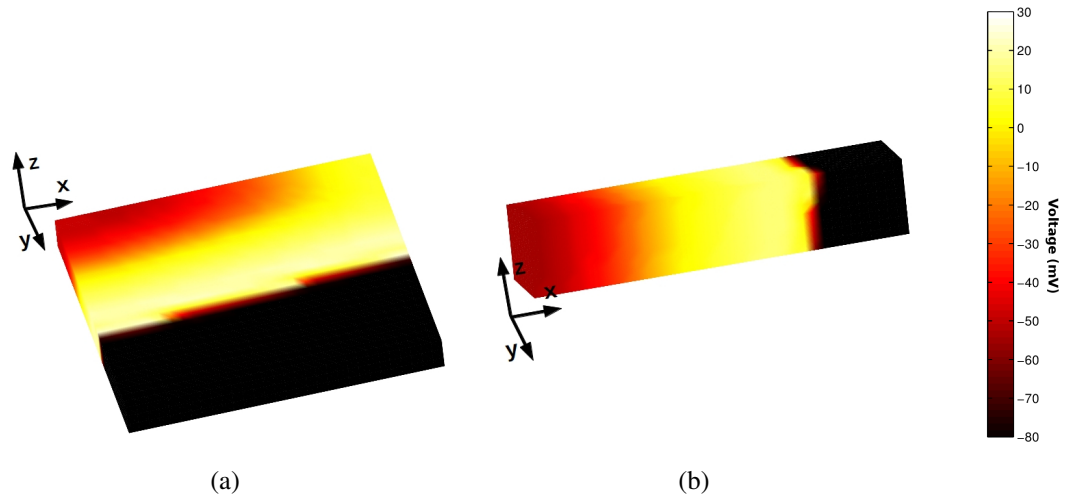


Figure 4.3: (a) Snapshot from one of the electrophysiological simulations used to determine the conductivity tensor ϵ (Section 4.3.2). (b) Snapshot from one of the electrophysiological simulations for electrical mesh resolution determination (Section 4.3.3).

Table 4.2: Parameters of the monodomain equation (eqn. (3.1))

Parameter	Value(s)
C_m	$1.0 \mu\text{F/cm}^2$
χ	$8.4 \cdot 10^3 \text{ cm}^{-1}$
I_{stim}^{tissue}	$6.0 \cdot 10^5 \mu\text{A/cm}^3$
t_{stim}	1 ms
ϵ_f	3.0 mS/cm
ϵ_s	1.0 mS/cm
ϵ_n	1.0 mS/cm

4.3.3 Numerical parameters for the electrophysiological problem

In this section the choice of the temporal and spatial discretisation steps is briefly described. In the case of the temporal resolution, the default values for monodomain simulations provided by Chaste [123] are: $\Delta t_{ODE}^e = 0.01 \text{ ms}$, $\Delta t_{PDE}^e = 0.01 \text{ ms}$, but I found that Wang2008 needed a smaller time step to ensure stability. Hence the final choice was: $\Delta t_{ODE}^e = 0.005 \text{ ms}$, $\Delta t_{PDE}^e = 0.01 \text{ ms}$. In the case of the spatial resolution, the suggested discretisation step size for electrical meshes is in the range 0.025-0.03 cm [162]. However, I designed a series of simulations to test the effect of different mesh resolutions on the shape of AP and on conduction velocity, with the aim of determining a threshold in mesh resolution suitable for the type of electromechanical simulations I wanted to run. For this purpose, a series of 3D slab meshes was generated with dimensions $l_x = 2.0 \text{ cm}$, $l_y = 0.4 \text{ cm}$ and $l_z = 0.4 \text{ cm}$ in the x, y, z directions, respectively, and decreasing discretisation steps 0.2, 0.1, 0.05, 0.04, 0.025 (cm). The electrophysiological parameters were those summarised in Table 4.2. The area electrically stimulated was the plane $x = 0$. Simulation duration was set to 200 ms to ensure full depolarisation to occur in the slab, especially at lower mesh resolutions for which conduction velocity is significantly lower. Table 4.3 summarises the parameters taken into account in order to compare the different mesh resolutions. The number of elements as well as the average edge length $\langle \text{edge} \rangle$ were computed. The conduction velocity in the fibre direction cv_f was also measured by taking two watch nodes $\mathbf{x}_i^* = (0.2, 0.2, 0.2)$ and $\mathbf{x}_f^* = (1.2, 0.2, 0.2)$. The mesh resolution has in fact to be high enough to ensure cv_f to be in the physiological range. Figure 4.4(a) shows that cv_f is greatly influenced by mesh resolution (expressed in terms of average edge length). Finally, the computational time t_{comp} required to complete the simulation was also taken into account.

Table 4.3: Results of the numerical test performed to evaluate different mesh resolutions for the electrical mesh $mesh_e$.

Step size cm	No of elements	$\langle \text{edge} \rangle (\text{cm})$	$cv_f (\text{cm ms}^{-1})$	$t_{comp} (\text{s})$
0.2	240	0.252	$7.5 \cdot 10^{-3}$	7
0.1	1920	0.126	$1.47 \cdot 10^{-2}$	38
0.05	$1.5 \cdot 10^4$	$6.3 \cdot 10^{-2}$	$2.17 \cdot 10^{-2}$	237
0.04	$3 \cdot 10^4$	$5.04 \cdot 10^{-2}$	$2.51 \cdot 10^{-2}$	442
0.025	$1.2 \cdot 10^5$	$3.15 \cdot 10^{-2}$	$3.0 \cdot 10^{-2}$	1670

I also took into account the smoothness of electrical propagation by analysing how the shape of AP is affected at watch node \mathbf{x}_i^* , as shown in Figure 4.4(b). At low mesh resolu-

tions (such as mesh step size 0.2 cm), the upstroke is not a sharp vertical line and there is a delay in the initiation of the AP with respect to the finer meshes due to the lower conduction velocity.

From the results of this numerical test it can be concluded that any mesh with average edge length equal to $\langle edge \rangle = 5.0 \cdot 10^{-2}\text{ cm}$ or lower was acceptable for my simulations studies, since at this resolution the value of cv_f was within the physiological range $2.5 \cdot 10^{-2} \pm 0.7 \cdot 10^{-2}\text{ cm/ms}$ [20], and the shape of AP is similar to that obtained at finer resolutions. As described in Section 4.2, the average edge length for the ellipsoidal electrical mesh was $\langle edge \rangle = 3.06 \cdot 10^{-2}\text{ cm}$ similar to the finest mesh used in this numerical test. However, in the simulations of Chapter 6 a coarser mesh for the electrical problem was employed, but still within the chosen threshold for $\langle edge \rangle$.

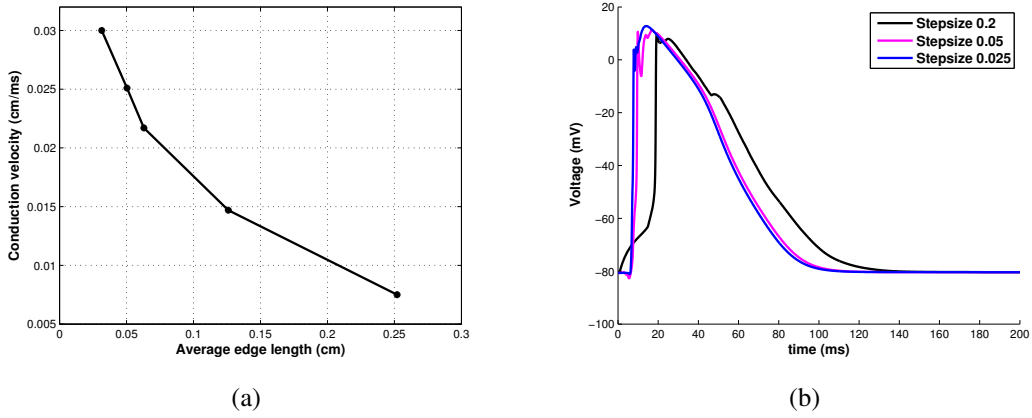


Figure 4.4: (a) Conduction velocity in the fibre direction versus average edge length of the elements in the electrics mesh. (b) AP shape at different mesh resolutions for watch node \mathbf{x}_i^* .

4.4 Modelling rat mechanics

As explained at the beginning of this chapter, some of the tests carried out to assess passive behaviour, cross-fibre tension generation and boundary conditions will be discussed in later chapters, as it was more natural to do so after having defined the scientific questions related to my simulation study. In this section the cellular contraction model and the constitutive law are discussed. Furthermore, the tests performed to determine the numerical parameters for the mechanical problem are described.

4.4.1 The contraction model

Three contraction models were considered: a phenomenological model by Nash and Panfilov [110], a simple biophysical model by Kerkchoffs et al. [75] and a detailed rat-specific model by Niederer et al. [115]. I chose the Kerkchoffs et al. model as it represents a good compromise between the other two models, and it appeared easy to adjust to rat physiological temporal scales. The rat-specific contraction model by Niederer et al. contains a biophysical level of detail that was considered not necessary for the purpose of the study. Additionally, the model increased significantly the computational cost of the simulations with respect to the Kerkchoffs et al. model. On the other hand, the model developed by Nash and Panfilov generated higher levels of active tension that caused the mechanical problem to diverge. From now on I will refer to Kerkchoffs et al. model as K2003 for simplicity.

The equations for K2003 are given below [75]. The model is based on a simple representation of the sarcomere as a sequence of one contractile element and an elastic one, in line with the modelling approach described earlier in Section 1.2.2, and whose schematic is provided in Figure 1.6(b). The active stress generated by the myocyte $\sigma_a = \sigma_a(t_a, l_s, l_c)$, is function of t_a , the time elapsed since electrical activation, l_s the sarcomere length, and l_c , the length of the contractile unit of the sarcomere.

$$\sigma_a = \frac{l_s}{l_{s0}} f_{iso}(l_c) f_{twitch}(t_a, l_s) (l_s - l_c) E_a \quad \text{where} \quad (4.3)$$

$$f_{iso}(l_c) = \begin{cases} 0 & l_c \leq a_7 \\ T_0 \tanh^2(a_6(l_c - a_7)) & l_c > a_7 \end{cases} \quad \text{and} \quad (4.4)$$

$$f_{twitch}(t_a, l_s) = \begin{cases} 0 & t_a < 0 \\ \tanh^2\left(\frac{t_a}{t_r}\right) \tanh^2\left(\frac{t_{max} - t_a}{t_d}\right) & 0 < t_a \leq t_{max} \\ 0 & t_a > t_{max} \end{cases} \quad (4.5)$$

$$t_{max} = b(l_s - l_d) \quad (4.6)$$

$$\frac{\partial l_c}{\partial t} = v_0 [E_a(l_s - l_c) - 1], \quad (4.7)$$

where t_{max} is activation duration, l_{s0} is the the sarcomere length at rest, E_a is the material stiffness, t_r is activation rise time constant, t_d is activation decay time constant, l_d is the sarcomere length at which no mechanical activation occurs, while the others are fitting parameters. Table 4.4 shows the parameters values for the original model.

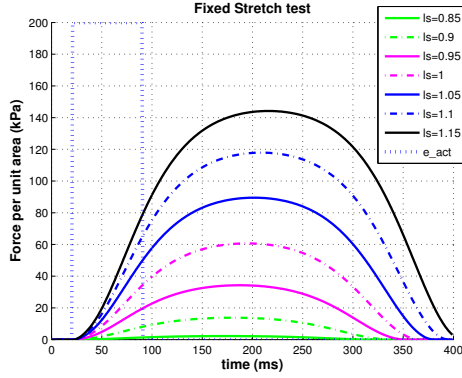


Figure 4.5: Active stress generated by K2003 under constant stretch at different stretch values. The time window of electrical activation (e_{act}) is shown as a dotted rectangle.

$a_6 (\mu m^{-1})$	2.0
$a_7 (\mu m)$	1.5
$T_0 (kPa)$	180
$E_a (\mu m^{-1})$	20
$v_0 (\mu m ms^{-1})$	$7.5 \cdot 10^{-3}$
$l_{s0} (\mu m)$	1.9
$l_d (\mu m)$	-0.4
$b(ms \mu m^{-1})$	150
$t_r (ms)$	75
$t_d (ms)$	75

Table 4.4: K2003 parameters values [75].

K2003 was originally developed for canine myocytes, therefore a full cycle of contraction and relaxation lasts approximately 400 ms. In order to match the duration of a typical rat cardiac cycle I needed to find suitable parameters to modify in the model. Rat heart rate is approximately 300-400 bpm (Table 1.2) which gives a range 150-200 ms for a full cardiac cycle. Therefore I aimed to at least halve the duration of the active stress curve generated by K2003. Figure 4.5 shows the active stress generated by the model for a range of physiological stretch values for the cardiac myocyte [0.85, 0.9, 0.95, 1.0, 1.05, 1.1, 1.15] (within $\pm 15\%$ of resting sarcomere length). In this example the stretch was held fixed to a single value during the whole simulation, lasting 400 ms. This simulation is similar to the experiments done to study isometric contraction in isolated cells and it is useful to understand the span of forces that the model generates and on what time interval. In order to reduce the duration of contraction the constant parameters b , t_r , t_d were modified. The stretch trace for a chosen element from one of the electromechanical simulations described in Chapter 5 was used as an input for the K2003 model. The simulation was based on fibre model *Sn1R70* and transversely isotropic material law (for details on the fibre model see Section 4.5.2, while for the simulation details refer to Section 5.4). The element whose stress trace was employed had centroid coordinates (0.29, 0.05, -0.49), approximately in the equatorial midwall of the mechanics mesh. The stretch trace is shown in Figure 4.6(a).

The effect of scaling the parameters b , t_r and t_d by multiplying them for scaling factors $2/3$ ($b = 100$, $t_r = 50$, $t_d = 50$) and $1/2$ ($b = 75$, $t_r = 25$, $t_d = 25$) is shown in Figure 4.6(b). In both cases the duration of active stress generation lasts approximately or less than 200 ms. In the simulations without pressure boundary conditions described in Chapter 5, the scaling by $2/3$ was sufficient, whereas in the simulations including pressure the

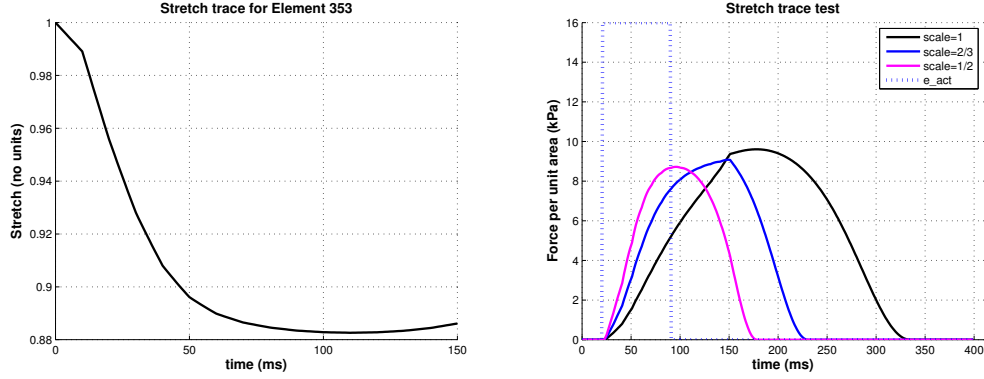


Figure 4.6: (a) Stretch trace for a midwall element of the mechanical mesh, details found in text. (b) Active stress generated by K2003 with the stretch trace of a midwall mesh element with different sets of values for the parameters b , t_d and t_r (original values, values scaled by 1/2 and 2/3). The time window of electrical activation (e_{act}) is shown as a dotted rectangle.

scaling factor 1/2 was necessary, as explained in Chapter 6. It is important to notice that in Figure 4.6(b) the force curves generated with no scaling and with 2/3 scaling both present a point of discontinuity. This is probably due to the simple implementation of the model employed to produce this explanatory plot. However, the implementation of the contraction model within Chaste is more robust in terms of numerical solvers and should prevent such discontinuities to occur, although it has not been tested explicitly.

4.4.2 Passive deformation

For the purpose of my computational studies I was interested in both transversely isotropic and orthotropic passive behaviour. However I did not find published orthotropic stiffness parameters values for exponential constitutive laws for rat. For this reason I chose the nearly incompressible constitutive law by Usyk et al. [166] given by eqn. (3.9). In their paper Usyk et al. explore the stiffness parameters space in order to study their effect on the mechanics of the canine left ventricle, providing a range of variation for each of the parameters. Although developed on experimental data for the dog, the resulting orthotropic parameter set showed magnitudes comparable with the values reported for rat in transverse isotropy by Omens et al. [119]. Original parameters sets for both material behaviours from Usyk et al. are shown in Table 4.5 and denoted by t_{iso}^U and $ortho^U$ respectively. Preliminary tests on these two parameters sets showed that the transversely isotropic law was actually not fully transversely isotropic. By changing b_{ns} from 2.8 to 3.58, and therefore setting $b_{ss} = b_{nn} = b_{ns}$, the desired material symmetry was obtained. The resulting set of parameters is given in the t_{iso}^* column of Table 4.5. In the column t_{iso} the parameters are given of the transversely isotropic law obtained from $ortho^U$ by (a) averaging b_{ss} b_{nn}

and b_{ns} and replacing their value by their average, and (b) doing the same for b_{fs} and b_{fn} . The result is a transversely isotropic material law with magnitude of the stiffness parameters directly comparable with that of the orthotropic law $ortho^U$. In this way, the effect of different material behaviours on mechanics can be analysed without taking into account differences in average stiffness.

Table 4.5: Stiffness parameters values for the material law (eq. (3.9))

Parameter	t_{iso}^U	t_{iso}^*	t_{iso}	$ortho^U$
b_{ff}	18.5	18.5	6.0	6.0
b_{ss}	3.58	3.58	4.3	7.0
b_{nn}	3.58	3.58	4.3	3.0
b_{fs}	2.8	2.8	7.5	12.0
b_{fn}	2.8	2.8	7.5	3.0
b_{ns}	2.8	3.58	4.3	3.0

The other two parameters in eqn. (3.9) are $C_a = 0.88 \text{ kPa}$ [166] and C_b , the level of compressibility whose original value employed by Usyk et al. [166] in combination with t_{iso}^U , was $C_b = 100 \text{ kPa}$. C_b enforces near incompressibility in the model. Different values of C_b were tested in order to study the effect of varying its magnitude on tissue passive response, as explained in Section 5.3.2. The effect of the material laws t_{iso}^* , t_{iso} and $ortho^U$ on mechanics was evaluated as part of the simulation studies of Chapters 5 and 6, therefore it will be discussed there.

4.4.3 Numerical parameters for the mechanical problem

It has been shown that the numerical solution of the mechanical problem can be successfully treated with a time step up to three orders of magnitude bigger than the suggested time step for solving the electrophysiological component [125]. In all the simulations the standard time steps suggested in Chaste for tissue mechanics were employed: $\Delta t_{PDE}^m = 0.1 \text{ ms}$ $\Delta t_{ODE}^m = 0.05 \text{ ms}$ (for K2003).

Similarly, the spatial step for the mechanics mesh can be one order of magnitude larger than the suggested step for the electrophysiological mesh [125]. As with the electrophysiological mesh, I designed a numerical test in order to determine a threshold for the mechanics mesh step size required to obtain sufficient accuracy in tissue displacement. The size of the 3D slab and the electrophysiological parameters were as in the tests of Section 4.3.3.

The electrophysiological mesh step size was kept fixed at 0.04 cm , while the mechanics step sizes tested were 0.4, 0.2, 0.1, 0.05, 0.04 (cm) . The mechanical problem was defined as follows: for the passive material law the corrected t_{iso}^* (stiffness parameters in Table 4.5) with $C_b = 100\text{ kPa}$ (see Section 4.4.2 for details) was used. The contraction model was K2003 with 2/3 scaling of the temporal parameters (see Section 4.4.1). Figure 4.7(a) shows the overlay of two snapshots from the simulation with step size 0.2 cm . The mesh in black shows the slab at the beginning of the simulation (0 ms) and that in blue is approximately at the end of contraction (130 ms). Mesh characteristics for step sizes 0.2, 0.1, 0.05, 0.04(cm) were the same as in Table 4.3. The coarsest mesh employed in this test, with step size 0.4 cm , had 30 elements and $\langle edge \rangle = 0.504\text{ cm}$.

Table 4.6: Displacement RMSE for watch points \mathbf{x}_i^* and \mathbf{x}_f^*

Step size	\mathbf{x}_i^*			\mathbf{x}_f^*		
	$RMSE_x$	$RMSE_y$	$RMSE_z$	$RMSE_x$	$RMSE_y$	$RMSE_z$
0.4	0.0042	0.0071	0.0071	0.0037	0.0033	0.0033
0.2	0.0009	0.0009	0.0009	0.0007	0.0016	0.0016
0.1	0.0004	0.0004	0.0004	0.0004	0.0009	0.0009
0.05	0.0001	0.0001	0.0001	0.0001	0.0002	0.0002

The displacement in the x , y and z directions for the watch nodes $\mathbf{x}_i^* = (0.4, 0.4, 0.4)$ and $\mathbf{x}_f^* = (1.2, 0.4, 0.4)$ was compared between the various mesh resolutions. Table 4.6 shows the root mean squared error (RMSE) in displacement between mesh resolutions 0.4, 0.2, 0.1, 0.05, and the finest mesh resolution 0.04, that is taken as the reference. For example, the RMSE for the displacement in the x direction for watch point \mathbf{x}_i^* is computed as

$$RMSE_x = \left[\frac{1}{t_{sim}} \sum_{j=1}^{t_{sim}} \left(dx_i^j - \bar{dx}_i^j \right)^2 \right]^{\frac{1}{2}}. \quad (4.8)$$

Here, dx_i^j is the displacement at time j of watch point \mathbf{x}_i^* for a given mesh resolution, whereas \bar{dx}_i^j is the corresponding displacement for mesh step size 0.04 cm .

The displacement is also plotted in Figures 4.7(b)-4.7(e) for all the mesh resolutions. The displacement in the x direction for watch points \mathbf{x}_i^* (Figure 4.7(b)) and \mathbf{x}_f^* (Figure 4.7(c)) tend to be rather similar across the step sizes. Wider discrepancy is instead found in the displacement in the y and z directions, that are identical given the geometry, fibre distribution and material properties of the slab. The displacement in the y direction (or equivalently in

the z direction) for watch point \mathbf{x}_i^* (Figure 4.7(d)) shows that step size 0.4 is not converging to the same solution as the other meshes, which are all close to each other. The displacement in the y direction for watch point \mathbf{x}_f^* (Figure 4.7(e)) shows that both step sizes 0.4 and 0.2 produce a slightly oscillatory behaviour during the first 50 ms .

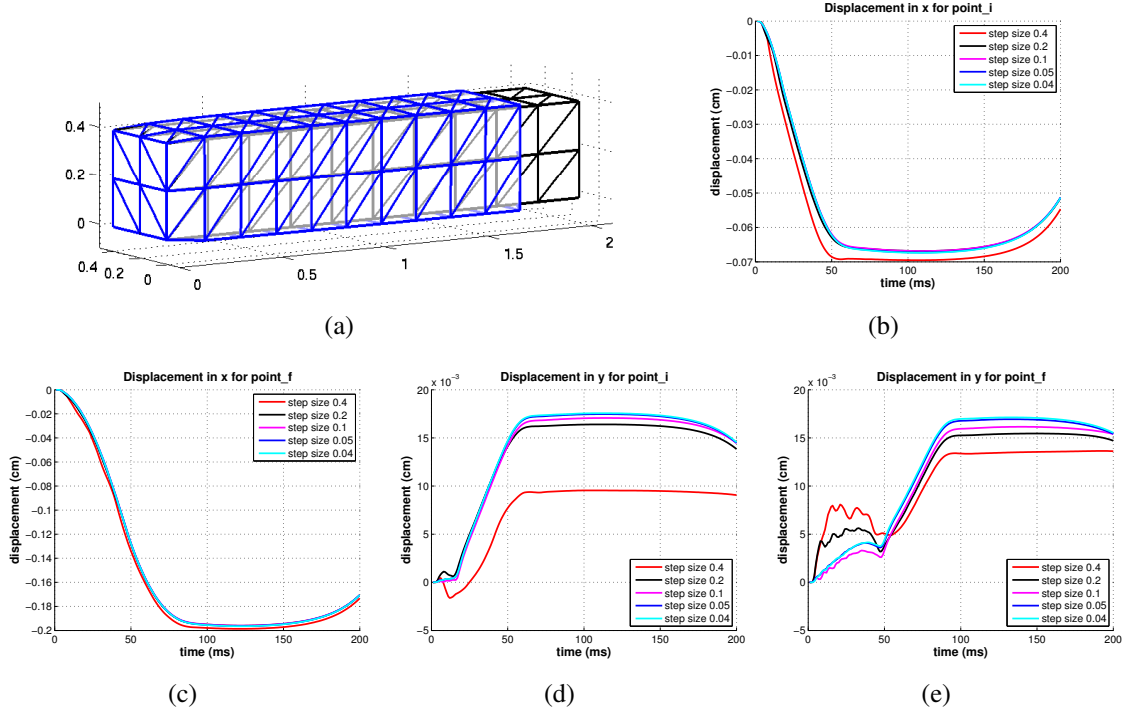


Figure 4.7: (a) Overlay of two snapshots from the mechanical simulation with step size 0.2 cm . The mesh in black is that at 0 ms and that in blue is approximately at 130 ms . (b)-(e) Results of the simulations to determine mechanics mesh resolution.

The conclusion of this test was that a suitable mesh resolution for the mechanical problem should at least have $\langle edge \rangle < 0.126$, (as the slab mesh with step size 0.1 cm , see Table 4.3) in order to ensure sufficient accuracy in the prediction of tissue displacement ($RMSE_x \leq 5 \cdot 10^{-4}$ was chosen as a threshold). Therefore the ellipsoidal mechanical mesh $mesh_m$ (Section 4.2), with its $\langle edge \rangle = 7 \cdot 10^{-2}$ cm has a suitable resolution.

4.5 Mathematical definition of tissue structure

In this section it is explained how tissue structure distribution is assigned to the ellipsoidal mesh. A set of fibre, sheet and sheet-normal directions (\mathbf{f} , \mathbf{s} , \mathbf{n}) is defined at the centroid of each element of the mechanical mesh, as explained below (Section 4.5.1). This orthonormal local system of coordinates is assigned according to a well-established approach [94]. Once

the general framework for the assignment of tissue structure to the mesh is set up, it is possible to vary the fibre and sheet distribution by using rule-based methods (Sections 4.5.2-4.5.4).

4.5.1 Tissue structure definition on the ellipsoidal mesh

In order to prescribe the orthonormal basis $(\mathbf{f}, \mathbf{s}, \mathbf{n})$ to the centroid of a given element, a local cylindrical coordinate system (radial \mathbf{u} , circumferential \mathbf{v} and longitudinal \mathbf{w}) is defined at that point. The three vectors are defined as in Section 2.3.1. First, the radial direction \mathbf{u} is taken along the normal to the epicardial surface passing through the point and set to be pointing outwards with respect to the left ventricular cavity. Then, \mathbf{v} is the cross-product of \mathbf{u} and the unit vector of the z -axis. Finally \mathbf{w} is the cross-product of \mathbf{u} and \mathbf{v} . Once the local material coordinates are assigned, a first rotation about the radial direction \mathbf{u} is performed, that transforms the vectors \mathbf{v} and \mathbf{w} into $\mathbf{v}_{\tilde{\alpha}}$ and $\mathbf{w}_{\tilde{\alpha}}$. The rotation angle $\tilde{\alpha}$ is the intrinsic helix angle that defines the fibre direction $\mathbf{f} = \mathbf{v}_{\tilde{\alpha}}$. Figure 4.8(a) is a representation of this first rotation.

The second step consists of a rotation about the fibre direction \mathbf{f} of the angle $\tilde{\beta}$, the intrinsic sheet angle. The vector \mathbf{u} is rotated to $\mathbf{u}_{\tilde{\beta}}$ that represents the sheet direction \mathbf{s} , while the vector $\mathbf{w}_{\tilde{\alpha}}$ is rotated into $\mathbf{w}_{\tilde{\alpha}\tilde{\beta}}$ that gives the sheet-normal direction \mathbf{n} . Figure 4.8(b) illustrates this step.

A third rotation of the intrinsic transverse angle $\tilde{\gamma}$ about the local longitudinal direction \mathbf{w} can be applied. However, in all the tissue structure models considered in this thesis, $\tilde{\gamma} = 0$ throughout the left ventricle.

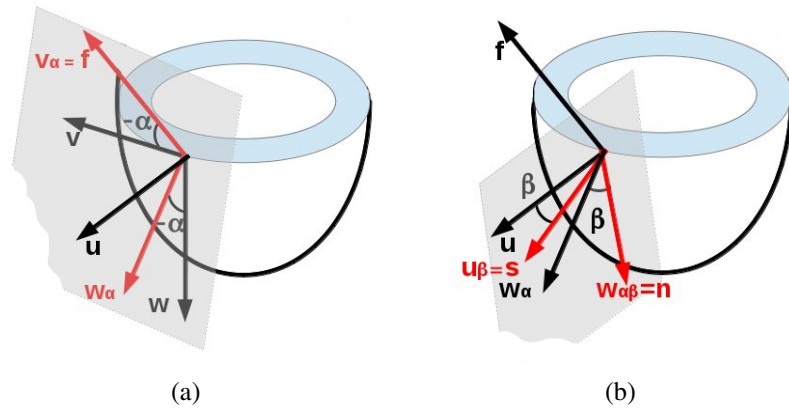


Figure 4.8: (a) First rotation of helix angle $\tilde{\alpha}$ about the local radial direction \mathbf{u} , used to determine the fibre direction. (b) Second rotation of sheet angle $\tilde{\beta}$ about the fibre direction \mathbf{f} , used to determine the sheet and sheet-normal directions.

There is a fundamental difference between the intrinsic helix, sheet and transverse angles $\tilde{\alpha}$, $\tilde{\beta}$ and $\tilde{\gamma}$ used to prescribe tissue structure to the mesh, and the extrinsic helix, sheet and transverse angles α , β and γ used to measure tissue structure on imaging data (Section 2.3), as explained in Section 4.5.5.

Different models of fibre and sheet orientation are introduced in this tissue structure generation framework by modelling the transmural variation of the intrinsic helix and sheet angles as described below.

4.5.2 Global models of fibre direction

For the purposes of my simulation study, a set of rule-based globally defined fibres was generated by assigning to each element of the mesh a value of the (intrinsic) helix angle $\tilde{\alpha}$, defined as the function $\tilde{\alpha} = \tilde{\alpha}(R, n, d)$ and calculated by eqn. (4.9)

$$\tilde{\alpha} = R * \text{sgn}(1 - 2d)|1 - 2d|^n \quad \text{where} \quad (4.9)$$

$$d = \frac{d_{\text{endo}}}{d_{\text{epi}} + d_{\text{endo}}} . \quad (4.10)$$

In the equations above, sgn stands for the sign function, d is the normalised transmural depth, varying from 0 to 1 from endocardium to epicardium, and obtained from the distance to endocardium d_{endo} and the distance to epicardium d_{epi} . R is the transmural rotation, that is the maximum absolute value of $\tilde{\alpha}$ allowed by the model, which will span between $-R$ at epicardium and $+R$ at endocardium. Finally, the exponent n modulates the transmural variation of $\tilde{\alpha}$, so for $n = 1$ it will be linear, $n = 3$ cubic, and so on. This is a standard approach for globally prescribed fibres [158]. Four values of R , $R = 50, 60, 70, 80$ were considered that are representative of the range of helix angle measured experimentally [158] [57]. For each value of R , four values of the exponent n , $n = 0.5, 1, 2, 3$ were tested, for a total of 16 globally defined fibre models. The chosen values for n reflect the experimental findings of previous studies performed in rat [71][16], dog [158] and human [53]. In the rest of the thesis, these models are referred to as $\text{Sn}x\text{R}y$, where S stands for Streeter-based and $nx\text{R}y$ refers to the value of the exponent n and of the parameter R used. As an example, the fibre model $\text{Sn}0.5\text{R}70$ is that obtained by imposing $R = 70$ and $n = 0.5$ in eqn. (4.9). Figure 4.9(a) shows the transmural variation of $\tilde{\alpha}$ for a subset of these fibre models. I define these rule-based fibre models as global because a single couple (R, n) determines the transmural variation of the fibre direction that is the same throughout the ellipsoidal mesh.

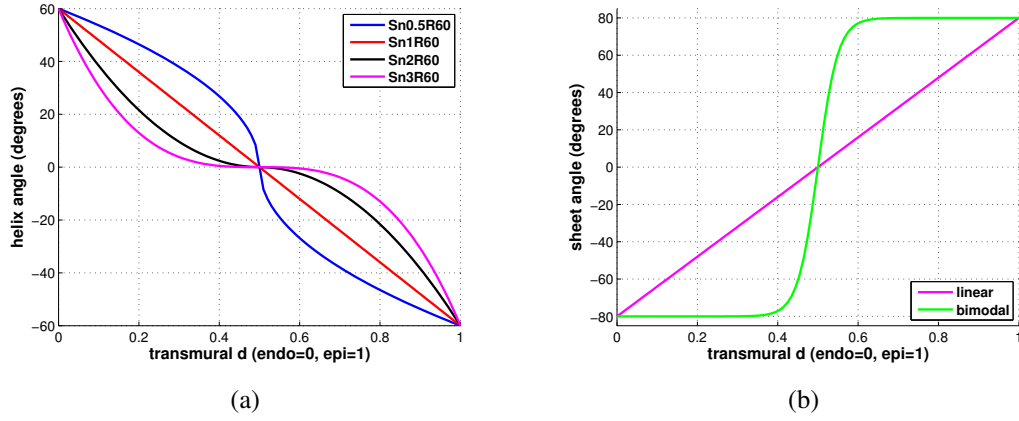


Figure 4.9: (a) Transmural models of the helix angle $\tilde{\alpha}$ for the four global rule-based fibre models. This figure is my own published work and is reproduced with permission from Springer. (b) Transmural models of sheet angle $\tilde{\beta}$.

4.5.3 Locally optimised model of fibre direction

A subject-specific fibre model developed by Karadag et al. [71] was also considered. This fibre model is based on a local optimisation of R and n carried out onto DT-MRI data from *dataset*₁ (Section 2.4), as the cine-MRI scan used to estimate the dimensions of the ellipsoidal mesh. They divided the left ventricle into 16 regions, an adaptation of the 17-region classification of the American Heart Association [25] (described in Section 1.3), and for each region they fitted eqn. (4.9) in order to minimise the angular difference with the imaging data. The result is a 16-region model of fibres as depicted in the bulls-eye diagram of Figure 4.10, with a single couple (R, n) obtained for each region, whose values are provided in Table 4.7. The reliability of the values obtained for some regions might be questioned, for example MI shows an almost constant value for the helix angle throughout the subregion (due to n being close to zero). This might be due, for example, to partial volume effects in the DT-MRI data (Section 2.2.3). However, this regional helix angle map is overall in line with previous global results obtained from DT-MRI in rats [16]. From now on I will refer to this model as Karadag.

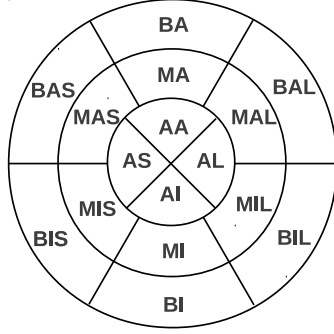


Figure 4.10: Bulls-eye diagram for 16-regions subdivision of left ventricle.

Region	(R, n)	Region	(R, n)
BAS	(81.0, 0.83)	MAS	(75.3, 0.78)
BA	(79.0, 1.22)	MA	(78.3, 1.15)
BAL	(71.6, 0.97)	MAL	(73.5, 0.94)
BIL	(76.2, 0.90)	MIL	(63.6, 0.67)
BI	(53.1, 0.51)	MI	(33.3, 0.08)
BIS	(77.7, 0.71)	MIS	(72.4, 0.68)
AA	(57.7, 0.82)	AL	(54.3, 0.36)
AI	(25.5, 0.18)	AS	(56.7, 0.7)

Table 4.7: (R, n) values for each region of the 16-region adaptation of the 17-region AHA classification of the left ventricle [25]. **Legend:** B=basal, M=mid, A=apical (for the first letter code). A=anterior/antero-, I=inferior/infero-, L=lateral, S=septal (for the second and third letter code).

4.5.4 Models of sheet orientation

Two main models have been proposed for the transmural distribution of sheets, a continuously varying model (such as the one proposed by LeGrice et al. [94]) and a discontinuous bimodal distribution (which has been experimentally supported, for example, by the work of Arts et al. [6]). Experimental evidence exists that support both models but, none of the two approaches seems able to fully capture the high complexity of sheet organisation in the myocardial wall [51]. I have modelled the two types of distribution by a simple linear transmural variation of the (intrinsic) sheet angle $\tilde{\beta}$ for the continuously varying distribution, and a sigmoidal transmural variation to represent the bimodal model. The linear model for $\tilde{\beta}$ goes from $B = -80$ at endocardium to $B = +80$ at epicardium, and is described by $\tilde{\beta} = B(2d - 1)$. The sigmoidal function for the bimodal model is given by eqn. (4.11)

$$\tilde{\beta} = B(2H - 1) \text{ where } H = (1 + \exp(-K(2d - 1)))^{-1}, \quad (4.11)$$

where K is a parameter affecting the steepness of the sigmoidal function. The value of $K = 20$ was chosen in order to obtain a steep sigmoidal. Figure 4.9(b) shows the transmural variation of the sheet angle $\tilde{\beta}$ for the two models used in this study.

4.5.5 Relation between extrinsic and intrinsic angles

In Section 2.3 the helix, sheet and transverse angles (α, β, γ) were introduced as a way to quantify tissue structure distribution in imaging data such as DT-MRI. Those angles were defined with respect to a fixed system of coordinates, either global or local. Hence (α, β, γ) are an extrinsic representation of tissue structure. In Section 4.5.1 three analogous

angles were defined $(\tilde{\alpha}, \tilde{\beta}, \tilde{\gamma})$, the intrinsic helix, sheet and transverse angles, respectively, in order to prescribe tissue structure to the elements of the mechanical mesh. In the intrinsic approach a rotating frame of reference is employed to sequentially define \mathbf{f} , \mathbf{s} and \mathbf{n} by means of rotations of two axes of the reference frame with respect to the third one. The definition of two separate sets of angles, the extrinsic one α, β, γ for measuring angles on imaging data such as DT-MRI, and the intrinsic one $\tilde{\alpha}, \tilde{\beta}, \tilde{\gamma}$ may at first seem confusing. However, if we consider the extrinsic angles α, β, γ measured with respect to the local coordinate system $(\mathbf{u}, \mathbf{v}, \mathbf{w})$, that is the same system employed to prescribe $\tilde{\alpha}, \tilde{\beta}, \tilde{\gamma}$, then the two sets are easily convertible one into the other.

Given the sequence of rotations applied when prescribing tissue structure to the mesh, the definition of α is by all means identical to that of $\tilde{\alpha}$. The rotation about the intrinsic helix angle $\tilde{\alpha}$ is applied to the original coordinate system $(\mathbf{u}, \mathbf{v}, \mathbf{w})$, the same used to measure α in the local coordinate system approach. In other words, if α is measured on the ellipsoidal mesh using the local coordinate system, the measured transmural distribution is the same as the prescribed distribution for $\tilde{\alpha}$ (Figure 4.8(a)).

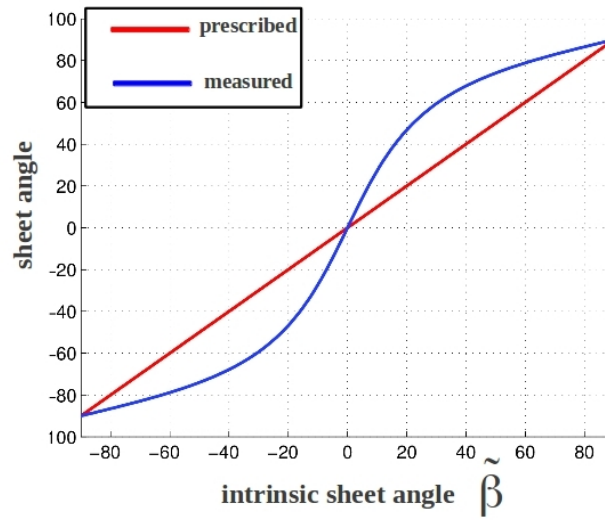


Figure 4.11: Difference between prescribed intrinsic sheet angle $\tilde{\beta}$ (red) and corresponding measured sheet angle β (blue) (measured with respect to a local cylindrical coordinate system).

In the case of the relationship between β and $\tilde{\beta}$, they differ by one rotation, exactly the rotation about \mathbf{u} of angle $\tilde{\alpha}$. The angle β is still measured with respect to the same local cylindrical coordinate system $(\mathbf{u}, \mathbf{v}, \mathbf{w})$ as α . Conversely, in the algorithm to assign tissue structure to the mesh, the rotation of angle $\tilde{\beta}$ is about the unit vector $\mathbf{v}_{\tilde{\alpha}}$ of the rotated coordinate system $(\mathbf{u}, \mathbf{v}_{\tilde{\alpha}}, \mathbf{w}_{\tilde{\alpha}})$. If, for example, a linear transmural variation of $\tilde{\beta}$ is prescribed

(as in Figure 4.9(b)) to the mesh, then the measured β with respect to the local cylindrical coordinate system is going to be sigmoidal. Figure 4.11 shows the difference between prescribed $\tilde{\beta}$ (red) and measured β (blue).

The relationship between γ and $\tilde{\gamma}$ was not tested, because for all simulations $\tilde{\gamma}$ was not considered.

In this chapter the development of the electromechanical model is described. The generation of the mesh representing the left ventricle is discussed. The process to determine electrophysiological and mechanical parameters is also addressed. Finally, the framework to assign tissue structure to the geometrical mesh is described. In the following chapter, the first simulation study employing the developed electromechanical model is presented.

Chapter 5

Effect of fibre orientation optimisation in an electromechanical model of left ventricular contraction in rat

In this chapter the results are presented of the first computational study performed on the effect of fibre orientation on contraction in rat left ventricle [24] by means of the electromechanical model described in the previous chapter. First, the scientific questions and goals of the study are provided, then the methods are described. Finally, the results are presented.

5.1 Introduction

The role of tissue structure for cardiac function was described in Section 1.1.2, while in Section 3.1.6 the use of tissue structure within cardiac models was discussed. The topic of patient-specific or, in the case of animal models, subject-specific modelling was introduced highlighting how personalised tissue structure distribution plays an important role in it. However, although the motivation underlying such an approach is absolutely compelling, in my opinion, the effective improvement it brings to the field of cardiac electromechanics has not been thoroughly tested yet. For example, Geerts et al. [48] showed that the use of realistic geometries for the left ventricle, as opposed to ellipsoidal representations, produced changes in the predicted fibre orientation rearrangement that was lower than the accuracy of experimental measurements, therefore questioning the need for personalised geometries in their modelling setting. Similarly, the aim of my study was to investigate whether simple rule-based models of fibre direction can have a predictive power comparable to that of subject-specific fibre models. To this purpose, the 16 global rule-based fibre models described in Section 4.5.2 and the local fibre model by Karadag et al. (Section 4.5.3) were considered and their effect on global left ventricular function in electrome-

chanical simulations of contraction was compared. The simulation output for the different fibre models was evaluated using three metrics of cardiac function: ejection fraction, wall-thickening and shortening in the base-to-apex direction (Section 5.2). The predicted values of these metrics were compared with direct measures taken on the same rat cine-MRI dataset from *dataset*₁ used to define the ellipsoidal meshes (Section 5.2.1). The hypothesis is that Karadag model, which can be considered as a subject-specific model, will not produce a great improvement in the agreement between predicted and measured global measures, with respect to at least some of the global fibre models. The results seem to be in line with this hypothesis, as shown and discussed in Section 5.4.

A first analysis of the effect of sheet distribution on cardiac mechanics was also carried out by comparing two constitutive behaviours, transversely isotropic and orthotropic. As already discussed in Section 3.1.3, the orthotropic material law allows the orientation of sheets across the tissue to be taken into account, whereas the transversely isotropic law treats as uniform the mechanical properties in the cross-fibre plane. In this study, only the linear model of sheet angle transmural variation (Section 4.5.4) was considered, while the bimodal model was employed in the study presented in Chapter 6. The hypothesis is that taking into account the orientation of sheet planes in the model, by means of the orthotropic material law, will increase the model's predictive power. The results seem to support such hypothesis (Section 5.4).

Overall, although the two hypotheses defined were not contradicted by this study, all predicted values of global metrics fell below the measured values. This suggests that there are some important limitations to the electromechanical model itself that need to be addressed.

5.2 Global metrics for the evaluation of cardiac function

Three metrics were chosen to evaluate in a quantitative way the performance of the electromechanical simulations in terms of global cardiac function, hence the name global metrics. These quantities were employed both in the model development phase, as explained in Section 5.3 and in the computational study phase in order to compare the effect of different fibre models and mechanical behaviours on contraction, as described in Section 5.4.

Ejection fraction (*EF*) and wall-thickening (*WT*) are two common indices of cardiac function routinely measured in clinical assessment, as explained in Section 1.3. The shortening in the base-to-apex direction *SL* was also evaluated as a measure of the changes in apico-basal length due to the movement downwards in the direction of the apex of the atrio-ventricular valve plane during contraction. This parameter is important because in some

electromechanical models, instead of the expected reduction in apico-basal length during contraction, elongation occurs, see for example [89]. The metrics were computed on the mechanics mesh by comparing the mesh state at the beginning and end of contraction. For the set of simulations presented in this chapter, beginning of contraction was at time $t_0 = 0 \text{ ms}$, while contraction ended approximately at $t_f = 130 \text{ ms}$. EF was calculated as the relative difference between the mesh cavity volume vol at t_0 and t_f ,

$$EF = \frac{vol_{t_0} - vol_{t_f}}{vol_{t_0}} 100\% . \quad (5.1)$$

WT was computed as the average difference in wall-thickness w between t_0 and t_f at a chosen short-axis slice. At a given time, w was obtained by averaging four measures taken symmetrically onto the short-axis slice located 25% along the long axis from the base, that is approximately in the equatorial (or midventricular region). This specific short-axis slice was chosen in order to compare with the cine images, since WT is more easily measured in the midventricular region. The formula for WT is:

$$WT = \frac{w_{t_f} - w_{t_0}}{w_{t_0}} 100\% . \quad (5.2)$$

For all the electromechanical simulations on the ellipsoid, mechanical boundary conditions fix the nodes of the base in the z axis only, as explained in more detail in Section 5.3.1. For this reason, in order to compute SL , the z coordinate of the epicardial apical node along the z axis (which coincides with the long axis of the left ventricle, see Figure 4.1(a)) was measured at t_0 and t_f . The formula for SL is:

$$SL = \frac{z_{t_f} - z_{t_0}}{z_{t_0}} 100\% . \quad (5.3)$$

This is an adequate measure of the shortening along the base-to-apex direction since the base is kept fixed in the model and the apex moves almost exclusively along the long axis (of course, *in situ*, the movement is in the opposite direction, but in terms of changes in apico-basal length, this parameter offers a satisfactory approximation within the modelling framework used). Negative values of SL represent shortening, while positive values represent elongation of the ventricle during contraction.

5.2.1 Global metrics measurements on cine-MRI

In order to compare the predicted values with experimental data, these metrics were measured on the cine-MRI scan from *dataset*₁. The measured values are $EF_{cine} = 77\%$, $WT_{cine} = 54\%$ which are consistent with values in the literature [36], and $SL_{cine} = -10\%$, for which I could not find references.

5.3 Further model development

This Section is strictly related to the work described in Chapter 4, for it deals with further model testing and implementation that was carried out on the ellipsoidal geometry prior to the computational study. In particular, the choice of appropriate boundary conditions for the electromechanical problem and the preliminary tests run to determine the most appropriate parameter sets for the material law are described. The results of the preliminary tests carried out to decide whether to include cross-fibre active tension generation in the model are also presented.

5.3.1 Boundary conditions

In order to initiate electrical propagation in the model, external stimulation to the lowest portion of the apical region was applied. The apical region was defined as the set of nodes of the electrical mesh whose z coordinate is lower than 95% of the base-to-apex length (in other words 95% of c_{epi} , see Table 4.1), since the z axis is oriented from apex to base. This choice is justified by the fact that apical stimulation is the typical protocol in Langendorff-perfused experiments, and its straightforward to implement. However, it is not a physiologically accurate stimulation of the left ventricle. Since it is likely that changes in stimulation pattern will affect contraction patterns as well, the use of more physiologically accurate stimulation patterns is one of the short-term future projects I plan to carry out, as discussed in Chapter 8.

Regarding mechanical boundary conditions, I first attempted to fix a small portion of the apical area, motivated by the observation that in cine-MRI scans the apex hardly moves during the cardiac cycle, whereas the atrio-ventricular plane, or more simply the base of the ventricle, moves significantly to accommodate the change in blood volumes inside the ventricles. However, fixing the apex proved to be numerically unstable. Simulations with some of the fibre models did not converge, and for those simulations that did, the ventricular mesh was subject to totally non-physiological local distortions in the apical region and a tendency to precess around the long axis (z axis). Therefore, I chose to fix the base nodes instead (defined as the nodes with $z > -1 \cdot 10^{-6}$), but only along the z axis, so that the related elements were free to contract and expand in the xy plane. This choice proved to be stable. This type of boundary condition was required because the electromechanical model is not coupled with a model of circulation, which would enforce the movement of the atrioventricular plane in response to changes in pressure and volume.

In relation to pressure, a constant zero pressure boundary condition was applied for the study presented in this chapter.

5.3.2 Passive deformation

In Section 4.4.2 the constitutive law [166] chosen to model passive mechanics and the stiffness parameters sets that define two transversely isotropic laws t_{iso}^* and t_{iso} and one orthotropic law $ortho^U$ (see Table 4.5) were described. This section focuses on two preliminary groups of electromechanical simulations that were run on the ellipsoidal geometry in order to

- Differentiate the effect on cardiac mechanics due to average stiffness of the material law and the effect due to material symmetry.
- Find a value of the level of compressibility C_b in the strain-energy equation (eqn. (3.9)) that ensures near-incompressibility of the tissue.

The details of the simulation set-up for these two tests are summarised in Table 5.1.

Table 5.1: Details of the simulation set-up for the simulations of Section 5.3.2

geometry	ellipsoid
electrics mesh	$mesh_e$ (Table 4.1)
mechanics mesh	$mesh_m$ (Table 4.1)
AP model	Wang2008 (Section 4.3.1)
electrophysiological parameters	Table 4.2
contraction model	K2003 with 2/3 scaling of b , t_r , t_d (Section 4.4.1)
constitutive law	test-dependent
fibre models	Sn1R60, Sn1R70, Karadag, Sn3R60, Sn3R70 (Section 4.5)
sheet model	linear (Section 4.5)
simulation duration	130 ms
stimulation site	lower apical region (Section 5.3.1)
fixed nodes	base nodes fixed in z direction (Section 5.3.1)
pressure boundary condition	constant zero pressure

5.3.2.1 Effect of average stiffness versus material symmetry

One of the aims of my simulation study was to compare transversely isotropic and orthotropic passive behaviour as a way to evaluate the effect of sheet distribution on deformation. Hence, I needed to find suitable stiffness parameters for the strain-energy equation (eqn. (3.9)). The transversely isotropic parameters provided by Usyk et al. [166] had average magnitude significantly higher than the orthotropic ones. I thus decided to test how

much this difference in average magnitude affected the comparison between the two material symmetries. As explained in Section 4.4.2, t_{iso}^* is the high stiffness transversely isotropic material law by Usyk et al. [166] (with a minor correction) and $ortho^U$ is the orthotropic material law the authors obtain after an optimisation process. Stiffness parameters of $ortho^U$ are on average significantly lower than those of t_{iso}^* , hence I decided to generate a transversely isotropic material law t_{iso} by averaging the relevant parameters of $ortho^U$ (details can be found in Section 4.4.2).

In order to differentiate the effect of different average stiffness and material symmetry a set of 5×3 electromechanical simulations (simulation details in Table 5.1) was run. Five fibre models were considered, four global (Sn1R60, Sn1R70, Sn3R60, Sn3R70) and the Karadag local fibre model. This set of five simulations was repeated with the three different material laws and then the simulation output evaluated in terms of the global metrics introduced in Section 5.2. For all these simulations the value of the level of compressibility was $C_b = 200 \text{ kPa}$ (and not 100 kPa as in Usyk et al. [166]). Further details on the choice of C_b are given in Section 5.3.2.2).

The results of this test are shown in Figures 5.1(a) (for EF), 5.1(b) (for WT) and 5.1(c) (for SL). With the material law t_{iso}^* , given its higher stiffness, the simulation with Sn1R70 did not converge. The three plots show that the two laws with similar stiffness (t_{iso} and $ortho^U$) give results that are more similar between them than those of the two transversely isotropic material laws t_{iso}^* . Average stiffness has an important effect on the global metrics values, higher than the sole difference in material symmetry, especially when considering EF . Therefore it needs to be taken into account when comparing different material behaviours. For this reason, I chose to use t_{iso} and $ortho^U$ as material laws representative of transverse isotropy and orthotropy for the simulation studies of this thesis. The analysis of the results in terms of the effect of fibre models onto global metrics will be provided in Section 5.4.1.

5.3.2.2 Finding C_b value for near incompressibility

The choice of a nearly incompressible model was made in order to ensure the best compromise between numerical stability on one side and spatial and temporal resolutions on the other. In order to evaluate to what level this choice would have affected the simulations' results, I performed a preliminary study of the effect of the level of compressibility C_b (in the strain-energy eqn. (3.9)) on volume reduction VR

$$VR = \frac{tissue_vol_{t_f} - tissue_vol_{t_0}}{tissue_vol_{t_0}} 100\%. \quad (5.4)$$

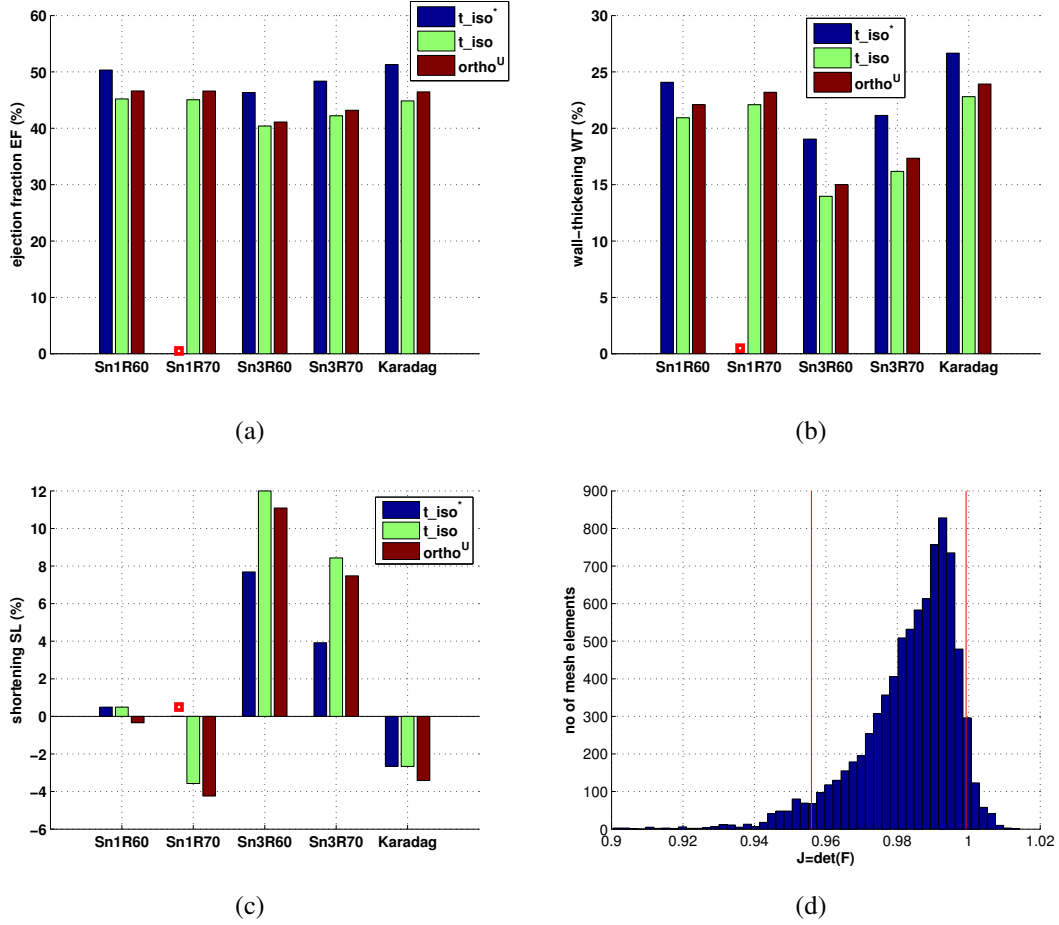


Figure 5.1: (a)-(c) Global metrics for the three material laws considered : (a) EF , (b) WT and (c) SL . The red square indicates that the simulation did not converge. (d) Distribution of the Jacobian of the deformation over the mesh elements.

Here the mesh volume at beginning ($tissue_vol_{t_0}$) and end of contraction ($tissue_vol_{t_f}$) is computed by summing the volume of all the elements of the mesh. To this purpose, a set of 5×2 simulations was performed, employing the five fibre models Sn1R60, Sn1R70, Sn3R60, Sn3R70, and Karadag, and t_{iso} and $ortho^U$ as material laws (simulation details in Table 5.1). The set of simulations was repeated for three values of the parameter $C_b = 200, 100$ and 50 kPa respectively. The average VR for $C_b = 200 \text{ kPa}$ is -1.63% , for $C_b = 100 \text{ kPa}$ is -2.36% and for $C_b = 50 \text{ kPa}$ is -3.59% . A threshold of $VR \leq \pm 2\%$ was considered reasonable to ensure near incompressibility, hence the value of $C_b = 200 \text{ kPa}$ was chosen for the simulation study.

In order to get a better understanding of the local effect of the chosen C_b value, the distribution of the Jacobian of the deformation, $J = \det(F)$, was also considered. J was computed at end contraction for each element of the mechanical mesh $mesh_m$. As an example, the

resulting histogram for the simulation with $C_b = 200 \text{ kPa}$, Sn1R70 fibre model, linear sheet model and orthotropic material law, is shown in Figure 5.1(d). The distribution of J over the mesh elements between beginning and end of contraction has an average 5th-95th percentile range of 0.95-1.00 over all the simulations performed for this test, confirming that the model is nearly incompressible.

5.3.3 Cross-fibre active tension

In order to test the effect of cross-fibre active tension generation on cardiac mechanics, a set of simulations was run with fibre model Sn1R70, orthotropic material law $ortho^U$ and $C_b = 200 \text{ kPa}$, and varying fractions of active tension generation in the sheet and sheet-normal directions, while the rest of simulation details are as in Table 5.1. Active tension generation in the sheet and sheet-normal direction were modelled as in eqn. (3.11). The amount of active tension in those directions was a fraction of that generated in the fibre direction by the contraction model σ_a , specifically $k_s \sigma_a$ in the sheet direction and $k_n \sigma_a$ in the sheet-normal direction.

Table 5.2: Table summarising the fractions of active tension in the fibre direction that were assigned in the sheet (k_s) and sheet-normal (k_n) directions for the preliminary study of cross-fibre active tension generation.

Isotropic cross-fibre active tension					
Sim no	1	2	3	4	5
$k_s = k_n$	0.05	0.1	0.15	0.2	0.25
Anisotropic cross-fibre active tension					
Sim no	6	7	8		
k_s	0.1	0.1	0.1		
k_n	0.0	0.025	0.05		

In this preliminary study, both isotropic ($k_s = k_n$) and anisotropic ($k_s \neq k_n$) cross-fibre active tension generation were considered. Table 5.2 summarises the set of fraction values tested. The simulation results were then evaluated by computing the global metrics EF , WT and SL .

Figures 5.2(a)-5.2(c) show the results for the isotropic cross-fibre active tension. The common value k , assigned to the two fractions $k_s = k_n = k$, is shown on the x axis of the plots. The first value $k = 0$ represents the reference simulation without cross-fibre active tension. The introduction of cross-fibre active tension causes more force to be generated in total and this produces an increase in the three metrics. However, by increasing the fraction

of cross-fibre active tension from $k = 0.05$ to $k = 0.2$ the results are less consistent. While EF and WT decrease, SL increase in absolute value, that is more shortening takes place. The simulation with $k = 0.25$ did not converge, hence no results can be shown.

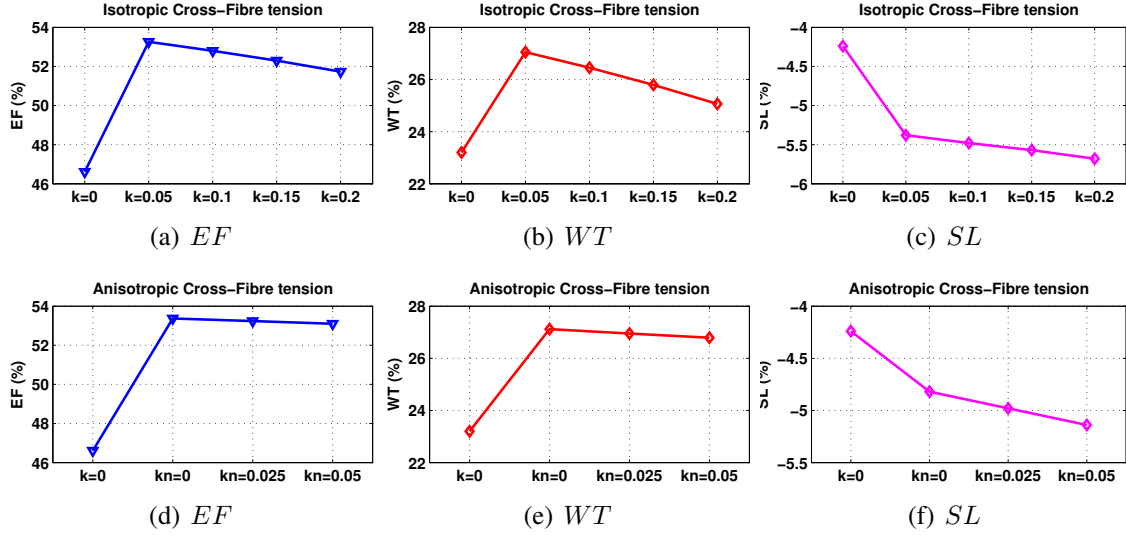


Figure 5.2: (a)-(c) Global metrics results for the simulations with isotropic cross-fibre active tension. (d)-(f) Global metrics results for the simulations with anisotropic cross-fibre active tension. See text for details.

Figures 5.2(d)-5.2(f) show the global metrics results for the simulations with anisotropic cross-fibre tension. In this case, the value of tension in the sheet direction ($k_s = 0.1$) was fixed, while varying tension in the sheet-normal direction ($k_n = 0, 0.025, 0.05$) was applied. Again, the first value $k = 0$ represents the reference simulation without cross-fibre active tension. Increasing tension in the sheet-normal direction had almost no effect on EF and WT while it increased the shortening SL .

Although the values of the global metrics are all significantly below the corresponding experimental values (Section 5.2.1), the increase in total force generated had the effect of increasing the global metrics values, hence going towards more physiological ranges. However, while a small amount of force improves the prediction of the global metrics, further increase of the force magnitude has the opposite effect. This could be due to the fact that the higher force generated in the tissue produces higher compression of its volume. The conclusion of this study was that the use of cross-fibre tension generation requires a more thorough analysis. Therefore, I decided that it was preferable to use only uni-axial active tension generation and focus on ways to increase the contractile force generated in the tissue, for example by introducing pressure, as discussed in the next chapter.

Table 5.3: Details of the simulation set-up for the simulations of Section 5.4

geometry	ellipsoid
electrics mesh	$mesh_e$ (Table 4.1)
mechanics mesh	$mesh_m$ (Table 4.1)
AP model	Wang2008 (Section 4.3.1)
electrophysiological parameters	Table 4.2
contraction model	K2003 with 2/3 scaling of b , t_r , t_d (Section 4.4.1)
constitutive law	t_{iso} or $ortho^U$ with $C_b = 200 \text{ kPa}$
fibre models	all 16 global fibre models and Karadag (Section 4.5)
sheet model	linear (Section 4.5)
simulation duration	130 ms
stimulation site	lower apical region (Section 5.3.1)
fixed nodes	base nodes fixed in z direction (Section 5.3.1)
pressure boundary condition	constant zero pressure

5.4 Effect of fibre optimisation on contraction

In this section the results of the computational study of the effect of fibre orientation and material symmetry on contraction in rat left ventricle [24] are presented. The simulations details are shown in Table 5.3.

5.4.1 Results

In order to describe the results of the impact of the different fibre distributions on cardiac mechanics the case of the transversely isotropic material law t_{iso} is first considered. Figures 5.3(a), 5.3(b) and 5.4(a) show the results for EF , WT and SL , respectively. In these plots, the values of the global metric for the global fibre models $S_n x R_y$ are grouped for increasing values of R .

The variation in EF due to the different fibre models is shown in Figure 5.3(a). EF is the least affected by the change in fibre model among the three metrics considered. Only the exponent value $n = 0.5$ shows a decrease in EF for increasing values of R . Otherwise all the global fibre models together with the Karadag model produce EF values rather close to each other. The predicted values fall well below the measured one of $EF_{cine} = 77\%$ (Section 5.2).

In the case of SL , the choice of fibre model has a more substantial effect (Figure 5.4(a)). Within the global fibre models $S_n x R_y$, high values of the exponent n combined with low values of R produce elongation (positive values of SL), whereas there is increasing shortening for low values of the exponent and increasing R . In particular, the models

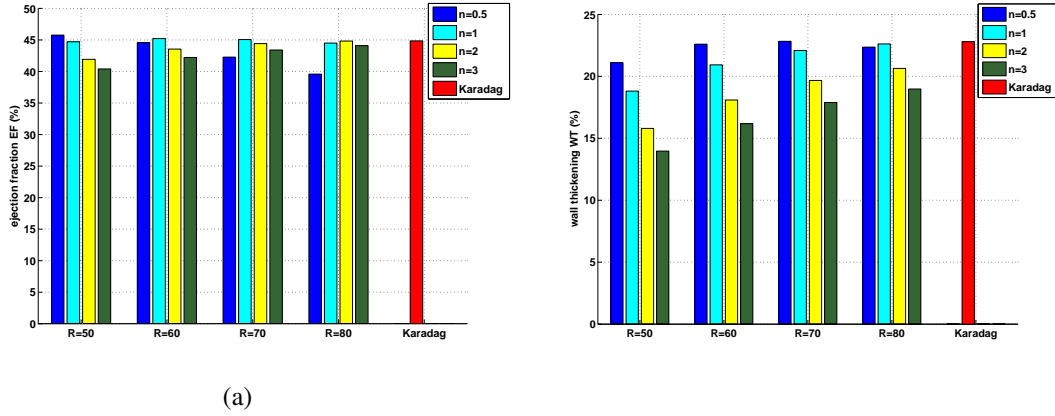


Figure 5.3: (a) EF and (b) WT values for the different fibre models with transversely isotropic material law. Both figures are my own published work and are reproduced with permission from Springer.

Sn0.5R70, Sn0.5R80 match and exceed the measured shortening $SL_{cine} = -10\%$, respectively. Karadag fibre model produces shortening but of a lower magnitude than the experimental measurements. The difference between fibre models that produce elongation and those that result in shortening can be explained by looking at the transmural variation of the helix angle defining these models and shown in Figure 5.4(b) (this is a copy of the previously shown Figure 4.9(a)). Fibre models, such as Sn3R60, that have a larger component of circumferential fibre directions, (that is, helix angle close to zero), are likely to be less efficient into producing shortening during contraction. On the contrary, fibre models with a larger component of more “vertical” fibre directions (that is, helix angle close to R), such as Sn0.5R60, will make more elements of the geometrical mesh contract in the longitudinal direction, hence the shortening.

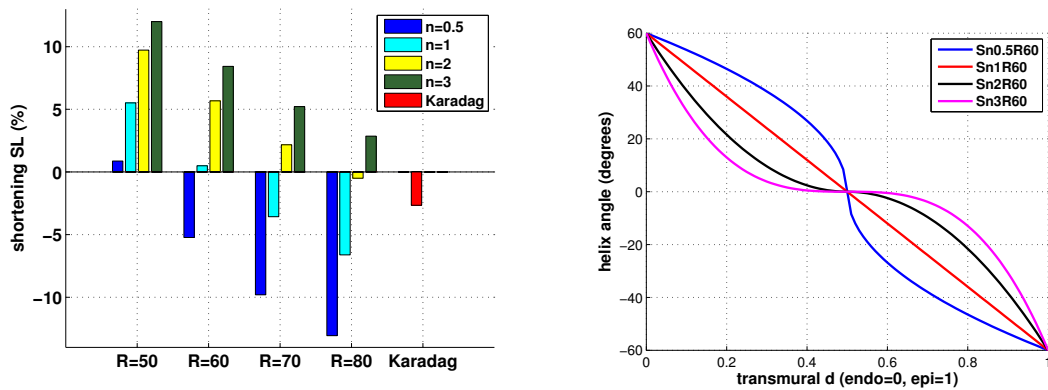


Figure 5.4: (a) SL values for the different fibre models with transversely isotropic material law. (b) Transmural models of the helix angle $\tilde{\alpha}$ for the four global rule-based fibre models (copy of Figure 4.9(a)). Both figures are my own published work and are reproduced with permission from Springer.

Figure 5.3(b) displays the results for WT . As in the case of SL , increasing values of the angle R combined with decreasing values of the exponent n produce an increase in WT , making its value more realistic although still well below the measured value of $WT_{cine} = 54\%$. Karadag fibres produce one of the highest values of WT (22.8%) together with other global models such as Sn0.5R70 (22.83%).

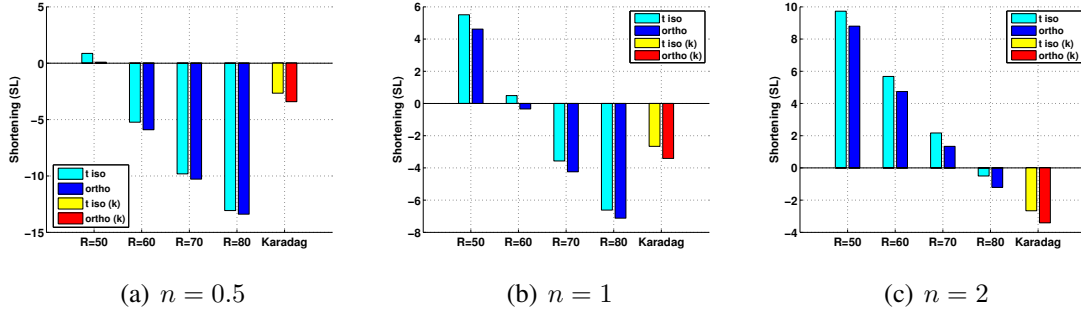


Figure 5.5: Comparison of SL values obtained with transversely isotropic (t_{iso}) and orthotropic ($ortho^U$) material law. Results are shown for fibres with exponent (a) $n = 0.5$, (b) $n = 1$ and (c) $n = 2$. Karadag fibre model is denoted by k. All figures are my own published work and are reproduced with permission from Springer.

Changing from transversely isotropic to orthotropic behaviour has the effect of improving all the three metrics predictions although WT and EF still fall below the experimental measurements. The value of WT increased for every fibre model, with an average percentage increase of 5.7%. EF values also increased by an average 3.0%. The predicted shortening was also increased, that is SL tended to become more negative of an average -10.9% , and for the fibre model Sn1R60, it allowed to switch from lengthening ($SL > 0$) to shortening ($SL < 0$). For example, the comparison between the two material laws is shown in Figures 5.5(a)-5.5(c) in the case of SL . Figure 5.5(a) shows the case of $n = 0.5$, while Figures 5.5(b) and 5.5(c) show the result for $n = 1$ and $n = 2$, respectively. In each plot, the value of SL for Karadag fibre model is reported for better comparison.

5.4.2 Discussion

In the previous section the results are shown of the quantitative analysis of the effect of different fibre models on contraction of rat left ventricle in an electromechanical computational study. The aim of the study was to investigate whether the use of a more subject-specific fibre model (Karadag) increases the predictive power of the model with respect to a series of global fibre models (Sn x R y for $x = 0.5, 1, 2, 3$ and $y = 50, 60, 70, 80$). The quantitative analysis was based on the evaluation of the three metrics chosen: ejection fraction (EF), wall thickening (WT) and base-to-apex shortening (SL). Additionally, predicted

metrics values were compared with measures taken on one rat cine-MRI dataset (Section 5.2.1), the same used to generate the ellipsoidal meshes of the left ventricle (Section 4.2).

In general, predicted values of EF and WT were substantially lower than the measured ones, while for SL , some global fibre models were able to reach the measured value. The subject-specific fibre model gave, together with a few global fibre models, the best values of EF and WT , but it failed to reproduce realistic values of SL . Furthermore, introducing the sheet orientation, by means of switching from transversely isotropic to orthotropic material behaviour, generally improved the prediction, although the predicted values for EF and WT were still below the measured values.

The computational study presented has limitations, in particular the use of a non physiological pressure boundary condition. Additionally, the simulation output was evaluated only by means of global metrics. A more thorough analysis should involve local metrics such as normal and shear strains profiles. In the study presented in the next chapter both aspects were addressed. A more thorough analysis of the limitations of the general modelling approach is presented in the next chapter, therefore is not repeated here.

It could be argued that there are many factors, other than the ones considered in our study, that could also have an important effect on the metrics values obtained, such as the average stiffness of the material law (Section 5.3.2.1). However, within the modelling framework employed, I believe that the results show that the use of subject-specific fibre models is not able to make a substantial difference compared to simple rule-based fibre models. On the other hand, the slight increase in the global metrics predictions provided by the orthotropic material law suggest that further investigation of the constitutive behaviour of cardiac tissue and a closer focus onto the role of sheet dynamics should be addressed before moving towards a subject-specific approach. The results shown in next chapter are one step forward in this direction.

In this chapter model development aspects related to passive material properties and active tension generation have been discussed. Then, the results of a computational study of the effect of fibre optimisation and material symmetry on contraction have been presented. In the next chapter a more complete study of the effect of tissue structure definition on contraction, that stems from the one presented here, but at the same is a significant extension to it, will be described.

Chapter 6

A quantitative study of the effect of tissue structure on contraction in a computational model of rat left ventricle

In this chapter an extended computational study of the effect of tissue structure on contraction of the left ventricle in rat is presented. This study is a substantial extension to the one described in the previous chapter. It includes blood pressure in the electromechanical model, and local metrics as well as global metrics are taken into account. In addition, the analysis of the effects of cardiac laminar structure includes the use of different models of sheet angle transmural variation as well as the comparison of transversely isotropic and orthotropic behaviour. In the following sections the motivation and aims of this study are introduced, model development related to the introduction of blood pressure is described and the results obtained are presented and discussed.

6.1 Introduction

One of the conclusions of the previous chapter was that the electromechanical model was unable to reproduce values of ejection fraction (EF) and wall thickening (WT) close to those measured on cine-MRI scans. One potential factor influencing this was the lack of a physiologically realistic endocardial pressure boundary condition. The idea underlying the introduction of a time-varying pressure trace was that the interplay between pressure and contraction model would enhance the contractile ability of the model, since more stretch and hence more force would be generated. This idea proved to be correct, increasing both EF and WT to levels close to physiological values found in the literature, although still below the ones from cine-MRI scans. With this more reliable electromechanical model I returned to the motivation and goals of the computational study and explored ways to

further investigate them. For this reason, the aims of the study presented in this chapter are a generalisation of the ones presented in the previous chapter.

The first aim of this study was to understand how the use of a time-varying pressure boundary condition would change the output of the electromechanical model. The second aim, as explained in Section 5.1, was to understand whether the use of subject-specific fibres would enhance the predictive power of the electromechanical model developed, or whether it would be as informative as simple globally prescribed fibres. Since the impact of pressure on electromechanics within the developed modelling framework was yet to be understood, it was important to address this aim again. The final aim was to further explore the effect of sheet dynamics on contraction. In order to test the impact of sheet orientation on left ventricular contraction, a transverse isotropic and a orthotropic material law for cardiac tissue were compared, as in the previous chapter. Additionally, under the orthotropic material properties, two global models of transmural variation of the sheet orientation, a linear and a bimodal model (Section 4.5.4) were tested. The hypothesis underlying this comparison was that the latest findings regarding the discontinuous multiple-population distribution of sheets [57] (mimicked by the bimodal model) would improve the accuracy of the electromechanical model, as opposed to the standard smooth variation of sheet orientation [94] (the linear model).

In order to quantify the effect of the different models of fibre and sheet orientation on contraction, both global and local metrics were considered. The global metrics are those introduced in Section 5.2. The local metrics considered are the Lagrangian circumferential strain, as a measure of contraction, circumferential-radial shear strain, as a measure of the relative twist of sub-endocardial and sub-epicardial layers, and circumferential-longitudinal shear strain, as a measure of torsion [21]. These metrics will be discussed in more detail in Section 6.2.

The contribution of the study is twofold. First, it shows that the fibre model affects significantly the prediction of the metrics considered. Therefore, it is important to choose the most suitable fibre setting for the specific scientific question to be addressed and the modelling approach employed. This might mean that a subject-specific fibre model is not necessary. As in the previous study, the results question the efficacy of using personalised myocyte orientations when compared to the limitations of state-of-the-art electromechanical models, since they do not seem to provide substantial improvements, both in terms of global and local measures, compared to simpler global rule-based fibre definitions, at least for the healthy left ventricle of rat. Second, the results obtained highlight the need

for further development of models of sheets. On the one hand, the introduction of sheet orientation in the model by switching from transverse isotropy to orthotropy shows a small but consistent improvement in the metrics predictions. On the other hand, although experimentally more realistic, the bimodal model for sheet orientation did not improve and in some cases counteracted the effect of introducing material orthotropy. This was not in line with the hypothesis, since such an important structural change was expected to affect more evidently the predicted deformation patterns. The results presented in this study are in agreement with the conclusions of the previous study (Chapter 5). The current electromechanical modelling approach may not be able to successfully make use of subject-specific tissue structure, with all its additional complexity and computational cost, unless a better understanding of the biological roles, and the computational modelling of sheets and their mechanical properties is achieved.

6.2 Local metrics for the evaluation of cardiac function

As discussed in Section 1.3, cardiac function can be assessed at a local level by taking into account strain or strain rate. For this purpose, the Lagrangian strain tensor of each element of the mechanical mesh was computed with respect to a global cylindrical coordinate system (Section 2.3.1) for each simulation. The cylindrical reference frame is preferable to the Cartesian one for it provides a more direct interpretation of the strain tensor components in terms of cardiac function.

In what follows, I simply focus on one element of the mechanical mesh and denote by E_{cyl} the Lagrangian strain tensor at the centroid. In order to compute E_{cyl} , it was first necessary to transform the deformation gradient tensor F_{cart} from the Cartesian to the cylindrical coordinate system. F_{cart} for each element of the mesh was sampled at 10 *ms* intervals for each simulation. Given the position (x, y, z) of the centroid of the element, the angle $\theta = \arctan(y/x)$ was determined. The radial unit vector was $\mathbf{r} = (\cos(\theta), \sin(\theta), 0)$, while the circumferential unit vector was $\mathbf{c} = (-\sin(\theta), \cos(\theta), 0)$. Finally the unit vector defining the longitudinal direction was simply $\mathbf{l} = (0, 0, 1)$, which coincides with the *z*-axis due to the way the ellipsoidal meshes are generated. Denoting the deformation gradient tensor in the cylindrical frame by F_{cyl} , the following relation holds

$$F_{cyl} = M^T F M \quad \text{where} \quad (6.1)$$

$$M = \begin{bmatrix} \cos(\theta) & -\sin(\theta) & 0 \\ \sin(\theta) & \cos(\theta) & 0 \\ 0 & 0 & 1 \end{bmatrix}. \quad (6.2)$$

E_{cyl} was computed for each element of the mesh and at each sampling time for a given simulation, as in Section 3.2.2.

Three components of the Lagrangian strain tensor were considered as local metrics. The circumferential strain, E_{cc} , was taken into account as a measure of contraction. Negative values of E_{cc} correspond to contraction, whereas positive values correspond to lengthening of the tissue in the circumferential direction. The circumferential-radial shear strain, E_{cr} , was considered as a measure of the relative twist of sub-endocardial and sub-epicardial layers. Finally, the circumferential-longitudinal shear strain, E_{cl} , was taken as a measure of torsion [21]. Figure 6.1 shows a schematic of the type of deformation that each component of the Lagrangian strain tensor measures with respect to the global cylindrical coordinate system in the ventricle.

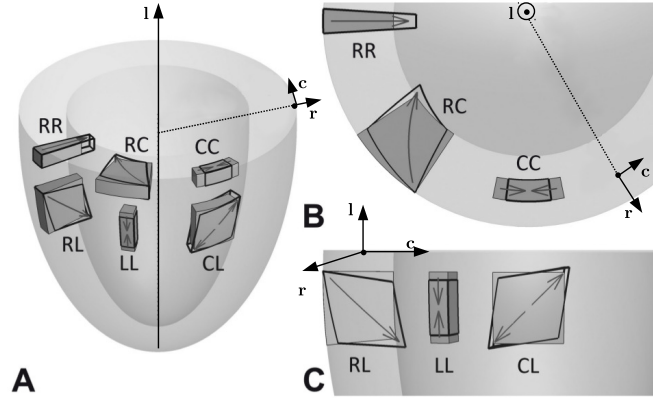


Figure 6.1: Diagram of the type of deformation that each component of the Lagrangian strain tensor measures with respect to the global cylindrical coordinate system in the ventricle. Adapted from [185] under Creative Commons Licence.

6.3 Adding pressure to the electromechanical model

In the electromechanical model pressure is applied to the endocardial surface as a traction time-dependent boundary condition (Section 3.2.2.4). Its sign is negative, meaning that the

pressure is applied along the normal to the surface pointing inwards. This might be confusing, since, for example an increase in pressure during contraction is therefore modelled as a decrease. To avoid confusion variations in pressure will be explicitly described as an increase or decrease in magnitude. Pressure during contraction is explicitly provided as a time-varying pressure trace, not computed -for example - from a circulatory model. The modelling choice made is the simplest approach to the introduction of blood pressure in the electromechanical model. However, as previously described in Section 3.1.4, this choice has the important limitation of not being able to enforce a left ventricular volume trace with a precise separation between isovolumic and non-isovolumic phases. In order to achieve that, volume constraints should be included in the model. At the time this study was performed, it was still an open discussion within the group whether such volume constraints were necessary or whether it was possible to obtain a sufficiently realistic volume trace in response to the sole introduction of an appropriate time-varying pressure boundary condition. Figure 6.3(a) shows the final pressure trace employed and the resulting volume trace. Although the volume trace obtained shows an isovolumic phase followed by contraction of the cavity, this has been obtained at the expenses of the physiological range employed for pressure, as described later on. Therefore, future work will aim at introducing volume constraints in the model.

In this section the two steps applied to add pressure to the model are described. The first step is the passive expansion of the initial mesh from zero pressure to the end-diastolic pressure. The second step describes the pressure trace to be applied during the electromechanical simulation. I will discuss the two steps separately.

6.3.1 Passive expansion under constant pressure

The meshes generated for the study of the previous chapter represent a realistic approximation of the typical dimensions of rat left ventricle at end-diastole, that is the ventricle under end-diastolic pressure. Therefore they cannot be used directly in simulations with pressure boundary conditions, in which the mesh must be defined with respect to zero pressure. Starting from the mechanics mesh $mesh_m$ (Section 4.2), an iterative approach to estimate the shape of a mesh representative of the left ventricle in absence of blood pressure ($pre-P mesh_m$) was applied. The reference $mesh_m$ was shrunk by applying a uniform scaling matrix to give the $pre-P mesh_m$, which was then allowed to expand passively under a constant end-diastolic pressure $P_{ed} = -1 KPa$ to give the $post-P mesh_m$. A linear sweep over the scaling factor was performed until an optimal $pre-P mesh_m$ - producing a

$post-P mesh_m$ close to the reference $mesh_m$ - was obtained. A comparison of mesh details for $mesh_m$, $pre-P mesh_m$ and $post-P mesh_m$ is given in Table 6.1. The final uniform scaling factor was 0.8. This value was chosen as the resulting $post-P mesh_m$ had cavity volume (0.132 cm^3) similar to $mesh_m$ (0.137 cm^3).

An important disadvantage of this iterative process is the loss of control over the ellipticity of the mesh. The process of passive expansion affects the shape of the mechanical mesh making it closer to a prolate spheroid than an ellipsoid. In order to quantify this effect I measured the 2D ellipticity in the basal short-axis plane for the epicardial and endocardial surfaces as the ration between a_x/b_x ($x = endo$ or epi). The closer the ellipticity is to 1, the more the ellipse defined by a_x and b_x in the short-axis plane is close to a circle. As shown in Table 6.1, while the epicardial ellipticity remains similar ($a_{epi}/b_{epi} = 0.8$ for $mesh_m$ versus $a_{epi}/b_{epi} = 0.83$ for $post-P mesh_m$), the endocardial surface becomes significantly more spheroidal ($a_{endo}/b_{endo} = 0.78$ for $mesh_m$ versus $a_{endo}/b_{endo} = 0.87$ for $post-P mesh_m$). I aim to improve the process of determining $pre-P mesh_m$ in the future.

Table 6.1: Summary of mesh properties for the meshes employed in the simulations with pressure. See Figures 4.1(a)-4.1(b) for reference to the ellipsoid parameters; $\langle w \rangle$ is the average wall thickness, $\langle q \rangle$ is the average skewness of the mesh (eqn. (4.1)).

	$mesh_m$	$pre-P mesh_m$	$post-P mesh_m$	$post-P mesh_e$
$a_{epi} \text{ (cm)}$	0.4	0.34	0.40	0.40
$b_{epi} \text{ (cm)}$	0.5	0.48	0.48	0.48
$c_{epi} \text{ (cm)}$	1.0	0.95	0.99	0.99
$a_{endo} \text{ (cm)}$	0.35	0.16	0.26	0.26
$b_{endo} \text{ (cm)}$	0.35	0.27	0.3	0.3
$c_{endo} \text{ (cm)}$	0.85	0.79	0.84	0.84
$\langle w \rangle$	0.16	0.18	0.16	0.16
Cavity vol(cm^3)	0.137	0.07	0.132	0.132
Tissue vol (cm^3)	0.267	0.267	0.267	0.267
$\langle edge \rangle \text{ (cm)}$	$7.18 \cdot 10^{-2}$	$7.2 \cdot 10^{-2}$	$7.1 \cdot 10^{-2}$	$5.78 \cdot 10^{-2}$
$\langle q \rangle$	0.72 ± 0.2	0.69 ± 0.2	0.72 ± 0.2	0.71 ± 0.1
a_{epi}/b_{epi}	0.8	0.59	0.83	0.83
a_{endo}/b_{endo}	0.78	0.71	0.87	0.87

The mesh for the electrical component of the electromechanical problem was obtained by refining the $post-P mesh_m$. The details of this mesh (called $post-P mesh_e$) are given in the last column of Table 6.1. The mesh resolution is lower than the electrical mesh ($mesh_e$) employed in the study without pressure. The average edge length is $\langle edge \rangle = 5.78 \cdot 10^{-2} \text{ cm}$ for $post-P mesh_m$, while it is $\langle edge \rangle = 3.06 \cdot 10^{-2} \text{ cm}$ for $mesh_e$. However, it is still in the

same range as the threshold of $5.0 \cdot 10^{-2} \text{ cm}$ determined in the numerical tests of Section 4.3.3 to produce a conduction velocity in the fibre direction within the experimental range.

Finally, the quality of the meshes generated for the simulations with pressure and evaluated by means of the average skewness $\langle q \rangle$ defined in Section 4.2, is similar to that of $mesh_m$, as shown in Table 6.1.

6.3.2 Time-varying pressure trace

The simulations of this study focus only on contraction, that is approximately the systolic phase. As explained in Section 1.1.1, systole can further be divided into isovolumetric contraction (IVC) and ejection (both rapid and reduced). As shown in Wigger's diagram in Figure 1.2(a), left ventricular pressure has a rather steep rise during IVC and then increases very slowly during ejection. This is the general behaviour that I wanted to capture, both for the pressure trace and the resulting cavity volume trace. My first attempt was to model the pressure trace by means of a piecewise linear function whose steep component matched approximately the time interval of increasing contractile force generation (45-75 ms) in the model. As shown in Figure 6.2(a), the piecewise linear pressure trace (solid line in blue) begins with the constant value of pressure at end diastole, $P_{ed} = -1 \text{ kPa}$, and then between 45 and 75 ms its magnitude increases up to pressure $P_{es} = -5 \text{ kPa}$. While P_{ed} is a physiological value for end diastolic pressure, P_{es} is significantly smaller than the physiological range ($16.7 \pm 0.93 \text{ kPa}$ [31]). Preliminary tests showed in fact that the contraction model was not able to counteract higher end systolic pressures, resulting in a significant expansion rather than contraction of the ventricle. Reduced ranges for pressure have been employed for similar reasons in previous computational modelling literature [114]. However, I am aware that this is an important limitation of the model, and it will be addressed in the future. The piecewise linear pressure trace was useful to ensure that the chosen pressure trace induced the left ventricle to undergo first an isovolumetric contraction and then an ejection phase. However, the two points in which a sudden change occurs ($t = 45 \text{ ms}$ and $t = 75 \text{ ms}$) caused non-physiological 'jumps' in the relative volume trace. In other words, the ventricle would stop contracting, suddenly expand and then go back to contraction again.

A sigmoidal function was then considered as smoother model for the time-varying pressure trace $P(t)$:

$$P(t) = P_{ed} + \frac{P_{es} - P_{ed}}{[1 - Qe^{-B(t-60)}]} , \quad (6.3)$$

where P_{ed} and P_{es} are the lower and upper asymptotes, respectively. Q and B are free parameters governing the shape of the sigmoid, while 60 (ms) is such that maximal growth will occur around the middle point of the interval $45\text{--}75\text{ ms}$ (for the range of Q and B considered). I then varied B and Q , running each time a full contraction electromechanical simulation with the Sn1R70 fibre model and transverse isotropy. All the other simulation details are given in Table 5.3 with exception of the pressure boundary condition, that in this case is given by the pressure trace of eqn. (6.3). For each simulation, the resulting volume trace was monitored to ensure it had a certain amount of isovolumetric contraction before ejection took place. Three values of $B = 0.1, 0.3, 0.5$ were tested. For each of them, the values of $Q = 0.1, 0.5, 1, 2, 5, 10$ were considered in order to have a general understanding of how the volume trace varied in response to the pressure trace. This initial choice of parameters values and range was the result of a trial-and-error process aimed at finding a group of sigmoidal traces around the piecewise linear pressure trace. This first test allowed to identify $B = 0.1$ and the interval $Q = 2\text{--}5$ as the more promising. Figure 6.2(a) shows the pressure traces for $B = 0.1$ and all the values of Q , while Figure 6.2(b) provides the corresponding volume traces.

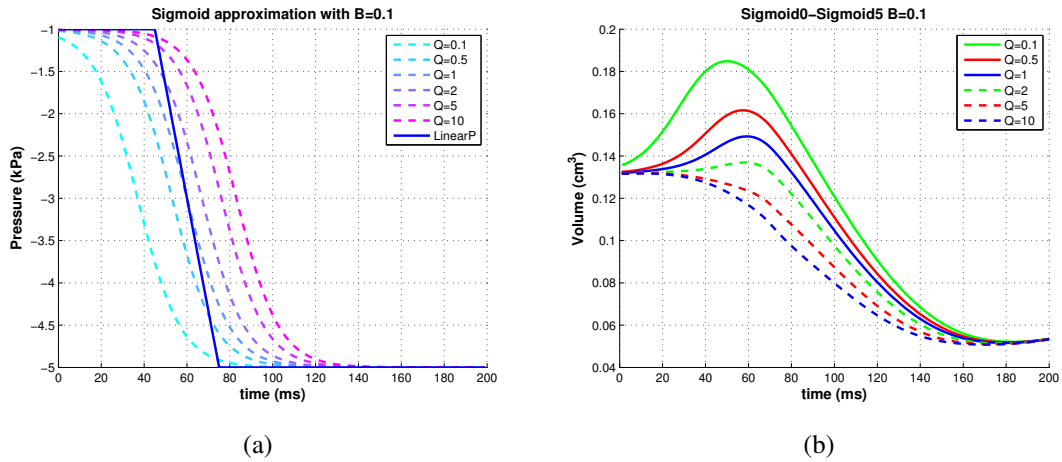


Figure 6.2: (a) Different pressure traces generated with $B = 0.1$ and varying values of Q (see eqn. (6.3)). The pressure trace in solid blue line is the piecewise linear function initially employed to test the effect of pressure on cavity volume. (b) Cavity volume traces corresponding to the sigmoidal pressure traces of figure (a).

This set of simulations revealed that full contraction was achieved around 170 ms , not 130 ms as in the simulations without pressure. This is likely to be due to the slightly different meshes involved and, most importantly, to the pressure boundary condition. For this reason, before continuing with the test and the simulation study I returned to the K2003

contraction model (Section 4.4.1) and further reduced the scaling of the temporal parameters b , t_r , t_d from $2/3$ to $1/2$ (see Section 4.4.1). With the new parameters for K2003, full contraction took place around 150 ms , closer to the previous contraction duration.

After changing the contraction model from K2003 with $2/3$ scaling, to K2003 with $1/2$ scaling, the test to determine the parameters for the pressure trace (eqn. (6.3)) needed to be repeated because the volume traces obtained in response to the pressure traces had changed. A further refinement of the interval 2-5 for Q showed that the best volume trace was obtained for $Q = 3$. The final pressure trace (blue line) for parameters $B = 0.1$, $Q = 3$ is shown in Figure 6.3(a) together with the corresponding volume trace (red line). Figure 6.3(b) shows the typical change in cavity volume in 3D between beginning and end contraction (in this case the simulation is with Karadag fibres and transverse isotropy).

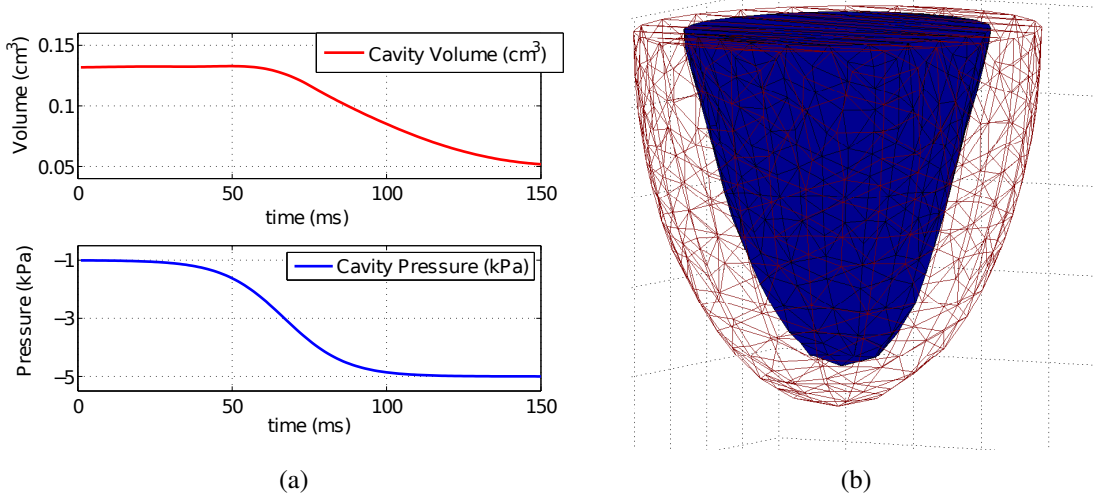


Figure 6.3: (a) Chosen sigmoid function for pressure trace (bottom panel) and resulting volume trace (top panel). (b) Left ventricular cavity at beginning (red wireframe mesh) and end of contraction (blue solid mesh) for the simulation with Karadag fibres and transverse isotropy.

6.4 Effect of tissue structure on left ventricular contraction

In this section the results of the computational study carried out using the electromechanical model with pressure boundary condition are presented. The study can be divided into two parts. The first part aims at comparing the effect of the 16 globally defined fibre models $\text{Sn}x\text{R}y$ for $x = 0.5, 1, 2, 3$ and $y = 50, 60, 70, 80$ (defined in Section 4.5.2) on left ventricular contraction with the impact of the subject-specific model by Karadag et al. [71] (Section 4.5.3). The second part of the study aims at evaluating the effect of introducing sheets by

first comparing transverse isotropic and orthotropic material behaviour, then under the orthotropic behaviour, by comparing a linear and a bimodal model of sheet angle transmural variation (Section 4.5.4). The general simulation details are shown in Table 6.2.

Table 6.2: Details of the simulation set-up for the simulations of Section 6.4

geometry	ellipsoid
electrics mesh	$post-P mesh_e$ (Table 6.1)
mechanics mesh	$pre-P mesh_m$ (Table 6.1)
AP model	Wang2008 (Section 4.3.1)
electrophysiological parameters	Table 4.2
contraction model	K2003 with 1/2 scaling of b , t_r , t_d (Section 4.4.1)
constitutive law	t_{iso} or $ortho^U$ with $C_b = 200 \text{ kPa}$
fibre models	all 16 global fibre models and Karadag (Section 4.5)
sheet model	linear versus bimodal (Section 4.5)
simulation duration	150 ms
stimulation site	lower apical region defined by $z \leq 0.94 \text{ cm}$
fixed nodes	base nodes fixed in z direction (Section 5.3.1)
pressure boundary condition	sigmoidal trace (Section 6.3.2)

6.4.1 Results for global metrics

The global measures EF , WT , and SL were computed for each simulation as described in Section 5.2. The variation in EF due to the different fibre models is shown in Figure 6.4(a), with the transversely isotropic material law. EF is plotted versus R , and the global fibre models $SnxRy$ are grouped according to the exponent n in order to highlight the pattern of EF with increasing values of R for each value of the exponent $n = 0.5, 1, 2, 3$. The single value of EF for the Karadag fibres is represented as an horizontal line, as it is the result of only one simulation. The predicted EF is overall in the range 50%-60%, which it was shown, for example, by Wise et al. [181] to be physiological, although it is still lower than the measured value $EF_{cine} = 77\%$. The discrepancy between the physiological range for EF found in Wise et al. [181] and the value measured on cine-MRI (which is in line, for example, with the measurements of Daire et al. [36]) might be due to differences in the method to measure EF but also in the range of ages of the animals considered. Wise et al. [181], for example, average over a wider range of animals going from young to ageing rats, whose EF tends to be lower than in younger subjects. However, given the values found in the literature, I consider a result of $EF > 50$ as already being in a physiological range. Among the global fibre models, for $n = 1, 2, 3$ increasing values of the angle R and decreasing values of the exponent n raise the value of EF . The reverse holds for $n = 0.5$, for which the increase in the maximum angle R causes a rapid decrease of the EF . The

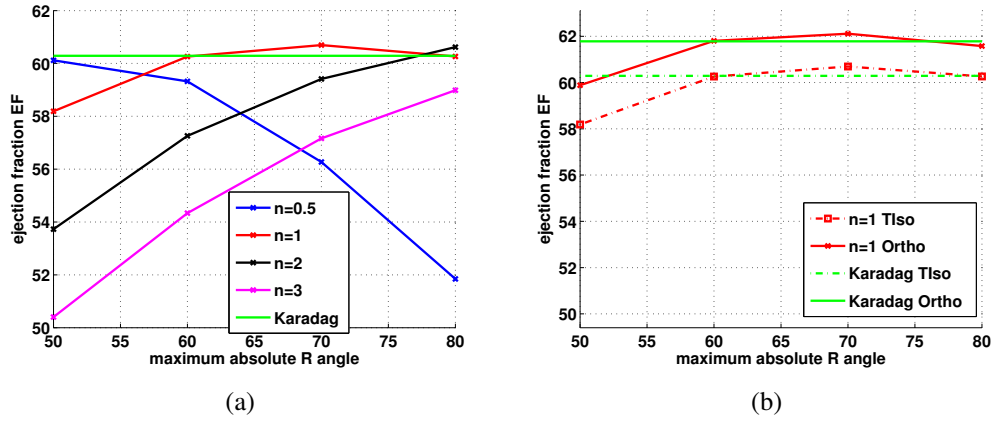


Figure 6.4: (a) EF for all fibre models, with transversely isotropic material law. (b) EF values obtained with t_{iso} and $ortho^U$ with linear sheet model for fibre models with exponent $n = 1$.

subject-specific Karadag model gives one of the highest values of EF together with the global models Sn1R70 and Sn2R80.

Changing from the transversely isotropic to the orthotropic material law (with the linear sheet model) has the general effect of increasing the EF value for all the fibre models, with an average increase of 2.7 pp (percentage points), resulting in EF values in the range 53%-63%, still below the measured value. Figure 6.4(b) shows the comparison of EF between transversely isotropic and orthotropic material laws with a linear sheet model for the simulations with global fibres with $n = 1$ and Karadag fibres. Similar results are obtained for the other values of n . Within the orthotropic case, the effect of using a linear or a bimodal sheet model has the interesting effect of producing predictions much closer to those obtained under transverse isotropy than to orthotropy with the linear sheet model, but in general with a less consistent pattern across the fibre models (and therefore this is not shown).

Figure 6.5(a) represents the wall thickening WT vs R , with the transversely isotropic material law. For the global fibre models, the same trend as with EF is observed: WT increases for increasing values of R and decreasing values of n . Karadag fibres still produce one of the highest values of WT , but some global fibres models also give good results. The use of the orthotropic material law with the linear sheet model further increases the value of WT for every fibre model, as shown in Figure 6.5(b), with an average increase of 4.3 pp . The effect of varying the sheet model from linear to bimodal again produces values closer to the transversely isotropic case. Overall, the range of variability for WT is 16%-37%, with only some fibre models giving values close to the physiological range. Despite the

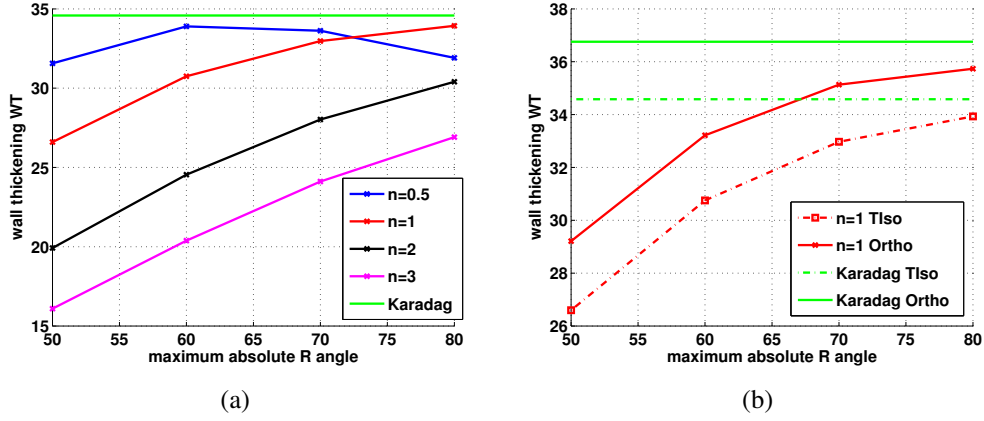


Figure 6.5: (a) WT for all fibre models, with transversely isotropic material law. (b) WT values obtained with t_{iso} and $ortho^U$ with linear sheet model for fibre models with exponent $n = 1$.

modifications presented in this chapter, there is a clear discrepancy between the predicted WT values and that measured on cine-MRI, $WT_{cine} = 54\%$.

The shortening in the base-to-apex direction (negative values of SL) is also substantially affected by the fibre type and material law, ranging from -15% to $+10\%$. Figure 6.6(a) shows SL vs R , with the transversely isotropic material law. Within the global fibre models $SnxRy$, high values of the exponent n combined with low values of R produce lengthening (positive values of SL), whereas there is increasing shortening for low values of n and increasing values of R . In particular, some global fibre models match or exceed the measured shortening $SL_{cine} = -10\%$. Karadag fibres produce a shortening value smaller than the measured one. The effect of changing from transversely isotropic to orthotropic material law (with the linear sheet model) is shown in Figure 6.6(b). The orthotropic material law increases the shortening by $3.5 pp$ on average. By changing the sheet model to bimodal approximately $1 pp$ less shortening was obtained.

6.4.2 Results for local metrics

For each simulation Ecc , Ecr and Ecl were computed for each element of the mechanical mesh and then uniformly averaged over the volume of the basal (upper 35% of the left ventricle), midventricular (middle 35%) and apical regions (lower 30%) (see Figure 4.1(a) for a representation of this subdivision of the left ventricle). Only the average strain in the midventricular region is shown, as it is a good measure of the average behaviour of the left ventricle and the other regions show similar trends. Figure 6.7(a) shows the Ecc trace for the subset of global fibres models with $n = 1$ and for the Karadag model in the

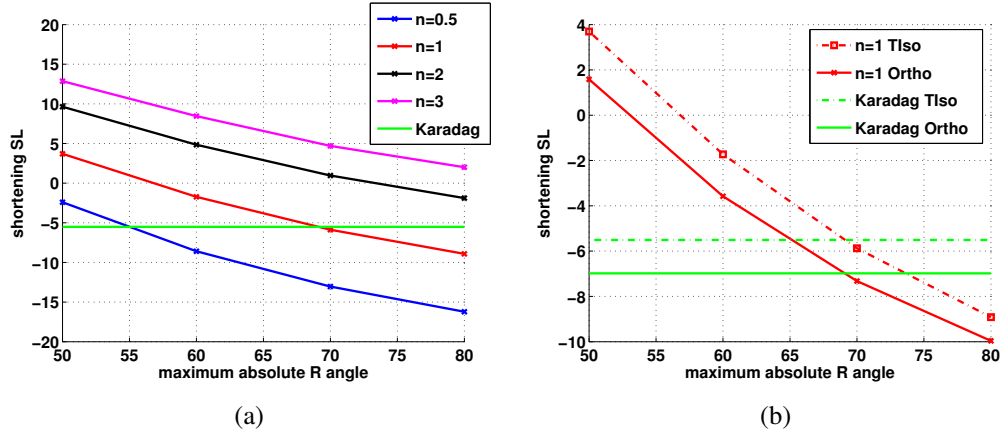


Figure 6.6: a) SL for all fibre models, with transversely isotropic material law. (b) SL values obtained with t_{iso} and $ortho^U$ with linear sheet model for fibre models with exponent $n = 1$.

case of transverse isotropy. The Karadag model has an intermediate behaviour between the fibre models Sn1R70 and Sn1R80, as already found for the global measures. Amongst the global fibre models, the magnitude of the strain decreases for increasing values of the angle R . All traces start from a positive value of E_{cc} rather than zero. This is due to the passive expansion performed prior to the electromechanical simulation, which leaves a residual strain component in E_{cc} .

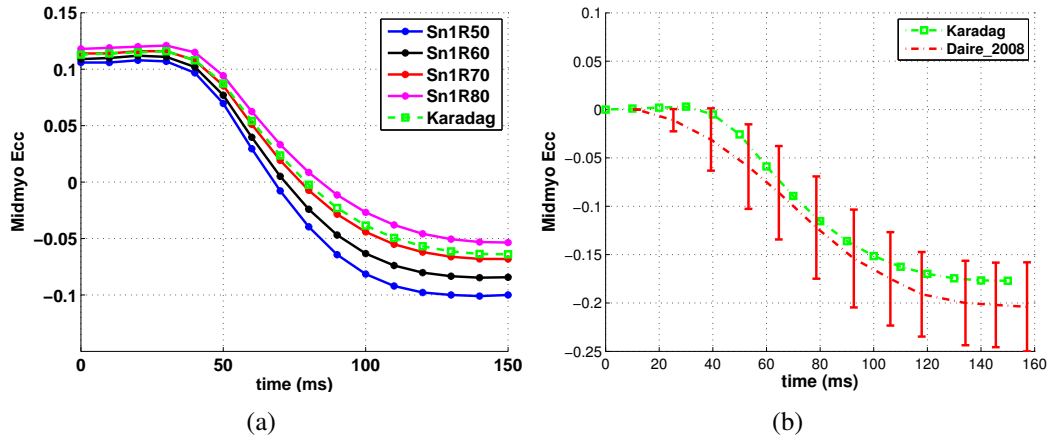


Figure 6.7: (a) Average midventricular E_{cc} for global fibre models (with $n = 1$) and the Karadag model. (b) Comparison of predicted E_{cc} for the simulation with the Karadag fibre model and transverse isotropy and measured E_{cc} in rat [36].

In order to compare to experimental results on E_{cc} in rat, the study by Daire et al. [36] was considered. In their study, Daire et al. imaged five healthy Sprague-Dawley rats with both cine-MRI and tagged MRI sequences. The measurements of E_{cc} were obtained from the tagged MRI dataset at fixed percentages of the cardiac cycle, therefore it was necessary to convert this temporal subdivision into a sequence of time points in the range 0-150 ms (that

is the simulation duration). The data (mean and standard deviation) for the first 50% of the cardiac cycle, which were assumed to correspond approximately to the simulation duration, are shown in red in Figure 6.7(b). The green line is the E_{cc} trace for the simulation with the Karadag fibre model and transverse isotropy, after subtraction of the residual strain from the pre-simulation passive expansion. Apart from the inevitable inaccuracy of the conversion from cardiac cycle percentages to the simulation time interval, there is very good agreement between predicted and measured E_{cc} .

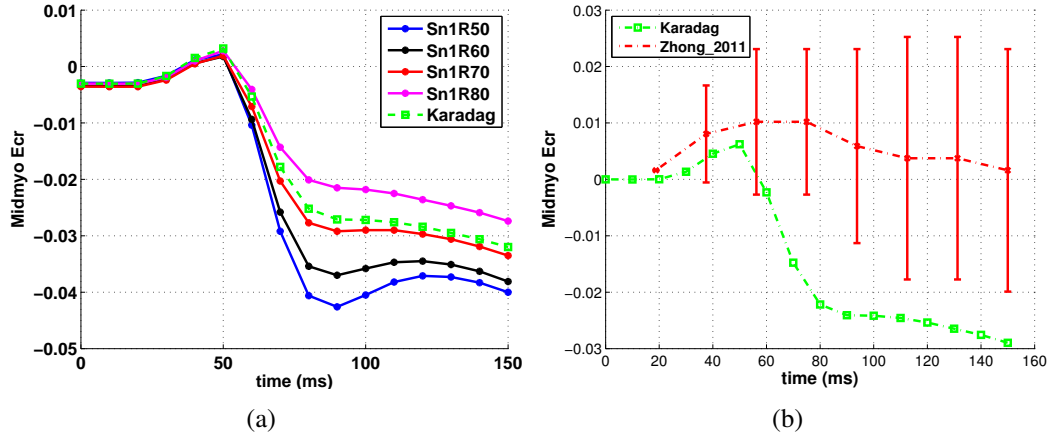


Figure 6.8: (a) Average E_{cr} for global fibre models (with $n = 1$) and the Karadag model. (b) Comparison of predicted E_{cr} for the simulation with the Karadag fibre model and transverse isotropy and measured E_{cr} in mouse [185].

Figures 6.8(a) and 6.9(a) show the E_{cr} and E_{cl} midventricular traces for the subset of global fibres models with $n = 1$ and for the Karadag model in the case of transverse isotropy. With regards to E_{cr} , Karadag shows an intermediate behaviour with respect to the other fibre models, for which the magnitude of the strain decreases for increasing values of the angle R .

To the best of my knowledge, experimental results for Lagrangian shear strains measured in rats are not available in the literature. Mice and rats, although they are both classified as small animal models, differ significantly in body and heart mass (about one order of magnitude), as well as typical timings of the cardiac cycle. However, the difference, for example, in circumferential strain measurements is less remarkable [88]. Therefore, I decided to use measures performed in mouse by Zhong et al. [185], at least for a qualitative comparison. Zhong et al. employed a displacement-encoded 3D cine-MRI technique (DENSE cine-MRI) on 7 mice. As with the E_{cc} , it was necessary to convert from percentages of cardiac cycle to time points in the range 0-150 ms. Figures 6.8(b) and 6.9(b) show the comparison between data (mean and standard deviation, shown in red) and predicted E_{cr} and E_{cl} (shown in green), respectively, for the simulation with the Karadag fibre model

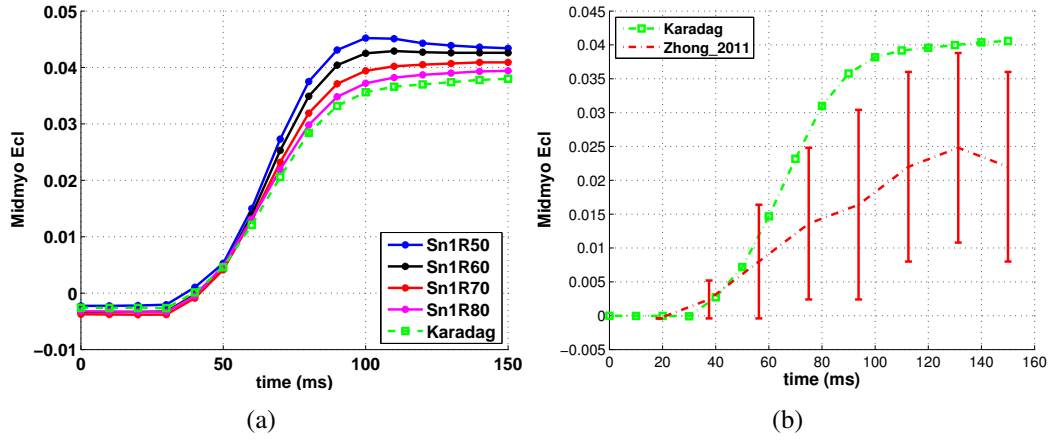


Figure 6.9: (a) Average midventricular E_{cl} for global fibre models (with $n = 1$) and the Karadag model. (b) Comparison of predicted E_{cl} for the simulation with the Karadag fibre model and transverse isotropy and measured E_{cl} in mouse[185].

and transverse isotropy. The agreement for E_{cr} is poorer than for E_{cl} . However, this is only a qualitative comparison, and in both cases the trends are close to the experimental ones.

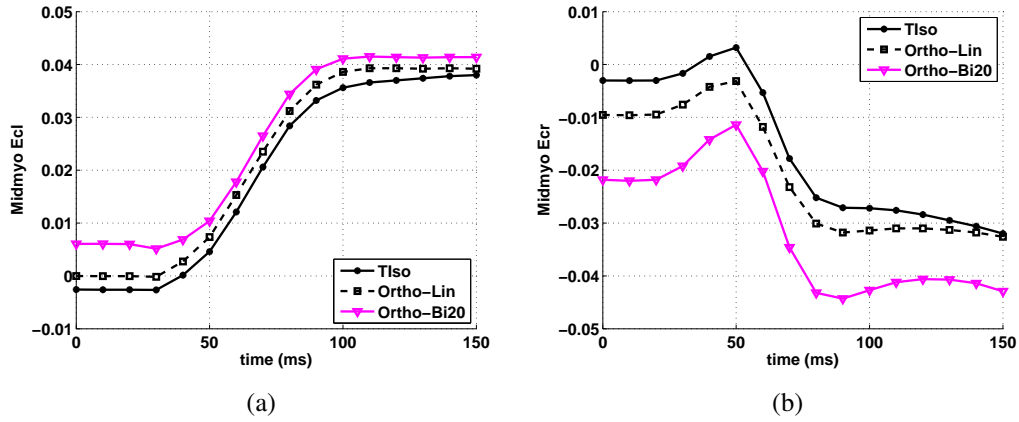


Figure 6.10: Average midventricular (a) E_{cl} and (b) E_{cr} with transverse isotropy, orthotropy with the linear sheet model and orthotropy with bimodal sheet model, in the case of the Karadag fibre model.

The effect of sheets was negligible on E_{cc} , while it was substantial on the shear strains. Changing from transverse isotropy to orthotropy, and within the orthotropic behaviour, from a linear to a bimodal model for the sheets, caused a consistent increase in the magnitude of E_{cr} and E_{cl} , as shown in Figures 6.10(a) and 6.10(b), respectively, for the Karadag fibre model in the midventricular region.

6.5 Discussion and concluding remarks

In this Section the results are discussed of the second computational study of the effect of tissue microstructure on contraction. As described in Section 6.4.1, the global measures are consistently affected by the fibre model and the material law, while they show smaller variation when changing the sheet model. Regarding the fibre models, the subject-specific fibre model does not produce values of the global measures that are notably closer to the measured values than those obtained using the best global fibre models. In particular, among the fibre models, those with low exponent n and high torsion angle R (such as Sn1R70 and Sn1R80) produce values of the global metrics that are comparable or better than those of the subject-specific model. These results are encouraging in that they suggest that, in the case of the Streeter-like fibre models (see eqn. (4.9)), the exponent $n = 1$ describes fibres in rat left ventricle better than other values, in accordance with previous comparisons of rule-based versus DT-MRI-derived fibres in rat [16]. The results presented for the global metrics are in good agreement with the trends found with the computational study of Chapter 5. The major difference between the simulations without and with pressure is the range of values obtained. Especially in the case of EF and WT , the simulations without pressure were not able to produce results in the physiological range. The addition of pressure to the model, although with a significantly smaller end-systolic pressure than the physiological range, improves significantly the ability the model to replicate global metrics. Overall, changing from transversely isotropic to orthotropic material properties (with the linear sheet model) increases the predicted values of the three metrics, but this is not enough to match the measured values for EF and WT . Within the orthotropic setting, no significant effect was seen on SL , while for EF and WT the bimodal model case gave results intermediate between those for transverse isotropy and orthotropy with the linear sheet model.

The Lagrangian strains E_{cc} , E_{cl} and E_{cr} are used as local measures. In general, the results show strain traces and magnitudes close to those reported in the literature for rat and mouse, as shown in Section 6.4.2. The Karadag subject-specific model has strain traces close to those of global fibre models with lower exponent n and higher angle R . In particular the models Sn1R70 and Sn1R80 are those that give similar results to the Karadag model in terms of strains. This is in line with the findings on the analysis of the global metrics. Interestingly, the fibre models that produce higher magnitude of strains (that is higher n and lower R) are the same that gave poorest results in terms of the global metrics. Conversely, this implies that fibre models such as Karadag, Sn1R70 and Sn1R80 are able to convert smaller strains into more efficient cardiac function. The possible biological conclusion is

that the model supports the expectation that microstructure is designed for cardiac function maximal efficiency, for example higher EF in combination with lower levels of strain, as found in the simulations.

Changing from transversely isotropic to orthotropic material properties has a negligible effect on E_{cc} , a small effect on E_{cl} , while a more pronounced change was evident in E_{cr} . In particular, introducing the bimodal model increases the average magnitude of E_{cr} in the midventricular region by more than 30% with respect to both transverse isotropy and orthotropy with the linear sheet model. This is as expected since the effect of introducing orthotropy is more likely to have a larger effect on E_{cr} rather than E_{cc} .

It is important to discuss the limitations of the model, which can be divided into several types: (a) *The use of a simplified geometry.* The natural geometrical variability of the left ventricle is not taken into account in this study, including the lack of a neighbouring contracting chamber (right ventricle), or of papillary muscles whose orientation is predominantly axial. Previous studies suggest this might not bring a significant improvement [48], nonetheless, it would be interesting to investigate whether the conclusions on the subject-specific vs global fibre models hold also in the case of a subject-specific geometry. (b) *The ad-hoc procedure to estimate the pre-pressure mechanical mesh.* The method to estimate the shape of the mesh prior to applying the pressure load has its limitations, as described in Section 6.3.1. (c) *The reduced range of pressures applied in the model.* This is probably the most important limitation of the model as pressure is one of the best characterised physiological parameters of the heart. The importance of introducing pressure in the model, and the limitation due to the maximum contractile force generated by the contraction model (Section 6.3.2), have been discussed already. In the future, further model development will address this limitation. (d) *The lack of the transverse angle in the fibre model definitions.* This angle regulates the level of crossover of fibres that may be important in a correct prediction of shear strains [21]. (d) *Cross-fibre generation of active tension.* Although I decided to exclude this additional component of active tension generation from the model (Section 5.3.3), its contribution has been shown to be important [166] [21] and should require further analysis. (e) *The sheet orientation models.* Two simplified models of sheet transmural variation were tested, both neglecting the great regional variability in terms of sheet patterns that has been found experimentally, and that is thought to give rise to a concertina-like re-arrangement during contraction and relaxation [57]. Overall the impact of sheet inclusion in the study was small, with the exception of changes in E_{cr} . However, this could be due to the high stiffness in the sheet direction imposed by the constitutive law. In general, introducing the more realistic bimodal sheet model did not affect the global

metrics as expected. For example, it did not cause a significant increase in the predicted wall-thickening, while it has been shown that this mechanism is directly related to sheets dynamics [27].

To conclude, an electromechanical model was developed and tested in order to perform a computational study of the impact of tissue microstructure on contraction of the left ventricle in rat. The results showed that the model predicts values of global metrics that are within physiological ranges but, except for SL , they fall below the values measured on cine-MRI scans. Introducing subject-specific fibre models, as opposed to global fibre models, does not provide a substantial increase in EF and WT values. The analysis of strains also showed that the subject-specific fibre model gave predictions similar to linear global fibre models with higher rotation angle R . Changing from transverse isotropy to orthotropy in the passive behaviour, therefore introducing the effect of tissue anisotropy due to the sheets, improves the predictions of EF and WT , but they still remain lower than the measured values. This means that including the sheet orientation in the model is an important factor, and a more detailed representation of angular reorientation of sheet material may be required. Therefore, I believe that, within the current modelling framework, (a) the subject-specific approach in fibre definition by itself is not able to compensate for the model limitations that are believed to come from the underestimation of sheet dynamics; (b) further investigation of the dynamics of sheet orientation should be carried out and novel approaches developed in order to fully represent its effect on cardiac mechanics.

In this chapter the results of the second computational study have been presented. The study was performed with the electromechanical model described in Chapter 4 with the addition of a time-varying pressure boundary condition. A general discussion of the results of the studies of this chapter and the previous chapter has also been given. The next chapter represents a change of focus. The image analysis study carried out on two-state DT-MRI scans of Langendorff-perfused rat hearts will be described. The aim of the study was to investigate the change in tissue structure distribution occurring between different mechanical states of the left ventricle to then validate those predicted by the simulations of this chapter.

Chapter 7

Measuring tissue structure distribution on two-state DT-MRI

In the preceding two chapters the computational study of the effect of tissue structure, in particular different tissue structure models, on left ventricular contraction has been presented. In this chapter the picture is complemented by taking a different perspective, focussing on how tissue structure distribution changes during contraction. First, results of the image analysis study carried out on one rat from the two-state DT-MRI dataset *dataset₂* (described in Section 2.4) are presented with the aim of determining the variation in angular metrics (Section 2.3.2) between slack and contracted phases for the left ventricle. Then, the comparison of measured and predicted variation in angular metrics for a subset of the simulations of the previous chapter is shown. This comparison can be considered as a microstructure-based validation of the electromechanical model and contributes to the analysis of the model's strength and limitations.

7.1 Introduction

The importance of tissue structure for cardiac function has been already discussed in Section 1.1.2 and its role in cardiac modelling has been addressed in Section 3.1.6. The limitations currently faced by experimentalists in assessing tissue structure distribution and its rearrangement in vivo and at the whole heart level have been commented on in Sections 2.2.5 and 2.2.6. In those sections, the two-state DT-MRI of Langendorff-perfused hearts developed by Hales et al. [57] has been introduced. Their experimental protocol has allowed tissue structure distribution of the whole-heart to be measured at two different mechanical states (relaxed and contracted). The imaging study described in this chapter is based on analysis of the scans of one rat heart from the two-state DT-MRI dataset (*dataset₂*, details in Section 2.4) acquired in the research group of Dr Jurgen E Schneider, Department of

Cardiovascular Medicine (University of Oxford), where the work of Hales et al. [57] was carried out.

The main aim of this chapter was to develop a validation framework, based on microstructural information, for the simulations carried out and described in Chapter 6. However, this raised methodological questions about the most appropriate way to measure angular metrics on DT-MRI data. In particular, this study advocates the use of a local reference frame method, as opposed to the commonly employed global reference frame approach, for the quantification of tissue structure distribution in DT-MRI images. Hence, the study can be divided into two parts. The first is related to the development and application of a new approach to the measurement of tissue structure distribution in DT-MRI images. The second is a preliminary validation of a subset of simulations from Chapter 6. In the remainder of this introductory section the methodological and the validation parts are addressed sequentially.

Part A: measuring angular metrics on DT-MRI. A standard approach to the quantification of tissue structure distribution in the heart is based on the use of the angular metrics introduced in Section 2.3.2. A common way to measure these angles on DT-MRI scans is to employ a global cylindrical coordinate system, such as the one described in Section 2.3.1 [47], [57], [98]. Conversely, a different approach is commonly employed in histological studies based on a local cylindrical coordinate system [158]. Figure 2.5 showed the difference between these two coordinate systems. While the global reference frame approximates each ventricle with a cylinder, the local one follows the curvature of the ventricular surface adapting to its regional and temporal changes. The curvature of the heart is an important parameter for the description of cardiac shape and a useful index that can be related to cardiac function. For example, in the left ventricle the apical region has a higher curvature than the midventricular or basal regions. Additionally, during the cardiac cycle the curvature of the ventricle changes significantly. Dramatic changes in curvature can also be a consequence of pathology, such as dilated cardiomyopathy [99]. Two hypotheses have been formulated in support of the use of a local reference frame for the measurement of angular metrics in DT-MRI and are reported below.

Hypothesis of the inherently local nature of tissue structure. The first hypothesis underlying this study is that tissue structure is locally determined, hence its distribution varies with parameters such as the curvature of the heart. Therefore, a local coordinate system for the measurement of angular metrics should be more sensitive to regional and inter-subject

variability as opposed to the global coordinate system, allowing for a better characterisation of tissue structure changes in space and time. Figures 7.1(a)-7.1(c) help visualising this hypothesis. Figure 7.1(a) reproduces a drawing from LeGrice et al. [94] showing the histological transmural slices they obtained in order to investigate the transmural distribution of sheets (shown in the drawing as smoothly varying curves within the myocardial wall). Although it has been pointed out previously in this thesis that the description of sheet distribution given by LeGrice et al. [94] has been questioned by more recent experimental findings (Section 3.1.6), it is useful to explain the hypothesis formulated. The fourth histological section from Figure 7.1(a) is magnified in Figure 7.1(b) as an example of the inherently local nature of tissue structure. The lines representing the transmural orientation of sheets change their angle relative to the curvature of the heart wall going from base to apex. Conversely, Figure 7.1(c) is a modification of Figure 7.1(b) showing how an inherently global tissue structure distribution might appear to be. Blocks of sheet lines are repeated from base to apex and are unaffected by the curvature of the heart.

Hypothesis of bulk motion neutralisation. Furthermore, tissue structure distribution in the ventricle changes during the cardiac cycle because of two factors: the overall motion of the ventricle (that in turn changes the orientation of fibres and sheets with respect to a fixed reference frame), and the inner reorganisation of sheets within moving blocks of tissue. The second hypothesis of this study is that the use of the local cylindrical reference frame to measure angular metrics, with its ability to follow the changing curvature of the ventricle, should be able to neutralise the effect of bulk motion, and measure only changes in angular metrics distribution due to inner reorganisation of the microstructural level. Figures 7.1(d)-7.1(e) depict the left ventricle at a slack (Figure 7.1(d)) and contracted (Figure 7.1(e)) phase, highlighting how the global and local coordinate systems at a given point are affected by motion.

Given the two hypotheses presented, the main aim of this study was to develop a method to measure angular metrics on DT-MRI scans based on a local cylindrical coordinate system and to compare the results with those obtained with the standard approach based on the global reference frame. The angular metrics measured with the two reference frames are by definition different, as the angles are measured with respect to different planes (Section 2.3.1), although it is possible to mathematically relate the two measurements (an example is provided in Appendix B, Section B.3.1). The aim of the comparison between angular metrics measured with the two reference frames presented in this chapter is rather to quantify the variability detected by the two methods both between different regions of the ventricle, and at different contraction states.

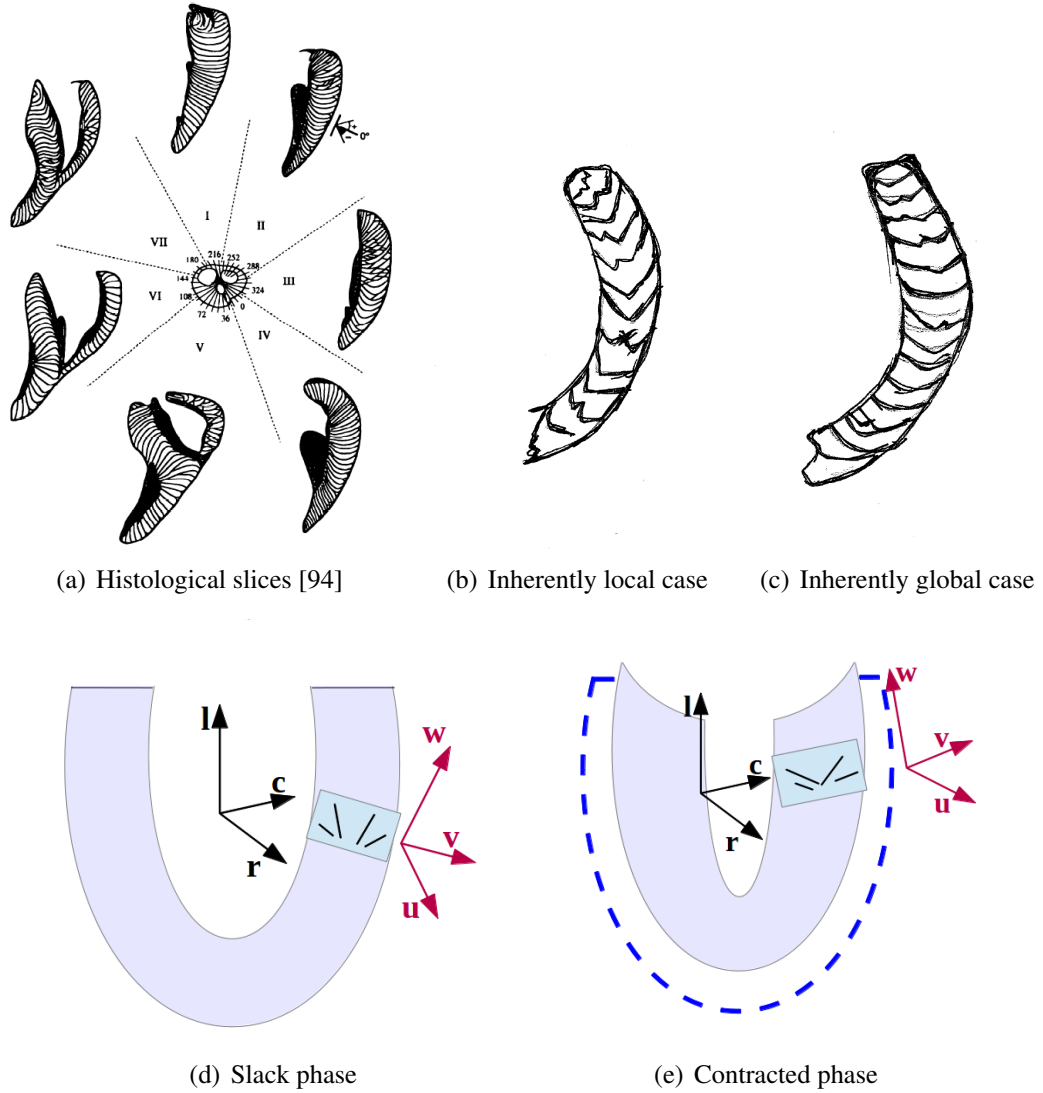


Figure 7.1: (a)-(c) Hypothesis of the inherently local nature of tissue structure. (a) Longitudinal-transmural histological slices of the ventricles showing sheet distribution in the myocardial wall [94]. (b) Sketch of a general longitudinal-transmural histological slice as an example of the local inherent nature of tissue structure. (c) Modification of panel (b) showing how tissue structure would be in the case of an inherently global nature of its distribution. (d)-(e) **Hypothesis of bulk motion neutralisation.** (d) The global (r, c, l) and local (u, v, w) reference frames at a given point in tissue in the slack state of the left ventricle. (e) In the contracted state, the global reference frame will detect variation in tissue structure that is due to both the bulk motion of the ventricle and reorganisation at the microscopic level. On the other hand, the local coordinate system should be able to neutralise the bulk motion effect.

A preliminary study was performed on a phantom dataset, that is a mathematical model of a DT-MRI dataset, with the aim of (a) developing the method based on the local coordinate system and (b) testing the two hypotheses presented under controlled conditions. On the one hand, the results of this preliminary tests show that the method for measuring angles based on the global coordinate system is more robust than the developed method based on

the local reference frame. Future work will address ways to stabilise the latter. On the other hand, the results do not reject the hypothesis that a local reference frame is a more appropriate approach to the measurement of angular metrics. The helix angle distributions measured on phantom with the two reference frames are in good agreement. This means that, regardless of the different definition of the helix angle in the two reference frames, both methods detect similar patterns of regional variation of the helix angle. On the contrary, in the case of sheet and transverse angles, the prescribed distribution is correctly detected in the local reference frame but not in the global one. The aim and results of this preliminary phantom-based study are described in detail in Appendix B.

The global and local methods for measuring angular metrics were then applied to one subject from *dataset*₂. The results obtained with the global coordinate system are in good agreement with those of Hales et al. [57]. The effect of the limitations of the method based on the local reference frame detected in the phantom-based study was enhanced in this case by the use of real images. The local method showed to be highly sensitive to segmentation errors and noise in the data. However, the results are in line with the conclusions of the phantom-based study for the helix and transverse distribution, while the analysis of sheet angle distribution was considered not reliable, as further commented on in Discussion (7.4). The methods and results of the measurement of angular metrics on the rat dataset are described in Section 7.2.

Part B: microstructurally-based validation of electromechanical simulations. The second aim of the study presented in this chapter was to test the agreement between measured and predicted angular metrics distributions for the simulations of Chapter 6. For this purpose, a representative subset of the fibre models was considered and only the global cylindrical coordinate system was employed to measure helix and sheet angle. The predicted changes in angular distributions were compared with the measurements carried out on the rat scan. The results of this comparison show that the predicted trends for the angular metrics are similar to the measured ones. The angular metrics estimation on the simulations and its comparison with experimental results is described in Section 7.3. The results show that the electromechanical model tends to underestimate the extent of variation in tissue structure distribution occurring during contraction. This conclusion is analogous to that of the simulation studies presented in Chapters 5 and 6. Hence, this study has shown that the comparison of simulations results with data on mechanical changes occurring at the microstructural level can be a further method for validating electromechanical simulations. Future work will address the use of the local reference frame measurements for validation.

Finally, discussion and concluding remarks on the entire work presented in this chapter are given in Section 7.4.

7.2 Part A: measuring angular metrics on DT-MRI

In this section the methods and results of the measurement of angular metrics on one rat heart from *dataset*₂ (Section 2.4) are presented. The first aim of this part of the study was to quantify tissue structure distribution in two different mechanical states (slack and contracted) with respect to a global and a local reference frame, in order to assess whether the method based on the local reference frame is more appropriate for the task, in the light of the two hypotheses defined in the Introduction (namely, the hypothesis of the inherently local nature of tissue structure and the hypothesis of bulk motion neutralisation). However, since the ultimate goal was to develop a microstructurally-based validation framework for the simulations presented in this thesis, the focus was only on tissue structure distribution in the left ventricle. A number of original and derived computed 3D images were available for each rat, as described in Section 2.4, some of which were employed to segment the left ventricle, while the others provided the eigenvalues and eigenvectors fields. Figure 7.2 gives a schematic of the structure of one rat dataset and the pipeline for image processing. The various steps of the processing of the images composing the single rat dataset analysed are explained in Methods (Section 7.2.1). For simplicity, from now on the slack and contracted phases for the same rat will be referred to as *Rat_S* and *Rat_C*, respectively.

7.2.1 Methods

The slack (*Rat_S*) and contracted (*Rat_C*) sub-datasets were both segmented in order to isolate the left ventricular geometry. The baseline signal image S_0 was used for segmentation in combination with the *ADC* image, obtained from the provided eigenvalues 3D images L_1 , L_2 and L_3 , as shown in the diagram of Figure 7.2. The segmented image was then used as a binary mask to extract the eigenvectors fields associated to the left ventricular part of the heart. The segmentation process is explained in Section 7.2.1.1. Once the eigenvectors fields for the left ventricles were obtained, their orientation with respect to the global and local cylindrical reference frames were quantified using the angular metrics (helix, transverse and sheet angles). In order to do so, the global and local reference frames needed to be computed for each tissue voxel of the left ventricular binary mask, as explained in Section 7.2.1.2.

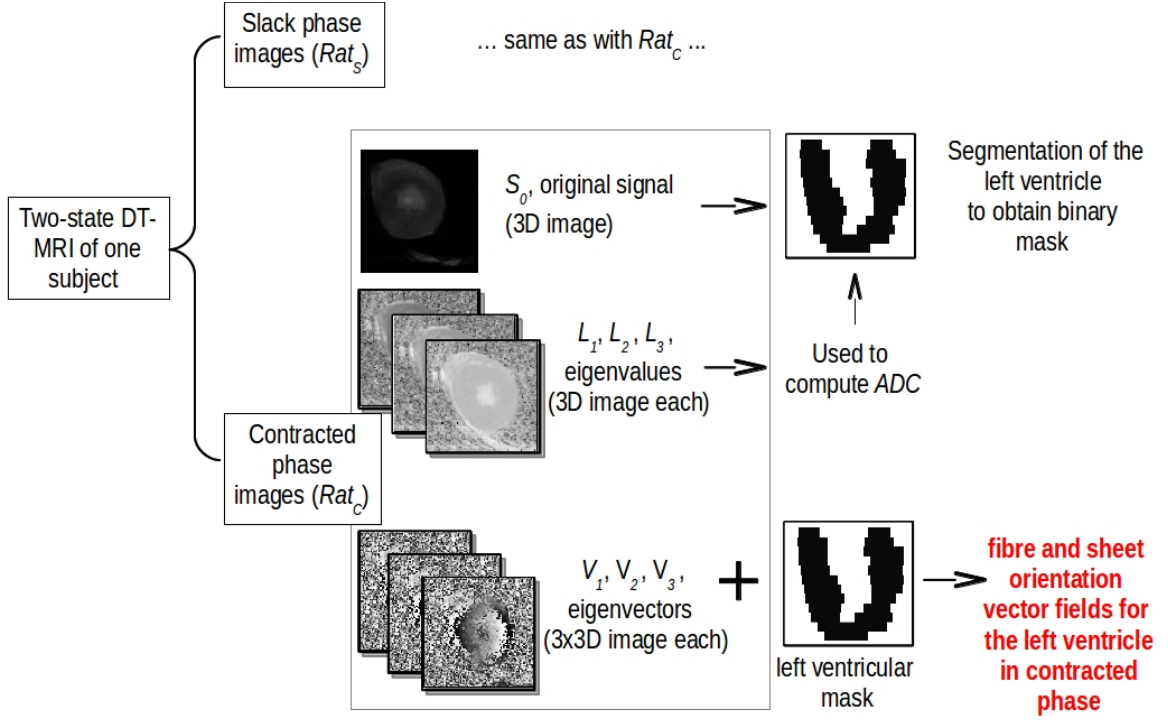


Figure 7.2: Pipeline for image processing of one rat (the subject) two-state DT-MRI dataset. A detailed description of the pipeline is given in Methods (Section 7.2.1).

7.2.1.1 Segmentation of the left ventricle on DT-MRI

In this section the segmentation of Rat_C is described, but the same process was applied to Rat_S as well. Segmentation was performed with `Seg3D` [29], an open-source tool for image analysis. In order to segment the left ventricle, the baseline image S_0 was chosen due to the good level of contrast. For example, a midventricular short-axis view of S_0 is shown in Figure 7.3(a). A first coarse separation amongst image background, cardiac tissue and ventricular cavities was obtained with an Otsu threshold with 3 thresholds [120], as shown in Figure 7.3(b). The outer border of the two ventricles was well separated at this step. In most of the slices the left ventricular cavity was also well delineated. However, when moving more towards the base, the separation between tissue and cavity within the biventricular area was not correctly detected, as shown in the basal short-axis vies of Figure 7.3(c). Therefore, the segmentation of the left ventricular cavity and right ventricle was extended manually, using the ADC (apparent diffusion coefficient) image as a reference. The ADC was calculated from the derived eigenvalues maps $L1$, $L2$ and $L3$ according to eqn. (2.4). The right ventricular cavity was also isolated using ADC , but the separation between left and right ventricle was manually performed, following the curvature of the right ventricular cavity. The corresponding basal short-axis view of the ADC image is

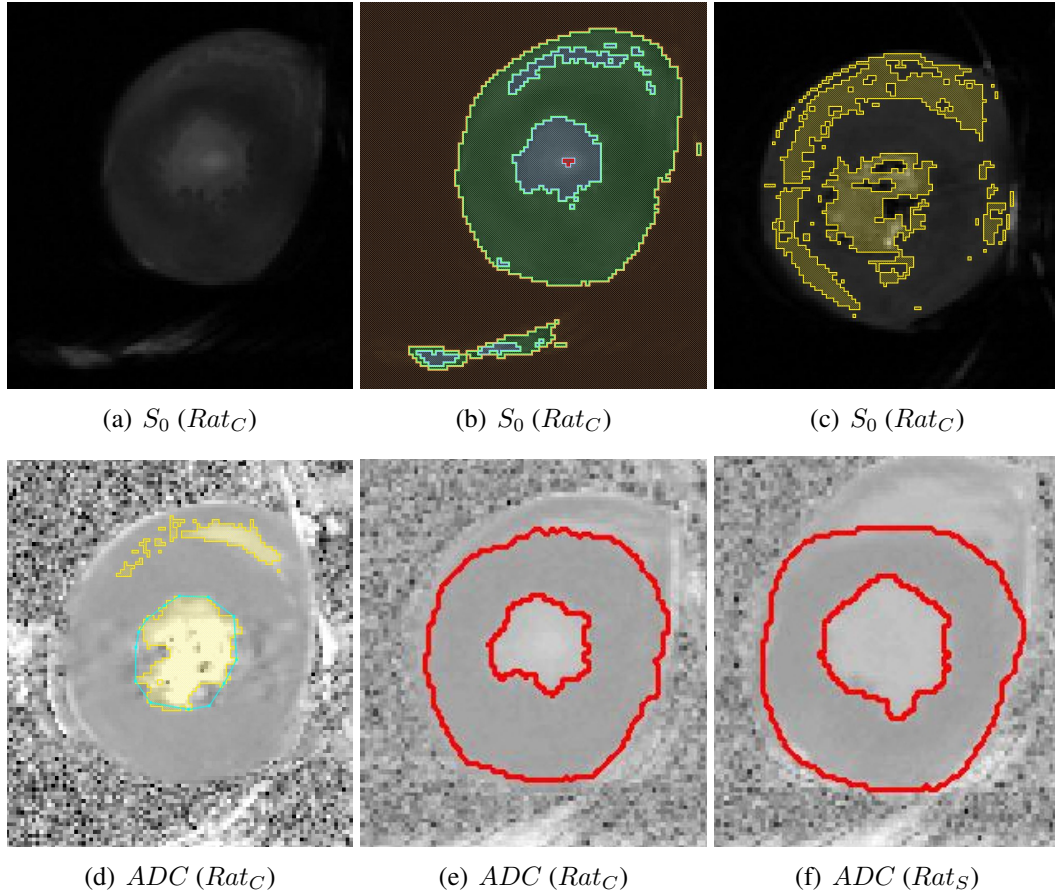


Figure 7.3: (a)-(b) Midventricular short-axis slice of (a) S_0 and (b) the result of multi-thresholding on the same slice for Rat_C . (c)-(d) Basal short-axis view of (c) the multi-thresholding results on S_0 and (d) ADC with the segmented left ventricular cavity delineated in cyan and the blood pools of the two ventricles coloured in yellow. (e)-(f) Midventricular short-axis view of the final segmentation (shown in red) of the left ventricle superimposed on the ADC image for (e) Rat_C and (f) Rat_S .

shown in Figure 7.3(d) where the border of the left ventricular cavity is shown in cyan.

The final segmentation of the left ventricle for Rat_C is shown in Figure 7.3(e). It is obtained by applying to each short-axis slice of the raw segmentation of the left ventricle a 2D dilation and subsequent erosion filter with radius 1 pixel in order to smooth the epicardial and endocardial surfaces obtained. The same protocol was applied to Rat_S , as shown in Figure 7.3(f).

7.2.1.2 Assignment of local and global reference frames to the segmented left ventricle

After the segmentation step, the algorithms to assign the global and local cylindrical coordinate systems were applied to the rat images for both the slack (Rat_S) and contracted (Rat_C) phase. The algorithm for the global reference frame is simply an adaptation of the

one employed by Hales et al. [57]. The development of the algorithm for the local reference frame is another contribution of this thesis. Please refer to Section 2.3.1 for the definition of the two coordinate systems, in particular to Figure 2.5, which provides a schematic showing the difference between the global basis $(\mathbf{r}, \mathbf{c}, \mathbf{l})$ and the local basis $(\mathbf{u}, \mathbf{v}, \mathbf{w})$ at a given point in the ventricle. The two algorithms for the assignment of the global and local reference frames were first developed in the case of the phantom image and are reported in detail in the Appendix B (Section B.2). In what follows, the results of their application to the rat DT-MRI datasets are described. For illustration purposes, all the figures shown in this section refer to the application of the two algorithms on Rat_C . Similar results were obtained for Rat_S .

Global cylindrical coordinate system. The first step in the definition of the global cylindrical coordinate system $(\mathbf{r}, \mathbf{c}, \mathbf{l})$ to each tissue voxel of the segmented left ventricle, consists in identifying the long axis of the ventricle. In the case of real images this is determined by finding the centroids of the binary mask (black and white image of the segmented left ventricle) at each short-axis slice and fitting a line across them, as shown in Figures 7.4(a)-7.4(c). Hence, for each voxel, the longitudinal direction \mathbf{l} is parallel to the ventricular long axis, as shown in Figure 7.4(d). The vector field of \mathbf{l} in the long-axis view is sparse because of the low number of short-axis slices of the DT-MRI datasets. The global radial direction \mathbf{r} is then identified for each voxel as the unit vector along the segment that provides the distance of the voxel from the ventricular long axis. The circumferential (\mathbf{c}) direction at a given voxel is the cross product $\mathbf{c} = \mathbf{l} \times \mathbf{r}$. Figures 7.4(e) and 7.4(f) show the radial and circumferential vectors fields, respectively, for the portion of short-axis slice contained in the grey rectangle of Figure 7.4(a). A detailed description of the method to assign the global reference frame can be found in Section B.2.1.

Local cylindrical system. The algorithm to assign the local coordinate system is based on the computation of the normalised transmural depth $d(x, y, z)$ for each voxel of the image, which is defined in the same way as the normalised transmural depth employed in the previous chapters (see, for example, Section 4.5.2). According to eqn. (4.10), two distance maps need to be computed, one with respect to the endocardial surface and one with respect to the epicardial surface, in order to compute $d(x, y, z)$ on the image. A distance map assigns to each pixel/voxel of an image a numerical label representing the distance of the pixel/voxel from a certain object, in this case either the epicardial or the endocardial surface. For this purpose, the euclidean distance was employed. The result is a 3D distance map of the normalised transmural depth $d(x, y, z)$ of each voxel of the left ventricle,

varying from 0 to 1 from endocardium to epicardium. The preliminary study performed on the phantom image already showed that the smoothness of this map is fundamental to the smoothness of the vectors fields of the unit vectors defining the local reference frame, hence affecting significantly the measurement of the angular metrics (Section B.2). This is particularly true in the case of the real DT-MRI images employed in this study where the distance map computed directly on the original rat datasets Rat_C and Rat_S suffered from the low spatial resolution in the long axis direction. In order to artificially increase the number of short-axis slices and hence the image resolution in the long axis direction, a shape-based interpolation [62] process was applied to the segmentation of the left ventricle in both the slack and contracted state. The algorithm for shape-based interpolation developed by Herman et al. [62] was implemented and the results on the segmentation of Rat_C are shown in Figures 7.4(g)-7.4(h). The distance map was computed on the interpolated geometry (see Figure 7.4(i)) and then sampled at the locations of the short-axis slices of the original image to produce the distance map for Rat_C .

Once the distance map $d(x, y, z)$ for Rat_C was obtained, the algorithm for the assignment of the local cylindrical reference frame was applied. Details can be found in Section B.2.2. First, the local radial direction \mathbf{u} was obtained as the gradient of the distance map for $d(x, y, z)$. The local radial vector field is overall smooth, as shown in Figure 7.4(k). However, there are small regions where groups of vectors deviate together from the average direction. This seems to happen, for example, where there are sharp changes of curvature in the epicardial surface, or a sudden bump. The local circumferential direction \mathbf{v} has a more regular vector field, as shown in Figure 7.4(l), with only a few epicardial and endocardial voxels presenting vectors with an incorrect orientation. Finally, the local longitudinal vector \mathbf{w} follows smoothly the epicardial surface curvature in most of the ventricle, but has a region of inconsistent directions in the apical part, as shown in Figure 7.4(j). Overall, the local coordinate system definition seems to be more sensitive to segmentation errors than the global reference frame. Additionally, it is sensitive to the smoothness of the transmural depth distance map. This will produce angular metrics distributions that are on average more noisy than those obtained with the global reference frame, especially close to endocardium and epicardium and in general in the apical region, as shown in the Results section.

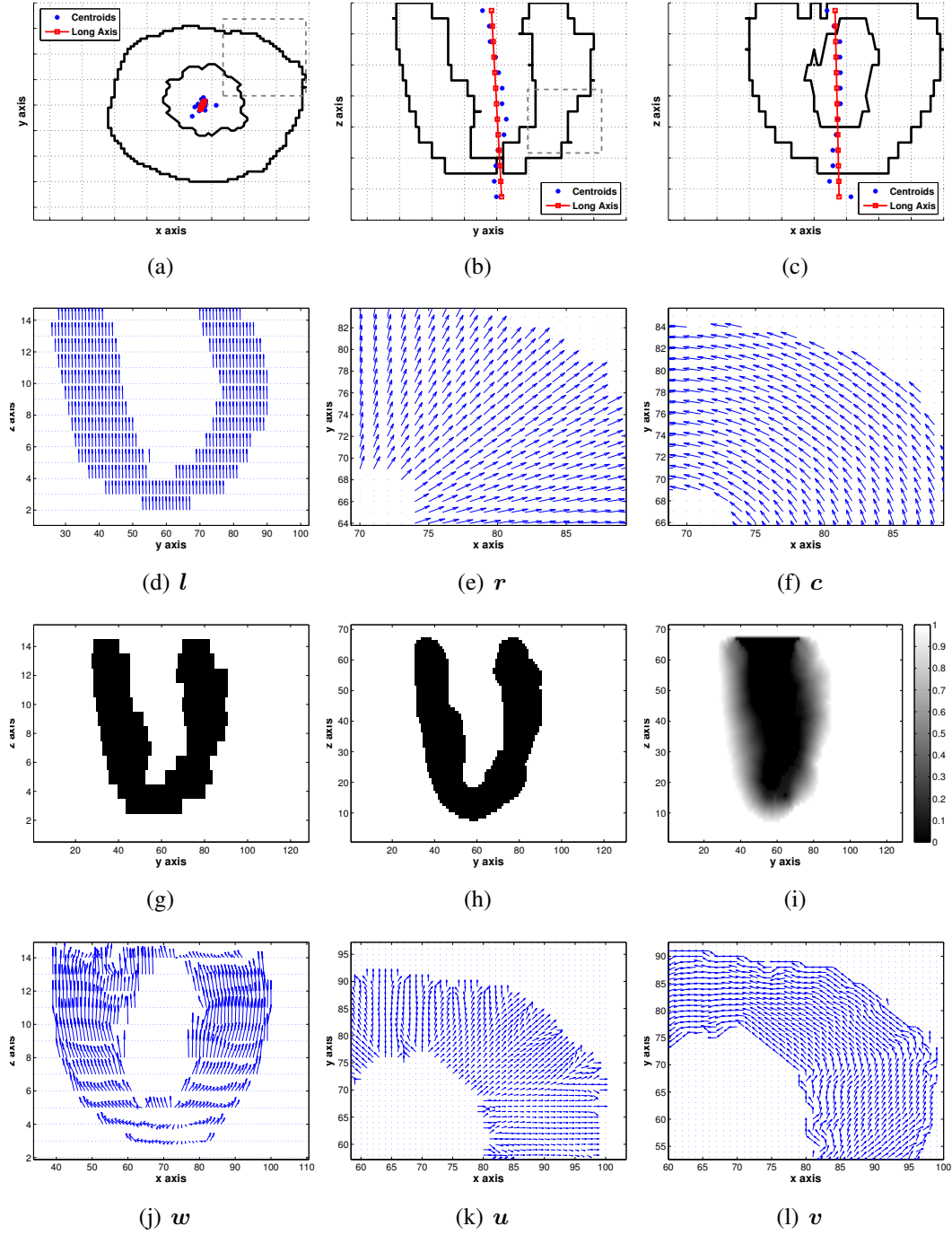


Figure 7.4: (a)-(c) Determination of the long axis of the left ventricle on Rat_C . The fitted long axis is a line (shown in red) fitted across the centroids (blue dots) to each short-axis slice for Rat_C , as shown in a (a) short-axis view, (b) long-axis view in the yz plane and a (c) long-axis view in the xz plane. (d)-(f) Global coordinate system assigned to the tissue voxels of Rat_C . (d) Longitudinal vector field is shown in a long-axis view in the yz plane. (e) Radial and (f) circumferential vector fields are shown for the portion of short-axis slice contained in the grey rectangle in Figure 7.4(a). (g)-(h) Long-axis view of Rat_C segmentation (g) before and (h) after the shape-based interpolation step. (i) Distance map of the transmural depth $d(x, y, z)$ computed on the shape-based interpolated image of Rat_C (shown in (h)). (j)-(l) Local coordinate system assigned to the tissue voxels of Rat_C . (j) Longitudinal vector field is shown in a long-axis view in the xz plane. (k) Radial and (l) circumferential vector fields are shown for the upper left portion of a midventricular short-axis slice.

The methods presented in this section for the assignment of global and local reference frames were developed in order to obtain a protocol for image analysis as image-driven as possible, in order to maintain the results as close as possible to the original images. However, the use of a shape-based interpolation algorithm can already be considered as a deviation from the idea of processing the original images with the least possible modification. Other approaches could have been considered such as the use of parametrised surfaces for the endocardial and epicardial walls. In this way, the distance map $d(x, y, z)$ could have been arbitrarily smooth. On the other hand, this would have significantly reduced the ability of the method to detect inter-regional and inter-subject variability in the geometry of the heart.

7.2.2 Results

In this section the results of the angular metrics measurements on the rat DT-MRI scans at slack and contracted phase are presented for both the global and local cylindrical coordinate system methods. The helix α , transverse γ and sheet β angles are treated separately. In the case of helix and sheet angles, the results are also compared with those of Hales et al. [57]. For visualisation purposes, two short-axis slices were chosen as representative of the basal and equatorial regions of the left ventricle. The basal slice was located at approximately 20% of the base-to-apex length starting from the atrial valve plane, while the location of the equatorial slice was at approximately the 50% along the same line. The results on the apical region were heavily affected by noise in the local coordinate system, therefore were considered not reliable and are not reported here. For each slice, a first qualitative analysis of the results is given by a short-axis view of the angle measured at each tissue voxel in a given slice. Then, a more quantitative analysis is shown with scatter plots of the angle values versus transmural depth. The variation between slack and contracted states is evaluated by comparing linear fits of the scatter plots.

7.2.2.1 Measuring the helix angle

The results for the helix angle are described separately for the basal and equatorial slice.

Helix angle at the basal slice in Rat_S and Rat_C . Figure 7.5 shows a short-axis view of the helix angle measured at the basal slice for both slack (Rat_S) and contracted (Rat_C) states and local and global reference frames. First, the distribution of α going from epicardium to endocardium appears smoother with the global method than with the local one. With the global reference frame, an increase in the thickness of the endocardial ring of high positive values ($\alpha > 30$) is found between the slack (Figure 7.5(a)) and contracted (Figure 7.5(b))

phase. In the case of the local reference frame, a similar observation can be made but, overall, the distribution of high positive values of α in the endocardial and subendocardial areas is less homogeneous (Figures 7.5(c) and 7.5(d) show the local helix angle distribution for Rat_S and Rat_C , respectively).

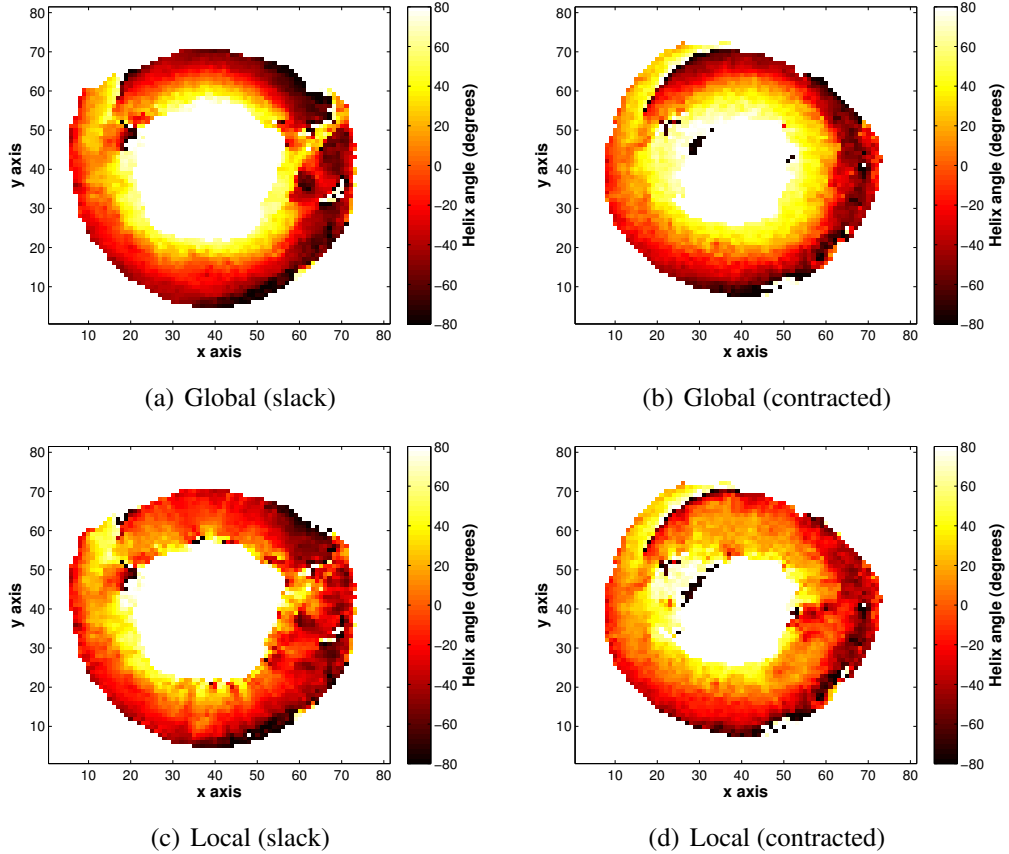


Figure 7.5: Basal short-axis view of helix angle measures. (a)-(b) Basal short-axis slice for the (a) slack (Rat_S) and (b) contracted (Rat_C) states are labelled with the values of helix angle α measured with respect to the global coordinate system. (c)-(d) The same basal short-axis slice for (c) Rat_S and (d) Rat_C show α measurements with respect to the local coordinate system.

Figure 7.6 shows the scatter plots of α versus transmural depth $d(x, y, z)$ and relative linear fit for the basal slice in Rat_C and Rat_S for both global and local reference frames. The choice of the linear fit is driven by the need to compare in a simple way the overall shift in the values of the angles between relaxation and contraction. In some cases, in fact, a higher degree polynomial, would have been a better fitting curve. The scatter plots of Figure 7.6 again show that the measurements in the global reference frame are less sensitive to noise than those in the local frame. The distribution of scatter points is less dispersed in the case of the global reference frame than in the case of the local coordinate system. Furthermore, the global approach detects on average a wider range of values from

endocardium to epicardium than the local approach. The linear fit shows that, for the global approach, the range changes from approximately $[-50 \ 40]$ to $[-40 \ 60]$ (Figure 7.6(c)), while for the local method the variation is approximately $[-40 \ 30]$ to $[-30 \ 40]$ (Figure 7.6(f)). This is different from what found in the preliminary tests performed on phantom, where the two reference frames would detect similar helix angle transmural distributions and ranges (Section B.3), suggesting that the two frames were actually measuring the same angle. Therefore, the difference in range between global and local methods on the rat image might be due to the fact that the local coordinate system vector fields are more sensitive to segmentation irregularities at epicardium and endocardium. However, the two methods detect the same type of shift in the range of angles between slack and contracted phase.

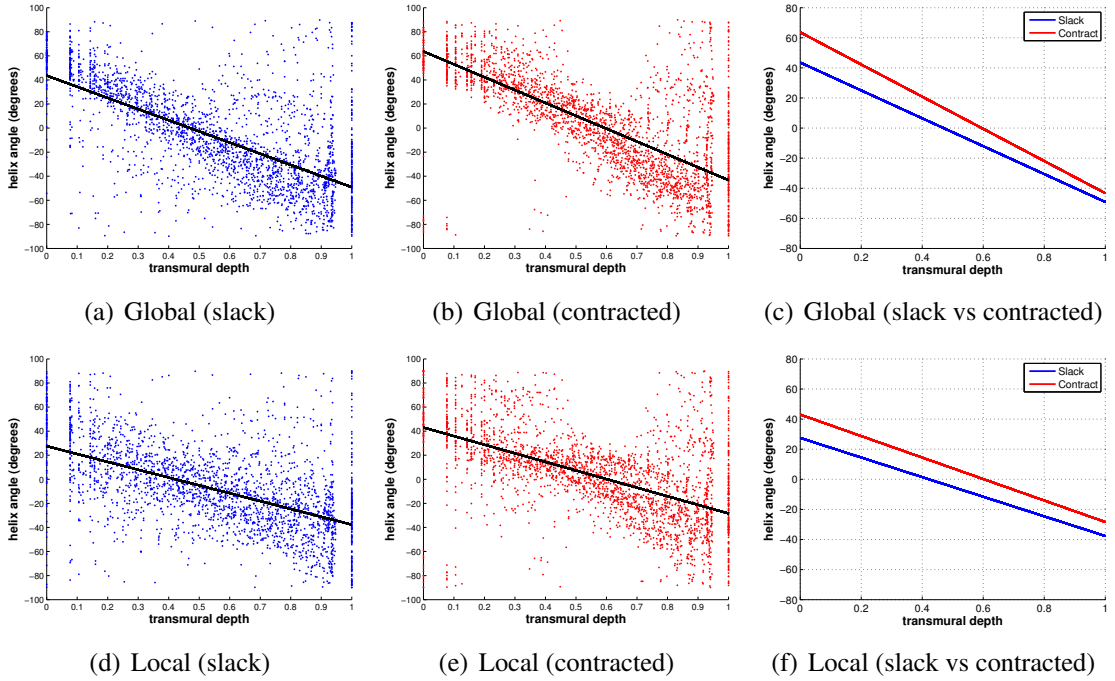


Figure 7.6: Scatter plots of helix angle (measured both in the global and local coordinate systems) versus transmural depth for the basal slice of *Rat_S* and *Rat_C*. (a)-(b) α versus transmural depth in the global reference frame for (a) *Rat_S* and (b) *Rat_C*. Linear fit is shown in black. (d)-(e) α versus transmural depth in the local reference frame for (d) *Rat_S* and (e) *Rat_C*. Linear fit is shown in black. (c) Comparison of linear fit of α versus $d(x, y, z)$ in *Rat_S* (blue) and *Rat_C* (red) for the global coordinate system. (f) Same comparison as (c) but for the local coordinate system.

Interestingly, in the global reference frame, α seems to become less linear in the contracted state, perhaps becoming closer to a distribution with the exponent of d becoming smaller than 1 (compare Figure 7.6(a) and 7.6(b) for the slack and contracted states, respectively). A similar change seems to be shown by the scatter plots for the local reference frame (compare Figures 7.6(d) and 7.6(e)), but it is less pronounced. This finding would need to be backed by more than one case. However, if detected in more than one subject, it

might shed a different light, for example, on the rule-base modelling of fibres. In that case, the different transmural variation models of Figure 4.9(a), might refer to the fibre distribution being better modelled by a linear ($n = 1$) or a sub-linear ($n < 1$) exponential rule depending on the mechanical state.

Helix angle at the equatorial slice in Rat_S and Rat_C . Figure 7.7 shows a short-axis view of the helix angle measured at the equatorial slice for both slack (Rat_S) and contracted (Rat_C) states and local and global reference frames. The segmentation of Rat_C includes probably a portion of the papillary muscle, corresponding to the black region ($\alpha < -70$) in the endocardial surface (see Figure 7.7(b) for example). As in the results for the basal slice (Figure 7.5), the distribution of α going from epicardium to endocardium appears smoother with the global method than with the local one. However, in both reference frames, an increase in the thickness of the endocardial ring of high positive values ($\alpha > 30$) is found between Rat_S and Rat_C .

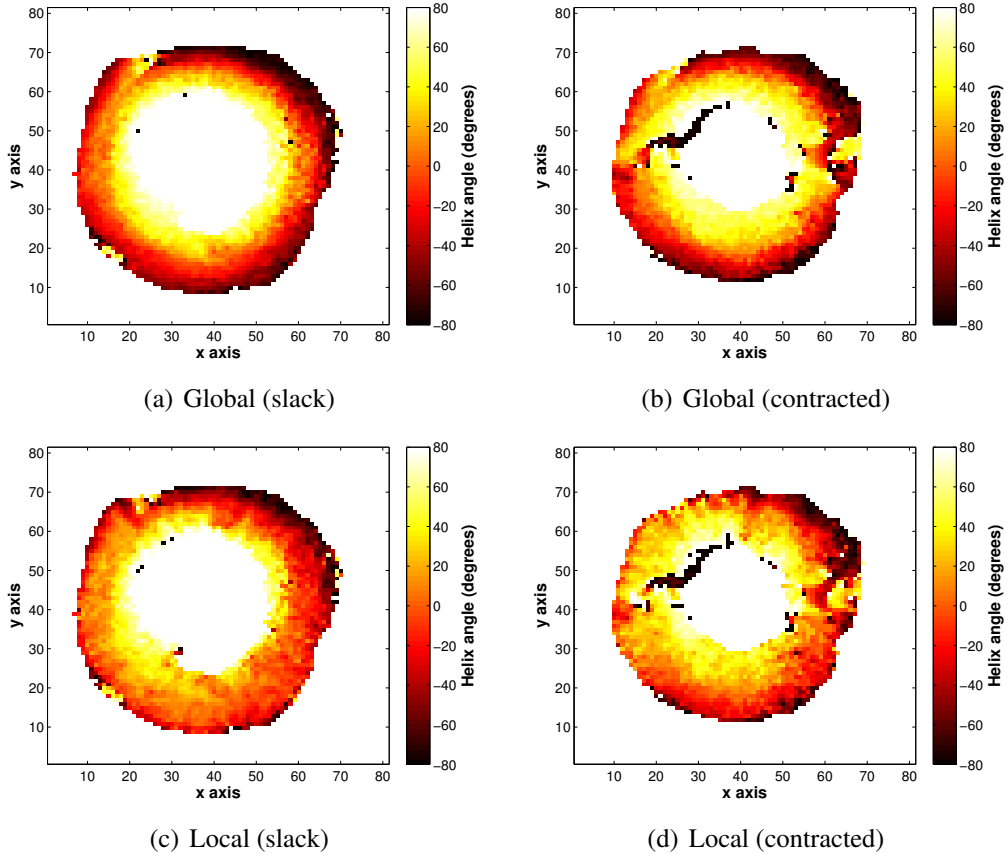


Figure 7.7: Equatorial short-axis view of helix angle measures. (a)-(b) Equatorial short-axis slice for the (a) slack (Rat_S) and (b) contracted (Rat_C) states are labelled with the values of helix angle α measured with respect to the global coordinate system. (c)-(d) The same equatorial short-axis slice for (c) Rat_S and (d) Rat_C show α measurements with respect to the local coordinate system.

Figure 7.8 shows the scatter plots of α versus transmural depth $d(x, y, z)$ and relative linear fit for the equatorial slice in Rat_C and Rat_S for both global and local reference frames. Overall, higher positive angles are detected in the equatorial slices with respect to the basal one, by both the reference frames and in both contraction states. On the other hand, the shift in the range of angles between Rat_C and Rat_S is reversed with respect to the basal slice. In the basal slices (Figures 7.6(c) and 7.6(f)), the increase in helix angle magnitude was bigger at the endocardium than at the epicardium. Conversely, in the equatorial slice, almost no change occurs in the endocardial area, while the gap between helix angle ranges in the slack and contracted states increases going towards the epicardium. Again, the global approach detects on average a wider range of values from endocardium to epicardium than the local approach. The linear fit shows that, for the global approach, the range changes from approximately $[-60 \ 70]$ to $[-40 \ 70]$ (Figure 7.6(c)), while for the local method the variation is approximately $[-40 \ 50]$ to $[-20 \ 50]$ (Figure 7.6(f)). Overall, the two methods are in good agreement for the equatorial slice in the detection of helix angle variation between relaxation and contraction.

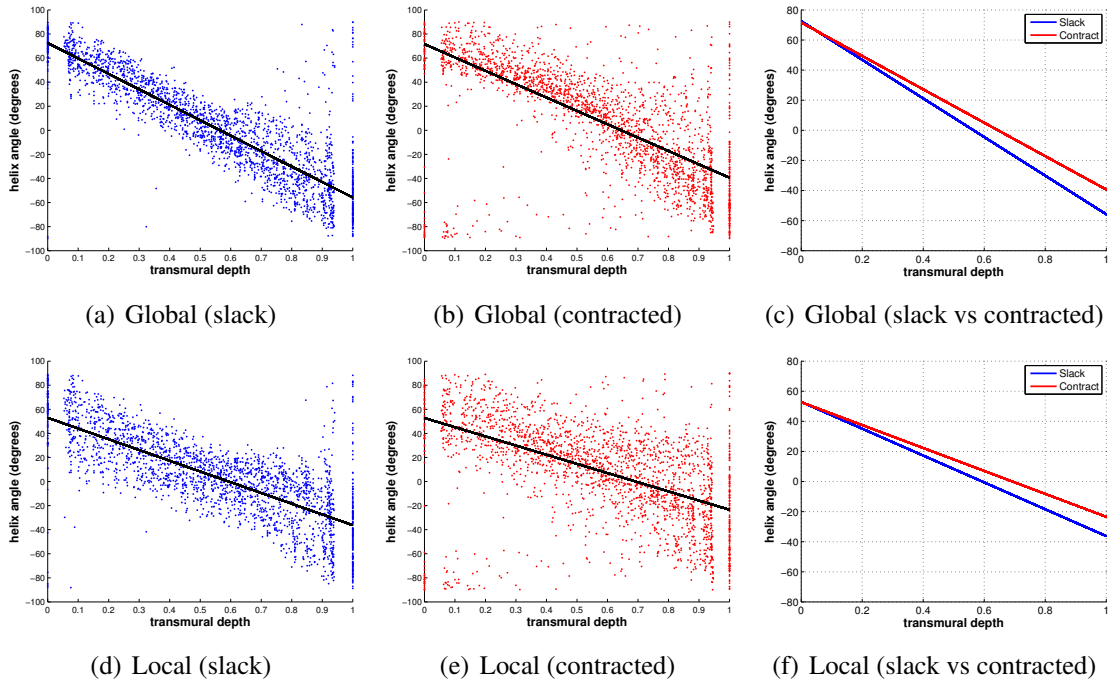


Figure 7.8: Scatter plots of helix angle (measured both in the global and local coordinate systems) versus transmural depth for the equatorial slice of Rat_S and Rat_C . (a)-(b) α versus transmural depth in the global reference frame for (a) Rat_S and (b) Rat_C . Linear fit is shown in black. (d)-(e) α versus transmural depth in the local reference frame for (d) Rat_S and (e) Rat_C . Linear fit is shown in black. (c) Comparison of linear fit of α versus $d(x, y, z)$ in Rat_S (blue) and Rat_C (red) for the global coordinate system. (f) Same comparison as (c) but for the local coordinate system.

Comparison of helix angle measurements with results of Hales et al. [57]. Finally, the

results obtained for the helix angle with both the global and local approach were compared with those published by Hales et al. [57], which were computed with respect to a global reference frame method analogous to the one employed in this study. Local helix angles were also compared with published results under the assumption that the helix angle measured by the global and local reference frame produces similar distributions. This assumption was based on the preliminary tests performed on phantom, and has been shown to be not valid in the case of the transverse and sheet angles (see Appendix B for more details).

According to the paper, the values of α were divided into three groups: left-handed helical fibres (LHF, $\alpha < -30$), circumferential fibres (CF, $-30 \leq \alpha \leq 30$) and right-handed helical fibres (RF, $\alpha > 30$).

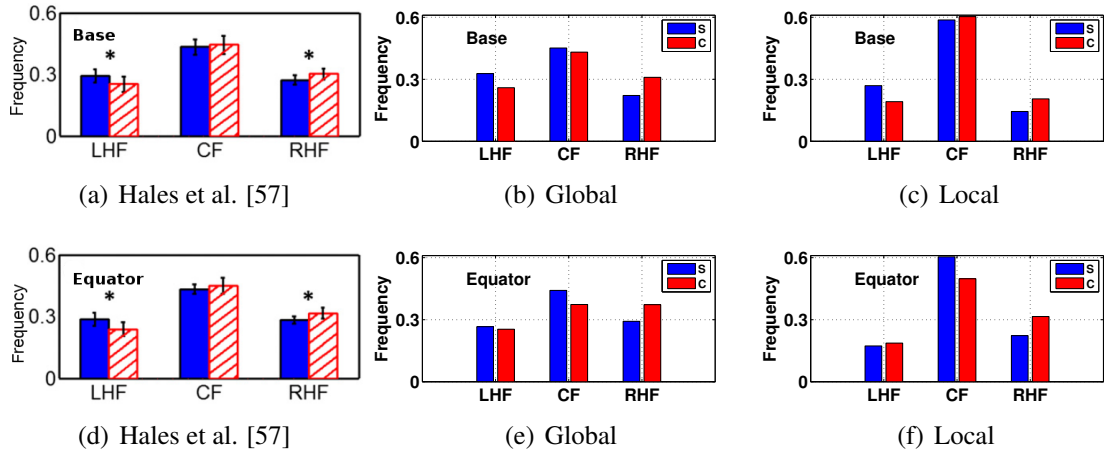


Figure 7.9: Changes in the fibre populations LHF ($\alpha < -30$), CF ($-30 \leq \alpha \leq 30$) and RHF ($\alpha > 30$) (see text for details) in the basal and equatorial regions. The results from Hales et al. [57] for the normalised frequency of these three fibre populations in both ventricles are shown for the (a) basal and (d) equatorial regions. Similarly, the results of the same measures performed on the left ventricle of the rat dataset are shown for the global and local reference frames. In particular, the results for the global reference frame are shown in (b) for the basal slice and in (d) for the equatorial slice. The results for the local reference frame are shown in (c) for the basal slice and in (e) for the equatorial slice. In the legends, “S” and “C” stand for slack and contracted, respectively. Figures from [57] are reproduced under Creative Commons Licence.

Figure 7.9 compares Hales et al. [57] measurements and those obtained on the rat dataset, both for the global and local reference frame. The results of Hales et al. [57] are for the two ventricles and are divided into basal (Figure 7.9(a)) and equatorial (Figure 7.9(d)) regions. They found a statistically significant decrease in the LHF population and increase in RHF when the heart goes from the slack (blue) to the contracted (red) state (shown by the star above the bars). The measurements with respect to the global coordinate system, although they are only for the left ventricle, show a similar behaviour in the basal (Figure 7.9(b)) and equatorial (Figure 7.9(b)) regions. Hales et al. [57] found a non statistically significant

increase in the CF population in the three regions, while the measurements with respect to the global reference frame support the opposite trend. The measurement carried out with respect to the local coordinate system are in agreement for the three populations with those of Hales et al. [57] in the basal slice, while the agreement in the equatorial slice only applies for the increase in RHF between slack and contracted phase.

Overall, there is good agreement between measured helix angle in both the global and local reference frame and the results of Hales et al. [57].

7.2.2.2 Measuring the transverse angle

The results for the transverse angle are described separately for the basal and equatorial slice.

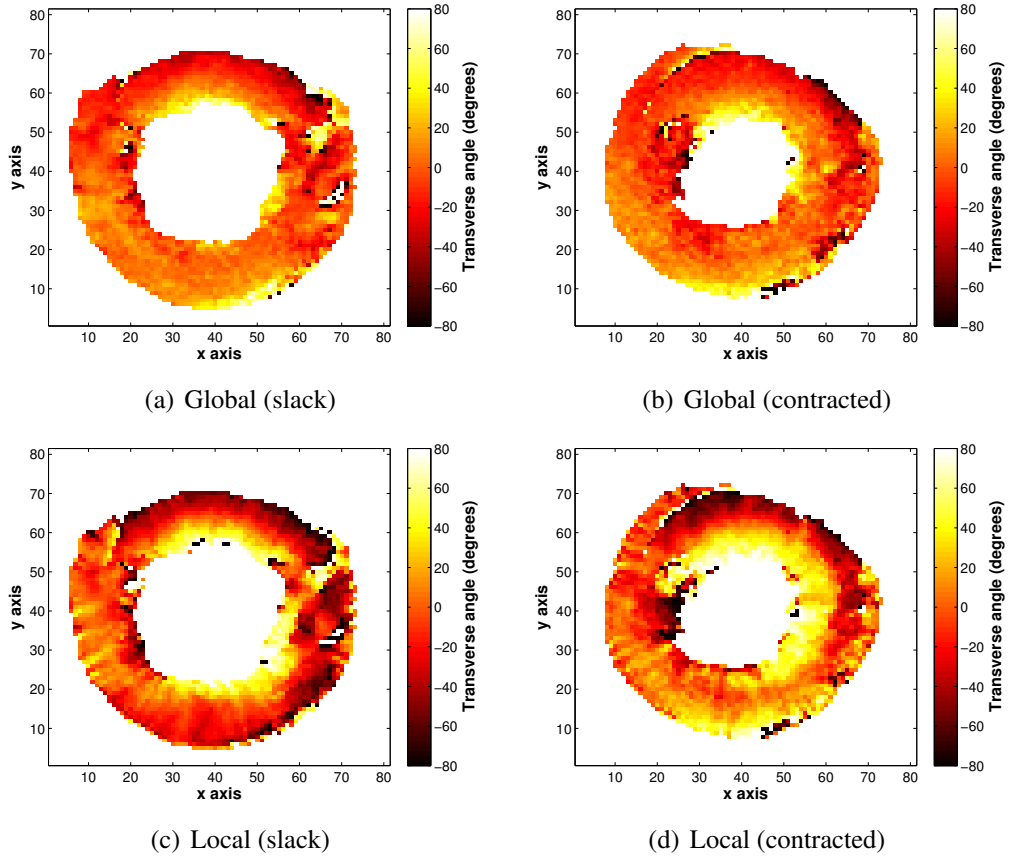


Figure 7.10: Basal short-axis view of transverse angle measures. (a)-(b) Basal short-axis slice for the (a) slack (Rat_S) and (b) contracted (Rat_C) states are labelled with the values of transverse angle γ measured with respect to the global coordinate system. (c)-(d) The same basal short-axis slice for (c) Rat_S and (d) Rat_C show γ measurements with respect to the local coordinate system.

Transverse angle at the basal slice in Rat_S and Rat_C . Figure 7.10 shows a short-axis view of the transverse angle γ measured at the basal slice for both slack (Rat_S) and contracted

(Rat_C) states and local and global reference frames. There is no clear transmural variation of the transverse angle in the global reference frame (see Figures 7.10(a) and 7.10(b) for Rat_S and Rat_C , respectively). Conversely, the local reference frame shows a trend similar to the one for helix angle, going from high negative angles at epicardium to positive angles at endocardium for Rat_S (Figure 7.10(c)). The transmural distribution of Rat_C seems similar to that in Rat_S only in a portion of the short-axis slice, while in the rest of the slice the similarity is less clear (Figure 7.10(d)). In particular, Rat_C seems to show the emergence of a bimodal population of transverse angles in the lower region of the slice. A similar observation can be made as well in the scatter plot for Rat_C (see later on Figure 7.11(e)).

Figure 7.11 shows the scatter plots of γ versus transmural depth $d(x, y, z)$ and relative linear fit for the basal slice in Rat_C and Rat_S for both global and local reference frames. The global reference frames detects a distribution of γ values around $\gamma = 0$ for both Rat_S (Figure 7.11(a)) and Rat_C (Figure 7.11(a)) with points that are more spread at the epicardium and the endocardium. This type of configuration is similar to what measured, for example in human DT-MRI with respect to a global reference frame [98]. There is almost no difference between the linear fit in the two contraction states (Figure 7.11(c)). For the local coordinate system, the scatter plots are in agreement with the qualitative analysis carried out on the basal short-axis slice. The slack phase shows a linear transmural variation of the transverse angle (Figure 7.11(d)) that is then mostly conserved in the contracted state (Figure 7.11(e)). The comparison between the two linear fits shows a shift in the range of angles from approximately $[-40 \ 30]$ to $[-10 \ 40]$ (Figure 7.11(f)). Hence, most of the variation in transverse angle occurs in the midmyocardial/epicardial area.

Furthermore, as mentioned before, the scatter plot for Rat_C suggests the emergence of a bimodal distribution, which was not detected by the global reference frame. This is an interesting point for further investigation. However, as in the case of the linear/sub-linear change in fit according to the change in mechanical state proposed earlier for the helix angle (Section 7.2.2.1), it needs to be detected on more subjects before any conclusion can be drawn.

Transverse angle at the equatorial slice in Rat_S and Rat_C . Figure 7.12 shows a short-axis view of the transverse angle measured at the equatorial slice for both the slack (Rat_S) and the contracted (Rat_C) states and local and global reference frames. As in the basal slice, there is no clear transmural variation of the transverse angle in the global reference frame (see Figures 7.12(a) and 7.12(b) for Rat_S and Rat_C , respectively). Conversely,

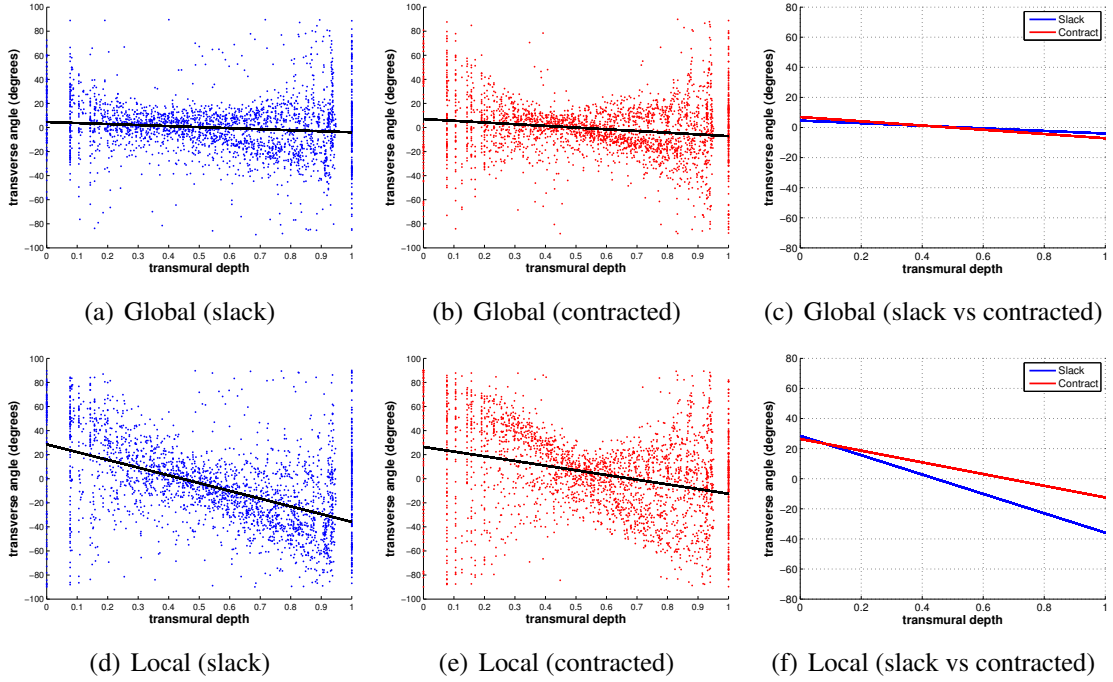


Figure 7.11: Scatter plots of transverse angle (measured both in the global and local coordinate systems) versus transmural depth for the basal slice of Rat_S and Rat_C . (a)-(b) γ versus transmural depth in the global reference frame for (a) Rat_S and (b) Rat_C . Linear fit is shown in black. (d)-(e) γ versus transmural depth in the local reference frame for (d) Rat_S and (e) Rat_C . Linear fit is shown in black. (c) Comparison of linear fit of γ versus $d(x, y, z)$ in Rat_S (blue) and Rat_C (red) for the global coordinate system. (f) Same comparison as (c) but for the local coordinate system.

the local reference frame shows a trend opposite to that found in the basal slice, with γ going from high positive angles at the epicardium to negative angles at the endocardium for Rat_S (Figure 7.12(c)) and Rat_C (Figure 7.12(d)). This difference between basal and equatorial regions detected by the local reference frame seems to support the hypothesis that the local reference frame is able to highlight regional variation in angular metrics that would otherwise go undetected by a global reference frame.

Figure 7.13 shows the scatter plots of γ versus transmural depth $d(x, y, z)$ and relative linear fit for the equatorial slice in Rat_C and Rat_S for both global and local reference frames. The global reference frames detects a distribution of γ values around $\gamma = 0$ for both Rat_S (Figure 7.13(a)) and Rat_C (Figure 7.13(b)) with points that are more spread at the epicardium and the endocardium, as in the case of the basal slice. However, by comparing the linear fits of the basal slice (Figure 7.11(c)) with those of the equatorial slice (Figure 7.13(c)) a slight inversion in the transmural trend between base and equator can be seen, as seen in the short-axis view of the local reference frame results before.

This inversion in the transmural variation of γ between base and equator is evident when

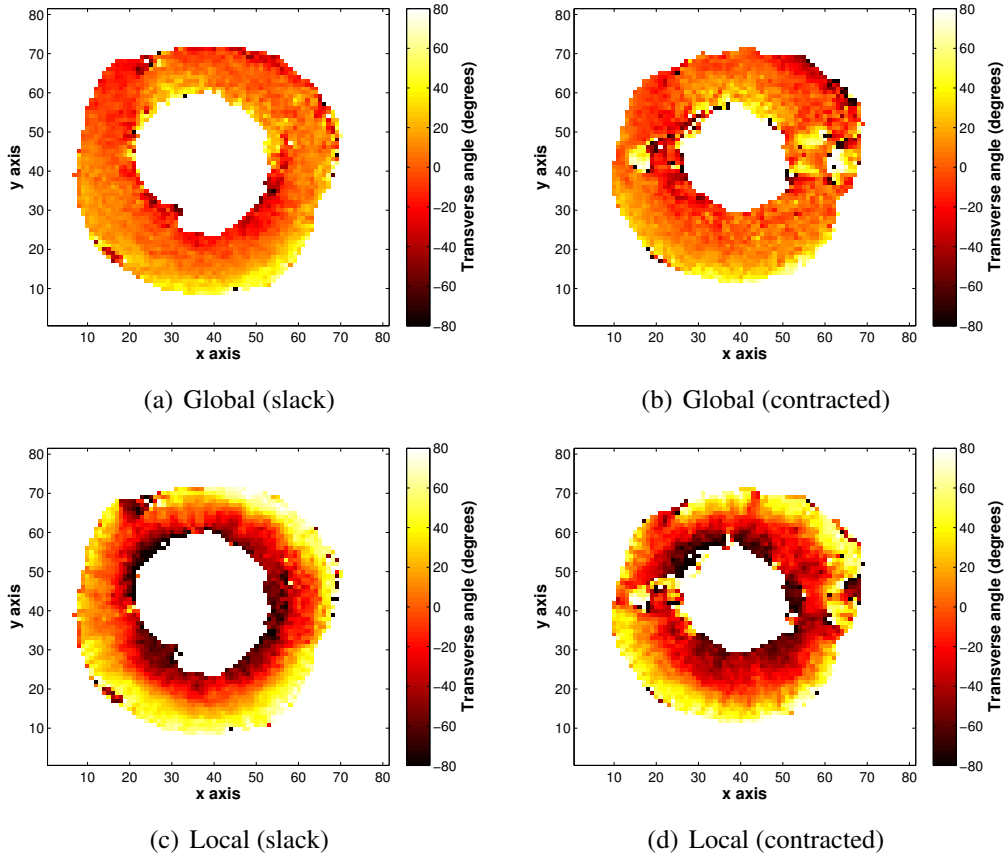


Figure 7.12: Equatorial short-axis view of transverse angle measures. (a)-(b) Equatorial short-axis slice of the (a) slack and (b) contracted states are labelled with the values of transverse angle γ measured with respect to the global coordinate system. (c)-(d) Equatorial short-axis slice of the (c) slack and (d) contracted states are labelled with the values of transverse angle γ measured with respect to the local coordinate system.

comparing the scatter plots for the local reference frame in the basal and equatorial slice. In the equator the transmural range for the linear fit goes from $[-60 \ 50]$ to approximately $[-50 \ 40]$ (Figure 7.13(f)), exactly the opposite of the results in the basal region (Figure 7.11(f)).

Regarding the presence of a bimodal distribution of the transverse angle found in the basal region of Rat_C in the local reference frame, no similar observation was made in the results for the equatorial slice.

The results of the measurements of the transverse angle on the rat dataset show that the global reference frame detects an average $\gamma = 0$ with values more dispersed around the mean in the sub-endocardial and sub-epicardial layers and analogous trends for the basal and equatorial regions. This is in line with previous findings obtained on DT-MRI using a global reference frame approach [98]. A different picture can be drawn by looking at the results from the local reference frame. Although it has been already pointed out that

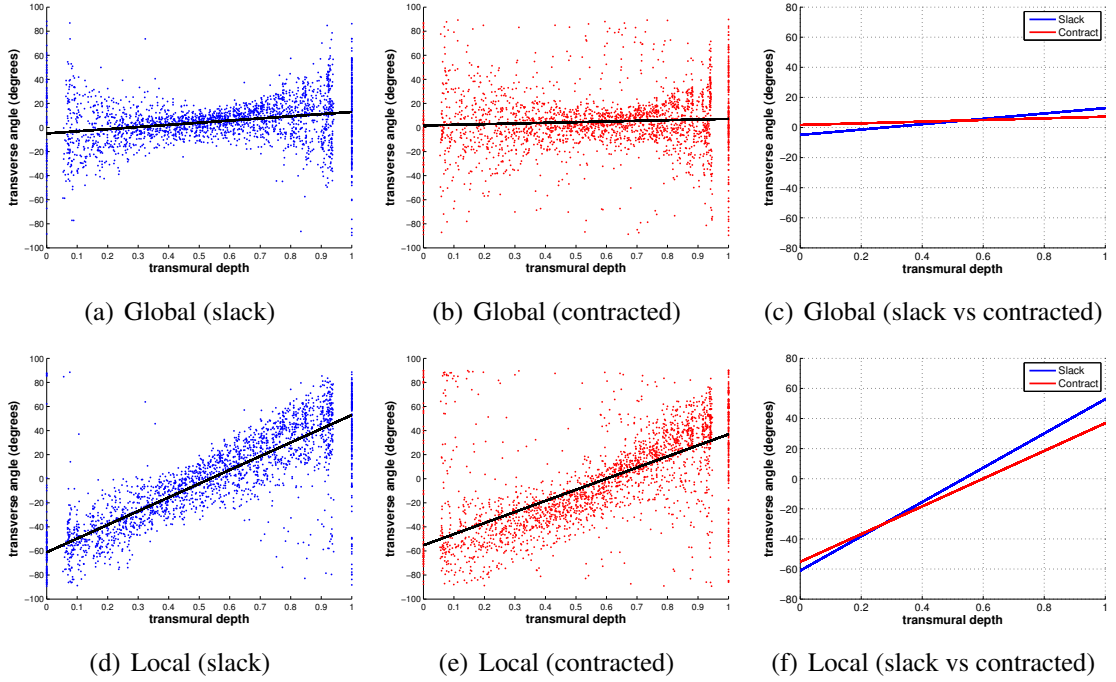


Figure 7.13: Scatter plots of transverse angle (measured both in the global and local coordinate systems) versus transmural depth for the equatorial slice of *Rat_S* and *Rat_C*. (a)-(b) γ versus transmural depth in the global reference frame for (a) *Rat_S* and (b) *Rat_C*. Linear fit is shown in black. (d)-(e) γ versus transmural depth in the local reference frame for (d) *Rat_S* and (e) *Rat_C*. Linear fit is shown in black. (c) Comparison of linear fit of γ versus $d(x, y, z)$ in *Rat_S* (blue) and *Rat_C* (red) for the global coordinate system. (f) Same comparison as (c) but for the local coordinate system.

the range of values of γ computed with the local and global methods cannot be directly compared as they are by definition different, some significant differences between the two methods can be seen. The local reference frame detects an inversion in the transmural distribution of γ when going from the basal to the equatorial region. Furthermore, in the basal region the contracted mechanical state shows the emergence of a bimodal distribution for γ which is not detected in the equatorial region. Given the substantial difference in the distribution of γ between the two regions, it is not clear at this stage what can be concluded about a bimodal distribution of the transverse angle, but this point will be further investigated in the future.

7.2.2.3 Measuring the sheet angle

The results for the sheet angle β are the most difficult to analyse both in the global and local reference frame. Figures 7.14(a)-7.14(b) show the equatorial short-axis view of *Rat_S* for global and local reference frames, respectively. The sheet angle in both reference frames does not seem to have a smooth transmural variation nor it is possible to identify clear regions of sheet angle populations. Similar results are obtained in the other regions.

As for the scatter plots, Figure 7.14(a) shows the transmural variation of β for Rat_S in the global coordinate system, while the analogous plot in the case of the local reference frame is provided in Figure 7.14(d) for the equatorial slice.

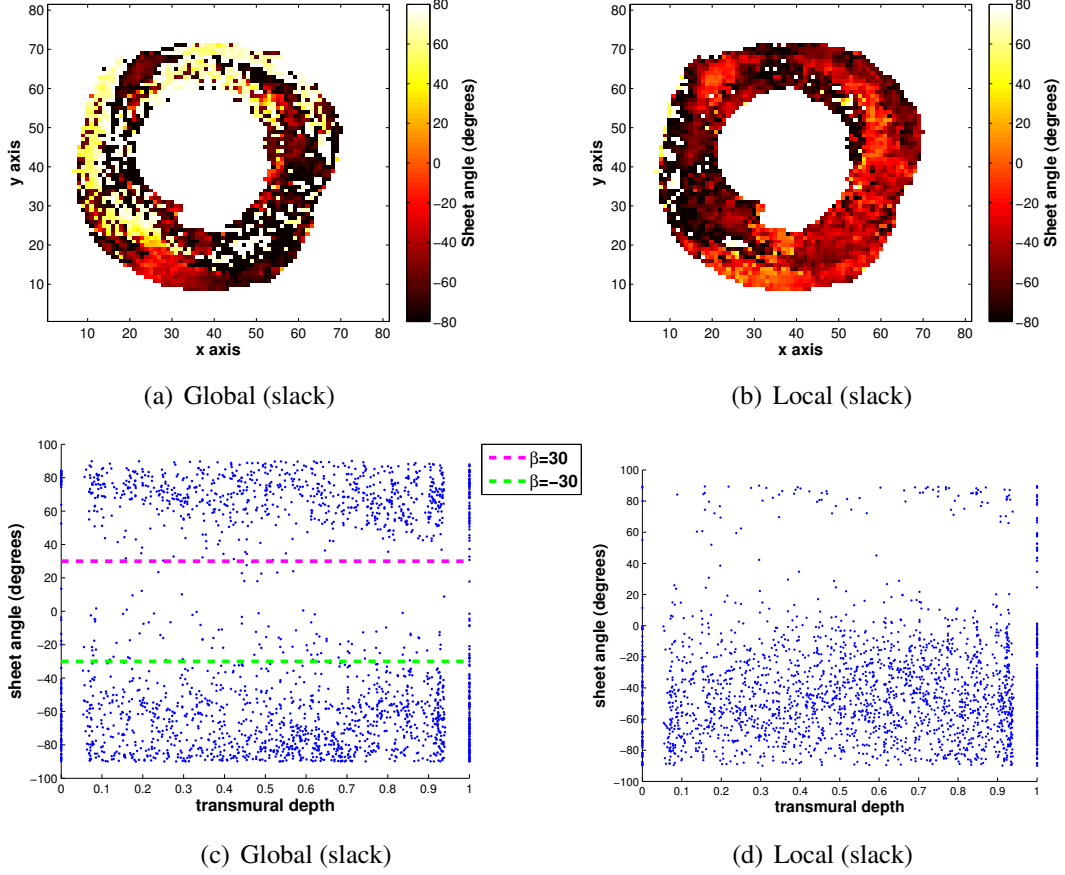


Figure 7.14: Sheet angle distribution in the equatorial slice for Rat_S in the global and local reference frames. (a)-(b) Equatorial short-axis views of β computed with respect to the (a) global and (b) local reference frames. (c)-(d) Scatter plots of β transmural variation in the equatorial slice in the case of (c) global and (d) local reference frames.

The global reference frame detects two opposing populations of sheet angles, as shown in Figure 7.14(c). Approximately 95% of the β values are contained above the $\beta = 30$ threshold (magenta dotted line) or below the $\beta = -30$ threshold (green dotted line). Therefore a population of positive angles ($\beta > 30$) and one of negative angles ($\beta < -30$) can be identified while there are almost no voxels with values of the sheet angle between these two groups. This result seems to be in line with previous studies of opposing sheet populations [6], however the level of noise in the scatter plot requires to consider it with caution. The local reference frame does not identify distinct populations but only a striking prevalence of negative sheet angle values, as shown by Figure 7.14(d). Little difference was found between Rat_S and Rat_C in both reference frames, hence the plots for the contracted state

are not reported.

Overall the results for the sheet angle are rather noisy, both for the global and local reference frames. The reason for this could be the level of noise in the tertiary eigenvector of the DT-MRI dataset. This is the eigenvector that is most likely to be affected by low signal-to-noise ratio and resolution. No previous filtering of the eigenvector field was employed, and that could have reduced the level of noise in the results of the sheet angle. Future work will address this issue.

Comparison of sheet angle measurements with results of Hales et al. [57]. The results obtained for the sheet angle with the global coordinate system are in good agreement with those published by Hales et al. [57]. Figures 7.15(a) and 7.15(b) show the normalised frequency of sheet angle values for the basal and equatorial regions, respectively. As in the case of the helix angle, the results of Hales et al. [57] are for the two ventricles, nonetheless the global reference frame detects similar frequencies for the sheet angle.

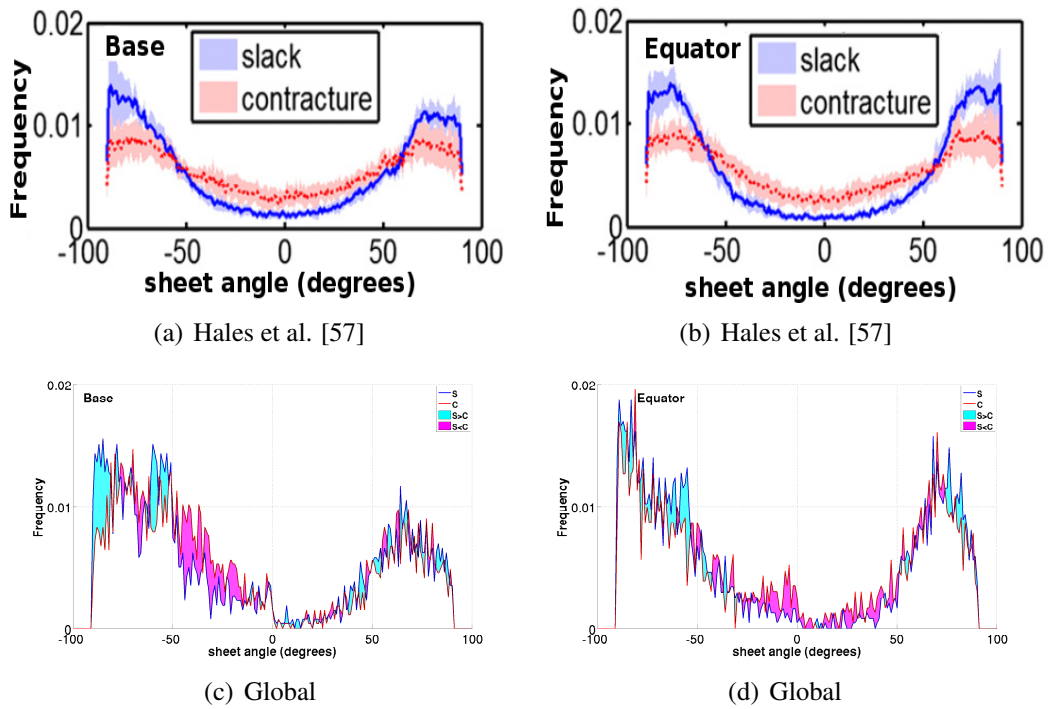


Figure 7.15: Histograms of sheet angle distribution.(a)-(b) Sheet angle distribution measured by Hales et al. [57] in the (a) basal and (b) equatorial regions of both the right and left ventricles, reproduced under Creative Commons Licence. (c)-(d) Sheet angle distribution measured on the rat dataset for the left ventricle only in the (c) basal and (d) equatorial regions.

Figures 7.15(c) and 7.15(d) show the frequency of sheet angle values for the basal and equatorial regions, respectively, measured on the rat dataset with respect to the global coordinate system. The regions of the plots where there is an increase in the frequency going

from slack to contracted are coloured in magenta, whereas the regions where a decrease is measured are in cyan. Both the results from Hales et al. [57] and those from the rat dataset show an decrease in high magnitude β values and an increase in low magnitude β values in the contracted state with respect to the slack one. This result suggests a general flattening of the sheets with respect to the short-axis plane during contraction [57]. Given the substantial difference in the definition of the sheet angle in the local and global reference frames, the frequencies of β for the local frame were not considered for comparison with the literature.

7.3 Angular measures on simulations

The global reference frame method to measure angular metrics was applied to a subset of the simulations of Chapter 6 in order to determine whether the predicted change in tissue structure distribution was consistent with the results described in the previous section. Only helix and sheet angles were considered, since null transverse angle was prescribed throughout the left ventricle in all simulations (see Section 4.5.1). The angles distributions were measured at $t = 0 \text{ ms}$ and $t = 150 \text{ ms}$, for the slack and contracted states, respectively.

In this section the results for the α and β distributions in the equatorial region are discussed for three fibre models: $Sn3R50$, $Sn1R70$ and *Karadag*. The first two fibre models are representative of the two extremes of the global-rule based set of fibre models (see Section 4.5.2). $Sn3R50$ has both high exponent n and low rotation angle R , and is representative of the group of fibre models that show the least physiological values of the global and local metrics employed to assess the simulations output (the results were presented in Sections 6.4.1 and 6.4.2). On the contrary, $Sn1R70$ has low exponent n and high rotation angle R and it is one of the global rule-based fibre models that produced the best values of global and local metrics together with the locally optimised fibre modelled referred to as *Karadag* (Section 4.5.3). The three simulations have transversely isotropic material law (t_{iso} , see Table 4.5 for details) and linear sheet model (Section 4.5.4).

Figures 7.16(a)-7.16(c) show the equatorial distribution of α at slack and contracted states for the three fibre models considered. The transmural variation of helix angle was obtained by the same averaging process applied to the phantom (Section B.3). There is little variation between the two mechanical states for $Sn1R70$ (Figure 7.16(b)) and *Karadag* (Figure 7.16(c)). The simulation with $Sn3R50$ (Figure 7.16(a)) produces a shift in the range of values for the helix angle but it is in the opposite direction with respect to the shift measured on rat, as shown in Figure 7.16(g) (this is a copy of Figure 7.8(c)).

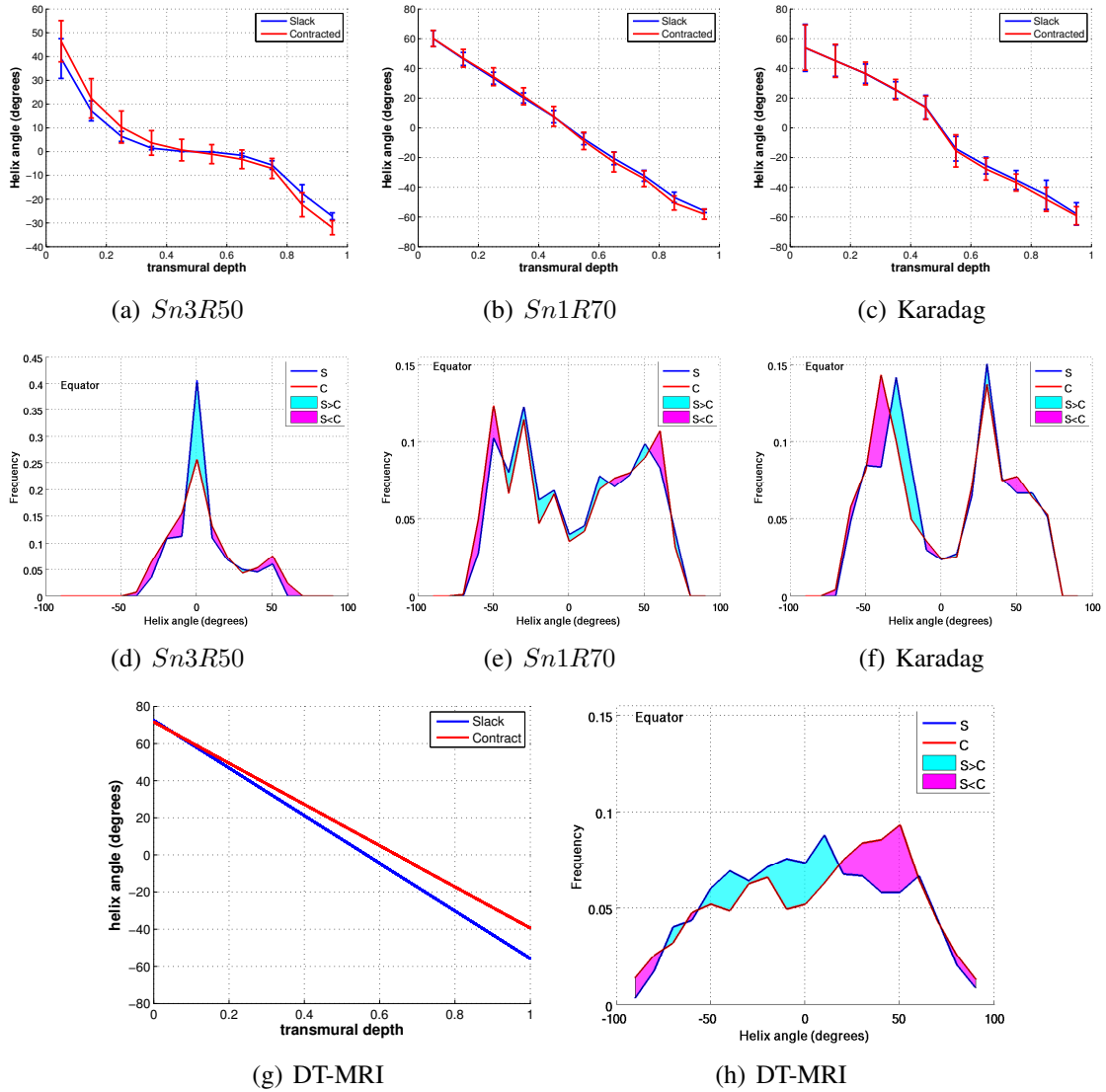


Figure 7.16: Helix angle distribution in the equatorial region, comparison between simulations and images. (a)-(c) Equatorial helix angle transmural distribution at slack ($t = 0$ ms) and contracted ($t = 150$ ms) states in simulations with transversely isotropic material law, linear sheet model and (a) *Sn3R50*, (b) *Sn1R70* and (c) Karadag fibre models. (d)-(f) Helix angle frequency distribution at slack (“S” in the legend) and contracted (“C” in the legend) states in the equatorial region for the same simulations in the case of (d) *Sn3R50*, (e) *Sn1R70* and (f) Karadag fibre models. (g) Linear fit of the equatorial helix angle distribution for the rat dataset in the slack and contracted states (it is a repetition of Figure 7.8(c)). (h) Helix angle frequency distribution at slack (“S” in the legend) and contracted (“C” in the legend) states for the rat dataset.

The change in the normalised frequency for the helix angle is given for the three fibre models in Figures 7.16(d)-7.16(f). These plots can be directly compared with the normalised frequency of the helix angle in the equatorial slice for the rat dataset shown in Figure 7.16(h). There is a substantial difference in the overall shape of the frequency curve, with the fibre model *Sn1R70* being the one that more closely resembles what found in rat. However, the increase in high magnitude helix angles and the decrease in low magnitude

helix angles found in rat when going from slack to contracted state is replicated by the simulations, although to a lesser extent.

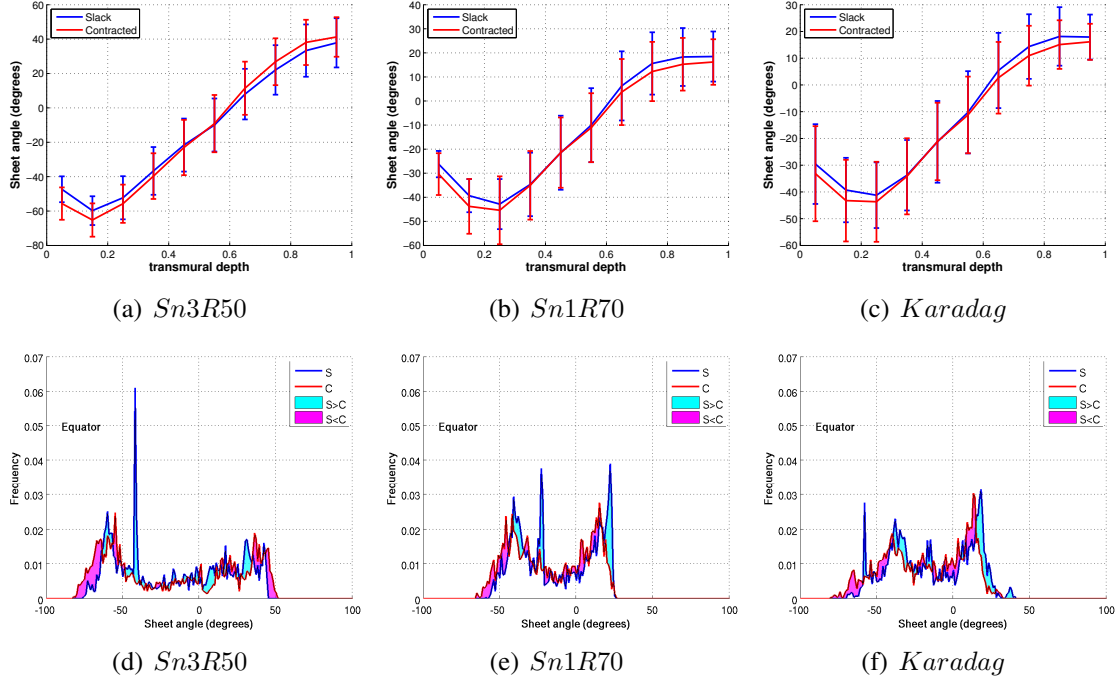


Figure 7.17: (a)-(c) Equatorial sheet angle transmural distribution at slack ($t = 0 \text{ ms}$) and contracted ($t = 150 \text{ ms}$) state in simulations with transversely isotropic material law, linear sheet model and (a) Sn3R50, (b) Sn1R70 and (c) Karadag fibre models. (d)-(f) Histograms of sheet angle distribution comparing slack and contracted states in simulations with transversely isotropic material law, linear sheet model and (d) Sn3R50, (e) Sn1R70 and (f) Karadag fibre models.

Figure 7.17 shows the sheet angle distribution for the three fibre models. The prescribed linear model for the sheet transmural variation is detected by the global coordinate system as a sigmoidal variation. This effect is due to the difference between the angle $\tilde{\beta}$ (intrinsic sheet angle), used to prescribe the sheet model, and the measured angle β , as already commented on in Section 4.5.5. The predicted frequency profiles for the sheet angle (Figures 7.17(d)-7.17(f)) do not seem to be in good agreement with the experimental ones (Figure 7.15) as there is no clear separation between regions of increase/decrease in the sheet angle frequency as found both in Hales et al. [57] and in the rat dataset. Notice also that the frequency scale is higher for the simulations (up to 0.07) with respect to those of Figure 7.15, making the comparison more difficult. However, this was necessary to accommodate the high peak in the plot for *Sn3R50*.

The results presented in this section show that the variation in tissue structure distribution predicted by the three simulations analysed tends to be in agreement with the measurement, although there are some inconsistencies, especially in the case of the sheet angle.

Similar results were obtained for the other simulations, but are not presented. Overall, the predicted variation in the helix and sheet angles distributions is less pronounced than the variation measured on the images. This could be another indicator of the limitations of the electromechanical model discussed in Section 6.5.

7.4 Discussion and concluding remarks

The focus of this chapter has been on the measurement of changes in tissue structure distribution between different mechanical states of the left ventricle on two-state DT-MRI scans. The first part of the chapter has dealt with the choice of the most appropriate method to measure angular metrics on DT-MRI data. In particular, it has been proposed that a method based on a local cylindrical coordinate system (as the one typically employed in histological studies) should be preferable to the more commonly employed approach based on a global coordinate system. Two hypotheses support this statement. First, tissue structure appears to be inherently local (Figures 7.1(a)-7.1(c)), that is changing in response to changes in shape of the heart, one aspect of which is, for example, the significant regional and temporal changes in surface curvature. Hence, a local coordinate system adapting to the curvature of the heart would be more consistent in the measurement of tissue structure distribution. The second hypothesis is that the global reference frame approach is biased by the bulk motion of the heart during the cardiac cycle (Figures 7.1(d) and 7.1(e)), whereas the local reference frame should not be. For these reasons, a method for measuring helix, sheet and transverse angles with respect to a local cylindrical coordinate system was developed and the results compared with the global reference frame approach (Section 7.2.1). The outcome of this analysis was that, with respect to the helix angle the two methods are comparable. However, the local coordinate system approach is much more sensitive to regional changes in transverse and sheet angle, as opposed to the method based on the global reference frame. Hence, for the study of these two angles, it appears to be more appropriate to employ the local reference frame.

The sensitivity of the method to noise in the image could be overcome by employing parametrisations of the endocardial and epicardial surfaces in the computation of the distance map for normalised transmural depth. However I believe that it is important to keep the overall process as image-driven as possible, as explained in Section 7.2.1.2. The use of a parametrised surface would dramatically reduce the regional and inter-subject variability detected as well as introducing approximation errors. For this reason, future work will be aiming at improving the image-driven approach rather than introducing surface modelling in the process.

The local and global coordinate systems were then employed to measure angular metrics on one rat scan from *dataset*₂ (Section 2.4). The results are in line with the conclusions drawn for the helix and transverse angles with the study on phantom, although they highlighted the higher sensitivity of the method based on the local coordinate system to segmentation errors and noise in the data. The transmural distributions of the helix angle measured on rat with the two coordinate system were comparable both in the basal and equatorial region. Interestingly, the transverse angle measured with the local coordinate frame showed an inversion in the slope of the transmural variation when going from the basal to the equatorial region. Such inversion was not detected by the global reference frame. The sheet angle was more difficult to measure in both coordinate systems, and no conclusive observations were made. This is probably due to the complex distribution of sheet planes in the ventricular wall, that cannot be successfully represented, for example, by means of a transmural average, as in the case of helix and transverse angles. In the future, new ways of quantifying and visualising sheet distribution need to be developed. Another source of noise is directly due to the DT-MRI dataset. The measurement of the sheet angles is based on the tertiary eigenvector field, which can be highly affected by the low resolution and signal-to-noise ratio of the images. Filtering methods to evaluate what regions of the tertiary eigenvector field can be associated with confidence to information about the sheet orientation are likely to increase the quality of the results for the sheet angle.

Finally, a preliminary study of the effect of deformation on tissue structure predicted by the electromechanical simulations with pressure boundary conditions (refer to Chapter 6) was carried out. The results were shown for three representative simulations. The predicted changes in helix and sheet angle distributions were compared with those measured on the rat scan and with those of Hales et al. [57]. The results are encouraging but they seem to confirm the limited ability of the electromechanical model to reproduce tissue structure dynamics during contraction.

The main limitations of the imaging study presented in this chapter are: (a) the local coordinate system seems to be more sensitive to segmentation details than expected, which would require further work trying, for example, filtering approaches; (b) due to time constraints, I could only analyse one rat dataset making these results only preliminary. However, the results obtained are promising and provide a solid base for future development.

In this chapter a study of the change in tissue structure distribution occurring between different mechanical states of the heart has been presented. First, methodological aspects

have been discussed in order to identify the most appropriate approach to the measurement of the helix, sheet and transverse angles on DT-MRI. Then, the measurements of these angular metrics performed on one rat from the two-states DT-MRI dataset have been presented and compared with results from the literature. Finally, the predicted variation in tissue structure distribution from the simulations of the previous chapter has been compared with experimental results. This is the final chapter of the thesis. In the next chapter future lines or research are discussed and conclusions provided.

Chapter 8

Conclusions and future directions

8.1 Summary

Tissue structure distribution and dynamics are fundamental components of cardiac function. In this thesis the role of tissue structure models was explored within an electromechanical modelling framework developed to simulate left ventricular contraction in rat. Two computational studies have been presented whose results showed that (a) despite the theoretical advantage of subject-specific approaches to tissue model description, the integration in the electromechanical model of subject-specific structural information did not produce a more physiological prediction of a number of cardiac function indices considered, with respect to global models of tissue structure; (b) the role of sheet planes distribution is an important component in the determination of cardiac mechanics, although this is not fully captured by the current electromechanical models. This study contributed to the evaluation of the strength and limitations of the subject-specific approach to cardiac modelling, suggesting that there are other aspects, such as the connection between sheet dynamics and mechanical behaviour, that need to be addressed prior to the successful application of common state-of-the-art electromechanical models to subject-specific studies.

An image analysis study was also performed on one subject from a two-state DT-MRI Langendorff-perfused rat dataset, with the aim of developing a validation set-up for the electromechanical simulations based on the comparison of measured and predicted tissue structure rearrangement between two different mechanical states of the heart. The study raised important methodological questions regarding the measurement of tissue structure distribution by means of angular metrics. In particular, a method based on a local cylindrical coordinate system, was proposed and developed, as a more accurate way to detect regional and temporal variability in tissue structure distribution, with respect to a standard method based on a global cylindrical reference frame. The two methods were compared

on a phantom image and on the real DT-MRI data, supporting the hypothesis that the local approach is to be preferred. A preliminary validation of a subset of the simulations, presented in this thesis, showed good agreement between predicted and measured trends of the angular metrics, at the same time confirming that the dynamics of tissue structure during contraction are not fully captured by the model. The study contributed to the image analysis field by pointing out that a different perspective is necessary on the quantification and visualisation of tissue structure from DT-MRI data. The contribution to the modelling field is the development of a validation protocol for cardiac mechanics simulations based on microstructural rearrangement between different mechanical states of the heart.

8.2 Future work

Throughout the thesis I have indicated starting points for future work, both in term of short-term and long-term plans. On the modelling side, some of the aspects that would be interesting to address further are :

- Evaluation of the effect of different stimulations protocols for the electromechanical simulation. In particular, the use of a realistic purkinje-like electrical stimulation pattern is likely to induce different mechanical patterns, at least at a local level.
- Further development of the process to apply time-varying pressure boundary conditions.
 - Development of an automatic optimisation process to determine the mechanics mesh prior to passive expansion (Section 6.3.1).
 - Implementation of an automatic method to enforce the constraint on the pressure-volume relationship during the cardiac cycle, for example by means of a Windkessel model (Section 3.1.3).
- Extension of the model to use a subject-specific mesh so that predicted tissue microstructure rearrangement can be compared locally to measurements from DT-MRI.
- Development of a model introducing important mechanisms related to sheet dynamics, such as sheet sliding (or shearing), as a potential way to overcome the current model limitations.
- Introduction of a more biophysically detailed cellular contraction model, in order to take into account calcium dynamics on tissue level contraction.

On the imaging side, it would be interesting to:

- Improve the method for measuring angular metrics based on the local cylindrical reference frame.
- Extend the study to other subjects from the DT-MRI dataset.
- Explore new ways to quantify and visualise the sheet plane distribution in order to take into account the regional complexity and variability of this distribution.

These are only some of the possible starting points for future work that this thesis can provide. Finally, I would like to mention that another important outcome of this thesis has been the new motivation it has provided to the Chaste team to work on the electromechanical problem. I also believe that electromechanical modelling cannot be successfully carried out by one person alone, even with the help of their supervisors, and in a long-term perspective more human resources will be necessary. My greatest wish is that the results I show in this thesis will prove that electromechanical modelling can successfully be carried out in the Computational Biology group and maybe encourage more students and researchers to invest time and resources in it.

Appendices

Appendix A

Protocol for Angular Metrics

In this Appendix the protocol for the measurement of the angular metrics defined in Section 2.3.2 is described. The formulas shown here were employed to measure angular metrics on the ellipsoidal phantom B.3, the DT-MRI images 7.2.2, and the simulations 7.3. They are valid for both the global and local coordinate system (remember the general definition of *cr*-plane, *cl*-plane and *lr*-plane of Section 2.3.1). Please refer to Section 2.3 for the formal definition of helix α , transverse γ and sheet β angles. This Appendix explains how these angles are estimated at a given point $\mathbf{x} = \mathbf{x}(x, y, z) \in \mathbf{R}^3$ from the fibre orientation $\mathbf{f} = \mathbf{f}(\mathbf{x})$ and sheet-normal orientation $\mathbf{n} = \mathbf{n}(\mathbf{x})$ with respect to either the global or local cylindrical coordinate systems.

It is useful to remind that, in order to find the projection \mathbf{m}_μ of a vector \mathbf{m} onto a plane μ the following equation can be employed:

$$\mathbf{m}_\mu = \frac{\mathbf{q} \times (\mathbf{m} \times \mathbf{q})}{\|\mathbf{q} \times (\mathbf{m} \times \mathbf{q})\|}, \quad (\text{A.1})$$

where \mathbf{q} is a generic vector normal to the plane μ .

Helix angle

The following protocol provides the measurement of the helix angle α with respect to a given reference frame.

- Project \mathbf{f} onto the *cl*-plane to obtain \mathbf{f}_{cl} by using eq. (A.1) with $\mathbf{m} = \mathbf{f}$ and $\mu = \mathbf{r}$.
- Calculate the angle θ between \mathbf{f}_{cl} and \mathbf{c} .
- Calculate the angle δ between \mathbf{f}_{cl} and \mathbf{l} .

The outcome of the previous steps will fall in one of these four possible cases:

- Case 1: \mathbf{f}_{cl} is in the first quadrant of the cl -plane. Therefore $\theta < \pi/2, \delta < \pi/2$, as shown in Figure A.1(a). Then the helix angle is $\alpha = \theta$.
- Case 2: \mathbf{f}_{cl} is in the second quadrant of the cl -plane. Therefore $\theta > \pi/2, \delta < \pi/2$, as shown in Figure A.1(b). The helix angle is assigned negative sign and value $\alpha = (-1)(\pi - \theta)$.

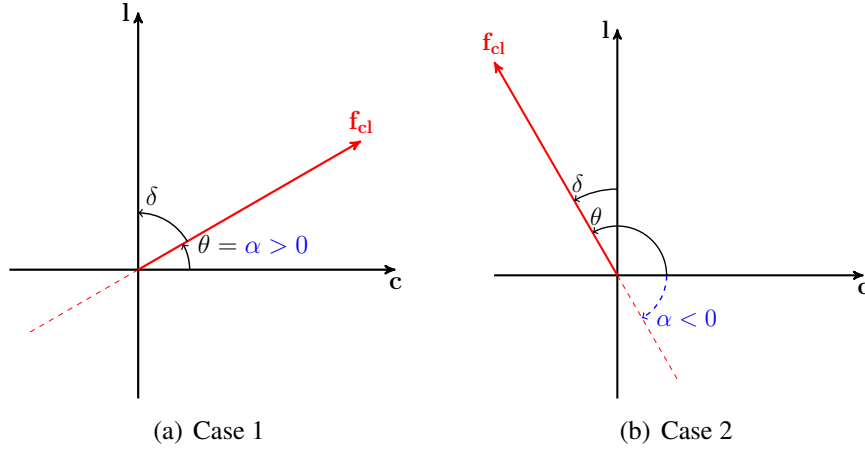


Figure A.1: Helix angle computation depending on the position of \mathbf{f}_{cl} in the cl -plane.

- Case 3: \mathbf{f}_{cl} is in the third quadrant of the cl -plane. Therefore $\theta > \pi/2, \delta > \pi/2$, as shown in Figure A.2(a). The helix angle is assigned positive sign and value $\alpha = \pi - \theta$.
- Case 4: \mathbf{f}_{cl} is in the fourth quadrant of the cl -plane. Therefore $\theta < \pi/2, \delta > \pi/2$, as shown in Figure A.2(b). The helix angle is assigned negative sign and value $\alpha = -\theta$.

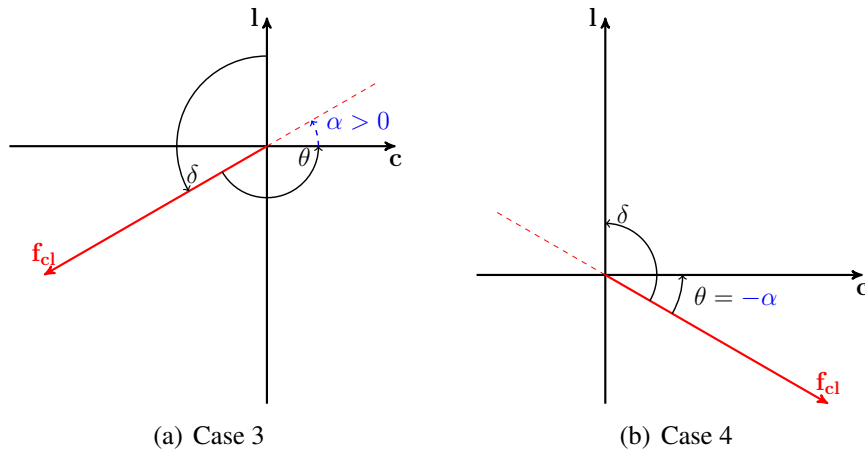


Figure A.2: Helix angle computation depending on the position of \mathbf{f}_{cl} in the cl -plane.

Transverse angle

The following protocol provide the measurement of the transverse angle γ with respect to a given reference frame.

- Project \mathbf{f} onto the cr -plane to obtain \mathbf{f}_{cr} by using eq. (A.1) with $\mathbf{m} = \mathbf{f}$ and $\boldsymbol{\mu} = \mathbf{l}$.
- Calculate the angle θ between \mathbf{f}_{cr} and \mathbf{c} .
- Calculate the angle δ between \mathbf{f}_{cr} and \mathbf{r} .

The outcome of the previous steps will fall in one of these four possible cases:

- Case 1: \mathbf{f}_{cr} is in the first quadrant of the cr -plane. Therefore $\theta < \pi/2, \delta < \pi/2$, as shown in Figure A.3(a). The transverse angle is $\gamma = \theta$.
- Case 2: \mathbf{f}_{cr} is in the second quadrant of the cr -plane. Therefore $\theta < \pi/2, \delta > \pi/2$, as shown in Figure A.3(b). The transverse angle is assigned negative sign and value $\gamma = -\theta$.

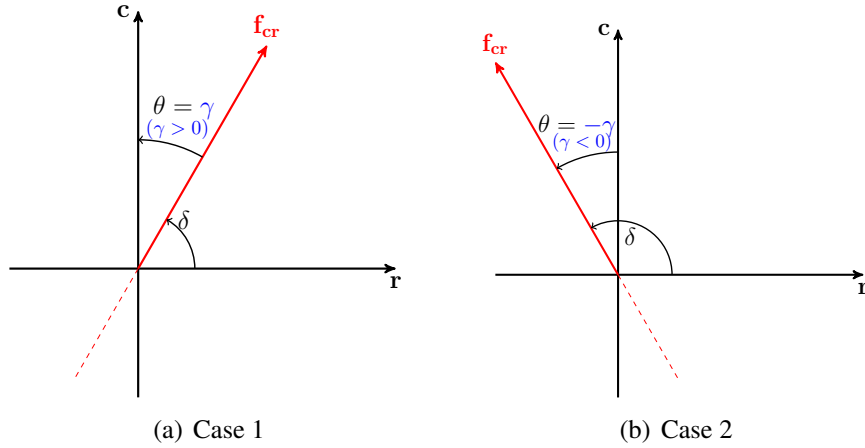


Figure A.3: Transverse angle computation depending on the position of \mathbf{f}_{cr} in the cr -plane.

- Case 3: \mathbf{f}_{cr} is in the third quadrant of the cr -plane. Therefore $\theta > \pi/2, \delta > \pi/2$, as shown in Figure A.4(a). The transverse angle is assigned positive sign and value $\gamma = \pi - \theta$.
- Case 4: \mathbf{f}_{cr} is in the fourth quadrant of the cr -plane. Therefore $\theta > \pi/2, \delta < \pi/2$, as shown in Figure A.4(b). The transverse angle is assigned negative sign and value $\gamma = (-1)(\pi - \theta)$.

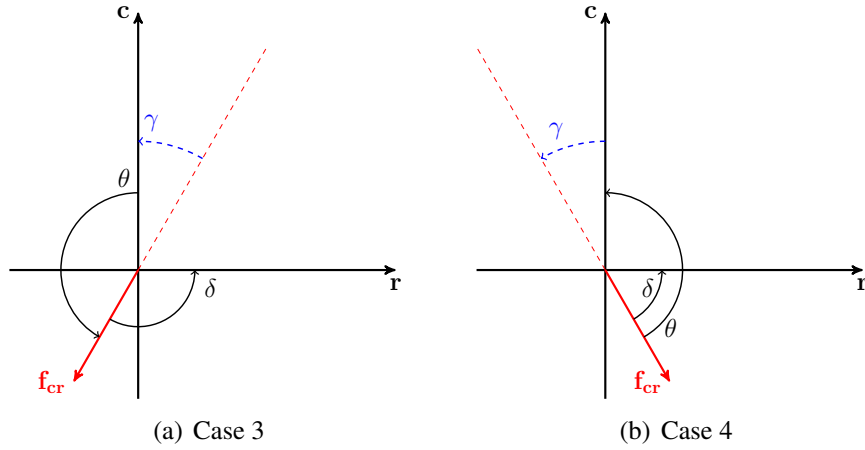


Figure A.4: Transverse angle computation depending on the position of \mathbf{f}_{cr} in the cr -plane.

Sheet angle

The sheet angle β is measured indirectly using the sheet-normal direction \mathbf{n} , which uniquely determines the sheet plane at each point in the tissue. While β is the angle between the sheet plane and \mathbf{r} , the angle that is actually measured is that between the projection \mathbf{n}_{lr} of \mathbf{n} onto the lr -plane and \mathbf{l} . Then the properties of complementary of angles in the plane are used to obtain β .

- Project \mathbf{n} onto the lr -plane to obtain \mathbf{n}_{lr} by using eq. (A.1) with $\mathbf{m} = \mathbf{n}$ and $\boldsymbol{\mu} = \mathbf{c}$.
- Calculate the angle θ between \mathbf{n}_{lr} and \mathbf{l} .
- Calculate the angle δ between \mathbf{n}_{lr} and \mathbf{r} .

The outcome of the previous steps will fall in one of these four possible cases:

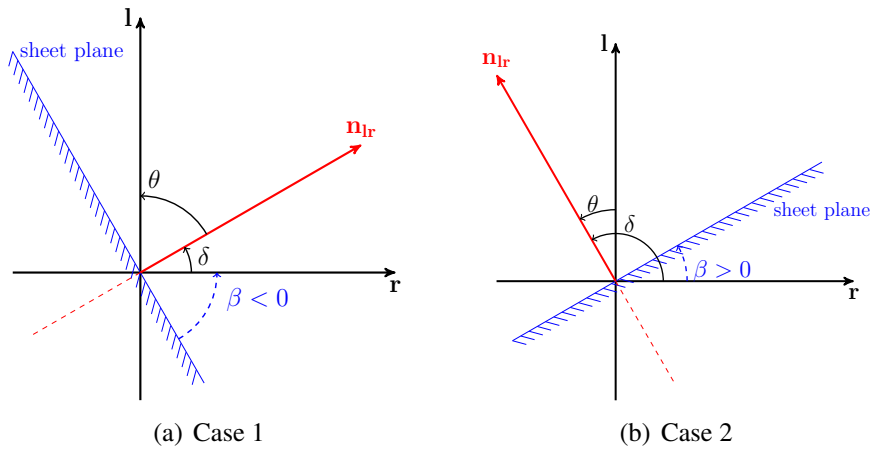


Figure A.5: Sheet angle computation depending on the position of \mathbf{n}_{lr} in the lr -plane.

- Case 1: \mathbf{n}_{lr} is in the first quadrant of the lr -plane. This means that the sheet plane crosses the second and fourth quadrants. We have $\theta < \pi/2, \delta < \pi/2$, as shown in Figure A.5(a). The sheet angle is negative and equals $\beta = -\theta$.
- Case 2: \mathbf{n}_{lr} is in the second quadrant of the lr -plane while the sheet plane is in the first and fourth quadrants. Therefore $\theta < \pi/2, \delta > \pi/2$, as shown in Figure A.5(b). The sheet angle is positive and has value $\beta = \theta$.
- Case 3: \mathbf{n}_{lr} is in the third quadrant of the lr -plane. Therefore $\theta > \pi/2, \delta > \pi/2$, as shown in Figure A.6(a). The sheet angle is assigned negative sign and value $\beta = (-1)(\pi - \theta)$.
- Case 4: \mathbf{n}_{lr} is in the fourth quadrant of the lr -plane. Therefore $\theta > \pi/2, \delta < \pi/2$, as shown in Figure A.6(b). The sheet angle is assigned positive sign and value $\beta = \pi - \theta$.

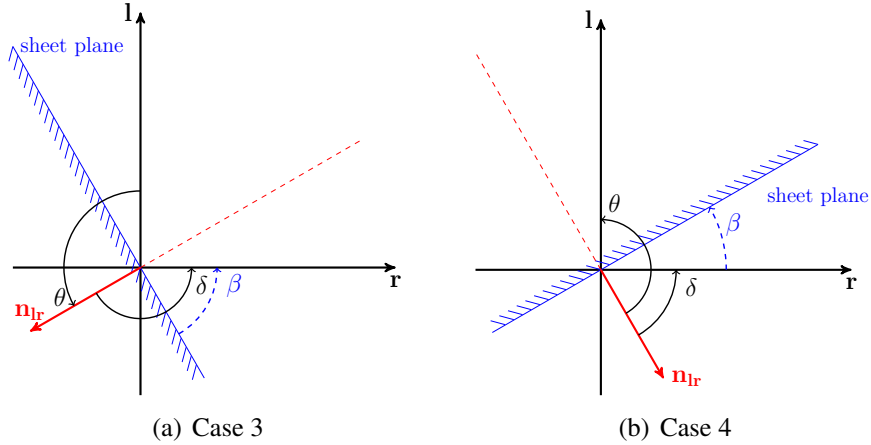


Figure A.6: Sheet angle computation depending on the position of \mathbf{n}_{lr} in the lr -plane.

Appendix B

Phantom imaging for validation and hypothesis testing

This appendix contains the supplementary material for the imaging study described in Chapter 7. In particular, the preliminary study performed on a phantom dataset, that is a mathematical model of a DT-MRI dataset, with the aim of (a) developing the method based on the local coordinate system and (b) testing the two hypotheses presented in Section 7.1 under controlled conditions, is presented.

The aim of the phantom dataset is to provide a simplified model for the DT-MRI rat dataset. With respect to Figure 7.2, which shows the pipeline for processing the DT-MRI images, the phantom provides directly the final binary mask for the left ventricle and the fibre and sheet orientation vector fields, for just one mechanical state. Therefore, it is possible to apply directly the methods to assign a global and a local reference frame to then measure the helix, transverse and sheet angles. In particular, the phantom generated for this preliminary study is a thick-walled ellipsoid representing the left ventricle, and the fibre and sheet orientation maps are rule-based.

In this appendix I first describe the generation of a phantom 3D image of the left ventricle with prescribed tissue structure distribution (Section B.1). The phantom was used in the development of the algorithm for the measurement of angular metrics with respect to the global and local cylindrical systems of coordinates which were then employed on the rat DT-MRI dataset (Section 7.2.2). The details of the algorithm development are provided in Section B.2. The results of the measurements carried out on the phantom dataset with the two reference frames are then shown and discussed in Section B.3.

B.1 Definition of the binary ellipsoidal phantom

The mechanical mesh $mesh_m$ for the thick-walled truncated ellipsoid described in Section 4.2 was employed to generate the phantom image. A 3D binary mask (that is a black and white image) of $mesh_m$ was obtained by means of the `Mesh voxelisation` tool for Matlab [3], which is based on a ray intersection method [126]. The result is a 3D binary mask of the ellipsoid of size $110 \times 110 \times 110$ voxels and spatial resolution $80 \mu m \times 100 \mu m \times 100 \mu m$.

Tissue structure was prescribed at the centroid of each voxel representing tissue in the phantom by applying a method analogous to the one described in Section 4.5 for the tetrahedral mesh. The resulting tissue structure distribution is in accordance with the hypothesis of the local inherent nature of tissue distribution, as described in the Introduction. First, a local cylindrical coordinate system $(\mathbf{u}, \mathbf{v}, \mathbf{w})$ has to be defined for each tissue voxel by applying the following three steps:

1. Local radial direction \mathbf{u} .

An ellipsoidal surface concentric to the epicardial one passing through the centroid of the voxel was defined. The local radial direction \mathbf{u} was then the unit vector along the normal to that surface through the centroid of the voxel, pointing outwards with respect to the ventricular cavity. If the implicit form of the ellipsoid to which the epicardial surface belongs is represented as

$$F_{epi}(x, y, z) = \frac{x^2}{a_{epi}^2} + \frac{y^2}{b_{epi}^2} + \frac{z^2}{c_{epi}^2} - 1 = 0, \quad (\text{B.1})$$

then, finding the ellipsoid through the centroid of the voxel becomes the problem of finding $k \in \mathbb{R}$ such that

$$\frac{x_{vox}^2}{a_{epi}^2} + \frac{y_{vox}^2}{b_{epi}^2} + \frac{z_{vox}^2}{c_{epi}^2} - k^2 = 0, \quad (\text{B.2})$$

where $(x_{vox}, y_{vox}, z_{vox})$ are the coordinates of the centroid of the voxel. Then k is given by

$$k = \pm \sqrt{\frac{x_{vox}^2}{a_{epi}^2} + \frac{y_{vox}^2}{b_{epi}^2} + \frac{z_{vox}^2}{c_{epi}^2}}, \quad (\text{B.3})$$

and since only the positive value is necessary, the final formula for the normal to the ellipsoidal surface through the voxel is given by

$$\nabla F_{vox} = \left(\frac{2x_{vox}}{(ka_{epi})^2}, \frac{2y_{vox}}{(kb_{epi})^2}, \frac{2z_{vox}}{(kc_{epi})^2} \right), \quad (\text{B.4})$$

2. Local circumferential direction v .

The unit vector v is given by the cross product between the z -axis unit vector $e_3 = (0, 0, 1)$ and u , $v = e_3 \times u$. The global long axis of the ellipsoidal mesh, and also of its binary image, coincides in fact with the Cartesian z -axis by definition.

3. Define the local longitudinal direction w .

The local longitudinal direction w is finally given by the cross product $w = u \times v$.

Once the local coordinate system was defined, the fibre, sheet and sheet-normal directions (f, s, n) were computed for each tissue voxel in the phantom by following the modelling approach used for the ellipsoidal mesh. This was based on the use of the three angles $\tilde{\alpha}$, $\tilde{\beta}$ and $\tilde{\gamma}$, representing the intrinsic helix, sheet and transverse angle, respectively (Section 4.5). These angles are the intrinsic analogues of the angular metrics, and their relationship with the measured angular metrics was discussed in Section 4.5.5. Following the notation of Section 4.5, I assigned global rule-based fibre model $Sn1R70$, linear sheet variation and null transverse angle to the phantom. In other words, $\tilde{\alpha}$ varies linearly in the transmural direction from -70 at epicardium to 70 at endocardium, $\tilde{\beta}$ varies linearly from 80 at epicardium to -80 at endocardium, and $\tilde{\gamma} = 0$ everywhere.

B.2 Assignment of global and local cylindrical system of coordinates to phantom

Once the phantom was generated, it was employed to develop the algorithms for the assignment of the global and local cylindrical coordinate systems for the measurement of angular metrics that were used on the real DT-MRI scans. The algorithm for the global reference frame case was simply an adaptation of the one employed by Hales et al. [57]. The development of the algorithm for the local reference frame is another contribution of this thesis.

B.2.1 Algorithm for the global coordinate system

The global coordinate system assigns a triple of unit vectors (r, c, l) to each tissue voxel on the image, by means of the following steps:

1. Global longitudinal direction l .

The longitudinal axis of the left ventricle in the 3D image is determined by first computing the centroid of the tissue area on each short-axis slice and then fitting

a line through all the centroids. Given the symmetry of the ellipsoid from which the phantom was generated, the longitudinal axis coincides with the z -axis (Figure B.1(a)). For a real DT-MRI scan, the orientation of the longitudinal axis varies (see Figures 7.4(a)-7.4(c)). The global longitudinal direction \mathbf{l} at a given tissue voxel is simply parallel to the longitudinal axis of the left ventricle, as shown in Figure B.1(b).

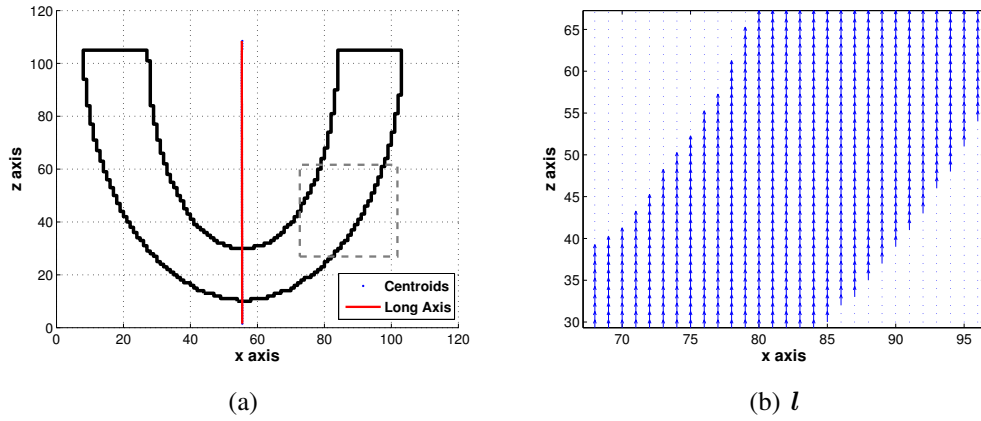


Figure B.1: (a) Long axis slice of the phantom showing the longitudinal line fitted through the centroids of each short-axis slice of the Phantom. The grey rectangle represents the area for which the vector field of the global longitudinal direction \mathbf{l} is shown in (b).

2. Global radial direction \mathbf{r} .

A fine sample \mathbf{x}_{long} of approximately 200 points belonging to the longitudinal axis of the ventricle is obtained. This refinement is not strictly necessary in the case of the phantom image, for which I could use the centroids from its 110 short-axis slices, but it becomes necessary for the real images, which only have about 12 short-axis slices showing left ventricular tissue. In order to identify the radial direction at each tissue voxel centroid, a nearest-neighbour search based on the Euclidean distance was performed. In this way, I found the closest point in the long axis sampling \mathbf{x}_{long} to each centroid. The unit global radial vector \mathbf{r} for each centroid lies on the segment connecting the centroid to its nearest neighbour along the long axis and is set to be pointing outwards with respect to the left ventricular cavity. Figure B.2(b) shows the radial directions at the centroids of the tissue voxels for the region enclosed by the grey rectangle in the short-axis slice of the phantom that is shown in Figure B.2(a).

3. Global circumferential direction \mathbf{c} .

The unit vector \mathbf{c} representing the global circumferential direction at each tissue voxel centroid is obtained by the cross product $\mathbf{c} = \mathbf{l} \times \mathbf{r}$. Figure B.2(c) shows

the circumferential directions at the centroids of the tissue voxels for the region enclosed by the grey rectangle in the short-axis slice of the phantom that is shown in Figure B.2(a).

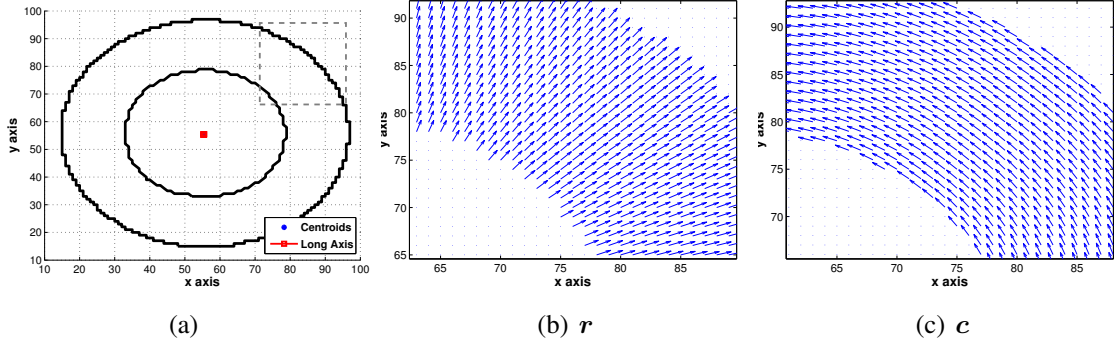


Figure B.2: (a) Short axis slice of the phantom with the centroid of the tissue shown in red. The grey rectangle represents the area for which the vector fields of the global (b) radial r and (c) circumferential c directions are shown.

B.2.2 Algorithm for the local coordinate system

In order to develop an algorithm for the definition of the local cylindrical coordinate system on a general ventricular geometry I could not use an approach similar to the ones previously employed to prescribe the fibres on the phantom (Section B.1) and the mechanical mesh (Section 4.5). Those approaches were based on the analytical properties of the ellipsoid, whereas in this case a general geometry for the left ventricle has to be assumed. To this purpose, the concept of distance map is used. A distance map assigns to each pixel/voxel of an image a numerical label representing the distance of the pixel/voxel from a certain object. In this case, the Euclidean distance was considered in order to generate a 3D distance map of the normalised transmural depth $d(x, y, z)$ of each voxel of the left ventricle, varying from 0 to 1 from endocardium to epicardium (eqn. (4.10)). Therefore, two distance maps were computed, representing the distance of each voxel to the endocardial and epicardial surfaces, respectively. They were then combined according to eqn. (4.10) to obtain the distance map for $d(x, y, z)$. Figures B.3(a) and B.3(b) show a short-axis and a long-axis view of the distance map for $d(x, y, z)$, respectively.

The algorithm to assign the local coordinate system to the centroid of each tissue voxel is composed of the following three steps:

1. Local radial direction u .

The unit vector for the local radial direction u at each voxel was given by the gradient

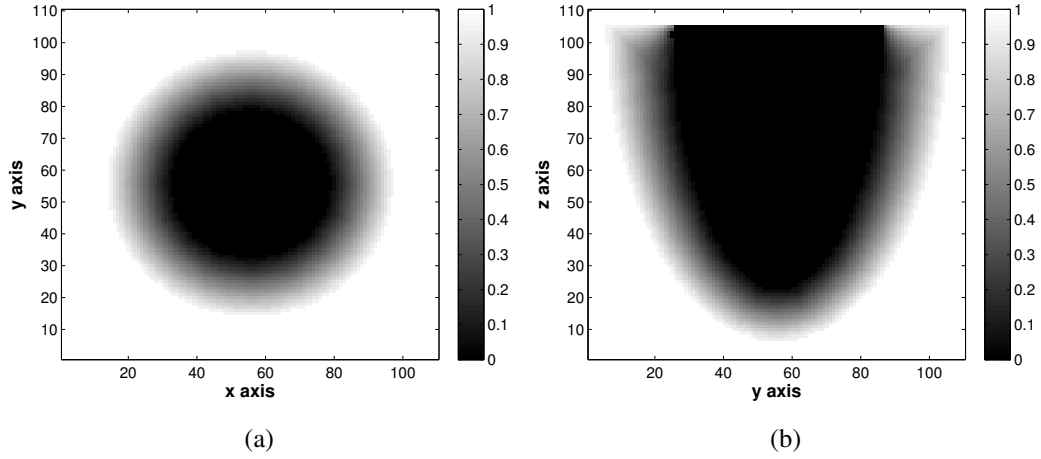


Figure B.3: (a) Short-axis and (b) long-axis views of the distance map for the normalised transmural depth $d(x, y, z)$.

of $d(x, y, z)$ for that voxel, since u identifies the direction of maximal variation of the normalised transmural depth in the ventricle.

2. Local circumferential direction v .

The cross product between the global longitudinal direction l and u provided the local circumferential direction at a given voxel, $v = l \times u$.

3. Local longitudinal direction w .

For each voxel w was defined as the cross product $w = u \times v$.

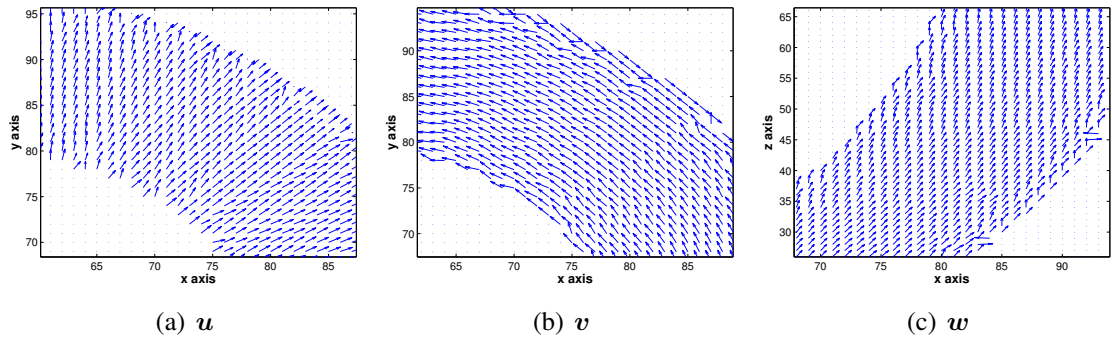


Figure B.4: Vector field for local (a) radial u , (b) circumferential v and (c) longitudinal w directions, for the region enclosed by the grey rectangle in the short-axis slice of the phantom that is shown in Figure B.2(a).

Figure B.4(a) shows the distribution of u for the region enclosed by the grey rectangle in the short-axis slice of the phantom that is shown in Figure B.2(a). Similarly, Figures B.4(b) and B.4(c) show the distribution of v and w , respectively. In comparison with the global system of coordinates, the distribution of the unit vectors of the local coordinate system

follow closely the changes in curvature of the left ventricle resulting in a less uniform vector distribution. Along the epicardial surface, some vectors seem to have an orientation that is not consistent with the neighbouring vectors. These artifacts in the vector field are due to the discrete nature of the epicardial surface of the phantom, which causes perturbations in the transmural depth $d(x, y, z)$, from which the local radial direction \mathbf{u} is computed. Noise in the distance map propagates in fact to the derived vector fields. This effect can be more dramatic in the case of the real DT-MRI images, as discussed in Section 7.2.1.2.

B.3 Measuring angular metrics on phantom

Once the methods to assign the global and local reference frames were developed, they were employed on the phantom to measure α , β and γ , the helix, sheet and transverse angles, according to their definition (provided in Section 2.3.2). A protocol to measure these angles for each tissue voxel with respect to a given coordinate system was developed from the angles formal definition, and it is described in detail in Appendix A.

In order to visualise the results of the measurements of the angular metrics on the phantom with respect to the two reference frames, two different approaches were considered. First a qualitative analysis of the results can be obtained by simply representing a short-axis slice of the phantom with each tissue voxel labelled with the corresponding value of the given angular metric. For example, Figures B.5(a), B.5(b) and B.5(c) show α , β and γ measured with respect to the global reference frame, while Figures B.5(d), B.5(e) and B.5(f) show α , β and γ measured with respect to the local reference frame. All figures represent the same midventricular (or equatorial) slice.

The distributions of helix angle values in the global (Figure B.5(a)) and local (Figure B.5(d)) reference frames seem rather similar. This suggests that the definition of α is analogous in the local and global frames. However, the distribution of sheet angles look remarkably different between global (Figure B.5(b)) and local B.5(e)) coordinate systems. A significantly different distribution of transverse angles is also measured between global (Figure B.5(c)) and local (Figure B.5(f)) frames. Therefore, the definition of sheet and transverse angles seems to be significantly different in the two reference frames.

A more quantitative method of analysing these results consists in computing the average value for the angular metrics for each one of a set of subintervals of the transmural depth, in order to show the average transmural variation of the angular metrics for a given region of the heart. In this case it is necessary to employ circular statistics measures of mean and

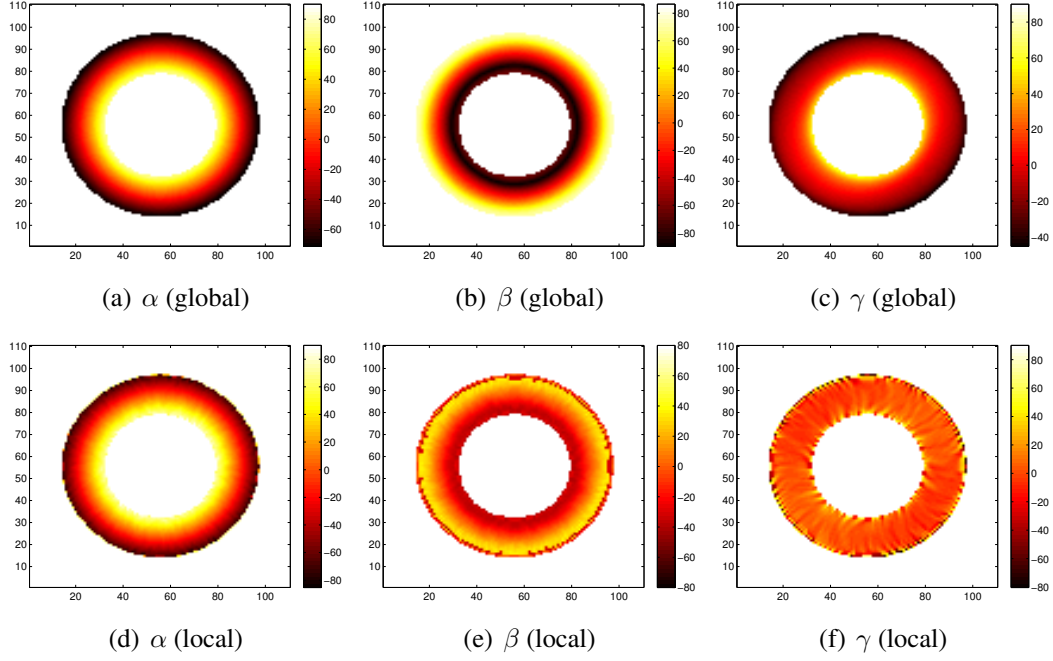


Figure B.5: (a)-(c) Midventricular short-axis slice showing (a) helix (b) sheet and (c) transverse angles measured in the global reference frame. (d)-(f) Midventricular short-axis slice showing (d) helix (e) sheet and (f) transverse angles measured in the local reference frame.

standard deviation [13]. For this purpose, the range $[0 \ 1]$ for the normalised transmural depth $d(x, y, z)$ was divided into 10 subintervals of length 0.1. The measures of a given angular metric θ were first divided into three regions in the longitudinal direction: the basal, midventricular (or equatorial) and apical region. For each region and over each subinterval of transmural depth, the circular mean $\langle \theta \rangle_{circ}$ for the angular metric θ was obtained by applying the formula

$$\langle \theta \rangle_{circ} = \arctan \left(\frac{\langle \sin(\theta) \rangle}{\langle \cos(\theta) \rangle} \right). \quad (\text{B.5})$$

Here, $\langle \cos(\theta) \rangle = N^{-1} \sum_i \cos(\theta_i)$ and $\langle \sin(\theta) \rangle = N^{-1} \sum_i \sin(\theta_i)$, with N being the number of measurements in the sample [13]. The angular deviation $\delta(\theta)_{circ}$, a form of circular standard deviation, was then obtained starting from the mean resultant vector $\rho_\theta = \sqrt{\langle \cos(\theta) \rangle^2 + \langle \sin(\theta) \rangle^2}$, as follows

$$\delta(\theta)_{circ} = \sqrt{2(1 - \rho_\theta)}, \quad (\text{B.6})$$

and is always in the range $[0 \ \sqrt{2}]$ radians (that is approximately $[0 \ 81]$ degrees) [13].

The comparison between the average transmural variation for the global and local helix angles is shown in Figure B.6 and is divided into basal (Figure B.6(a)), equatorial (Figure

B.6(b)) and apical (Figure B.6(c)) regions. The average values of α in the two reference frames are almost identical in the basal and equatorial regions for all the transmural depth except that in the epicardial subinterval ($d \in [0.85 \ 0.95]$). Global and local helix angle distributions differ more in the apical region.

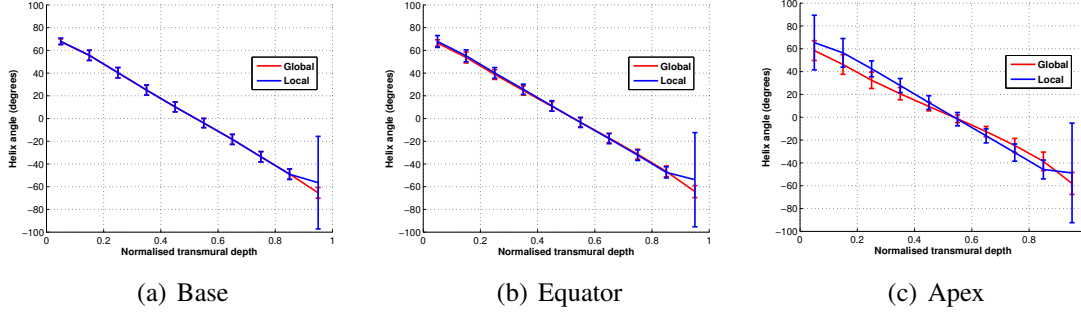


Figure B.6: Global (red) versus local (blue) average transmural variation of the helix angle in the (a) basal, (b) equatorial and (c) apical regions.

Figure B.7(a) compares the average helix angle transmural distribution for the basal, equatorial and apical regions for the global reference frame. Basal and equatorial traces overlap almost completely, whereas the apical trace seems rotated with respect to the previous two traces and has a maximum difference 9 degrees with respect to the basal trace. Figure B.7(b) shows the analogous comparison for the local coordinate system. In this case, basal, equatorial and apical traces are all essentially overlapping through the depth of the ventricle except for the epicardial subinterval. Therefore, when measuring the helix angle, the local

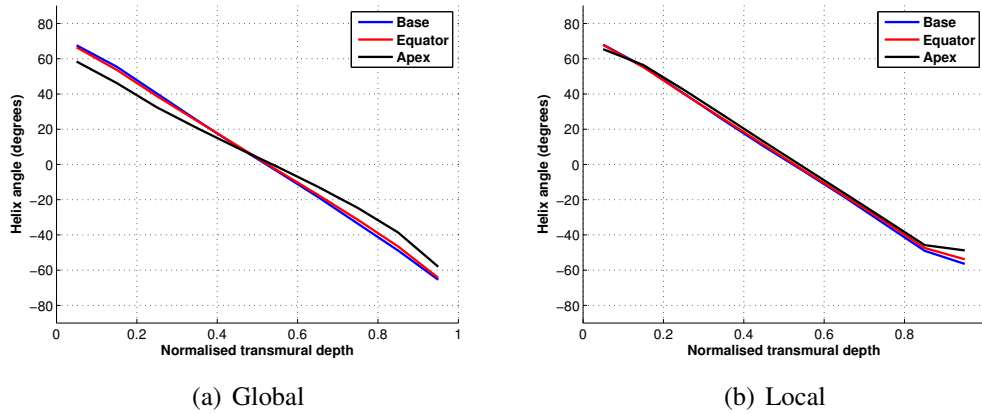


Figure B.7: Average helix angle for the basal, equatorial and apical regions measured with respect to the (a) global and (b) local coordinate systems.

and global reference frames produce similar results in the basal and equatorial regions. This comparison is in line with what emerged from the previous qualitative analysis of helix angle distribution (Figures B.5(a) and B.5(d)). In the apical region the global reference frame

fails to measure the same trace obtained in the upper regions, as it should, since the phantom was designed to have the same transmural variation for the three angles throughout the ventricle. However, the discrepancy is small, with a maximum difference of 9 degrees in the endocardial and epicardial subintervals between apical and basal/equatorial traces. It is safe to conclude that, when measuring the helix transmural variation in the ventricle, both global and local coordinate systems measure the regional variability present in the ventricle with good approximation.

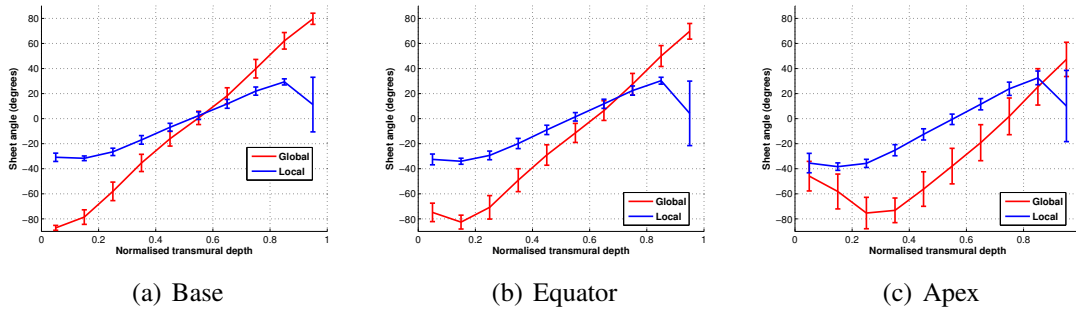


Figure B.8: Global versus local average transmural variation of the sheet angle in the (a) basal, (b) equatorial and (c) apical regions.

Different conclusions can be drawn when considering the sheet and transverse angles. The comparison between the average transmural variation for the global and local sheet angles is shown in Figure B.8 for the basal (Figure B.8(a)), equatorial (Figure B.8(b)) and apical (Figure B.8(c)) regions. In this case, the values obtained with the two definitions of β are dramatically different. In the global reference frame a linear transmural variation is detected in the basal and equatorial regions, whereas in the apical region the linear behaviour is measured in the midmyocardial and epicardial regions ($d \in [0.35 \ 0.95]$). The local reference frame approach detects a more sigmoidal type of transmural variation for β and with an average range of values significantly smaller than the one detected by the global reference frame method. While the different range of values is to be expected since they are two inherently different definitions of β , the different type of variation detected (linear versus sigmoidal) is interesting and suggests caution in the inference of sheet planes dynamics in the tissue from the measurement of β . For example, in Section 4.5.4 two models of transmural variation of the intrinsic sheet angle $\tilde{\beta}$ were employed, a linear and a sigmoidal one. The modelling assumption was that a sigmoidal trace was a good approximation to a sheet bimodal population, or at least closer to represent the bimodal population than the linear trace. Using the same approach to interpret the results for β in either the global or local reference frame would be misleading, as further commented on in Section 7.4.

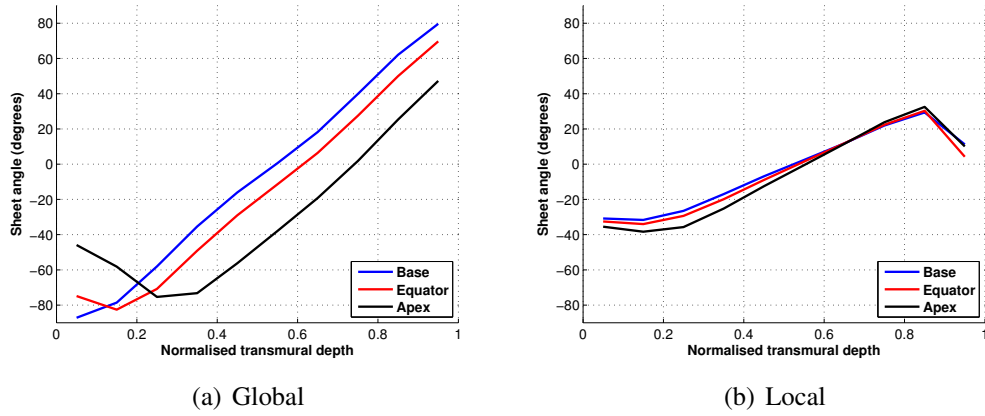


Figure B.9: Average sheet angle for the basal, equatorial and apical regions measured with respect to the (a) global and (b) local coordinate systems.

In the case of the sheet angle, the local reference frame should be preferred to the global one, as suggested by the results of Figure B.9. With the global system of coordinates, the basal, equatorial and apical traces run approximately parallel but distant to one another, with an average difference between basal and equatorial of 9 degrees, and of 22 degrees between basal and apical trace, as shown in Figure B.9(a). With the local reference frame the three traces are considerably closer and show the same trend, with an average difference between basal and equatorial of 2 degrees, and of 3 degrees between basal and apical trace (Figure B.9(b)). This is not surprising since the same transmural variation of the sheet angle was prescribed to the phantom.

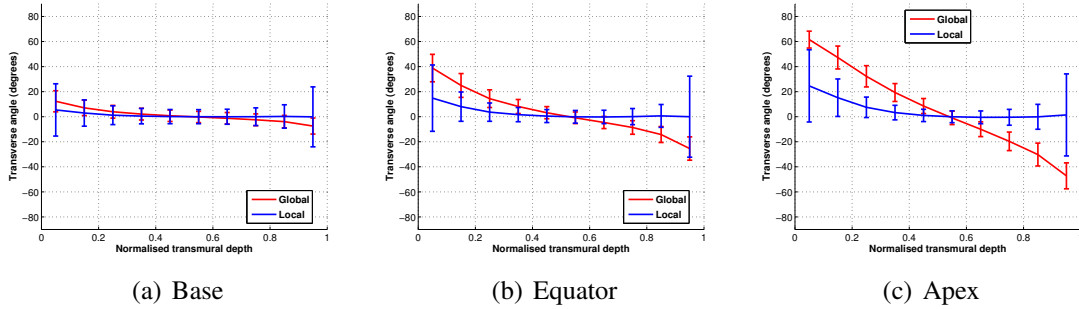


Figure B.10: Global versus local average transmural variation of the transverse angle in the (a) basal, (b) equatorial and (c) apical regions.

Similar conclusions are suggested by the results of the transverse angle. Figure B.10 compares the average transmural distribution of γ detected by the global and local reference frame methods. The two approaches coincide in the basal region where they detect an average null transverse angle throughout the transmural depth (Figure B.10(a)). Conversely, the results of the two measures diverge in the equatorial (Figure B.10(b)) and apical (Figure

B.10(c)) regions. Figure B.11(a) shows how the trace for γ changes remarkably between basal, equatorial and apical regions, with the basal, equatorial and apical traces being altered by the effect of an apparent rotation, resulting from the different local orientations of the myocardium. The maximum difference between the basal and equatorial trace is 18 degrees, while the maximum difference between basal and apical traces is 40 degrees. On the contrary, with the exception of the endocardial subintervals ($d < 0.35$) the average traces for γ measured in the local system of coordinates all show a null average value of the angle across the depth of the ventricle. The discrepancy in the endocardial subinterval is probably due to the noise in the vector fields of the local coordinate system, where inconsistency in the direction of neighbouring vectors was detected, as discussed in Section B.2.2.

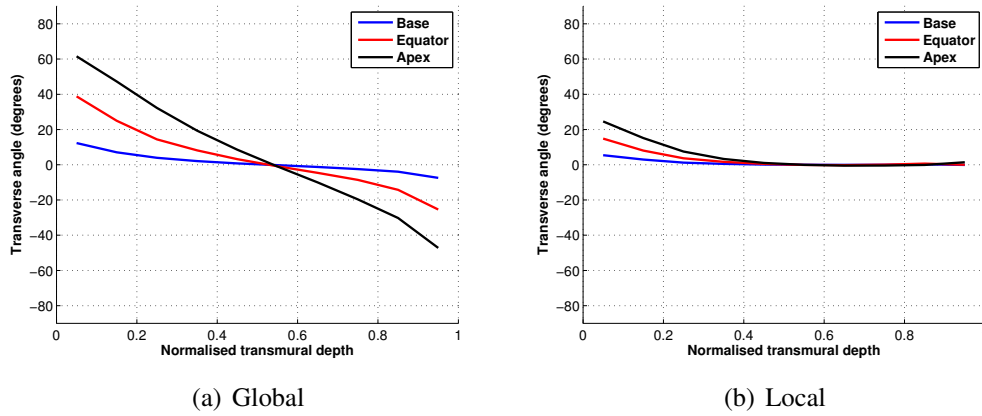


Figure B.11: Average transverse angle for the basal, equatorial and apical regions measured with respect to the (a) global and (b) local coordinate systems.

B.3.1 Alternative method for computing local angular metrics based on projection

This section describes an alternative method to compute the angular metrics for the local reference frame directly from the results obtained in the global reference frame. In the algorithms developed and described earlier in this appendix, the two coordinate systems are assigned to the left ventricular binary mask and the angles are measured independently in both reference frames. However, it is also possible to mathematically relate the global and local reference frames at each voxel by finding a rotation matrix from one frame to the other. Then, this rotation matrix can be used to compute, for example, the local helix angle from the global one. The idea underlying this alternative approach is that of having for each tissue voxel a direct mapping between the global angular metric value and the expected local analogous. However, as shown in this section in the case of the helix angle,

the resulting mapping is not simple to interpret and is not in total agreement with the results from the algorithms described earlier.

What follows is a brief description of this alternative method, which at this stage should be considered as a proof of concept, because the advantages and disadvantages of the two approaches still need to be fully evaluated in order to choose which of them is more reliable. Future work will aim at further exploring this alternative method.

Given a tissue voxel in the left ventricular binary mask, two orthonormal bases can be assigned: the global cylindrical basis $(\mathbf{r}, \mathbf{c}, \mathbf{l})$ and the local cylindrical basis $(\mathbf{u}, \mathbf{v}, \mathbf{w})$, as described in Section B.2. A rotation matrix M can be found such that

$$\begin{aligned} (\mathbf{r}, \mathbf{c}, \mathbf{l}) &= M(\mathbf{u}, \mathbf{v}, \mathbf{w}) \quad \text{that is} \\ \mathbf{r} &= M\mathbf{u} \\ \mathbf{c} &= M\mathbf{v} \\ \mathbf{l} &= M\mathbf{w}. \end{aligned} \tag{B.7}$$

It has been shown in Appendix A that the helix angle with respect to a given reference frame is obtained from the projection of the fibre direction into the cl -plane, \mathbf{f}_{cl} . Therefore, in the global reference frame, $\mathbf{f}_{cl} = (0, \cos(\alpha_G), \sin(\alpha_G))$ (assuming it has norm $|\mathbf{f}_{cl}| = 1$), where for simplicity α_G stands for the helix angle measured with respect to the global reference frame. Analogously, in the local reference frame, $\mathbf{f}_{cl} = (0, \cos(\alpha_L), \sin(\alpha_L))$, where α_L stands for the helix angle measured with respect to the local reference frame. In other words

$$\begin{aligned} \mathbf{f}_{cl} &= 0\mathbf{r} + \cos(\alpha_G)\mathbf{c} + \sin(\alpha_G)\mathbf{l} \\ \mathbf{f}_{cl} &= 0\mathbf{u} + \cos(\alpha_L)\mathbf{v} + \sin(\alpha_L)\mathbf{w} \end{aligned} \tag{B.8}$$

By equating the right-hand side of the two formulas in eqn. (B.8) and rearranging according to eqn. (B.7), the following result is obtained

$$\begin{bmatrix} 0 \\ \cos(\alpha_L) \\ \sin(\alpha_L) \end{bmatrix} = M \begin{bmatrix} 0 \\ \cos(\alpha_G) \\ \sin(\alpha_G) \end{bmatrix}. \tag{B.9}$$

According to eqn. (B.9) it is possible to measure the global helix angle α_G for each tissue voxel and then compute the local helix angle α_L , rather than measuring it with respect to the local reference frame. In theory, however, the resulting values for α_L should be consistent, since in both cases the local reference frame is unchanged. Surprisingly, this

was not the case, as shown in Figure B.12. An evenly distributed sample from the whole set of tissue voxels contained in the left ventricular mask was obtained, and the associated values of α_G sorted in ascending order. The measured value of α_G (red points) and the corresponding computed α_L (black points) for each of the sample voxels is shown in Figure B.12(a). Analogously, the values of α_G (red points) and α_L (blue points), both measured by means of the algorithms of Section B.2 for the same sample of voxels are shown in Figure B.12(b). The computed and measured α_L distributions are in good agreement in terms of the general trend, however the computed α_L values are more spread. It is not clear how this difference in results arises, whether it is due to rounding errors in the computation of the rotation matrix, or it depends on inaccuracies introduced by the method to measure angular metrics. However, the spread distributions of α_L in the plots of Figure B.12 seem to support the idea that local measures are more appropriate to capture variability as opposed to global measures.

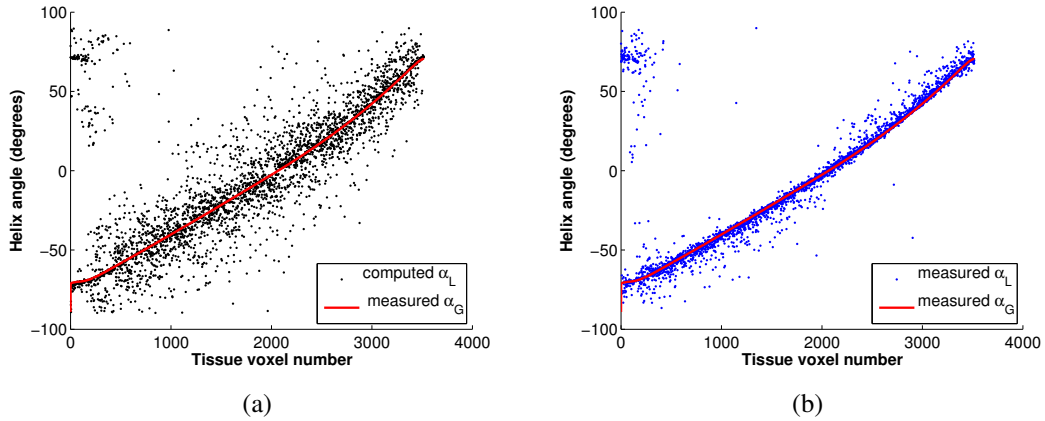


Figure B.12: Helix angle measures obtained with respect to the global coordinate system α_G for a sample of tissue voxels are sorted in ascending order (red points) and compared with corresponding (a) computed values of α_L (according to eqn. (B.9), black points); and (b) measured α_L (according to algorithms described in Section B.2, blue points).

B.4 Conclusions

In this appendix the results are shown of the preliminary study performed on a phantom dataset with the aim of developing the algorithms employed in Chapter 7 to measure angular metrics on DT-MRI images with respect to both a global and a local cylindrical reference frame. The phantom study aimed also at testing the hypotheses set in Section 7.1 about how, from a theoretical point of view, the local coordinate system approach to the measurement of angular metrics would be preferable to the one based on the global approach, in that it is

able to provide measurements that are not biased by the variability in the curvature of the ventricle and by the overall bulk motion of the tissue. The preliminary results of this section seem to support such hypotheses in that they show how the choice of the reference frame can affect the level of variability detected in tissue structure distribution, with considerable differences in the case of sheet and transverse angles. However, the comparison between the two methods leaves some important questions open, such as how to relate measured transmural variation of the sheet angle to the underlying sheet distribution, that need to be addressed in the future.

References

- [1] T. P. Abraham, V. L. Dimaano, and H.-Y. Y. Liang. Role of tissue doppler and strain echocardiography in current clinical practice. *Circulation*, 116(22):2597–2609, Nov. 2007.
- [2] J. Aguado-Sierra, A. Krishnamurthy, C. Villongco, J. Chuang, E. Howard, M. J. Gonzales, J. Omens, D. E. Krummen, S. Narayan, R. C. Kerckhoffs, and A. D. McCulloch. Patient-specific modeling of dyssynchronous heart failure: a case study. *Progress in biophysics and molecular biology*, 107(1):147–155, Oct. 2011.
- [3] A. H. Aitkenhead. *Mesh voxelisation (2010)*. MATLAB Central File Exchange. Retrieved 7 Feb 2011.
- [4] A. L. Alexander, K. M. Hasan, M. Lazar, J. S. Tsuruda, and D. L. Parker. Analysis of partial volume effects in diffusion-tensor MRI. *Magnetic resonance in medicine*, 45(5):770–780, May 2001.
- [5] H. Arevalo, B. Rodriguez, and N. Trayanova. Arrhythmogenesis in the heart: Multiscale modeling of the effects of defibrillation shocks and the role of electrophysiological heterogeneity. *Chaos (Woodbury, N.Y.)*, 17(1), Mar. 2007.
- [6] T. Arts, K. D. Costa, J. W. Covell, and A. D. McCulloch. Relating myocardial laminar architecture to shear strain and muscle fiber orientation. *American Journal of Physiology - Heart and Circulatory Physiology*, 280(5):H2222–H2229, May 2001.
- [7] T. Arts, J. Lumens, W. Kroon, D. Donker, F. Prinzen, and T. Delhaas. Patient-specific modeling of cardiovascular dynamics with a major role for adaptation. In R. C. Kerckhoffs, editor, *Patient-Specific Modeling of the Cardiovascular System*, pages 21–41. Springer New York, 2010.
- [8] K. F. Augenstein, B. R. Cowan, I. J. LeGrice, and A. A. Young. Estimation of cardiac hyperelastic material properties from MRI tissue tagging and diffusion tensor

- imaging. In R. Larsen, M. Nielsen, and J. Sporring, editors, *Medical Image Computing and Computer-Assisted Intervention MICCAI 2006*, volume 4190 of *Lecture Notes in Computer Science*, pages 628–635. Springer Berlin Heidelberg, 2006.
- [9] L. Axel, A. Montillo, and D. Kim. Tagged magnetic resonance imaging of the heart: a survey. *Medical Image Analysis*, 9(4):376–393, Aug. 2005.
- [10] P. J. Basser, J. Mattiello, and D. LeBihan. MR diffusion tensor spectroscopy and imaging. *Biophysical journal*, 66(1):259–267, Jan. 1994.
- [11] P. J. Basser and C. Pierpaoli. Microstructural and physiological features of tissues elucidated by quantitative-diffusion-tensor MRI. 1996. *Journal of magnetic resonance (San Diego, Calif. : 1997)*, 213(2):560–570, Dec. 2011.
- [12] G. W. Beeler and H. Reuter. Reconstruction of the action potential of ventricular myocardial fibres. *The Journal of physiology*, 268(1):177–210, June 1977.
- [13] P. Berens. Circstat: A MATLAB toolbox for circular statistics. *Journal of Statistical Software*, 31(10), 2009.
- [14] R. Berne and M. Levy. *Cardiovascular Physiology*. Mosby, 2001.
- [15] F. Billet, M. Sermesant, H. Delingette, and N. Ayache. Cardiac motion recovery by coupling an electromechanical model and Cine-MRI data: First steps. *The MIDAS journal*, Aug. 2008.
- [16] M. Bishop, P. Hales, G. Plank, D. Gavaghan, J. Scheider, and V. Grau. Comparison of Rule-Based and DTMRI-derived fibre architecture in a whole rat ventricular computational model. In N. Ayache, H. Delingette, and M. Sermesant, editors, *Functional Imaging and Modeling of the Heart*, volume 5528 of *Lecture Notes in Computer Science*, chapter 10, pages 87–96. Springer Berlin / Heidelberg, Berlin, Heidelberg, 2009.
- [17] M. J. Bishop, G. Plank, R. A. B. Burton, J. E. Schneider, D. J. Gavaghan, V. Grau, and P. Kohl. Development of an anatomically detailed MRI-derived rabbit ventricular model and assessment of its impact on simulations of electrophysiological function. *American Journal of Physiology - Heart and Circulatory Physiology*, 298(2):H699–H718, Feb. 2010.
- [18] P. M. Boiselle. *New Techniques in Cardiothoracic Imaging*. Taylor and Francis, 2007.

- [19] S. Bonekamp, C. P. Corona-Villalobos, and I. R. Kamel. Oncologic applications of diffusion-weighted MRI in the body. *Journal of magnetic resonance imaging : JMRI*, 35(2):257–279, Feb. 2012.
- [20] E. B. Bourgeois, V. G. Fast, R. L. Collins, J. D. Gladden, and J. M. Rogers. Change in conduction velocity due to fiber curvature in cultured neonatal rat ventricular myocytes. *IEEE transactions on bio-medical engineering*, 56(3):855–861, Mar. 2009.
- [21] P. H. M. Bovendeerd, W. Kroon, and T. Delhaas. Determinants of left ventricular shear strain. *American Journal of Physiology - Heart and Circulatory Physiology*, 297(3):H1058–H1068, 2009.
- [22] A. Bueno-Orovio, E. M. Cherry, and F. H. Fenton. Minimal model for human ventricular action potentials in tissue. *Journal of theoretical biology*, 253(3):544–560, Aug. 2008.
- [23] R. A. Burton, G. Plank, J. E. Schneider, V. Grau, H. Ahammer, S. L. Keeling, J. Lee, N. P. Smith, D. Gavaghan, N. A. Trayanova, and P. Kohl. Three-Dimensional models of individual cardiac histology: Tools and challenges. *Annals of the New York Academy of Sciences*, 1080(1):301–319, Oct. 2006.
- [24] V. Carapella, R. Bordas, P. Pathmanathan, J. E. Schneider, P. Kohl, K. Burrage, and V. Grau. Effect of fibre orientation optimisation in an electromechanical model of left ventricular contraction in rat. In S. Ourselin, D. Rueckert, and N. Smith, editors, *Functional Imaging and Modeling of the Heart*, volume 7945 of *Lecture Notes in Computer Science*, pages 46–53. Springer Berlin Heidelberg, 2013.
- [25] M. D. Cerqueira, N. J. Weissman, V. Dilsizian, A. K. Jacobs, S. Kaul, W. K. Laskey, D. J. Pennell, J. A. Rumberger, T. Ryan, M. S. Verani, and American Heart Association Writing Group on Myocardial Segmentation and Registration for Cardiac Imaging. Standardized myocardial segmentation and nomenclature for tomographic imaging of the heart: a statement for healthcare professionals from the cardiac imaging committee of the council on clinical cardiology of the american heart association. *Circulation*, 105(4):539–542, Jan. 2002.
- [26] D. Chemla, J. L. Hébert, C. Coirault, K. Zamani, I. Suard, P. Colin, and Y. Lecarpentier. Total arterial compliance estimated by stroke volume-to-aortic pulse pressure ratio in humans. *The American journal of physiology*, 274(2 Pt 2), Feb. 1998.

- [27] A. Cheng, T. C. Nguyen, M. Malinowski, G. T. Daughters, D. C. Miller, and N. B. Ingels. Heterogeneity of Left Ventricular Wall Thickening Mechanisms. *Circulation*, 118(7):713–721, Aug. 2008.
- [28] H. F. F. Choi, F. E. Rademakers, and P. Claus. Left-ventricular shape determines intramyocardial mechanical heterogeneity. *American journal of physiology. Heart and circulatory physiology*, 301(6), Dec. 2011.
- [29] CIBC, 2013. Seg3D: Volumetric Image Segmentation and Visualization. Scientific Computing and Imaging Institute (SCI), Download from: <http://www.seg3d.org>.
- [30] P. Colli-Franzone, L. Guerri, and B. Taccardi. Modeling ventricular excitation: axial and orthotropic anisotropy effects on wavefronts and potentials. *Mathematical Biosciences*, 188(1-2):191–205, Mar. 2004.
- [31] K. A. Connelly, D. L. Prior, D. J. Kelly, M. P. Feneley, H. Krum, and R. E. Gilbert. Load-sensitive measures may overestimate global systolic function in the presence of left ventricular hypertrophy: a comparison with load-insensitive measures. *American Journal of Physiology - Heart and Circulatory Physiology*, 290(4):H1699–H1705, Apr. 2006.
- [32] B. A. Coppola and J. H. Omens. Role of tissue structure on ventricular wall mechanics. *Molecular & cellular biomechanics : MCB*, 5(3):183–196, Sept. 2008.
- [33] J. M. Cordeiro, L. Greene, C. Heilmann, D. Antzelevitch, and C. Antzelevitch. Transmural heterogeneity of calcium activity and mechanical function in the canine left ventricle. *American journal of physiology. Heart and circulatory physiology*, 286(4):H1471–H1479, Apr. 2004.
- [34] K. D. Costa, J. W. Holmes, and A. D. McCulloch. Modelling cardiac mechanical properties in three dimensions. *Philosophical transactions of the Royal Society of London. Series A: Mathematical, physical and engineering sciences*, 359(1783):1233–1250, 2001.
- [35] J. W. Covell. Tissue structure and ventricular wall mechanics. *Circulation*, 118(7):699–701, Aug. 2008.
- [36] J.-L. Daire, J.-P. Jacob, J.-N. Hyacinthe, P. Croisille, K. Montet-Abou, S. Richter, D. Botsikas, M. Lepetit-Coiffé, D. Morel, and J.-P. Vallée. Cine and tagged cardiovascular magnetic resonance imaging in normal rat at 1.5 t: a rest and stress study. 10(1):1–10, 2008.

- [37] E. Dall'Armellina, B. A. Jung, C. A. Lygate, S. Neubauer, M. Markl, and J. E. Schneider. Improved method for quantification of regional cardiac function in mice using phase-contrast MRI. *Magnetic resonance in medicine*, 67(2):541–551, Feb. 2012.
- [38] B. Davies and T. Morris. Physiological parameters in laboratory animals and humans. 10(7):1093–1095, 1993.
- [39] E. H. de Figueiredo, A. F. Borgonovi, and T. M. Doring. Basic concepts of MR imaging, diffusion MR imaging, and diffusion tensor imaging. *Magnetic resonance imaging clinics of North America*, 19(1):1–22, Feb. 2011.
- [40] S. Dokos, B. H. Smaill, A. A. Young, and I. J. LeGrice. Shear properties of passive ventricular myocardium. *American journal of physiology. Heart and circulatory physiology*, 283(6), Dec. 2002.
- [41] F. Dorri, P. F. Niederer, P. P. Lunkenheimer, and R. H. Anderson. The architecture of the left ventricular myocytes relative to left ventricular systolic function. *European journal of cardio-thoracic surgery*, 37(2):384–392, Feb. 2010.
- [42] T. S. E. Eriksson, A. J. Prassl, G. Plank, and G. A. Holzapfel. Influence of myocardial fiber/sheet orientations on left ventricular mechanical contraction. *Mathematics and Mechanics of Solids*, 18(6):592–606, Aug. 2013.
- [43] R. Fitzhugh. Impulses and physiological states in theoretical models of nerve membrane. *Biophysical journal*, 1(6):445–466, July 1961.
- [44] G. M. Fomovsky, J. R. Macadangdang, G. Ailawadi, and J. W. Holmes. Model-based design of mechanical therapies for myocardial infarction. *Journal of cardiovascular translational research*, 4(1):82–91, Feb. 2011.
- [45] Y.-c. Fung. *Biomechanics : mechanical properties of living tissues*. New York ; London : Springer-Verlag, 2nd ed. edition, c1993.
- [46] A. Garny and P. Kohl. Mechanical induction of arrhythmias during ventricular repolarization. *Annals New York Academy of Science*, 1015:133–143, 2004.
- [47] L. Geerts, P. Bovendeerd, K. Nicolay, and T. Arts. Characterization of the normal cardiac myofiber field in goat measured with MR-diffusion tensor imaging. *American Journal of Physiology - Heart and Circulatory Physiology*, 283(1), July 2002.

- [48] L. Geerts, R. Kerckhoffs, P. Bovendeerd, and T. Arts. Towards patient specific models of cardiac mechanics: A sensitivity study. In I. E. Magnin, J. Montagnat, P. Clarysse, J. Nenonen, and T. Katila, editors, *Functional Imaging and Modeling of the Heart*, volume 2674 of *Lecture Notes in Computer Science*, chapter 9, pages 1006–1007. Springer Berlin / Heidelberg, 2003.
- [49] C. Geuzaine and J.-F. Remacle. Gmsh: a three-dimensional finite element mesh generator with built-in pre- and post-processing facilities. *International Journal for Numerical Methods in Engineering*, 79(11):1309–1331, 2009.
- [50] S. H. Gilbert, D. Benoist, A. P. Benson, E. White, S. F. Tanner, A. V. Holden, H. Dobrzynski, O. Bernus, and A. Radjenovic. Visualization and quantification of whole rat heart laminar structure using high-spatial resolution contrast-enhanced MRI. *American journal of physiology. Heart and circulatory physiology*, 302(1), jan 2012.
- [51] S. H. Gilbert, A. P. Benson, P. Li, and A. V. Holden. Regional localisation of left ventricular sheet structure: integration with current models of cardiac fibre, sheet and band structure. *European Journal of Cardio-Thoracic Surgery*, 32(2):231–249, Aug. 2007.
- [52] A. V. Glukhov, V. V. Fedorov, Q. Lou, V. K. Ravikumar, P. W. Kalish, R. B. Schuessler, N. Moazami, and I. R. Efimov. Transmural dispersion of repolarization in failing and nonfailing human ventricle. *Circulation Research*, 106(5):981–991, Mar. 2010.
- [53] R. A. Greenbaum, S. Y. Ho, D. G. Gibson, A. E. Becker, and R. H. Anderson. Left ventricular fibre architecture in man. *British heart journal*, 45(3):248–263, Mar. 1981.
- [54] J. M. Guccione, A. D. McCulloch, and L. K. Waldman. Passive material properties of intact ventricular myocardium determined from a cylindrical model. *Journal of biomechanical engineering*, 113(1):42–55, Feb. 1991.
- [55] A. Guimond, C. R. G. Guttman, S. K. Warfield, and C. F. Westin. Deformable registration of DT-MRI data based on transformation invariant tensor characteristics. In *IEEE, Biomedical Imaging, 2005, Proceedings of*, pages 761–764, 2002.

- [56] V. Gurev, J. Constantino, J. J. Rice, and N. A. Trayanova. Distribution of electromechanical delay in the heart: insights from a three-dimensional electromechanical model. *Biophysical journal*, 99(3):745–754, Aug. 2010.
- [57] P. W. Hales, J. E. Schneider, R. A. Burton, B. J. Wright, C. Bollensdorff, and P. Kohl. Histo-anatomical structure of the living isolated rat heart in two contraction states assessed by diffusion tensor MRI. *Progress in biophysics and molecular biology*, 110(2-3):319–330, Oct. 2012.
- [58] P. A. Helm, P. Caravan, B. A. French, V. Jacques, L. Shen, Y. Xu, R. J. Beyers, R. J. Roy, C. M. Kramer, and F. H. Epstein. Postinfarction myocardial scarring in mice: molecular MR imaging with use of a collagen-targeting contrast agent. *Radiology*, 247(3):788–796, June 2008.
- [59] P. A. Helm, H.-J. Tseng, L. Younes, E. R. McVeigh, and R. L. Winslow. Ex vivo 3D diffusion tensor imaging and quantification of cardiac laminar structure. *Magn. Reson. Med.*, 54(4):850–859, Oct. 2005.
- [60] R. M. Henkelman, G. J. Stanisz, J. K. Kim, and M. J. Bronskill. Anisotropy of NMR properties of tissues. *Magnetic resonance in medicine*, 32(5):592–601, Nov. 1994.
- [61] C. S. Henriquez. Simulating the electrical behavior of cardiac tissue using the bidomain model. *Critical reviews in biomedical engineering*, 21(1):1–77, 1993.
- [62] G. T. Herman, J. Zheng, and C. A. Bucholtz. Shape-based interpolation. *IEEE Computer Graphics and Applications*, 12(3):69–79, May 1992.
- [63] S. L. Herz, T. Hasegawa, A. N. Makaryus, K. M. Parker, S. Homma, J. Wang, and J. W. Holmes. Quantitative three-dimensional wall motion analysis predicts ischemic region size and location. *Annals of biomedical engineering*, 38(4):1367–1376, Apr. 2010.
- [64] S. L. Herz, C. M. Ingrassia, S. Homma, K. D. Costa, and J. W. Holmes. Parameterization of left ventricular wall motion for detection of regional ischemia. *Annals of Biomedical Engineering*, 33(7):912–919, July 2005.
- [65] A. L. Hodgkin and A. F. Huxley. A quantitative description of membrane current and its application to conduction and excitation in nerve. *The Journal of physiology*, 117(4):500–544, Aug. 1952.

- [66] G. Holzapfel and R. Ogden. Constitutive modelling of passive myocardium: a structurally based framework for material characterization. *Philosophical Transactions of the Royal Society A: Mathematical, Physical and Engineering Sciences*, 367(1902):3445–3475, Sept. 2009.
- [67] G. A. Holzapfel. *Nonlinear solid mechanics : a continuum approach for engineering*. Chichester : Wiley, 2000.
- [68] D. A. Hooks, M. L. Trew, B. J. Caldwell, G. B. Sands, I. J. LeGrice, and B. H. Smaill. Laminar arrangement of ventricular myocytes influences electrical behaviour in the heart. *Circulation Research*, 101(10):e103–e112, nov 2007.
- [69] H. J. Jacob, D. M. Brown, R. K. Bunker, M. J. Daly, V. J. Dzau, A. Goodman, G. Koike, V. Kren, T. Kurtz, A. Lernmark, G. Levan, Y.-p. Mao, A. Pettersson, M. Pravenec, J. S. Simon, C. Szpirer, J. Szpirer, M. R. Trolliet, E. S. Winer, and E. S. Lander. A genetic linkage map of the laboratory rat, *rattus norvegicus*. *Nature Genetics*, 9(1):63–69, Jan. 1995.
- [70] X. Jie and N. A. Trayanova. Mechanisms for initiation of reentry in acute regional ischemia phase 1B. *Heart rhythm : the official journal of the Heart Rhythm Society*, 7(3):379–386, Mar. 2010.
- [71] I. E. Karadag, M. Bishop, P. W. Hales, J. E. Schneider, P. Kohl, D. Gavaghan, and V. Grau. Regionally optimised mathematical models of cardiac myocyte orientation in rat hearts. volume 6666 of *Lecture Notes in Computer Science*, chapter 36, pages 294–301. Springer Berlin / Heidelberg, 2011.
- [72] A. M. Katz. *Physiology of the heart (3rd ed.)*. Philadelphia ; London : Lippincott Williams & Wilkins, 2001.
- [73] J. Keener and J. Sneyd. *Mathematical Physiology*. Springer-Verlag, New York, 1998.
- [74] R. H. Keldermann, M. P. Nash, H. Gelderblom, V. Y. Wang, and A. V. Panfilov. Electromechanical wavebreak in a model of the human left ventricle. *American Journal of Physiology - Heart and Circulatory Physiology*, 299(1):H134–H143, July 2010.

- [75] R. C. Kerckhoffs, P. H. Bovendeerd, J. C. Kotte, F. W. Prinzen, K. Smits, and T. Arts. Homogeneity of Cardiac Contraction Despite Physiological Asynchrony of Depolarization: A Model Study. *Annals of Biomedical Engineering*, 31(5):536–547, May 2003.
- [76] R. C. Kerckhoffs, Faris, P. H. Bovendeerd, F. W. Prinzen, K. Smits, E. R. McVeigh, and T. Arts. Electromechanics of paced left ventricle simulated by straightforward mathematical model: comparison with experiments. *American journal of physiology. Heart and circulatory physiology.*, 289(5), Nov. 2005.
- [77] R. C. P. Kerckhoffs, S. N. Healy, T. P. Usyk, and A. D. McCulloch. Computational methods for cardiac electromechanics. *Proceedings of the IEEE*, 94(4):769–783, Apr. 2006.
- [78] R. C. P. Kerckhoffs, J. H. Omens, A. D. McCulloch, and L. J. Mulligan. Ventricular dilation and electrical dyssynchrony synergistically increase regional mechanical nonuniformity but not mechanical dyssynchrony. *Circulation: Heart Failure*, 3(4):528–536, July 2010.
- [79] N. Kim, M. B. Cannell, and P. J. Hunter. Changes in the calcium current among different transmural regions contributes to action potential heterogeneity in rat heart. *Progress in Biophysics and Molecular Biology*, 103(1):28–34, Sept. 2010.
- [80] P. B. Kingsley. Introduction to diffusion tensor imaging mathematics: Part II. anisotropy, diffusion-weighting factors, and gradient encoding schemes. *Concepts Magn. Reson.*, 28A(2):123–154, Mar. 2006.
- [81] R. E. Klabunde. *Cardiovascular Physiology Concepts*. Lippincott Williams & Wilkins, 2005.
- [82] M. Kobylecka, J. Mczewska, K. Fronczewska-Wieniawska, T. Mazurek, M. T. T. Płazińska, and L. Królicki. Myocardial viability assessment in 18FDG PET/CT study (18FDG PET myocardial viability assessment). *Nuclear medicine review. Central & Eastern Europe*, 15(1):52–60, 2012.
- [83] P. Kohl, F. Sachs, and M. R. Franz. *Cardiac Mechano-Electric Feedback and Arrhythmias: from pipette to patient*. Elsevier Saunders, 2005.
- [84] S. Köhler, K.-H. H. Hiller, C. Waller, W. R. Bauer, A. Haase, and P. M. Jakob. Investigation of the microstructure of the isolated rat heart: a comparison between

- t*2- and diffusion-weighted MRI. *Magnetic resonance in medicine*, 50(6):1144–1150, Dec. 2003.
- [85] G. J. Krinke, editor. *The Laboratory rat*. Academic Press, 2000.
- [86] W. Kroon, T. Delhaas, P. H. Bovendeerd, and T. Arts. Computational analysis of the myocardial structure: Adaptation of cardiac myofiber orientations through deformation. *Medical Image Analysis*, 13(2):346–353, Apr. 2009.
- [87] N. H. Kuijpers, E. Hermeling, P. H. Bovendeerd, T. Delhaas, and F. W. Prinzen. Modeling cardiac electromechanics and mechano-electrical coupling in dyssynchronous and failing hearts: insight from adaptive computer models. *Journal of cardiovascular translational research*, 5(2):159–169, Apr. 2012.
- [88] K. Kusunose, M. S. Penn, Y. Zhang, Y. Cheng, J. D. Thomas, T. H. Marwick, and Z. B. Popović. How similar are the mice to men? between-species comparison of left ventricular mechanics using strain imaging. *PloS one*, 7(6), 2012.
- [89] P. Lafortune, R. Aris, M. Vazquez, and G. Houzeaux. Coupled electromechanical model of the heart: Parallel finite element formulation. *International Journal for Numerical Methods in Biomedical Engineering*, 28(1):72–86, 2012.
- [90] S. Land, S. A. Niederer, J. M. Aronsen, E. K. S. Espe, L. Zhang, W. E. Louch, I. Sjaastad, O. M. Sejersted, and N. P. Smith. An analysis of deformation-dependent electromechanical coupling in the mouse heart. *The Journal of Physiology*, 590(18):4553–4569, Sept. 2012.
- [91] D. Le Bihan, E. Breton, D. Lallemand, P. Grenier, E. Cabanis, and M. Laval-Jeantet. MR imaging of intravoxel incoherent motions: application to diffusion and perfusion in neurologic disorders. *Radiology*, 161(2):401–407, Nov. 1986.
- [92] J. Lee, S. A. Niederer, D. A. Nordsletten, I. J. LeGrice, B. Smail, D. Kay, and N. P. Smith. Coupling contraction, excitation, ventricular and coronary blood flow across scale and physics in the heart. *Physical and Engineering Sciences*, 367(1896):2311–2331, June 2009.
- [93] I. J. LeGrice, P. J. Hunter, and B. H. Smaill. Laminar structure of the heart: a mathematical model. *American Journal of Physiology - Heart and Circulatory Physiology*, 272(5):H2466–H2476, 1997.

- [94] I. J. LeGrice, B. H. Smaill, L. Z. Chai, S. G. Edgar, J. B. Gavin, and P. J. Hunter. Laminar structure of the heart: ventricular myocyte arrangement and connective tissue architecture in the dog. *American Journal of Physiology - Heart and Circulatory Physiology*, 269(2):H571–H582, Aug. 1995.
- [95] C. Levy, H. E. Ter Keurs, Y. Yaniv, and A. Landesberg. The sarcomeric control of energy conversion. *Annals of the New York Academy of Sciences*, 1047:219–231, June 2005.
- [96] D. H. Lin and F. C. Yin. A multiaxial constitutive law for mammalian left ventricular myocardium in steady-state barium contracture or tetanus. *Journal of biomechanical engineering*, 120(4):504–517, Aug. 1998.
- [97] C. M. Lloyd, M. D. Halstead, and P. F. Nielsen. CellML: its future, present and past. *Progress in biophysics and molecular biology*, 85(2-3):433–450, July 2004.
- [98] H. Lombaert, J.-M. M. Peyrat, P. Croisille, S. Rapacchi, L. Fanton, F. Cheriet, P. Clarysse, I. Magnin, H. Delingette, and N. Ayache. Human atlas of the cardiac fiber architecture: study on a healthy population. *IEEE transactions on medical imaging*, 31(7):1436–1447, July 2012.
- [99] A. Luk, E. Ahn, G. S. Soor, and J. Butany. Dilated cardiomyopathy: a review. *Journal of clinical pathology*, 62(3):219–225, Mar. 2009.
- [100] C. H. Luo and Y. Rudy. A model of the ventricular cardiac action potential. depolarization, repolarization, and their interaction. *Circulation Research*, 68(6):1501–1526, June 1991.
- [101] C. H. Luo and Y. Rudy. A dynamic model of the cardiac ventricular action potential. i. simulations of ionic currents and concentration changes. *Circulation research*, 74(6):1071–1096, June 1994.
- [102] A. Mahajan, Y. Shiferaw, D. Sato, A. Baher, R. Olcese, L.-H. H. Xie, M.-J. J. Yang, P.-S. S. Chen, J. G. Restrepo, A. Karma, A. Garfinkel, Z. Qu, and J. N. Weiss. A rabbit ventricular action potential model replicating cardiac dynamics at rapid heart rates. *Biophysical journal*, 94(2):392–410, Jan. 2008.
- [103] T. H. Marwick and M. Schwaiger. The future of cardiovascular imaging in the diagnosis and management of heart failure, part 1. *Circulation: Cardiovascular Imaging*, 1(1):58–69, July 2008.

- [104] R. Mazhari, J. H. Omens, J. W. Covell, and A. D. McCulloch. Structural basis of regional dysfunction in acutely ischemic myocardium. *Cardiovascular research*, 47(2):284–293, Aug. 2000.
- [105] G. R. Mirams, C. J. Arthurs, M. O. Bernabeu, R. Bordas, J. Cooper, A. Corrias, Y. Davit, S.-J. Dunn, A. G. Fletcher, D. G. Harvey, M. E. Marsh, J. M. Osborne, P. Pathmanathan, J. Pitt-Francis, J. Southern, N. Zemzemi, and D. J. Gavaghan. Chaste: An open source c++ library for computational physiology and biology. *PLoS Comput Biol*, 9(3):e1002970+, Mar. 2013.
- [106] I. Mirsky. Assessment of passive elastic stiffness of cardiac muscle: mathematical concepts, physiologic and clinical considerations, directions of future research. *Progress in cardiovascular diseases*, 18(4):277–308, 1976.
- [107] P. D. Mullins and V. E. Bondarenko. A mathematical model of the mouse ventricular myocyte contraction. *PLoS ONE*, 8(5), May 2013.
- [108] J. Nagumo, S. Arimoto, and S. Yoshizawa. An active pulse transmission line simulating nerve axon. *Proceedings of the IRE*, 50(10):2061–2070, 1962.
- [109] M. Nash and P. Hunter. Computational mechanics of the heart. *Journal of Elasticity*, 61(1):113–141, July 2000.
- [110] M. P. Nash and A. V. Panfilov. Electromechanical model of excitable tissue to study reentrant cardiac arrhythmias. *Progress in Biophysics and Molecular Biology*, 85(2-3):501–522, 2004.
- [111] M. L. L. Neal and R. Kerckhoffs. Current progress in patient-specific modeling. *Briefings in bioinformatics*, 11(1):111–126, Jan. 2010.
- [112] S. A. Niederer, P. J. Hunter, and N. P. Smith. A quantitative analysis of cardiac myocyte relaxation: A simulation study. *Biophysical Journal*, 90(5):1697–1722, Mar. 2006.
- [113] S. A. Niederer, P. Lamata, G. Plank, P. Chinchapatnam, M. Ginks, K. Rhode, C. A. Rinaldi, R. Razavi, and N. P. Smith. Analyses of the redistribution of work following cardiac resynchronisation therapy in a patient specific model. *PLoS ONE*, 7(8):e43504+, Aug. 2012.

- [114] S. A. Niederer and N. P. Smith. The role of the FrankStarling law in the transduction of cellular work to whole organ pump function: A computational modeling analysis. *PLoS Comput Biol*, 5(4):e1000371+, Apr. 2009.
- [115] S. A. Niederer, H. E. D. J. Ter Keurs, and N. P. Smith. Modelling and measuring electromechanical coupling in the rat heart. *Experimental Physiology*, 94(5):529–540, 2009.
- [116] S. Nielles-Vallespin, C. Mekkaoui, P. Gatehouse, T. G. Reese, J. Keegan, P. F. Ferreira, S. Collins, P. Speier, T. Feiweier, R. de Silva, M. P. Jackowski, D. J. Pennell, D. E. Sosnovik, and D. Firmin. In vivo diffusion tensor MRI of the human heart: reproducibility of breath-hold and navigator-based approaches. *Magnetic resonance in medicine*, 70(2):454–465, Aug. 2013.
- [117] P. M. Nielsen, I. J. Le Grice, B. H. Smaill, and P. J. Hunter. Mathematical model of geometry and fibrous structure of the heart. *The American journal of physiology*, 260(4 Pt 2):H1365–1378, Apr. 1991.
- [118] D. Noble. A modification of the hodgkinhuxley equations applicable to purkinje fibre action and pacemaker potentials. *The Journal of Physiology*, 160(2):317–352, 1962.
- [119] J. H. Omens, D. A. MacKenna, and A. D. McCulloch. Measurement of strain and analysis of stress in resting rat left ventricular myocardium. *Journal of Biomechanics*, 26(6):665–676, June 1993.
- [120] N. Otsu. A threshold selection method from gray-level histograms. *Automatica*, 11(285-296):23–27, 1975.
- [121] L. Ou, W. Li, Y. Liu, Y. Zhang, S. Jie, D. Kong, G. Steinhoff, and N. Ma. Animal models of cardiac disease and stem cell therapy. *The open cardiovascular medicine journal*, 4:231–239, 2010.
- [122] S. V. Pandit, R. B. Clark, W. R. Giles, and S. S. Demir. A mathematical model of action potential heterogeneity in adult rat left ventricular myocytes. *Biophysical journal*, 81(6):3029–3051, Dec. 2001.
- [123] P. Pathmanathan, M. O. Bernabeu, R. Bordas, J. Cooper, A. Garny, J. M. Pitt-Francis, J. P. Whiteley, and D. J. Gavaghan. A numerical guide to the solution of the bidomain equations of cardiac electrophysiology. *Progress in Biophysics and Molecular Biology*, 102(2-3):136–155, June 2010.

- [124] P. Pathmanathan, S. J. Chapman, D. J. Gavaghan, and J. P. Whiteley. Cardiac Electromechanics: The Effect of Contraction Model on the Mathematical Problem and Accuracy of the Numerical Scheme. *The Quarterly Journal of Mechanics and Applied Mathematics*, 63(3):375–399, Aug. 2010.
- [125] P. Pathmanathan and J. Whiteley. A Numerical Method for Cardiac Mechanoelectric Simulations. *Annals of Biomedical Engineering*, 37(5):860–873, May 2009.
- [126] S. Patil and B. Ravi. Voxel-based representation, display and thickness analysis of intricate shapes. In *Computer Aided Design and Computer Graphics, 2005. Ninth International Conference on*, pages 6 pp.+. IEEE, Dec. 2005.
- [127] O. H. Petersen. *Lecture notes: Human physiology*. Wiley-Blackwell, 2007.
- [128] J. M. Peyrat, M. Sermesant, X. Pennec, H. Delingette, C. Xu, E. R. McVeigh, and N. Ayache. A computational framework for the statistical analysis of cardiac diffusion tensors: Application to a small database of canine hearts. *IEEE Transactions on Medical Imaging*, 26(11):1500–1514, Nov. 2007.
- [129] G. Plank, R. A. B. Burton, P. Hales, M. Bishop, T. Mansoori, M. O. Bernabeu, A. Garny, A. J. Prassl, C. Bollensdorff, F. Mason, F. Mahmood, B. Rodriguez, V. Grau, J. E. Schneider, D. Gavaghan, and P. Kohl. Generation of histo-anatomically representative models of the individual heart: tools and application. *Physical and Engineering Sciences*, 367(1896):2257–2292, June 2009.
- [130] R. A. Pooley. Fundamental physics of MR imaging. *Radiographics*, 25(4):1087–1099, July 2005.
- [131] A. J. Pope, G. B. Sands, B. H. Smaill, and I. J. LeGrice. Three-dimensional transmural organization of perimysial collagen in the heart. *American journal of physiology. Heart and circulatory physiology*, 295(3):H1243–1252, Sept. 2008.
- [132] M. Potse, B. Dube, A. Vinet, and R. M. Gulrajani. A comparison of monodomain and bidomain reaction-diffusion models for action potential propagation in the human heart. *IEEE Transactions on Biomedical Engineering*, 53(12):2425–2435, Aug. 2006.
- [133] A. J. Pullan, L. K. Cheng, and M. L. Buist. *Mathematically Modelling the Electrical Activity of the Heart: From Cell to Body Surface and Back Again*. World Scientific Publishing, 2005.

- [134] A. J. Pullan, K. A. Tomlinson, and P. J. Hunter. A finite element method for an eikonal equation model of myocardial excitation wavefront propagation. *SIAM J. Appl. Math.*, 63(1):324–350, 2002.
- [135] S. P. Raya and J. K. Udupa. Shape-based interpolation of multidimensional objects. *IEEE Transactions on Medical Imaging*, 9(1):32–42, Mar. 1990.
- [136] J. Reddy. *An Introduction to the Finite Element Method*. McGraw-Hill, 1993.
- [137] T. G. Reese, R. M. Weisskoff, R. N. Smith, B. R. Rosen, R. E. Dinsmore, and V. J. Wedeen. Imaging myocardial fiber architecture in vivo with magnetic resonance. *Magnetic Resonance in Medicine*, 34(6), Dec. 1995.
- [138] J. J. Rice, M. S. Jafri, and R. L. Winslow. Modeling short-term interval-force relations in cardiac muscle. *American journal of physiology. Heart and circulatory physiology*, 278(3), Mar. 2000.
- [139] B. Rodriguez, L. Li, J. C. Eason, I. R. Efimov, and N. A. Trayanova. Differences between left and right ventricular chamber geometry affect cardiac vulnerability to electric shocks. *Circulation Research*, 97(2):168–175, July 2005.
- [140] Y. Rudy and J. R. Silva. Computational biology in the study of cardiac ion channels and cell electrophysiology. *Quarterly reviews of biophysics*, 39(1):57–116, February 2006.
- [141] J. Sainte-Marie, D. Chapelle, R. Cimrman, and M. Sorine. Modeling and estimation of the cardiac electromechanical activity. *Computers & Structures*, 84(28):1743–1759, Nov. 2006.
- [142] K. J. Sampson and C. S. Henriquez. Electrotonic influences on action potential duration dispersion in small hearts: a simulation study. *American journal of physiology. Heart and circulatory physiology*, 289(1), July 2005.
- [143] G. B. Sands, D. A. Gerneke, D. A. Hooks, C. R. Green, B. H. Smaill, and I. J. Legrice. Automated imaging of extended tissue volumes using confocal microscopy. *Microscopy research and technique*, 67(5):227–239, Aug. 2005.
- [144] H. Satoh, L. M. Delbridge, L. A. Blatter, and D. M. Bers. Surface:volume relationship in cardiac myocytes studied with confocal microscopy and membrane capacitance measurements: species-dependence and developmental effects. *Biophysical journal*, 70(3):1494–1504, Mar. 1996.

- [145] D. F. Scollan, A. Holmes, R. Winslow, and J. Forder. Histological validation of myocardial microstructure obtained from diffusion tensor magnetic resonance imaging. *American Journal of Physiology - Heart and Circulatory Physiology*, 275(6):H2308–H2318, Dec. 1998.
- [146] M. Sermesant, R. Chabiniok, P. Chinchapatnam, T. Mansi, F. Billet, P. Moireau, J. M. Peyrat, K. Wong, J. Relan, K. Rhode, M. Ginks, P. Lambiase, H. Delingette, M. Sorine, C. A. Rinaldi, D. Chapelle, R. Razavi, and N. Ayache. Patient-specific electromechanical models of the heart for the prediction of pacing acute effects in CRT: a preliminary clinical validation. *Medical image analysis*, 16(1):201–215, Jan. 2012.
- [147] M. Sermesant, H. Delingette, and N. Ayache. An electromechanical model of the heart for image analysis and simulation. *IEEE Transactions on Medical Imaging*, 25(5):612–625, May 2006.
- [148] M. Sermesant, P. Moireau, O. Camara, J. Sainte-Marie, R. Andriantsimiavona, R. Cimrman, D. L. G. Hill, D. Chapelle, and R. Razavi. Cardiac function estimation from MRI using a heart model and data assimilation: Advances and difficulties. In A. F. Frangi, P. I. Radeva, A. Santos, and M. Hernandez, editors, *Functional Imaging and Modeling of the Heart*, volume 3504, chapter 33, pages 325–337. Springer Berlin Heidelberg, 2005.
- [149] M. E. Shenton, H. M. Hamoda, J. S. Schneiderman, S. Bouix, O. Pasternak, Y. Rath, M.-A. A. Vu, M. P. Purohit, K. Helmer, I. Koerte, A. P. Lin, C.-F. F. Westin, R. Kikinis, M. Kubicki, R. A. Stern, and R. Zafonte. A review of magnetic resonance imaging and diffusion tensor imaging findings in mild traumatic brain injury. *Brain imaging and behavior*, 6(2):137–192, June 2012.
- [150] S. Sicouri and C. Antzelevitch. A subpopulation of cells with unique electrophysiological properties in the deep subepicardium of the canine ventricle. the m cell. *Circulation research*, 68(6):1729–1741, June 1991.
- [151] R. M. Simpson, J. Keegan, and D. N. Firmin. MR assessment of regional myocardial mechanics. *Journal of magnetic resonance imaging : JMRI*, 37(3):576–599, Mar. 2013.
- [152] D. E. Sosnovik, R. Wang, G. Dai, T. G. Reese, and V. J. Wedeen. Diffusion MR tractography of the heart. *Journal of cardiovascular magnetic resonance*, 11, 2009.

- [153] M. R. Starling. Left ventricular-arterial coupling relations in the normal human heart. *American heart journal*, 125(6):1659–1666, June 1993.
- [154] M. R. Starling, D. G. Montgomery, G. B. Mancini, and R. A. Walsh. Load independence of the rate of isovolumic relaxation in man. *Circulation*, 76(6):1274–1281, Dec. 1987.
- [155] E. O. Stejskal and J. E. Tanner. Spin diffusion measurements: Spin echoes in the presence of a Time-Dependent field gradient. *The Journal of Chemical Physics*, 42(1):288–292, 1965.
- [156] C. Stevens, E. Remme, I. LeGrice, and P. Hunter. Ventricular mechanics in diastole: material parameter sensitivity. *Journal of biomechanics*, 36(5):737–748, May 2003.
- [157] D. D. Streeter and W. T. Hanna. Engineering mechanics for successive states in canine left ventricular myocardium. i. cavity and wall geometry. *Circulation Research*, 33(6):639–655, Dec. 1973.
- [158] D. D. Streeter, H. M. Spotnitz, D. Patel, J. Ross, and E. H. Sonnenblick. Fiber orientation in the canine left ventricle during diastole and systole. *Circ. Res.*, 24:339–347, 1969.
- [159] E. Süli and D. Mayers. *An Introduction to Numerical Analysis*. Cambridge University Press, 2003.
- [160] K. H. ten Tusscher, D. Noble, P. J. Noble, and A. V. Panfilov. A model for human ventricular tissue. *American journal of physiology. Heart and circulatory physiology*, 286(4):H1573–H1589, Apr. 2004.
- [161] N. Toussaint, C. T. Stoeck, T. Schaeffter, S. Kozerke, M. Sermesant, and P. G. Batchelor. In vivo human cardiac fibre architecture estimation using shape-based diffusion tensor processing. *Medical image analysis*, Mar. 2013.
- [162] N. A. Trayanova. Whole-Heart modeling: Applications to cardiac electrophysiology and electromechanics. *Circulation Research*, 108(1):113–128, Jan. 2011.
- [163] N. A. Trayanova, J. Constantino, and V. Gurev. Electromechanical models of the ventricles. *American journal of physiology. Heart and circulatory physiology*, 301(2), Aug. 2011.

- [164] W.-Y. Y. Tseng, V. J. Wedeen, T. G. Reese, R. N. Smith, and E. F. Halpern. Diffusion tensor MRI of myocardial fibers and sheets: correspondence with visible cut-face texture. *Journal of magnetic resonance imaging : JMRI*, 17(1):31–42, Jan. 2003.
- [165] S. W. Ubbink, P. H. Bovendeerd, T. Delhaas, T. Arts, and F. N. van de Vosse. Towards model-based analysis of cardiac MR tagging data: relation between left ventricular shear strain and myofiber orientation. *Medical image analysis*, 10(4):632–641, Aug. 2006.
- [166] T. P. Usyk, R. Mazhari, and A. D. McCulloch. Effect of Laminar Orthotropic Myofiber Architecture on Regional Stress and Strain in the Canine Left Ventricle. *Journal of Elasticity*, 61:143–164, 2000.
- [167] T. P. Usyk and A. McCulloch. Computational methods for soft tissue biomechanics. In G. A. Holzapfel and R. Ogden, editors, *Biomechanics of soft tissue in cardiovascular systems*. Springer-Verlag, 2003.
- [168] T. P. Usyk and A. D. McCulloch. Relationship between regional shortening and asynchronous electrical activation in a Three-Dimensional model of ventricular electromechanics. *Journal of Cardiovascular Electrophysiology*, 14:S196–S202, 2003.
- [169] F. Vadakkumpadan, H. Arevalo, A. J. Prassl, J. Chen, F. Kickinger, P. Kohl, G. Plank, and N. A. Trayanova. Image-based models of cardiac structure in health and disease. *Wiley interdisciplinary reviews. Systems biology and medicine*, 2(4):489–506, 2010.
- [170] A. Varghese and D. J. Pennell. *Cardiovascular Magnetic Resonance Made Easy*. Elsevier Health Sciences, 2007.
- [171] A. I. Veress, W. P. Segars, B. M. Tsui, and G. T. Gullberg. Incorporation of a left ventricle finite element model defining infarction into the XCAT imaging phantom. *IEEE transactions on medical imaging*, 30(4):915–927, Apr. 2011.
- [172] F. Vetter and A. D. McCulloch. Mechanoelectric feedback in a model of the passively inflated left ventricle. *Annals of Biomedical Engineering*, 29(5):414–426, May 2001.
- [173] J. C. Walker, M. B. Ratcliffe, P. Zhang, A. W. Wallace, B. Fata, E. W. Hsu, D. Saloner, and J. M. Guccione. MRI-based finite-element analysis of left ventricular aneurysm. *American journal of physiology. Heart and circulatory physiology*, 289(2), Aug. 2005.

- [174] R. D. Walton and O. Bernus. Electrotonic effects on action potential duration in perfused rat hearts. *Conf Proc IEEE Eng Med Biol Soc*, 2009:4190–4193, Sept. 2009.
- [175] H. M. Wang, H. Gao, X. Y. Luo, C. Berry, B. E. Griffith, R. W. Ogden, and T. J. Wang. Structure-based finite strain modelling of the human left ventricle in diastole. *Int. J. Numer. Meth. Biomed. Engng.*, 29(1):83–103, Jan. 2013.
- [176] L. J. Wang and E. A. Sobie. Mathematical model of the neonatal mouse ventricular action potential. *American journal of physiology. Heart and circulatory physiology*, 294(6):H2565–H2575, June 2008.
- [177] V. Y. Wang, H. I. Lam, D. B. Ennis, B. R. Cowan, A. A. Young, and M. P. Nash. Modelling passive diastolic mechanics with quantitative MRI of cardiac structure and function. *Medical image analysis*, 13(5):773–784, Oct. 2009.
- [178] H. Watanabe, S. Sugiura, H. Kafuku, and T. Hisada. Multiphysics simulation of left ventricular filling dynamics using fluid-structure interaction finite element method. *Biophysical journal*, 87(3):2074–2085, Sept. 2004.
- [179] J. F. Wenk, K. Sun, Z. Zhang, M. Soleimani, L. Ge, D. Saloner, A. W. Wallace, M. B. Ratcliffe, and J. M. Guccione. Regional left ventricular myocardial contractility and stress in a finite element model of posterobasal myocardial infarction. *Journal of biomechanical engineering*, 133(4), Apr. 2011.
- [180] J. Whiteley, M. Bishop, and D. Gavaghan. Soft tissue modelling of cardiac fibres for use in coupled Mechano-Electric simulations. *Bulletin of Mathematical Biology*, 69(7):2199–2225, Oct. 2007.
- [181] R. G. Wise, C. L. Huang, G. A. Gresham, A. I. M. Al-Shafei, T. A. Carpenter, and L. D. Hall. Magnetic resonance imaging analysis of left ventricular function in normal and spontaneously hypertensive rats. *The Journal of Physiology*, 513(3):873–887, Dec. 1998.
- [182] J. Xi, P. Lamata, S. Niederer, S. Land, W. Shi, X. Zhuang, S. Ourselin, S. G. Duckett, A. K. Shetty, C. A. Rinaldi, D. Rueckert, R. Razavi, and N. P. Smith. The estimation of patient-specific cardiac diastolic functions from clinical measurements. *Medical Image Analysis*, 17(2):133–146, Feb. 2013.

- [183] C. Xu, J. Pilla, G. Isaac, J. Gorman, A. Blom, R. Gorman, Z. Ling, and L. Dougherty. Deformation analysis of 3D tagged cardiac images using an optical flow method. *Journal of Cardiovascular Magnetic Resonance*, 12(1):19+, 2010.
- [184] H. Yuxuan, V. Gurev, J. Constantino, and N. Trayanova. Optimizing CRT to minimize ATP consumption heterogeneity throughout the left ventricle: A simulation analysis using a canine heart failure model. *Heart rhythm : the official journal of the Heart Rhythm Society*, Mar. 2014.
- [185] X. Zhong, L. Gibberman, B. Spottiswoode, A. Gilliam, C. Meyer, B. French, and F. Epstein. Comprehensive cardiovascular magnetic resonance of myocardial mechanics in mice using three-dimensional cine DENSE. *Journal of Cardiovascular Magnetic Resonance*, 13(1):83+, 2011.